

ISSN 2071-4726  
2071-0305

# Инженерно-строительный журнал

НАУЧНОЕ ИЗДАНИЕ

№1(93) 2020





**ПОЛИТЕХ**  
Санкт-Петербургский  
политехнический университет  
Петра Великого

**Инженерно-строительный институт**  
Центр дополнительных профессиональных программ  
195251, г. Санкт-Петербург, Политехническая ул., 29,  
тел/факс: 552-94-60, [www.stroikursi.spbstu.ru](http://www.stroikursi.spbstu.ru),  
[stroikursi@mail.ru](mailto:stroikursi@mail.ru)

**Приглашает специалистов организаций, вступающих в СРО,  
на курсы повышения квалификации (72 часа)**

Код	Наименование программы	Виды работ*
<b>Курсы по строительству</b>		
<b>БС-01-04</b>	«Безопасность и качество выполнения общестроительных работ»	п.1,2, 3, 5, 6, 7, 9, 10, 11, 12, 13, 14
<b>БС-01</b>	«Безопасность и качество выполнения геодезических, подготовительных и земляных работ, устройства оснований и фундаментов»	1,2,3,5
<b>БС-02</b>	«Безопасность и качество возведения бетонных и железобетонных конструкций»	6,7
<b>БС-03</b>	«Безопасность и качество возведения металлических, каменных и деревянных конструкций»	9,10,11
<b>БС-04</b>	«Безопасность и качество выполнения фасадных работ, устройства кровель, защиты строительных конструкций, трубопроводов и оборудования»	12,13,14
<b>БС-05</b>	«Безопасность и качество устройства инженерных сетей и систем»	15,16,17,18,19
<b>БС-06</b>	«Безопасность и качество устройства электрических сетей и линий связи»	20,21
<b>БС-08</b>	«Безопасность и качество выполнения монтажных и пусконаладочных работ»	23,24
<b>БС-12</b>	«Безопасность и качество устройства мостов, эстакад и путепроводов»	29
<b>БС-13</b>	«Безопасность и качество выполнения гидротехнических, водолазных работ»	30
<b>БС-14</b>	«Безопасность и качество устройства промышленных печей и дымовых труб»	31
<b>БС-15</b>	«Осуществление строительного контроля»	32
<b>БС-16</b>	«Организация строительства, реконструкции и капитального ремонта. Выполнение функций технического заказчика и генерального подрядчика»	33
<b>Курсы по проектированию</b>		
<b>БП-01</b>	«Разработка схемы планировочной организации земельного участка, архитектурных решений, мероприятий по обеспечению доступа маломобильных групп населения»	1,2,11
<b>БП-02</b>	«Разработка конструктивных и объемно-планировочных решений зданий и сооружений»	3
<b>БП-03</b>	«Проектирование внутренних сетей инженерно-технического обеспечения»	4
<b>БП-04</b>	«Проектирование наружных сетей инженерно-технического обеспечения»	5
<b>БП-05</b>	«Разработка технологических решений при проектировании зданий и сооружений»	6
<b>БП-06</b>	«Разработка специальных разделов проектной документации»	7
<b>БП-07</b>	«Разработка проектов организации строительства»	8
<b>БП-08</b>	«Проектные решения по охране окружающей среды»	9
<b>БП-09</b>	«Проектные решения по обеспечению пожарной безопасности»	10
<b>БП-10</b>	«Обследование строительных конструкций и грунтов основания зданий и сооружений»	12
<b>БП-11</b>	«Организация проектных работ. Выполнение функций генерального проектировщика»	13
<b>Э-01</b>	«Проведение энергетических обследований с целью повышения энергетической эффективности и энергосбережения»	
<b>Курсы по инженерным изысканиям</b>		
<b>И-01</b>	«Инженерно-геодезические изыскания в строительстве»	1
<b>И-02</b>	«Инженерно-геологические изыскания в строительстве»	2,5
<b>И-03</b>	«Инженерно-гидрометеорологические изыскания в строительстве»	3
<b>И-04</b>	«Инженерно-экологические изыскания в строительстве»	4
<b>И-05</b>	«Организация работ по инженерным изысканиям»	7

\*(согласно приказам Минрегионразвития РФ N 624 от 30 декабря 2009 г.)

**По окончании курса слушателю выдается удостоверение о краткосрочном повышении  
квалификации установленного образца (72 ак. часа)**

Для регистрации на курс необходимо выслать заявку на участие, и копию диплома об образовании по телефону/факсу: 8(812) 552-94-60, 535-79-92, , e-mail: [stroikursi@mail.ru](mailto:stroikursi@mail.ru).



DOI: 10.18720/MCE.93.1

## Lightweight geopolymers made of mineral wool production waste

V.T. Erofeev<sup>a</sup>, A.I. Rodin<sup>a\*</sup>, V.S. Bochkin<sup>b</sup>, V.V. Yakunin<sup>a</sup>, A.A. Ermakov<sup>a</sup>

<sup>a</sup> Ogarev Mordovia State University, Saransk, Russia

<sup>b</sup> LLC «Kombinat teploizolyacionnyh izdelij», Saransk, Respublika Mordoviya, Russia

\* E-mail: [al\\_rodin@mail.ru](mailto:al_rodin@mail.ru)

**Keywords:** geopolymers, slags, caustic soda, concretes, compressive strength, thermal insulation

**Abstract.** Reducing industrial slags and developing building materials on its basis is one of the priority areas for the development of the construction industry. The problem of obtaining cellular concrete from mineral wool production waste (lightweight geopolymers) is considered within the framework of the researches, the results of which are presented in the article. The research purpose was to establish the impact of composition of the raw material mixture and technological production features on the physical, mechanical and thermophysical properties of light geopolymers based on mineral wool production waste. Light geopolymers were obtained by preparing a mixture of ground slugs (specific surface is  $400 \pm 20$  m<sup>2</sup>/kg), alkaline activator (NaOH), water, a gas-forming additive (aluminum powder), fine aggregate and a water-holding additive. The resulting mixture was placed in the form without vibration. Molded products were steamed in order to accelerate hardening. The mobility of mortar mixtures was studied during the work, the average density, compressive strength, and thermal conductivity was studied for hardened samples. The compositions of lightweight geopolymers with an average density from 610 to 1,130 kg/m<sup>3</sup>, compressive strength from 1.7 to 5.4 MPa, and a thermal conductivity from 0.144 to 0.345 W/m·°C were obtained. The application of the results will contribute to the expansion of the raw material base for obtaining light geopolymers, thereby reducing the amount of waste generated during the mineral wool production. The developed materials can be used for the construction of walling, and also as the insulation of the roof and floor of industrial and civil facilities.

### 1. Introduction

One of the main development directions of the global construction industry is the production of building materials, products and structures with minimal negative impact on the environment. At the same time, environmental safety in the production and implementation of building materials becomes a determining factor while selecting the raw materials and technologies for their production. The use of industrial slags in the manufacture of building materials helps to reduce CO<sub>2</sub> emissions into the atmosphere, and also reduces pollution of soil, water and plants [1–3]. After the invention of geopolymers, the reuse of slags in the production of building materials has become more intense. Slags generated by industrial production and chemical industry (ferrous and non-ferrous metallurgy slags, ashes, etc.) are milled and tempered with an alkaline activator. The resulting materials have high strength, water and chemical resistance [4–12]. In [13, 14], we confirmed the possibility of using mineral wool production waste (MWPW) in the production of geopolymers.

An equally significant direction in the development of the global construction industry is the production of building materials with low density, sound and heat conductivity, as well as high physical and mechanical properties. Such materials include various types of cellular concrete. Products made of cellular concrete are used for constructing the external and internal walls of buildings, they can be used to insulate the floor, roof, etc [15, 16]. The studies of numerous researchers [2, 3, 7, 17–21] describe the compositions and technology for producing cellular concrete from industrial wastes (lightweight geopolymers). Since the beginning of the 20th century, two main technologies for producing cellular concrete have been known [3, 15]. The first is characterized by foaming of the concrete mix as a result of adding gas-forming components to the composition. These are mainly fine powders of certain metals (Zn, Al, Mg, etc.) [22–24], mixtures of acids with carbonates

Erofeev, V.T., Rodin, A.I., Bochkin, V.S., Yakunin, V.V., Ermakov, A.A. Lightweight geopolymers made of mineral wool production waste. Magazine of Civil Engineering. 2020. 93(1). Pp. 3–12. DOI: 10.18720/MCE.93.1

Ерофеев В.Т., Родин А.И., Бочкин В.С., Якунин В.В., Ермаков А.А. Легкие геополимеры из отходов производства минеральной ваты // Инженерно-строительный журнал. 2020. № 1(93). С. 3–12. DOI: 10.18720/MCE.93.1



(for example, HCl, H<sub>2</sub>SO<sub>4</sub> with MgCO<sub>3</sub>, CaCO<sub>3</sub>) [1], as well as oxidizing agents (H<sub>2</sub>O<sub>2</sub>, KMnO<sub>4</sub> and others) [22–25]. The second technology is associated with the use of foaming agents, such as synthetic surfactants [3, 5, 18] or based on protein raw materials [18, 26].

Studies regarding technology for producing lightweight geopolymer materials from MWPW are presented in the article. Up to 30 % of such waste from the mass of finished products is generated during production process [13, 14, 27, 28]. The main task in the technology for producing high-quality cellular concrete is the selection of such a composition that ensures the formation of products with the required physical and mechanical properties with minimal technological costs [29]. Mobility optimization of the mortar in the production of cellular concrete is the key to the quality of the final product. The mobility of the developed mortar mixtures is primarily affected by the amount of water in the composition. Excessive amount of water, as well as gas-forming or foaming components, leads to its «boiling» and subsequent settling, and their insufficient amount does not provide the necessary foaming [30–32]. The optimal amount of alkaline activator provides the material with specified strength characteristics [21, 32, 33]. Fine aggregate and water-retaining additives prevent shrinkage of the mortar mixture (at the manufacturing stage) and the final product (after 1 year of operation, the shrinkage of aerated concrete can reach 0.36 %) [1, 3, 34, 35].

The study is aimed at establishing the impact of the composition of the raw material mixture and production technological features on the physical, mechanical and thermophysical properties of lightweight geopolymers based on MWPW.

As a result of the work carried out, the following tasks were solved:

- the effect of alkaline activator and of the water/slag ratio (W/S) on the mobility of the mortar mixture was determined;
- the impact of the mobility of mortar mixture, the amount of alkaline activator and gas-forming additive in the composition on the average density and compressive strength of light geopolymers was determined;
- the correlations between the change in the thermal conductivity of light geopolymer samples and the change in their average density and humidity were obtained.

## 2. Methods

### 2.1. Materials

The following materials were used for the research:

- ground MWPW from LLC “Kombinat teploizolyacionnyh izdelij” (Saransk, Russia). The chemical composition of the waste is as follows: SiO<sub>2</sub> – 41.800 %, CaO – 26.228 %, Al<sub>2</sub>O<sub>3</sub> – 13.257 %, MgO – 11.412 %, Fe<sub>2</sub>O<sub>3</sub> – 2.392 %, Na<sub>2</sub>O – 1.171 %, K<sub>2</sub>O – 0.383 %, TiO<sub>2</sub> – 0.297 %, SO<sub>3</sub> – 0.277 %, MnO – 0.227 %, Sr<sub>2</sub>O<sub>3</sub> – 0.096 %, NiO – 0.024 %, P<sub>2</sub>O<sub>5</sub> – 0.013 %, CuO – 0.010 %, Cl – 0.009 %, Co<sub>3</sub>O<sub>4</sub> – 0.008 %, percentage of other impurities – 2.396 %. The mineralogical composition is mostly represented by the X-ray amorphous phase (>95 %). Waste was sifted through a sieve with a mesh diameter of 0.63 mm and grinded to a specific surface of 400±20 m<sup>2</sup>/kg;

- fine aggregate, which is MWPW sifted through a sieve with a mesh diameter of 1.25 mm. The chemical composition is given above;

- alkaline activator – granulated NaOH dissolved in water. Weight content of the main substance is not less than 99.5 %;

- gas-forming additive – aluminum powder with a covering power of 600±20 m<sup>2</sup>/kg in water;

- water-retaining additive – “Culminal C8360” cellulose ether. Chemical base: methylhydroxyethyl cellulose (MHEC). Viscosity: 33 000–45 000 MPa·s.

### 2.2. Sample production technology

The raw material mixture for light geopolymers was prepared according to the following technology. Water with an alkaline activator and a water-retaining additive dissolved in it was added to a working mixer. Then, ground MWPW and fine aggregate were alternately loaded and mixed for 3–4 minutes. The mobility of the mortar mixture was determined. At the same time, a suspension made of water and a gas-forming additive (water/additive ratio=10/1) was prepared. The prepared suspension was poured into a working mixer with the previously prepared mixture and mixed for 30 s. The finished mixture was fed into forms that were qualitatively filled without the use of vibration. The molded samples were kept in molds at a temperature of 50 °C and a relative humidity of at least 85 % for 5 hours. Then, samples outside the molds were steamed at atmospheric pressure according to the regime of 3+6+2 h at an isothermal heating temperature of 85±5 °C. The steamed samples were dried to constant weight at a temperature of 25–30 °C and relative humidity of not more than 50 %, after which they were tested.

### 2.3. Analytical techniques

The mobility of the mortar mixture for obtaining light geopolymers was determined according to the spread using a Southard viscosimeter.

The average density and compressive strength of material samples of each composition was determined by testing 3–5 cubic samples with a face of 150 mm.

The thermal conductivity of the samples was determined by the probe method using the MIT-1 device. The device is equipped with a measuring probe with a diameter of 6 mm and a length of 100 mm. The studies were carried out on cubic samples with a face of 150 mm at a temperature of  $25 \pm 2$  °C. The test samples had a normalized humidity (4 wt. %) and were also dried to constant weight (dry samples). A hole with a diameter of 6 mm and a depth of 80 to 100 mm, into which the probe was immersed, was drilled in the center of the face. Before testing, the samples with the probe were kept at a given temperature for at least 2 hours. The arithmetic mean of the thermal conductivity of three samples of each composition was taken as the final result.

## 3. Results and Discussion

### 3.1. Mortar mobility

Below are the results of researchers carried out to determine the impact of the quantitative content of alkaline activator (NaOH) and the water/slag ratio (W/S) on the mortar mixture mobility made of MWPW. During the experiment, 16 compositions of mortar mixtures were tested. The arithmetic mean value of the three test results for each composition is taken as the final spread value according to the Southard viscosimeter (cm). The compositions and experimental data are presented in Table 1.

**Table 1. Compositions and experimental data on the mobility of the mortar mixture made of MWPW.**

Exp. No.	Composition, % by weight			W/S ratio	Spread according to Southard viscosimeter, cm
	Ground MWPW	NaOH	water		
1	78.8	1.5	19.7	0.25	5.2
2	78.4	2	19.6		5.
3	78	2.5	19.5		5.1
4	77.6	3	19.4		5
5	75.77	1.5	22.73	0.30	10.1
6	75.38	2	22.62		10.3
7	75	2.5	22.5		9.8
8	74.62	3	22.38		7.8
9	72.96	1.5	25.54	0.35	20
10	72.59	2	25.41		21.5
11	72.22	2.5	25.28		20.7
12	71.85	3	25.15		20.1
13	70.36	1.5	28.14	0.40	25
14	70	2	28		26.4
15	69.64	2.5	27.86		25.9
16	69.29	3	27.71		24.3

As a result of the researches conducted, it was found that the mobility change of the mortar mixture (a mixture of ground MWPW, water and NaOH) is mostly affected by the W/S ratio. So, when the W/S ratio of the mixture changes from 0.25 to 0.30, the mobility slightly increases, from 5 cm to 9.5 cm on average (spread according to Southard viscosimeter). A further increase in the W/S ratio to 0.35 leads to a sharp mobility increase up to 20.5 cm on average. With an increase in the W/S ratio of the mortar mixture to 0.40, the mobility increases only slightly (up to 25.5 cm on average).

A change in the amount of NaOH in the composition from 1.5 to 3 % by weight has practically no effect on the change in the mobility of the mortar mixture. Similar results were obtained within the framework of researches carried out by other scientists [3, 7, 11, 12, 18, 31].

### 3.2. Average density and compression strength

Below are the results of tests carried out in order to determine the effect of the mortar mixture mobility and the amount of gas-forming additives (aluminum powder) on the average density and compressive strength of dry samples made of lightweight geopolymers based on MWPW. Fifteen formulations of three samples each were tested. The NaOH/slag by weight ratio in all formulations is 2.5/97.5. Light geopolymers were obtained

from a mortar mixture with mobility from 9 to 22 cm (according to Southard viscosimeter). The amount of gas-forming additive ranged from 0.06–0.12 % by weight of the total amount of all components in each composition.

Figure 1 presents the results of a studying the effect of the mortar mixture mobility and the amount of injected gas-forming additives on the average density and compressive strength of low density geopolymers.

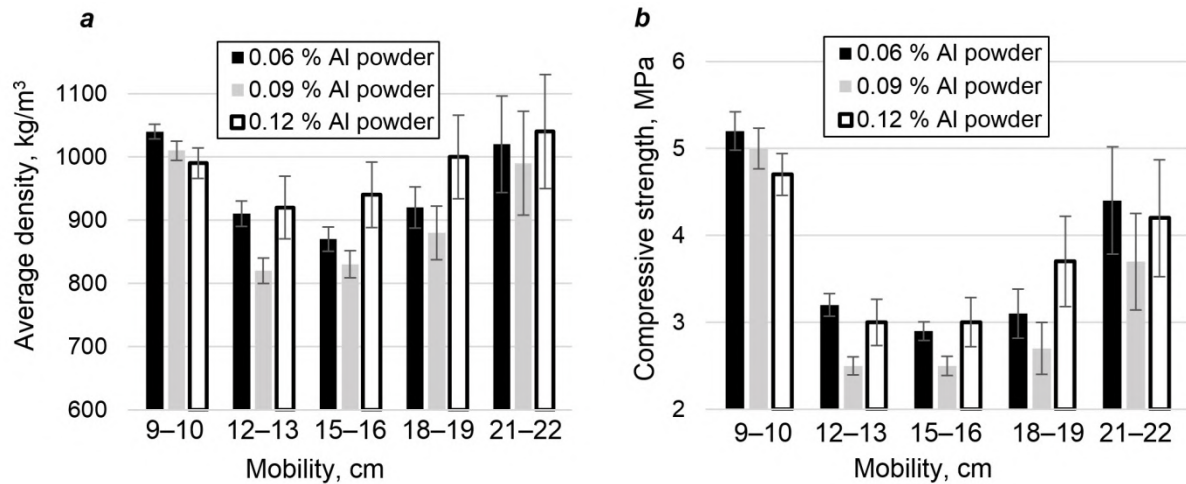


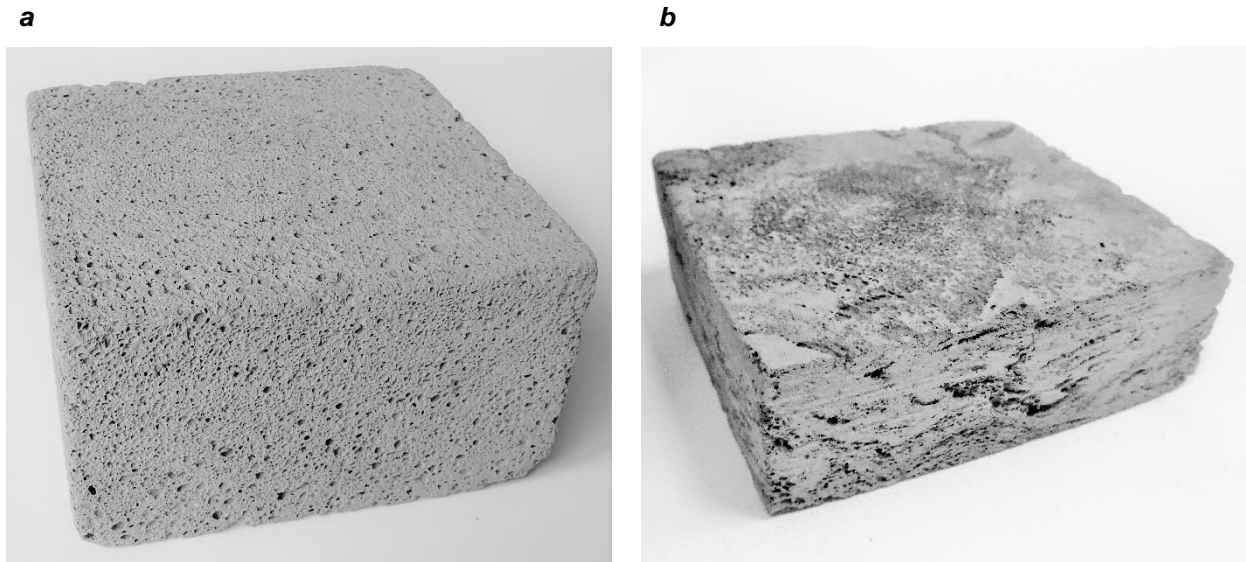
**Figure 1. The effect of the mortar mixture mobility and the amount of gas-forming additive on the average density (a) and compressive strength (b) of lightweight geopolymer samples.**

According to the data presented in Figure 1, a, the average density of light geopolymer samples made of MWPW, and obtained from a mortar mixture with a gas-forming additive in the amount of 0.06 %, decreases from 1,040 to 870 kg/m<sup>3</sup> with increasing mobility. The mobility is measured using a Southard viscosimeter and increases from 9.5 to 15.5 cm on average. A further increase in the mobility of the mortar mixture to 22 cm leads to its rapid rise and subsequent subsidence. The average density of samples increases up to 1,020 kg/m<sup>3</sup>. When the content of the gas-forming additive in the composition of the mortar mixture is 0.09 %, the minimum average density value of geopolymer hardened samples is 820 kg/m<sup>3</sup> (the mobility of the mixture is 12.5 cm on average). An increase in the mobility of the mixture up to 22 cm also leads to settling of the cellular mixture and an increase in the density of the samples to 990 kg/m<sup>3</sup>. The mortar mixture with the content of a gas-forming additive in an amount of 0.12 % intensively foams and settles. This is a consequence of the excess aluminum powder content in the composition.

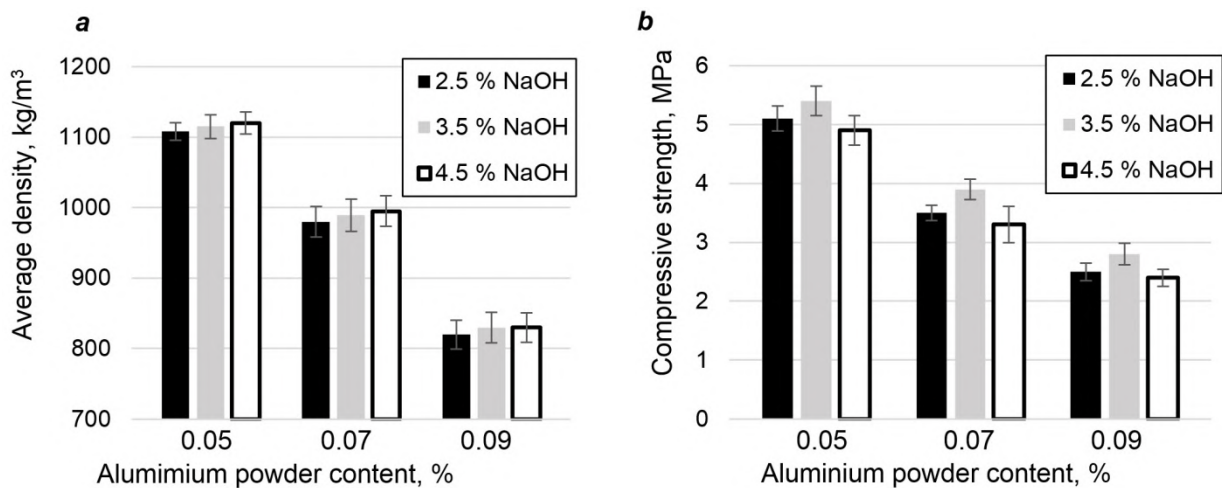
For light geopolymer samples made of MWPW (see Figure 2, a) with the lowest density ( $\approx 820$  kg/m<sup>3</sup>), the compressive strength is 2.5 MPa on average. The mobility of the mortar mixture for samples of these compositions is in the range from 12 to 16 cm. The aluminum powder content in the composition is 0.09 %. An increase in the mobility of the mortar mixture more than 16 cm, and the content of the gas-forming additive more than 0.09 % leads to a wide spread in the values of compressive strength. Samples have a defective structure in which porous regions alternate with dense interlayers (see Figure 2, b).

Figure 3 presents the results of studying the impact of the alkaline component amount in the mortar mixture composition on the average density and compressive strength of light geopolymer samples. During the experiment, 12 compositions of 3 samples in each were tested. During the manufacture of samples, the same mobility of the mortar mixture was achieved (13–14 cm). The NaOH content in the composition ranged from 2.5 to 4.5 % of the total weight of all components in the composition, and the amount of gas-forming additives was from 0.05 to 0.09 %.

According to the data obtained (Figure 3, a), an increase in the NaOH content from 2.5 to 4.5 % in the compositions does not significantly affect the change in the average density of lightweight geopolymer samples. The average density of samples based on MWPW depends to a greater extent on the amount of gas-forming additives in the mortar mixture composition. In order to obtain such cellular concrete with a density of not more than 1,000 kg/m<sup>3</sup>, the content of aluminum powder in the composition must be at least 0.07 %. Samples of cellular concrete made of MWPW with the lowest density (less than 850 kg/m<sup>3</sup>) without the use of modifying additives can be obtained using the mortar mixture with a mobility between 12–16 cm. The amount of aluminum powder in the composition should be 0.09 %.



**Figure 2.** Photo of light geopolymer samples made of MWPW: *a* – the mobility of the mortar mixture is 13 cm, the amount of aluminum powder is 0.09 %; *b* – the mobility of the mortar mixture is 19 cm, the amount of aluminum powder is 0.12 %.



**Figure 3.** The effect of the alkaline component on the average density (*a*) and compressive strength (*b*) of lightweight geopolymer samples.

According to the data presented in Figure 3, *b*, 3.5 % NaOH in the composition of the mortar mixture provides the greatest compressive strength of light geopolymers made of MWPW. With a decrease in the density of the samples from an average of 1,120 to 830 kg/m<sup>3</sup>, the compressive strength decreases in direct proportion from 5.4 to 2.8 MPa. The obtained data on compressive strength of lightweight geopolymer samples made of MWPW is almost identical to the values obtained when testing samples based on slag of ferrous and non-ferrous metallurgy, ashes, glass wastes (the same method of foaming the mortar mixture and similar average density of the hardened samples) [3, 7, 11, 19, 21–23, 31].

The following can be noticed while comparing the compositions of mortar mixtures for obtaining lightweight geopolymers from MWPW with data coming from other researchers. The amount of water and aluminum powder in the composition of the MWPW mortar mixture providing its maximum foaming without settling, as well as the amount of alkaline component providing maximum compressive strength of the samples at a given density, is lower in comparison with compositions based on fly ash or blastfurnace slag [7, 11, 19, 22]. The optimal W/S ratio of the MWPW-based mortar mixture is on average 0.33, for compositions with fly ash it is around 0.37 [7], and with blastfurnace slag is at least 0.4 [11]. In order to achieve the minimum density of lightweight MWPW-based geopolymers, the maximum amount of introduced gas-forming component (aluminum powder) should not exceed 0.09 %, which is also lower comparing to compositions based on fly ash or blastfurnace slag (>0.1 %) [7, 11, 19, 22]. To achieve high compressive strength of foamed materials and products made of geopolymers based on slags of ferrous and non-ferrous metallurgy, as well as on ashes, a rather large amount of alkaline activator is used: 4.5 % water glass and 10 % NaOH [22, 23], at least 10 % Ca(OH)<sub>2</sub> and Mg(NO<sub>3</sub>)<sub>2</sub> [11], up to 10 % NaOH [21], etc. This indicator is at least two times lower for compositions based on MWPW (3.5 % NaOH).

### 3.3. Thermal conductivity

The thermal conductivity test results of samples made of lightweight geopolymers based on MWPW with various average densities are presented in Figure 4. During the experiment, 8 dry samples and 8 samples with a humidity of 4 % were tested. Samples obtained from the mortar mixture with a mobility of 12–16 cm were selected for testing. The content of the gas-forming component in the composition was in the range of 0.05–0.09 %, and the content of alkaline component was 2.5–3.5 %.

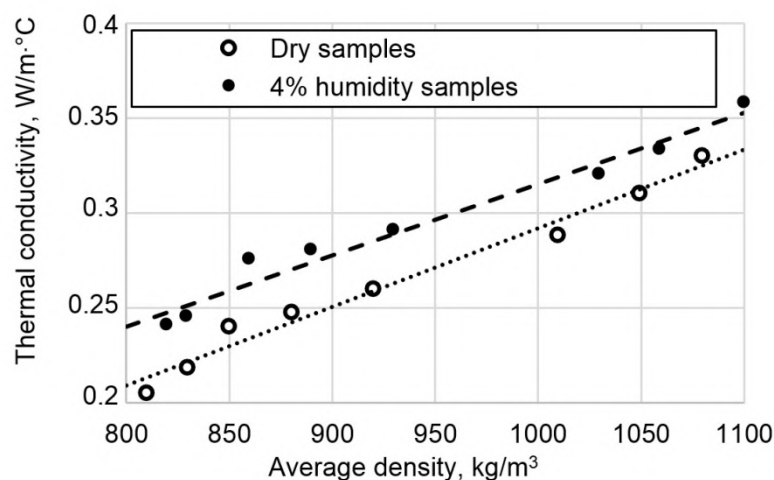


**Figure 4. Thermal conductivity of light geopolymers made of MWPW.**

According to the data presented in Figure 4, the thermal conductivity of dry samples of lightweight geopolymers made of MWPW increases directly proportionally from 0.208 to 0.332 W/m·°C with an increase in the material density from 800 to 1,100 kg/m<sup>3</sup>. With an increase in material humidity up to 4 %, the thermal conductivity of samples increases by 15 % on average for compositions with a density of 800 kg/m<sup>3</sup> and by 6 % for compositions with a density of 1,100 kg/m<sup>3</sup>. The resulting changes in the thermal conductivity of lightweight geopolymers according to their density are almost identical to the data presented in the research [3]. The results of many researchers are summarized by the study.

As a result of the conducted researches, it was found that the material density should not exceed 820 kg/m<sup>3</sup> in order to obtain light geopolymers made of MWPW with a thermal conductivity of not more than 0.250 W/m·°C. And the material density should not exceed 950 kg/m<sup>3</sup> for a desirable thermal conductivity of not more than 0.300 W/m·°C.

### 3.4. Compositions and properties of modified lightweight geopolymers

The compositions and properties of lightweight geopolymers made of MWPW and modified with fine aggregate and water-retaining additive Culminal C8360 are presented in Table 2. The significance of the introduction of these modifiers into the mortar mixture is described above.

**Table 2. Compositions and properties of modified lightweight geopolymers.**

Components	Composition, weight parts								
	1	2	3	4	5	6	7	8	9
Ground MWPW	100	100	100	100	100	100	100	100	100
Fine aggregate	10	15	20	10	15	20	10	15	20
Alkaline activator	3.5	3.5	3.5	3.5	3.5	3.5	3.5	3.5	3.5
Water	36.67	37.65	38.75	37.78	38.82	40	38.85	40	41.29
Gas-forming additive	0.05	0.07	0.09	0.05	0.07	0.09	0.09	0.07	0.05
Water-retaining additive	0	0	0	0.03	0.03	0.03	0.06	0.06	0.06
Properties	Indicators for composition								
	1	2	3	4	5	6	7	8	9
Average density, kg/m <sup>3</sup>	1 130	1 020	840	1 080	950	670	610	920	1 060
Compression strength, MPa	5.4	3.5	2.7	4.9	3.1	2.2	1.7	2.9	4.5
Thermal conductivity, W/m·°C (dry samples)	0.345	0.303	0.221	0.335	0.273	0.167	0.144	0.259	0.320
Thermal conductivity, W/m·°C (4 % humidity samples)	0.358	0.325	0.258	0.351	0.305	0.197	0.171	0.275	0.338

According to the data presented in Table 2, the introduction of up to 20 weight parts of fine aggregate into the mortar does not significantly affect the change in average density, compressive strength, and thermal

conductivity of lightweight geopolymers. This component also helps to reduce material shrinkage during operation, as well as reduce the cost of the final product.

With the introduction of the Culminal C8360 water-retaining additive, a decrease in the density of geopolymer samples to  $610 \text{ kg/m}^3$  was detected, as well as a decrease in the thermal conductivity of dry samples to  $0.144 \text{ W/m}\cdot^\circ\text{C}$ , and to  $0.171 \text{ W/m}\cdot^\circ\text{C}$  for 4 % humidity samples. It was also determined that an increase of this additive over 0.06 % in the composition leads to a decrease in compressive strength of lightweight geopolymer samples.

The positive effect caused by the modification of lightweight geopolymers with a fine aggregate and a water-retaining additive was also noted in several studies [1, 3, 34, 35].

#### 4. Conclusion

1. Compositions have been developed and technological methods have been described for obtaining lightweight geopolymers (cellular concrete) from mineral wool production waste with an average density of 610 to  $1,130 \text{ kg/m}^3$ , compressive strength of 1.7 to 5.4 MPa, and thermal conductivity of 0.144 to  $0.345 \text{ W/m}\cdot^\circ\text{C}$ .

2. In the production of light geopolymers made of MWPW, the mobility of the mortar mixture should be 12–16 cm according to Southard viscosimeter, the amount of alkaline activator (NaOH) in the mortar mixture should be equal to 3.5 %, and the content of aluminum powder should not exceed 0.09 %.

3. The introduction of up to 20 % of fine aggregate into the mortar mixture composition in the form of mineral wool production waste fractions of less than 1.25 mm does not significantly affect the change in average density, compressive strength and thermal conductivity of lightweight geopolymers.

4. In order to obtain cellular concrete from mineral wool production waste with a density of less than  $830 \text{ kg/m}^3$  (up to and including  $610 \text{ kg/m}^3$ ), it is necessary to add a water-retaining additive, for example, Culminal C8360, in an amount up to 0.06 %.

5. The use of ground mineral wool production waste in the production of lightweight geopolymers will significantly reduce the amount of expensive components in the mortar mixture (up to 2 times or more for NaOH, more than 10 % for aluminum powder) compared with compositions based on blastfurnace slag and fly ash glass waste (while maintaining the strength and thermophysical properties of the material).

6. The conducted researches will contribute to the expansion of the raw material base for the production of lightweight geopolymers, thereby reducing the amount of slags generated during the mineral wool production. The developed materials will find application in the manufacture of building envelopes, as well as insulation of roofs and floors in the construction of industrial and civil facilities.

#### 5. Acknowledgments

The work was carried out within the framework of the Grant of the President of the Russian Federation MK-6416.2018.3.

#### References

- Posi, P., Teerachanwit, C., Tanutong, C., Limkamoltip, S., Lertnimoolchai, S., Sata, V., Chindaprasit, P. Lightweight geopolymer concrete containing aggregate from recycle lightweight block. *Materials and Design*. 2013. No. 52. Pp. 580–586. DOI: 10.1016/j.matdes.2013.06.001.
- Wu, H.-C., Sun, P. New building materials from fly ash-based lightweight inorganic polymer. *Construction and Building Materials*. 2007. 21(1). Pp. 211–217. DOI: 10.1016/j.conbuildmat.2005.06.052.
- Zhang, Z., Provis, J.L., Reid, A., Wang, H. Geopolymer foam concrete: An emerging material for sustainable construction. *Construction and Building Materials*. 2014. No. 56. Pp. 113–127. DOI: 10.1016/j.conbuildmat.2014.01.081
- Abdulkareem, O.A., Mustafa Al Bakri, A.M., Kamarudin, H., Khairul Nizar, I., Saif, A.A. Effects of elevated temperatures on the thermal behavior and mechanical performance of fly ash geopolymer paste, mortar and lightweight concrete. *Construction and Building Materials*. 2014. No. 50. Pp. 377–387. DOI: 10.1016/j.conbuildmat.2013.09.047.
- Bing, C., Zhen, W., Ning, L. Experimental Research on Properties of High-Strength Foamed Concrete. *Journal of Materials in Civil Engineering*. 2012. 24(1). Pp. 113–118. DOI: 10.1061/(ASCE)MT.1943-5533.0000353.
- Grinfeldi, G.I., Gorshkov, A.S., Vatin, N.I. Tests results strength and thermophysical properties of aerated concrete block wall samples with the use of polyurethane adhesive. *Advanced Materials Research*. 2014. No. 941–944. Pp. 786–799. DOI: 10.4028/www.scientific.net/AMR.941-944.786.
- Hlaváček, P., Šmilauer, V., Škvára, F., Kopecký, L., Šulc, R. Inorganic foams made from alkali-activated fly ash: Mechanical, chemical and physical properties. *Journal of the European Ceramic Society*. 2015. 35(2). Pp. 703–709. DOI: 10.1016/j.jeurceramsoc.2014.08.024.
- Huiskes, D.M.A., Keulen, A., Yu, Q.L., Brouwers, H.J.H. Design and performance evaluation of ultra-lightweight geopolymer concrete. *Materials and Design*. 2016. No. 89. Pp. 516–526. DOI: 10.1016/j.matdes.2015.09.167.
- Sirotyuk V.V., Lunev A.A. Strength and deformation characteristics of ash and slag mixture. *Magazine of Civil Engineering*. 2017. No. 6. Pp. 3–16. DOI: 10.18720/MCE.74.1.
- Vatin, N., Gorshkov, A., Nemova, D., Gamayunova, O., Tarasova, D. Humidity conditions of homogeneous wall from gas-concrete blocks with finishing plaster compounds. *Applied Mechanics and Materials*. 2014. No. 670–671. Pp. 349–354. DOI: 10.4028/www.scientific.net/AMM.670-671.349.

11. Yang, K.-H., Lee, K.-H., Song, J.-K., Gong, M.-H. Properties and sustainability of alkali-activated slag foamed concrete. *Journal of Cleaner Production*. 2014. No. 68. Pp. 226–233. DOI: 10.1016/j.jclepro.2013.12.068.
12. Zhang, Z., Provis, J.L., Reid, A., Wang, H. Mechanical, thermal insulation, thermal resistance and acoustic absorption properties of geopolymer foam concrete. *Cement and Concrete Composites*. 2015. No. 62. Pp. 97–105. DOI: 10.1016/j.cemconcomp.2015.03.013.
13. Erofeev, V.T., Rodin, A.I., Yakunin, V.V., Bogatov, A.D., Bochkin, V.S., Chegodajkin, A.M. Alkali-activated slag binders from rock-wool production wastes. *Magazine of Civil Engineering*. 2018. 82(6). Pp. 219–227. DOI: 10.18720/MCE.82.20.
14. Erofeev, V.T., Rodin, A.I., Yakunin, V.V., Tuvin, M.N. Structure, composition and properties of geopolymers from mineral wool waste. *Magazine of Civil Engineering*. 2019. 90(6). Pp. 3–14. DOI: 10.18720/MCE.90.1.
15. Amran, Y.H.M., Farzadnia, N., Ali, A.A.A. Properties and applications of foamed concrete; A review. *Construction and Building Materials*. 2015. No. 101. Pp. 990–1005. DOI: 10.1016/j.conbuildmat.2015.10.112.
16. Steshenko, A.B., Kudyakov, A.I. Cement based foam concrete with aluminosilicate microspheres for monolithic construction. *Magazine of Civil Engineering*. 2018. 84(8). Pp. 86–96. DOI: 10.18720/MCE.84.9.
17. Abdollahnejad, Z., Pacheco-Torgal, F., Félix, T., Tahri, W., Barroso Aguiar, J. Mix design, properties and cost analysis of fly ash-based geopolymer foam. *Construction and Building Materials*. 2015. No. 80. Pp. 18–30. DOI: 10.1016/j.conbuildmat.2015.01.063.
18. Al Bakri Abdullah, M.M., Tahir, M.F.M., Hussin, K., Binhussain, M., Sandu, I.G., Yahya, Z., Sandu, A.V. Fly ash based lightweight geopolymer concrete using foaming agent technology. *Revista de Chimie*. 2015. 66(7). Pp. 1001–1003.
19. Arellano Aguilar, R., Burciaga Díaz, O., Escalante García, J.I. Lightweight concretes of activated metakaolin-fly ash binders, with blast furnace slag aggregates. *Construction and Building Materials*. 2010. 24(7). Pp. 1166–1175. DOI: 10.1016/j.conbuildmat.2009.12.024.
20. Badanoiu, A.I., Al Saadi, T.H.A., Stoleriu, S., Voicu, G. Preparation and characterization of foamed geopolymers from waste glass and red mud. *Construction and Building Materials*. 2015. No. 84. Pp. 284–293. DOI: 10.1016/j.conbuildmat.2015.03.004.
21. Pimraksa, K., Chindaprasirt, P., Rungchet, A., Sagoe-Crentsil, K., Sato, T. Lightweight geopolymer made of highly porous siliceous materials with various  $\text{Na}_2\text{O}/\text{Al}_2\text{O}_3$  and  $\text{SiO}_2/\text{Al}_2\text{O}_3$  ratios. *Materials Science and Engineering A*. 2011. 528(21). Pp. 6616–6623. DOI: 10.1016/j.msea.2011.04.044.
22. Ducman, V., Korat, L. Characterization of geopolymer fly-ash based foams obtained with the addition of Al powder or  $\text{H}_2\text{O}_2$  as foaming agents. *Materials Characterization*. 2016. No. 113. Pp. 207–213. DOI: 10.1016/j.matchar.2016.01.019.
23. Korat, L., Ducman, V. The influence of the stabilizing agent SDS on porosity development in alkali-activated fly-ash based foams. *Cement and Concrete Composites*. 2017. No. 80. Pp. 168–174. DOI: 10.1016/j.cemconcomp.2017.03.010.
24. Masi, G., Rickard, W.D.A., Vickers, L., Bignozzi, M.C., Van Riessen, A. A comparison between different foaming methods for the synthesis of light weight geopolymers. *Ceramics International*. 2014. 40(9, PART A). Pp. 13891–13902. DOI: 10.1016/j.ceramint.2014.05.108.
25. Hajimohammadi, A., Ngo, T., Mendis, P., Nguyen, T., Kashani, A., van Deventer, J.S.J. Pore characteristics in one-part mix geopolymers foamed by  $\text{H}_2\text{O}_2$ : The impact of mix design. *Materials and Design*. 2017. No. 130. Pp. 381–391. DOI: 10.1016/j.matdes.2017.05.084.
26. Nambiar, E.K.K., Ramamurthy, K. Air-void characterisation of foam concrete. *Cement and Concrete Research*. 2007. 37(2). Pp. 221–230. DOI: 10.1016/j.cemconres.2006.10.009.
27. Vatin, N.I., Pestryakov, I.I., Sultanov, Sh.T., Ogidan, T.O., Yarunicheva, Y.A., Kiryushina, A.P. Water vapour by diffusion and mineral wool thermal insulation materials. *Magazine of Civil Engineering*. 2018. 81(5). Pp. 183–192. DOI: 10.18720/MCE.81.18.
28. Vatin, N., Sultanov, S., Krupina, A. Comparison of Thermal Insulation Characteristics of PIR, Mineral Wool, Carbon Fiber, and Aerogel. *Advances in Intelligent Systems and Computing*. 2019. No. 983. Pp. 877–883. DOI: 10.1007/978-3-030-19868-8\_86.
29. Gorshkov, A.S., Vatin, N.I., Rymkevich, P.P., Kydrevich O.O. Payback period of investments in energy saving. *Magazine of Civil Engineering*. 2018. No. 2. Pp. 65–75. DOI: 10.18720/MCE.78.5.
30. Hajimohammadi, A., Ngo, T., Mendis, P. How does aluminium foaming agent impact the geopolymer formation mechanism? *Cement and Concrete Composites*. 2017. No. 80. Pp. 277–286. DOI: 10.1016/j.cemconcomp.2017.03.022.
31. Hajimohammadi, A., Ngo, T., Mendis, P., Sanjayan, J. Regulating the chemical foaming reaction to control the porosity of geopolymer foams. *Materials and Design*. 2017. No. 120. Pp. 255–265. DOI: 10.1016/j.matdes.2017.02.026.
32. Prud'Homme, E., Michaud, P., Joussein, E., Clacens, J.-M., Rossignol, S. Role of alkaline cations and water content on geomaterial foams: Monitoring during formation. *Journal of Non-Crystalline Solids*. 2011. 357(4). Pp. 1270–1278. DOI: 10.1016/j.jnoncrysol.2010.12.030.
33. Hajimohammadi, A., Ngo, T., Mendis, P., Kashani, A., van Deventer, J.S.J. Alkali activated slag foams: The effect of the alkali reaction on foam characteristics. *Journal of Cleaner Production*. 2017. No. 147. Pp. 330–339. DOI: 10.1016/j.jclepro.2017.01.134.
34. Erofeev, V.T., Fedortsov, A.P., Bogatov, A.D., Fedortsov, V.A., Gusev, B.V. Evaluation of corrosion of alkali-glass composites, predicting their physico-chemical resistance and ways to improve it. *Izvestiya Vysshikh Uchebnykh Zavedenii, Seriya Tekhnologiya Tekstil'noi Promyshlennosti*. 2018. 2(374). Pp. 238–246.
35. Hajimohammadi, A., Ngo, T., Kashani, A. Sustainable one-part geopolymer foams with glass fines versus sand as aggregates. *Construction and Building Materials*. 2018. No. 171. Pp. 223–231. DOI: 10.1016/j.conbuildmat.2018.03.120.

### **Contacts:**

*Vladimir Erofeev, (8342)47-40-19; al\_rodin@mail.ru*

*Alexander Rodin, +7-951-051-45-28; al\_rodin@mail.ru*

*Viktor Bochkin, (8342)29-49-12; sovelitnew@mail.ru*

*Vladislav Yakunin, +7-953-029-70-58; vladisjakunin@yandex.ru*

*Anatolij Ermakov, +79879944209; anatoly.ermakov97@mail.ru*



DOI: 10.18720/MCE.93.1

## Легкие геополимеры из отходов производства минеральной ваты

**В.Т. Ерофеев<sup>а</sup>, А.И. Родин<sup>а\*</sup>, В.С. Бочкин<sup>б</sup>, В.В. Якунин<sup>а</sup>, А.А. Ермаков<sup>а</sup>**

<sup>а</sup> Мордовский государственный университет им. Н.П. Огарёва, Республика Мордовия, Россия

<sup>б</sup> ООО «Комбинат теплоизоляционных изделий», г. Саранск, Республика Мордовия, Россия

\* E-mail: [al\\_rodin@mail.ru](mailto:al_rodin@mail.ru)

**Ключевые слова:** геополимеры, отходы, едкий натр, бетоны, прочность при сжатии, теплоизоляция

**Аннотация.** Сокращение отходов промышленного производства и разработка на их основе строительных материалов является одним из приоритетных направлений развития строительной индустрии. В рамках исследований, результаты которых представлены в данной статье, рассматриваются вопросы получения ячеистых бетонов из отходов производства минеральной ваты (легких геополимеров). Цель исследования заключалась в установлении влияния состава сырьевой смеси и технологических особенностей получения на физико-механические и теплофизические свойства легких геополимеров на основе отходов производства минеральной ваты. Легкие геополимеры получали путем подготовки смеси из размолотых отходов (удельная поверхность равна  $400 \pm 20$  м<sup>2</sup>/кг), щелочного активатора (NaOH), воды, газообразующей добавки (алюминиевой пудры), мелкого заполнителя и водоудерживающей добавки. Полученные смеси укладывали в формы без применения вибрации. Для ускорения твердения отформованные изделия пропаривались. В работе у растворных смесей исследована подвижность, а у затвердевших образцов средняя плотность, прочность при сжатии и теплопроводность. Получены составы легких геополимеров со средней плотностью от 610 до 1 130 кг/м<sup>3</sup>, прочностью при сжатии от 1,7 до 5,4 МПа, коэффициентом теплопроводности от 0,144 до 0,345 Вт/м·°С. Применение полученных результатов будет способствовать расширению сырьевой базы для получения легких геополимеров, тем самым сократится количество образующихся при производстве минеральной ваты отходов. Разработанные материалы могут быть использованы при строительстве ограждающих конструкций, а также утепления крыши и пола объектов промышленного и гражданского назначения.

### Литература

1. Posi P., Teerachanwit C., Tanutong C., Limkamoltip S., Lertnimoolchai S., Sata V., Chindapasirt, P. Lightweight geopolymer concrete containing aggregate from recycle lightweight block // *Materials and Design*. 2013. No. 52. Pp. 580–586.
2. Wu H.-C., Sun P. New building materials from fly ash-based lightweight inorganic polymer // *Construction and Building Materials*. 2007. 21(1). Pp. 211–217.
3. Zhang Z., Provis J.L., Reid A., Wang H. Geopolymer foam concrete: An emerging material for sustainable construction // *Construction and Building Materials*. 2014. No. 56. Pp. 113–127.
4. Abdulkareem O.A., Mustafa Al Bakri A.M., Kamarudin H., Khairul Nizar I., Saif A.A. Effects of elevated temperatures on the thermal behavior and mechanical performance of fly ash geopolymer paste, mortar and lightweight concrete // *Construction and Building Materials*. 2014. No. 50. Pp. 377–387.
5. Bing C., Zhen W., Ning L. Experimental Research on Properties of High-Strength Foamed Concrete // *Journal of Materials in Civil Engineering*. 2012. 24(1). Pp. 113–118.
6. Grinfeld G.I., Gorshkov A.S., Vatin N.I. Tests results strength and thermophysical properties of aerated concrete block wall samples with the use of polyurethane adhesive // *Advanced Materials Research*. 2014. No. 941–944. Pp. 786–799.
7. Hlaváček P., Šmilauer V., Škvára F., Kopecký L., Šulc R. Inorganic foams made from alkali-activated fly ash: Mechanical, chemical and physical properties // *Journal of the European Ceramic Society*. 2015. 35(2). Pp. 703–709.
8. Huiskes D.M.A., Keulen A., Yu Q.L., Brouwers H.J.H. Design and performance evaluation of ultra-lightweight geopolymer concrete // *Materials and Design*. 2016. No. 89. Pp. 516–526.
9. Сиротюк В.В., Лунёв А.А. Прочностные и деформационные характеристики золошлаковой смеси // *Инженерно-строительный журнал*. 2017. № 6(74). С. 3–16.
10. Vatin N., Gorshkov A., Nemova D., Gamayunova O., Tarasova D. Humidity conditions of homogeneous wall from gas-concrete blocks with finishing plaster compounds // *Applied Mechanics and Materials*. 2014. No. 670–671. Pp. 349–354.
11. Yang K.-H., Lee K.-H., Song J.-K., Gong M.-H. Properties and sustainability of alkali-activated slag foamed concrete // *Journal of Cleaner Production*. 2014. No. 68. Pp. 226–233.
12. Zhang Z., Provis J.L., Reid A., Wang H. Mechanical, thermal insulation, thermal resistance and acoustic absorption properties of geopolymer foam concrete // *Cement and Concrete Composites*. 2015. No. 62. Pp. 97–105.

13. Ерофеев В.Т., Родин А.И., Якунин В.В., Богатов А.Д., Бочкин В.С., Чегодайкин А.М. Шлакощелочные вяжущие из отходов производства минеральной ваты // Инженерно-строительный журнал. 2018. № 6(82). С. 219–227.
14. Ерофеев В.Т., Родин А.И., Якунин В.В., Тувин М.Н. Структура, состав и свойства геополимеров из отходов минеральной ваты // Инженерно-строительный журнал. 2019. № 6(90). С. 3–14. DOI: 10.18720/MCE.90.1
15. Amran Y.H.M., Farzadnia N., Ali A.A.A. Properties and applications of foamed concrete; A review // Construction and Building Materials. 2015. No. 101. Pp. 990–1005.
16. Стешенко А.Б., Кудряков А.И. Цементный пенобетон с алюмосиликатной микросферой для монолитного домостроения // Инженерно-строительный журнал. 2018. № 8(84). С. 86–96.
17. Abdollahnejad Z., Pacheco-Torgal F., Félix T., Tahri W., Barroso Aguiar J. Mix design, properties and cost analysis of fly ash-based geopolymer foam // Construction and Building Materials. 2015. No. 80. Pp. 18–30.
18. Al Bakri Abdullah M.M., Tahir M.F.M., Hussin K., Binhussain M., Sandu I.G., Yahya Z., Sandu A.V. Fly ash based lightweight geopolymer concrete using foaming agent technology // Revista de Chimie. 2015. 66(7). Pp. 1001–1003.
19. Arellano Aguilar R., Burciaga Díaz O., Escalante García J.I. Lightweight concretes of activated metakaolin-fly ash binders, with blast furnace slag aggregates // Construction and Building Materials. 2010. 24(7). Pp. 1166–1175.
20. Badanoiu A.I., Al Saadi T.H.A., Stoleriu S., Voicu G. Preparation and characterization of foamed geopolymers from waste glass and red mud // Construction and Building Materials. 2015. No. 84. Pp. 284–293.
21. Pimraksa K., Chindaprasit P., Rungchet A., Sagoe-Crentsil K., Sato T. Lightweight geopolymer made of highly porous siliceous materials with various  $\text{Na}_2\text{O}/\text{Al}_2\text{O}_3$  and  $\text{SiO}_2/\text{Al}_2\text{O}_3$  ratios // Materials Science and Engineering A. 2011. 528(21). Pp. 6616–6623.
22. Ducman V., Korat L. Characterization of geopolymer fly-ash based foams obtained with the addition of Al powder or  $\text{H}_2\text{O}_2$  as foaming agents // Materials Characterization. 2016. No. 113. Pp. 207–213.
23. Korat L., Ducman V. The influence of the stabilizing agent SDS on porosity development in alkali-activated fly-ash based foams // Cement and Concrete Composites. 2017. No. 80. Pp. 168–174.
24. Masi G., Rickard W.D.A., Vickers L., Bignozzi M.C., Van Riessen A. A comparison between different foaming methods for the synthesis of light weight geopolymers // Ceramics International. 2014. 40(9, PART A). Pp. 13891–13902.
25. Hajimohammadi A., Ngo T., Mendis P., Nguyen T., Kashani A., van Deventer J.S.J. Pore characteristics in one-part mix geopolymers foamed by  $\text{H}_2\text{O}_2$ : The impact of mix design // Materials and Design. 2017. No. 130. Pp. 381–391.
26. Nambiar E.K.K., Ramamurthy, K. Air-void characterisation of foam concrete // Cement and Concrete Research. 2007. 37(2). Pp. 221–230.
27. Ватин Н.И., Пестряков И.И., Султанов Ш.Т., Огидан О.Т., Яруничева Ю.А., Кирюшина А. Диффузионное влагопоглощение теплоизоляционных изделий и минеральной ваты // Инженерно-строительный журнал. 2018. № 5(81). С. 183–192.
28. Vatin N., Sultanov S., Krupina A. Comparison of Thermal Insulation Characteristics of PIR, Mineral Wool, Carbon Fiber, and Aerogel // Advances in Intelligent Systems and Computing. 2019. No. 983. Pp. 877–883.
29. Горшков А.С., Ватин Н.И., Рымкевич П.П., Кудревич О.О. Период возврата инвестиций в энергосбережение // Инженерно-строительный журнал. 2018. № 2(78). С. 65–75.
30. Hajimohammadi A., Ngo T., Mendis P. How does aluminium foaming agent impact the geopolymer formation mechanism? // Cement and Concrete Composites. 2017. No. 80. Pp. 277–286.
31. Hajimohammadi A., Ngo T., Mendis P., Sanjayan J. Regulating the chemical foaming reaction to control the porosity of geopolymer foams // Materials and Design. 2017. No. 120. Pp. 255–265.
32. Prud'Homme E., Michaud P., Joussein E., Clacens J.-M., Rossignol S. Role of alkaline cations and water content on geomaterial foams: Monitoring during formation // Journal of Non-Crystalline Solids. 2011. 357(4). Pp. 1270–1278.
33. Hajimohammadi A., Ngo T., Mendis P., Kashani A., van Deventer J.S.J. Alkali activated slag foams: The effect of the alkali reaction on foam characteristics // Journal of Cleaner Production. 2017. No. 147. Pp. 330–339.
34. Ерофеев В.Т., Федорцов А.П., Богатов А.Д., Федорцов В.А., Гусев Б.В. Оценка коррозии стеклощелочных композитов, прогнозирование их физико-химического сопротивления и способы его повышения // Известия высших учебных заведений. Технология текстильной промышленности. 2018. 2(374). С. 238–246.
35. Hajimohammadi A., Ngo T., Kashani A. Sustainable one-part geopolymer foams with glass fines versus sand as aggregates // Construction and Building Materials. 2018. No. 171. Pp. 223–231.

#### **Контактные данные:**

*Владимир Трофимович Ерофеев, (8342)47-40-19; эл. почта: al\_rodin@mail.ru*

*Александр Иванович Родин, +7-951-051-45-28; эл. почта: al\_rodin@mail.ru*

*Виктор Семенович Бочкин, (8342)29-49-12; эл. почта: sovelitnew@mail.ru*

*Владислав Васильевич Якунин, +7-953-029-70-58; эл. почта: vladisjakunin@yandex.ru*

*Анатолий Анатольевич Ермаков, +79879944209; эл. почта: anatoly.ermakov97@mail.ru*

© Ерофеев В.Т., Родин А.И., Бочкин В.С., Якунин В.В., Ермаков А.А., 2020



DOI: 10.18720/MCE.93.2

## Technical diagnostics of reinforced concrete structures using intelligent systems

**G.G. Kashevarova\*, Yu L Tonkov**

*Perm National Research Polytechnic University, Perm, Russia*

\* E-mail: [ggkash@mail.ru](mailto:ggkash@mail.ru)

**Keywords:** buildings and structures diagnostics, reinforced concrete structures, technical condition category, expert system, fuzzy logic, ontological analysis

**Abstract.** The results of the development of an effective intelligent system for technical diagnostics of reinforced concrete structures are presented. The category of technical condition is the main criterion in deciding on the degree of accident or the need to take measures to bring it to further safe operation of a building construction. For the purposes of this study, an expert system was developed based on the mathematical apparatus of the theory of fuzzy sets and fuzzy logic, which can take into account the scatter of individual opinions of experts, significantly reduce the examination time and improve the quality of the diagnostics. A hierarchical structure of the organization of expert knowledge is proposed for assessing the technical condition of building structures taking into account the universality of information and the possibility of its expansion based on ontological analysis. Moreover, a technique was developed for formalizing expert information using membership functions for input and output control parameters. To implement a fuzzy logical inference, an algorithm adapted to the given problem is developed. A computer program has been developed that implements the method of identification of the category of technical condition of building structures on the basis of fuzzy knowledge bases. The results of using this program in a survey of a real industrial building are given. The results of the technical state evaluation examined structure, obtained using the expert system, are confirmed by expert opinions of specialists who did not participate in the creation of the program and have extensive experience in examining the building structures. The present work is motivated by a need to transfer knowledge from the technical books and experienced experts in the domain field of diagnostics of building structures to make that knowledge and expertise available to practicing engineers.

### 1. Introduction

The main tasks of buildings and structures technical diagnostics are detection of defects and damage to building structures, identification of the causes of their occurrence, definition of operational suitability of the object at the time of the survey. The condition of existing structure needs to be evaluated for a variety of reasons. Such as: changes in use or increase of loads, new regulations with higher load requirements, effects of deterioration, and damage as result of extreme loading events, and concern about design and construction errors and about the quality of building material and workmanship [1–3]. The procedures used to evaluate the structural safety and condition of existing buildings may vary depending on the behavior of the structure and the reason for the evaluation.

There are numerous references describing methods for investigating the condition of a structure. These include methods presented by the International Standards Institutions e. g. Committee of the Russian Federation on Standardization and Metrology (GOST), American Concrete Institute (ACI), British Standards Institute (BSI), International Organization for Standardization (ISO), European Norm standards and others. All

Kashevarova, G.G., Tonkov, Yu.L. Technical diagnostics of reinforced concrete structures using intelligent systems. Magazine of Civil Engineering. 2020. 93(1). Pp. 13–26. DOI: 10.18720/MCE.93.2

Кашеварова Г.Г., Тонков Ю.Л. Техническая диагностика железобетонных конструкций с применением интеллектуальных систем // Инженерно-строительный журнал. 2020. № 1(93). С. 13–26. DOI: 10.18720/MCE.93.2



This work is licensed under a [CC BY-NC 4.0](https://creativecommons.org/licenses/by-nc/4.0/)

of these documents adopt a planned regime of investigation for existing structures with variable levels of complexity according to the situation and the structure importance.

There is large amount of methodological literature on the diagnosis of damage to buildings and engineering structures. [4–6]. Different approaches and methods for assessing the technical condition of reinforced concrete structures are presented in the publications: Z. Zhao, C. Chen, Y.M Kim, C.M. Kim, S.G. Hong (2006), S. Sasmal, K. Ramanjaneyulu (2008), F.M. Zain, M.N. Islam, I.H. Basri (2005), J. Sobhani, A.A. Ramezaniapour (2011), F. Pakdamar., K. Guler (2016), F. Moodi (2004), Khader M. Hamdia (2010), [7–13]; methods for diagnosing damage to brickwork are described in publications by Van Balen (2001), S.D. Shtovba, O.D. Pankevich (2002, 2011, 2018) [13–17] and others.

The technical condition category (TCC), determined by engineering inspection of buildings and structures is the main criterion in deciding on the degree of accident or in deciding whether measures are necessary to bring the construction object to further safe operation. GOST (Russian state standard) scale that includes only 4 TCC – normative, operational, limited operational or emergency. The "transition" of a construction structure from one technical state to another actually does not take place "abruptly", but through a multitude of intermediate states, the boundaries between which are blurred. All this requires from the expert when appointing TCC designs to make strong-willed decisions, increasing the undesirable share of subjectivity in the technical conclusion.

The examiner conducting the examination should establish most significant characteristics from the selected set of parameters characterizing the state of the construction, and for this is needed experience that develops individual, personal knowledge from the specialist. This knowledge, called heuristic, allows experts to make reasonable assumptions, find approaches to problems and make effective decisions, which are based mainly on personal interpretations, intuitions and engineering judgments of experienced engineers. But humans are unable to retain large amounts of data in memory. Humans get tired from physical or mental workload, forget crucial details of a problem; They are inconsistent in their day-to-day decisions and unable to comprehend large amounts of data quickly.

It is advisable to strengthen and expand the professional capabilities of specialists through the application of intellectual technologies in the form expert systems (ES), built on generalized systematized expert knowledge. This will ensure the transition to a new, higher-quality and cost-effective technological level of inspection of construction sites, characterized by high efficiency in decision-making, reliability and validity of the results issued in problem situations.

Analysis of world experience shows that the technology of expert systems is used to solve various types of problems (management, interpretation, diagnostics, planning, design, control, etc.) in a wide variety of problem areas. Among them – the oil and gas industry, energy, transport, medicine, space, metallurgy, mining, chemistry, telecommunications and communications, ecology, etc. In Russia, research and development in the field of expert systems are included in a number of state and sectoral scientific and technical programs. The technology of expert systems is of interest and has great prospects to specialists in the construction industry, as evidenced by both Russian and foreign publications: V.A. Sokolov, (2010, 2016), T.N. Soldatenko (2011), A. Badiru A and J. Cheung (2002), Khader M. Hamdia (2010) and others [18–22].

Expert systems are intelligent computer programs that mimic the decision-making and reasoning process of human experts. They can provide advice, answer questions and justify their conclusions. In such a computer program, human expertise in the designated domain is well represented and saved in the form of a knowledge base. It uses a systematic approach for finding the answer to the problem.

The architecture of expert systems (Figure 1) is typical for most projects from the point of view program modules [24].

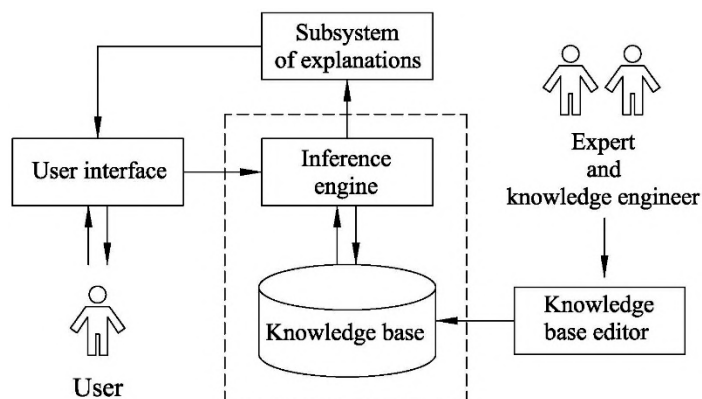


Figure 1. The architecture of the expert system.

Modules of ES can be differently implemented, but their composition and interaction have a clear purpose. When creating an expert system, the main efforts of developers are concentrated on creating a knowledge base, namely on the choice of knowledge representation models and a solver – decision-making methods expert knowledge is understood as a combination of theoretical understanding of the problem and empirical rules (heuristics) for solving it. The nature of knowledge has two sides. It's description of facts, signs, states, phenomena, (declarative knowledge) and description of manipulations with them (procedural knowledge) [24].

Collecting informal information in the knowledge base is a strategically important and most difficult task in the development of ES. This important function provided by only one person or a small group frequently. Two major sources exist for the knowledge: human expert(s) who have been identified as possessing the special skill or mastery and an extensive base of practical and theoretical research on the technical diagnostics of buildings and structures [4–6] (documents or text). The knowledge base can be developed gradually over an extended period of time, much of the knowledge can be changing and these knowledge units need to be updated.

When the knowledge is acquired, it is necessary to represent them into machine-readable form. That is, actually taking the knowledge and putting it into some computer code. For this purpose, it is advisable to use ontological analysis [26, 27], which is aimed at researching and interpreting systemic links in complex objects using methods and tools of computer modeling. The term "ontology" in the theory of artificial intelligence is knowledge formally presented in the form of a description of a set of objects, concepts and connections between them. The formal ontology of the organizational and functional structure of diagnostics of a construction object is the basis for developing a hierarchy of indicators that are used in the decision support system.

When diagnosing the state of a building object, experts often use approximate parameter estimates that have some degree of error and ambiguity. For example, in the process of measuring quantitative parameters, almost always there is an error that depends on the instrument base used and the qualifications of the specialist. The expert's answers on the questions about the preference of factors affecting the evaluation of the technical condition of the structure, their number and interconnection are largely subjective and fuzzy. This is due to the fuzzy of the criteria for assessing the structure, building or structure, formulated in regulatory documents, as well as a short scale GOST (Russian state standard), which includes only 4 categories [3].

There are several approaches used to uncertainty management for expert systems. The best-known and used methods in existence are; Bayesian inference, Certainty factors and Fuzzy set. Fuzzy set theory is one of the major approaches used to handle uncertainties and ambiguities and has important applications in the field of knowledge based expert systems [3, 23, 27, 28]. Professor Lofti Zadeh [29] first introduced fuzzy logic in 1960's. This theory provides a major paradigm in modeling and reasoning with uncertainty and provide decision support. Fuzzy logic theory is not a fuzzy theory but it is logic interpret the fuzziness. In other words, fuzzy theory itself is precise; and the "fuzziness" appears in the phenomena that the theory tries to study [30].

Fuzzy set theory allows one to formalize and process the most heterogeneous information contained in the description of the signs of the technical state of structures, to simulate loosely formalized reasoning such as: "many," "little," "often," "rarely," "about ...," "approximately ...", "not less than ...", "no more ...", "in the range from ... to ...", etc. There is knowledge the reliability of which is expressed by some coefficient, for example 0.8 or 0.5.

The application of fuzzy sets theory and its applications makes it possible to construct formal schemes for solving problems with approximate quantitative or qualitative estimates of parameters, using linguistic variables [12]. The concept of a linguistic variable is the basis of approximate reasoning. Its meanings can be words or phrases (terms) in natural or formal language. At the same time, information from the subject area (technical diagnostics of buildings and structures) must be formalized in terms of fuzzy sets – as membership functions [24, 31] for both input and output parameters describing the current state structural damage and possible causes of these damage.

The membership function  $\mu_A \{x\}$  (Figure 2) quantitatively indicates the degree of belonging of an element  $x$  to a fuzzy set  $A$  of the argument space  $X$ . Value of 0 means that the element is not included in the fuzzy set, 1 describes the fully included element. Values between 0 and 1 characterize the fuzzy elements included.

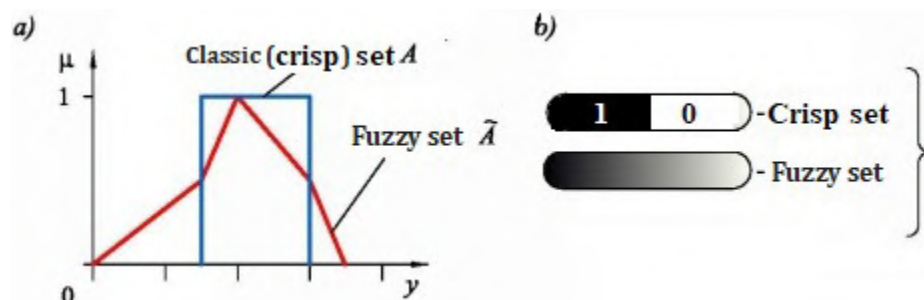


**Figure 2. Graphs of the membership functions of the classical (crisp) and fuzzy set (a) and their semantic difference (b).**

Finite fuzzy sets are usually written in the form

$$\bar{A} = \{ \langle X, \mu A(x) \rangle \} \text{ or } = \{ \langle x / \mu A(x) \rangle \}, x \in X. \quad (1)$$

The membership functions, in a sense, are a database that is necessary to convert for both input and output heterogeneous information into the format of the subsequent dialogue with the knowledge base. The quality of solutions issued by a fuzzy system is most dependent on the professional knowledge of experts and the adequacy of their reflection by membership functions.

Fuzzy logic output systems perform the transformation of the values of input variables into output variables. To do this, they must contain a procedural knowledge base of fuzzy inference based on rules compiled in natural language (embedded in the ES at its creation) of the form: "**IF** <prerequisite>, **THEN** <conclusion>". Fuzzy logic allows to technically implement the linguistic links of the rules "IF-THEN", "and", "or" with the help of mathematical operations.

As a result of logical inference, a fuzzy value of the structure technical state category with the maximum degree of confidence is obtained. Crisp value of the category (both integer and fractional) can be determined using the defuzzification operation (for example, using the "center of gravity" method) [24].

Automated search for an expert solution, using intellectual expert systems, can help in the work not only for a beginner, but also an experienced expert. The present work is motivated by a need to transfer knowledge from the technical books and experienced experts in the domain field to make that knowledge and expertise available to practicing engineers.

## 2. Methods

When diagnosing real construction objects, it is necessary to identify all possible causes leading to change of technical condition category and suggest possible solutions for their elimination. The expert's tasks in technical inspection of various types of building structures include visual and instrumental assessment of structural damage (presence and parameters of defects, cracks), assessment of the condition of materials (wood, reinforced concrete, metal), carrying out the necessary calculations of the stress-strain state taking into account the existing damage, and also check of compliance of the characteristics of the structures established during the inspection with the current regulatory requirements.

Conceptual model of the knowledge base [24] was obtained in the form of a hierarchical 4-level structure of interrelated solution stages (Figure 3), as a result of the research. It implements the principle of decomposition of a set of controlled parameters of the technical condition and connections between them of any building structures. TCC of the structure or building (1 – normative, 2 – operational, 3 – limited operational, 4 – emergency) is determined at the target level as for a complex system as a whole

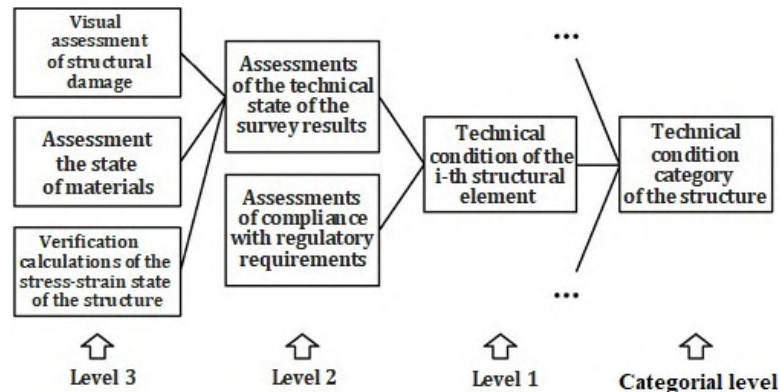


**Figure 3. Conceptual model of the knowledge base "Definition of the category of technical condition of building structures".**

For the automated search of an expert opinion on the TCC of a building object, it is necessary to provide all possible causes leading to a change in the category of technical condition. Sources of knowledge are an extensive base of practical and theoretical research on the technical diagnostics of buildings and structures, regulatory documentation, heuristic knowledge and reasoning of specialists.

It is proposed to formalize the declarative knowledge about the technical state of constructions by the method of computer ontologies ( $O$ ), which allows establishing mathematical and logical connections between parameters. Ontological analysis begins with an analytical work on the allocation and consolidation of subject knowledge, i.e. an informal conceptual model of knowledge is constructed by defining a set of basic concepts and the relationships between them.

The formal expression of declarative knowledge or computer ontology ( $O$ ) for the considered area, which provides the possibility of unified and repeated use on different computer platforms, can be represented [26]:

$$O = \langle K, R, F \rangle, \quad (2)$$

where  $K = \{k_1, k_2, \dots, k_i, \dots, k_n\}$ ,  $i = \overline{1, n}$ ,  $n = \text{Card } K$  – finite set of concepts of the studied subject area (input, intermediate and output controlled parameters);

$R = \{r_1, r_2, \dots, r_j, \dots, r_m\}$ ,  $R: k_1 \times k_2 \times \dots \times k_m$ ,  $j = \overline{1, m}$ ,  $m = \text{card } R$  – a finite set of semantically meaningful relationships between concepts;

$F: K \times R$  – a finite set of interpretation functions defined on concepts and / or relationships.

Formal ontological models have good computational properties. They provide computer processing and automatic formal inference when solving specific problems.

The state and damage assessment of structures are inherently subject to vagueness, ambiguity and consequently to uncertainty, where subjective opinion and incomplete numeric data are unavoidable [12]. When diagnosing the state of a building object, experts often use approximate parameter estimates that cannot be interpreted as completely true or completely false. The expert's answers on the questions about the preference of factors affecting the evaluation of the technical condition of the structure, their number and interconnection are largely subjective.

Expert Systems are relatively new and can be attractive to structural engineers. The system has the advantage of enhancing the efficiency and reliability of assessment and flexibility concerning missing or inadequate criteria. The most effective solutions to problems containing blurring and inaccuracy can be obtained using the mathematical apparatus of the theory of fuzzy sets and fuzzy logic which makes it possible to take into account the scatter of individual opinions.

The process of the technical condition category determining is a set ( $p$ ) of solutions of interrelated subtasks of a multilevel task. For fuzzy parameters  $X_p^{l+1}, Y_p^{l+1}$ , the parameter  $y_p^l$  is a fuzzy subset  $\tilde{B}$ :

$$\tilde{B} = \tilde{A} \circ \tilde{R}, \quad (3)$$

where  $\tilde{A}$  is a fuzzy subset of the input variables sets (term-set),

$\tilde{B}$  is a fuzzy subset of the output variable sets  $y_p^l$ ; (term-set);

$l$  is the level of subtask  $p$ ;

$\circ$  is the symbol of the maximin composition L. Zade;

$\tilde{R}$  is a fuzzy relation  $PA \times PB$ , represented by control rules of the form "IF <prerequisite>, THEN <conclusion>";

$PA$  is the set of input values of the parameters  $X_p^{l+1}, Y_p^{l+1}$ ;

$PB$  is the set of output values of the parameter  $y_p^l$  [32].

Monitored parameters of the diagnosed object state can be quantitative (actual and estimated values of deflections, crack opening width, strength of concrete, etc.) and qualitative (operating conditions, visible damage, etc.)

Information in the subject area of buildings and structures technical diagnostics containing fuzziness must be formalized in terms of fuzzy sets. For this, membership functions and linguistic variables are used. The concept of a linguistic variable is the basis of approximate reasoning. Its meanings can be words or phrases (terms) in a natural or formal language, for example, "high", "above average", "below average", "low" [24].

The person designing the ES creates from the rules in the verbal representation specific membership functions. Usually he defines their values by the method of questions and answers; instructs experts to perform operations and recreate the situation from time-stamped data; can correct the values of membership functions, getting the best results from experiments, previous experiences that simulate this situation.

Each membership function in this case indicates a degree of confidence in the value of the output variables for given values of the input parameters and the use of rules that determine the ratio of input and output variables.

Each controlled qualitative and quantitative parameter of the technical state ( $x_i, i = 1: n$ ) of structures (inputs), as well as the result of the state estimation or category  $y$  (output) are represented by linguistic variables on the corresponding universal sets  $X_i = [\underline{x}_i, \bar{x}_i]$ , where  $\underline{x}_i$  and  $\bar{x}_i$  are the minimum and maximum values of the input variable,  $\underline{y}$  and  $\bar{y}$  – output variable, respectively.

For quality variables, rank measurements are used that reflect the preferences of experts. When constructing the functions of controlling parameters, it is convenient (but not necessary) to use 4 linguistic estimates: "high", "above average", "below average", "low", which are called "terms" and constitute a term-sets  $T$  for the variables  $x$ . These term-sets of inputs can be described by analytic functions or be displayed graphically in the form of a triangular, trapezoidal, bell-shaped, singleton and other forms.

To describe concepts characterized by measurable properties, the optimal methods from the point of view of labor costs are direct methods of constructing membership functions. To describe concepts and attributes that are not measured (qualitative) properties, such as color of concrete or a description of the results of visual inspection of reinforcement damaged by corrosion, indirect methods are usually used. Studies have shown that the joint use of indirect methods of Saati [34], in combination with the method of P.J.M. Laarhoven and W.A. Pedrycz, [34], Chang [35], for the construction of membership functions, makes it possible to control distortions of information, inconsistencies in statements in order to obtain more adequate results in comparison with other known methods [31].

Technical state of any construction is represented by the Cartesian product of the input and exit spaces [32]:

$$C \subset X^* \times Y^*, \quad X_i^* = [x_i, \bar{x}_i], \quad Y^* = [y, \bar{y}]. \quad (4)$$

Expert opinion on the category of technical condition is determined by the expression:

$$X = \{x_1, x_2, \dots, x_n\} \rightarrow y.$$

there  $x_i$  is set of input monitored parameters of the structure, taking the values  $X^*$ ;

$Y^*$  is set of output values of monitored parameters;

$y$  is the category of the structure technical state (the output parameter takes the value  $Y^*$ ).

The development and application of fuzzy inference systems include a number of steps (see Figure 4).

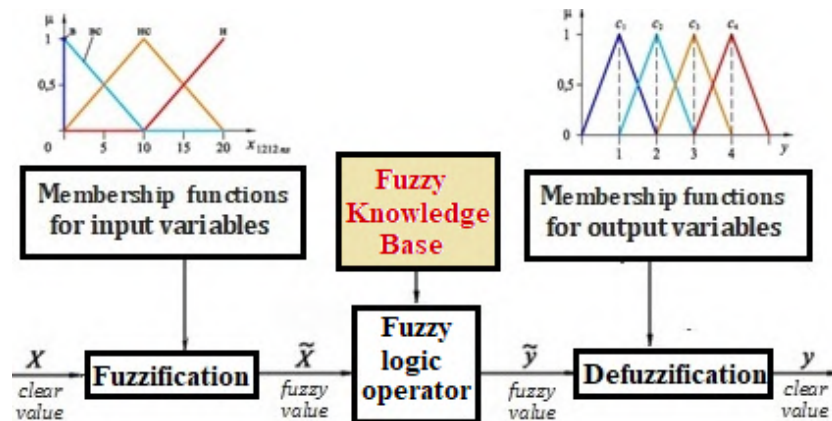


Figure 4. Fuzzy Inference Scheme.

Fuzzification is the process of taking actual real-world data and converting them into a fuzzy input. Defuzzification is the conversion of a fuzzy quantity to a precise quantity. Fuzzy logic operator includes procedures for aggregating and accumulating – determining the degree of truth conditions for each of the rules of fuzzy inference for each input and output linguistic variables. As a result of logical inference, an indistinct value of the output variable is obtained – the result of evaluating the category of the technical state of the construction as a class with the maximum degree of membership. A clear (numerical) value of the category  $Y$  (both integer and fractional) can be determined with the help defuzzification operation, for example, using the "center of gravity" method. The possibilities of using known algorithms for fuzzy inference are considered (Sugeno, Mamdani, Singleton and etc.). The choice is made in favor of the Mamdani algorithm, which is modified and adapted to the solution of this problem. Preference is due to the suitability of this algorithm for cases of complex sampling of experimental data (in the absence of an effective system for collecting information), as well as the inherent ability of the graphical interpretation of the resulting conclusion about the technical state of the design [24].

When assigning a TCC, the "space" of a technical state of any structure for the period of its existence is proposed to be divided into 4 parts with blurred boundaries (Figure 5) (similar to the number of categories corresponding to Russian State Standard GOST 31937–2011).

$$C_p = C = \{c_1, c_2, c_3, c_4\}, \quad (5)$$

where  $C$  are fuzzy terms corresponding to categories of technical states: normative is  $c_1$ , operational is  $c_2$ , limited operational is  $c_3$ , emergency is  $c_4$  [32].

Then a fuzzy set characterizing the result of solving a subtask  $\langle p \rangle$  – for a variable  $y_p^l$  takes the form:

$$\tilde{C}_p = \left\{ \frac{\mu_{c1}(X^{(p)})}{c_1}, \frac{\mu_{c2}(X^{(p)})}{c_2}, \frac{\mu_{c3}(X^{(p)})}{c_3}, \frac{\mu_{c4}(X^{(p)})}{c_4} \right\},$$

and a fuzzy set of variable  $y$  (the result of a comprehensive evaluation of the structure):

$$\tilde{C} = \left\{ \frac{\mu_{c1}(X)}{c_1}, \frac{\mu_{c2}(X)}{c_2}, \frac{\mu_{c3}(X)}{c_3}, \frac{\mu_{c4}(X)}{c_4} \right\}.$$

### 3. Results and Discussion

The technique of development of ES on definition of clear value of TCC is presented on through an example of the research module of estimation of a technical condition of bent reinforced concrete designs (plates, beams). As a result of the analysis of the subject area, an informal conceptual model of *declarative* knowledge is constructed. Categorical level 1 includes five groups of indicators: the state of supports, normal cross-sections, inclined cross-sections, fixed parts and connections, evaluation of rigidity (Figure 6).

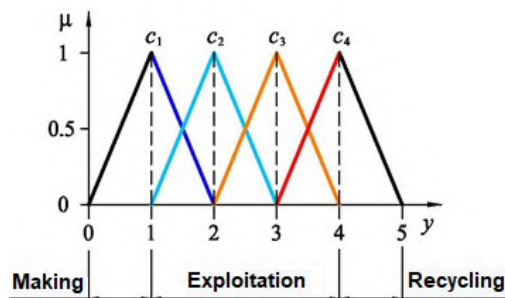


Figure 5. Fuzzy triangular numbers.

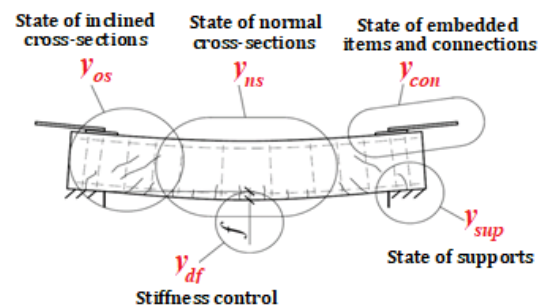


Figure 6. Indicators of the 1-level ontology "Technical condition of a bent reinforced concrete structure".

The formal representation of the ontology of the concepts used and the scheme of their relations is represented in the form of a graphical ontograph (Figure 7a), on which a system of notation and indexing is provided, which makes it possible to compress its visual representation. Figure 7b shows a fragment of this ontograph, which includes a part of the subsystem "State of normal cross-sections" with explanations of the concepts of the categorical level of ES [24]. Notation and indexing reflect that each concept characterizes: a class, a group of characteristics or a parameter, and also levels, sublevels and connections. The letter  $x$  denotes concepts that characterize the input monitored parameters,  $y$  is the output intermediate and final grades of the technical condition category. In the research module of the ES "Technical condition of the reinforced concrete bending structure" ~90 possible controllable parameters are included, for each of which the membership functions are constructed [24, 32].

The developed ES must contain knowledge that allows to search for the leading signs of damage to building structures among any number of defects (states), taking into account their degree of severity, subordination and mutual influence.

Let us explain the technology of constructing the membership functions by examining the corrosion index of the reinforcement of a reinforced concrete structure that is a part of the ontology "State of normal cross-sections" [25]. Linguistic variables: qualitative ( $x_{1211\ ns}$ ) – "Result of certification of corrosion of reinforcement" and quantitative ( $x_{1212\ ns}$ ) – "Result of measuring the residual cross-sectional area of the reinforcement" – are set by experts based on inspection of the surface of the reinforcement and measurement of the residual cross-section area of the reinforcement of reinforced concrete structures.

Universal set of the considered linguistic variable  $x_{1211\ ns}$  is defined by a finite number of qualitative attributes (1 – surface net reinforcement (at dissection), 2 – local areas of reinforcement damage by surface corrosion (dots and spots of corrosion), 3 – solid surface corrosion of reinforcement; 4 – local areas of ulcerated, lamellar corrosion of the reinforcement, cracking of the protective layer of concrete, 5 – lamellar corrosion of the reinforcement, cracking and extrusion of the protective layer of concrete by corrosion products). The set  $X_{1211\ ns} = \{1, 2, 3, 4, 5\}$  is discrete and exact. The linguistic variable  $x_{1212\ ns}$  "Result of measuring the residual cross-sectional area of the reinforcement" must evidently take quantitative values from the universal continuous set  $X_{1212\ ns}$  of the reduction in the cross-sectional area of the reinforcement in %.

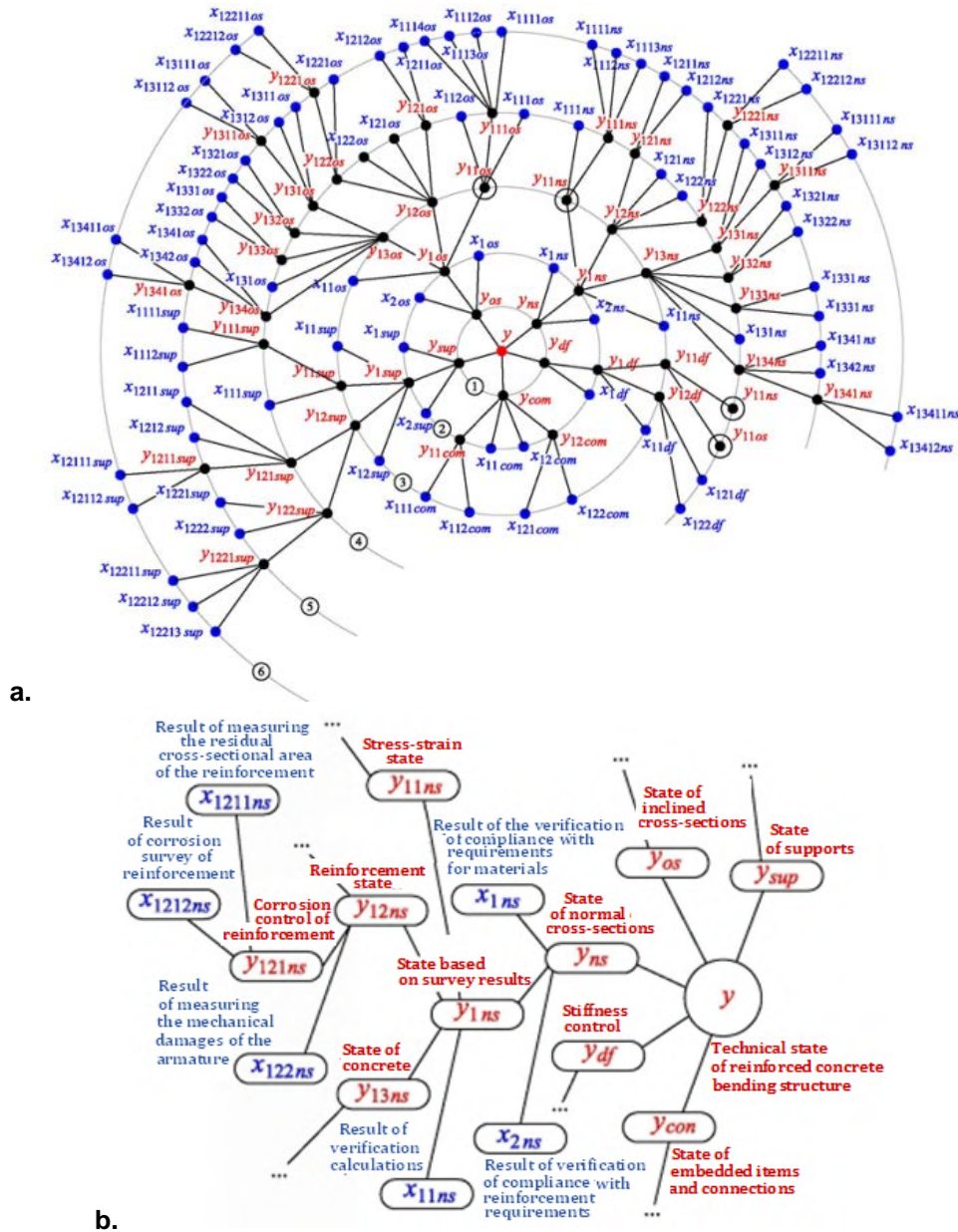


Figure 7. Indexed ontograph "Technical condition of the bent reinforced concrete structure".

As shown by our studies, in order to describe the parts of the membership functions between the characteristic points, the "classical" triangular function and its modified version is a triangular "broken line" are best suited. In Figure 8, for illustrative purposes, examples of graphs of the functions of the variables "

Result of the inspection of reinforcement corrosion "(a) and "Result of measurement of the residual cross-section area of the reinforcement "are shown (b) with the degree of belonging to terms (local areas of reinforcement damage and reduced cross-sectional area reinforcement by 2 %) [24, 32].

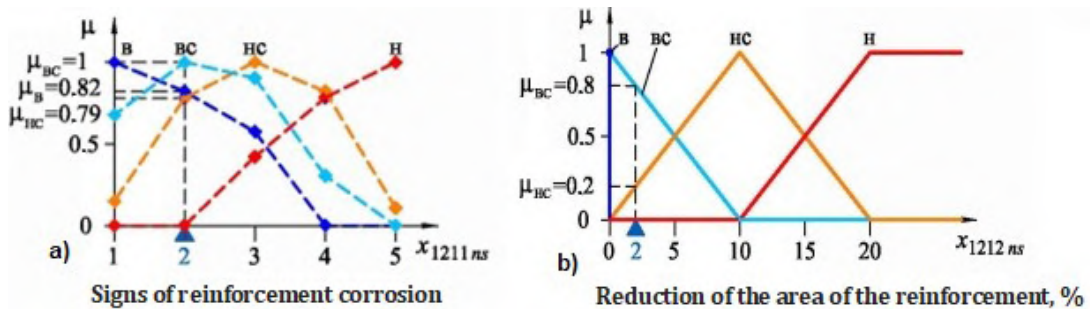


Figure 8. Examples of graphs of the membership functions of the terms of the variables  $X_{1211 ns}$  (a) and  $X_{1212 ns}$  (b) with the mapping of degrees of belonging to terms.

Fuzzy knowledge base for definition of the TCC of bent reinforced concrete elements is developed on the basis of experience (heuristic knowledge) of specialists in engineering survey of structures of buildings

and structures. Rules are linked together by logical operations "or", and the premise of a rule can consist of fragments that are linked by the operations "and" or/and "or". The knowledge base fragment for the controlled output variable  $y_{121ns}$  – "Reinforcement corrosion" control", which includes the first four (out of 16) rules has the following form:

*If  $x_{1211 ns} = "high"$  and  $x_{1212 ns} = "high"$ ,*  
*then  $y_{121 ns} = "high"$ , or,*  
*if  $x_{1211 ns} = "high"$  and  $x_{1212 ns} = "above average"$ ,*  
*then  $y_{121 ns} = "above average"$ , or,*  
*if  $x_{1211 ns} = "high"$  and  $x_{1212 ns} = "below average"$*   
*then  $y_{121 ns} = "below average"$ , or,*  
*if  $x_{1211 ns} = "high"$  and  $x_{1212 ns} = "low"$ ,*  
*then  $y_{121 ns} = "below average"$ , or ...*

In total, the knowledge base of the ES research module contains more than 5000 rules.

A series of double-girder truss beams of an I-section was inspected at a manufacturing plant in the Perm Territory (Figure 9a). The results of the evaluation of their technical condition are shown on the example of one of the surveyed beams in the form of histograms with grouping of characteristics into categories (from 1 to 4), obtained using the developed expert system (Figure 9b). Visualization of the results significantly increases the "transparency" of decisions taken on the degree of accident rate, forms an understanding of the causes and risks of a possible change in the technical condition of structures, buildings or structures. Figure 9c shows the location of the monitored parameters. Parameters with detected anomalies are marked. Table 1 shows their meaning.

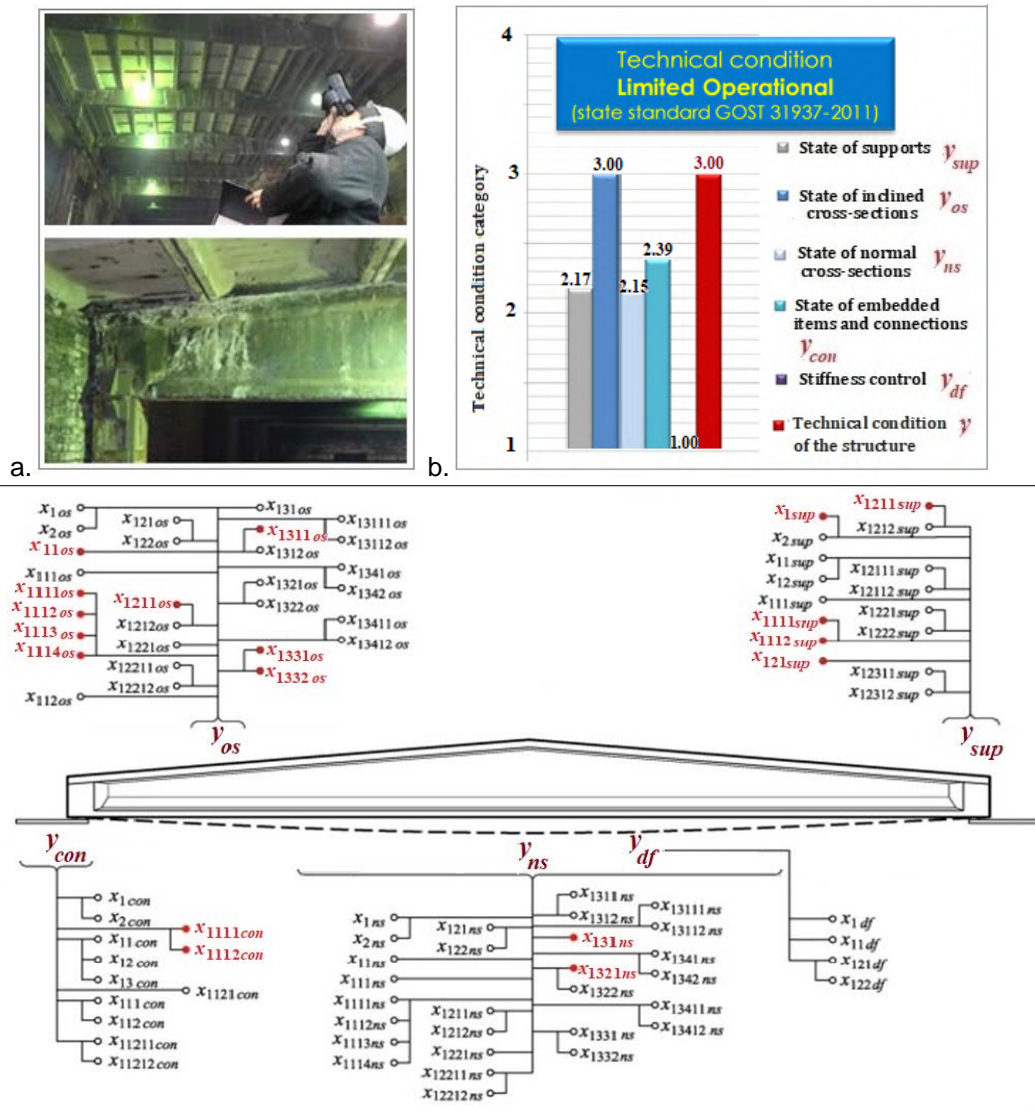


Figure 9. An example of displaying clear values of the technical condition category of a reinforced concrete beam at the stage of monitoring.

The results of the technical state evaluation examined structure, obtained using the expert system, are confirmed by expert opinions of specialists who did not participate in the creation of the program and have extensive experience in examining the building structures.

In the course of creating an expert system, Microsoft Excel was used in the spreadsheet, which is one of the most accessible software tools, providing the user with the opportunity to independently implement the mechanisms for solving mathematical problems. In a formalized form, the description of the navigation structure of the application is an XML file that allows processing, changing data in any other system regardless of the client platform or operating system [32].

**Table 1. Parameters of the surveyed beam with anomalies that affect the category of the structure technical state.**

Parameter designation $x_i$ (index $i$ )	Name of the controlled parameter	Expert's answer to the question of the system
<b>State of supports (<math>y_{sup}</math>) – 18 monitored parameters</b>		
1 <sup>sup</sup>	The result of checking compliance with design requirements	No deviations detected
1111 <sup>sup</sup>	The result of the inspection of corrosion of reinforcement	Pieces of continuous surface corrosion of reinforcement were found
1112 <sup>sup</sup>	Result of measuring the residual cross-sectional area of reinforcement	The cross-sectional area of reinforcement is reduced by 3 % as a result of corrosion
1211 <sup>sup</sup>	Measurement result of lime leaching from concrete	1 %
121 <sup>sup</sup>	Measurement result of mechanical damage to concrete	The cross-sectional area on the support has not changed
<b>State of inclined cross-sections (<math>y_{os}</math>) – 29 monitored parameters</b>		
11 <sup>os</sup>	The result of calibration calculations	Strength is not provided, overvoltage – 4 %;
1111 <sup>os</sup>	The result of the presence of inclined cracks on the support	Inclined crack opening width – 0.1 mm;
1112 <sup>os</sup>		distance between cracks – 910 mm;
1114 <sup>os</sup>		inclined crack angle – 48°
1211 <sup>os</sup>	The result of the inspection of corrosion of reinforcement	Pieces of continuous surface corrosion of shear reinforcement were found
1311 <sup>os</sup>	Measurement result of lime leaching from concrete	1 %
1331 <sup>os</sup>	Result of measuring the neutralization depth of the protective layer	No more than 35 %
1332 <sup>os</sup>	Measurement result of damage to the protective layer	Damage area – 14 %
<b>State of normal cross-sections (<math>y_{ns}</math>) – 28 monitored parameters</b>		
131 <sup>ns</sup>	Measurement result of mechanical damage to concrete	Cross- section area reduced by 3 %
1321 <sup>ns</sup>	The result of the examination of concrete	When you knock, a rather sonorous sound is emitted, barely visible chips on the surface of the concrete remain
<b>State of embedded items and connections (<math>y_{con}</math>) – 11 monitored parameters</b>		
1111 <sup>con</sup>	The result of the inspection of corrosion of items	Pieces of continuous surface corrosion of items were found
1112 <sup>con</sup>	Result of measuring the residual cross-sectional area of items	The cross-sectional area of item is reduced by 2 %

## 4. Conclusion

1. An expert opinion on the technical condition of building structures requires deep specialized knowledge and depends on the experience of the expert and the accuracy of the information. An expert system is a useful tool for solving ill-defined problems in which intuition and experience are necessary ingredients. An automated search for an expert solution using intelligent expert systems can help in the work of not only a beginner, but also an experienced specialist.

2. The organization structure of expert knowledge for an intelligent expert system for assessing the building structures technical condition, taking into account the hierarchy of knowledge, information universality and the possibility of expansion, based on ontological analysis, is proposed.

3. A technique has been developed for formalizing expert information on the basis of the theory of fuzzy sets, expert estimation methods and analysis of hierarchy.

4. An expert system has been developed to assess the technical condition of reinforced concrete bent elements, which can significantly reduce the time and improve the quality of the expert opinion. The assessment of the adequacy of the decisions issued by the EC was carried out on the basis of modeling scenarios for various damage to flexible concrete structures, analyzing data from a number of technical reports on the examination of real structures and tested on real construction sites.

5. The present work is motivated by a need to transfer knowledge from the technical books and experienced experts in the domain field to make that knowledge and expertise available to practicing engineers.

6. An intelligent fuzzy expert system patented in the Federal Service for Intellectual Property (Certificate No. 2018615097 dated 24/04/2018) was implemented in the Perm Territory.

## References

- Rücker, W., Rohrmann, R.G., Hille, F. Guidelines for monitoring and assessment – A SAMCO initiative as a basis for the international standardization. Structural Health Monitoring and Intelligent Infrastructure – Proceedings of the 2nd International Conference on Structural Health Monitoring of Intelligent Infrastructure, SHMII. 2005. Vol. 2. Pp. 1671–1676.
- Jeppsson, J. Reliability-Based Assessment Procedures for Existing Concrete Structures. Unpublished doctoral thesis. Lund University. Sweden. 2003. 199 p.
- Tonkov, I.L., Tonkov, Yu.L. Aktual'nyye problemy otsenki tekhnicheskogo sostoyaniya stroitel'nykh konstruksiy [Actual problems of assessing the technical condition of building structures]. Vestnik PNIPU, Prikladnaya ekologiya. Urbanistika. 2017. No. 3. Pp. 94–104. (rus)
- Groz dov, V.T. Priznaki avariynogo sostoyaniya nesushchikh konstruksiy zdaniy i sooruzheniy [Signs of an emergency condition of buildings and structures]. SPb.: Izdatel'skiy Dom KN+, 2000. 39 p. (rus)
- Guchkin, I.S. Diagnostika povrezhdeniy i vosstanovleniye ekspluatatsionnykh kachestv konstruksiy [Diagnosis of damage and restoration of performance of structures]. M.: Izdatel'stvo ASV, 2001. 171 p. (rus)
- Dobromyslov, A.N. Diagnostika povrezhdeniy zdaniy i inzhenernykh sooruzheniy [Diagnostics of damage to buildings and engineering structures]. Moskva: MGSU, 2006. 256 p. (rus)
- Kim, Y.M., Kim, C.M., Hong, S.G. Fuzzy based state assessment for reinforced concrete building structures. Engineering Structures. 2006. Vol. 28. Iss. 9. Pp. 1286–1297.
- Sasmal, S., Ramanjaneyulu K. Condition evaluation of existing reinforced concrete bridges using fuzzy based analytic hierarchy approach. Expert Systems with Applications. 2008. Vol. 35. Pp. 1430–1443.
- Pakdamar, F., Guler, K. Fuzzy logic approach in the performance evaluation of reinforced concrete structures (flexible performance). [Online]. System requirements: AdobeAcrobatReader. URL: [http://www.iitk.ac.in/nicee/wcee/article/14\\_05-03-0100.PDF](http://www.iitk.ac.in/nicee/wcee/article/14_05-03-0100.PDF) (date of the application: 11.08.2016).
- Zain, F.M., Islam, M.N., Basri, I.H. An expert system for mix design of high performance concrete. Advances in Engineering Software. 2005. Vol. 36. No. 5. Pp. 325–337.
- Moodi, F. Integration of knowledge management and Information Technology into the repair of concrete structures: an innovative approach. International Journal of IT in Architecture, Engineering and Construction. 2004. Vol. 2. Iss. 3. Pp. 173–190.
- Khader, M. Hamdia. Expert System for Structural Evaluation of Reinforced Concrete Buildings in Gaza Strip Using Fuzzy Logic. A Thesis Submitted in Partial Fulfillment of the Requirement for the Degree of Master of Science in Civil Engineering Rehabilitation and Design of Structure. 2010. 92 p.
- Sobhani, J., Ramezaniyanpour, A.A. Service life of the reinforced concrete bridge deck in corrosive environments: A soft computing system. Applied Soft Computing Journal. 2011. Vol. 11 (4). Pp. 3333–3346.
- Balen, K. Learning from damage of masonry structures, expert systems can help. International Seminar on Historical Constructions. 2001. November. Pp. 15–27.
- Pankevich, O.D., Shtovba, S.D. Application of fuzzy models for diagnostics of constructional structure. Bulletin of the Vinnytsia Polytechnic Institute. 2011. No. 4. Pp. 32–36.
- Shtovba, S., Rotshtein, A., Pankevich, O. Fuzzy rule based system for diagnosis of stone construction cracks of buildings. Advances in Computational intelligence and learning, methods and applications. Dordrecht: Kluwer Academic Publisher. 2002. Pp. 401–412.
- Shtovba, S.D., Pankevych, O.D. Fuzzy technology-based cause detection of structural cracks of stone buildings // Proceedings of the 14th International Conference on ICT in Education, Research and Industrial Applications. Integration, Harmonization and Knowledge Transfer. Kyiv, 2018. Vol. I: Main Conference. Pp. 209–218.
- Sokolov, V.A. Ocenka tekhnicheskogo sostoyaniya stroitel'nykh konstrukcij zdaniy na osnove mnogourovnevnogo veroyatnostnogo analiza [Building systems technical condition assessment based on the multilevel probabilistic analysis]. Magazine of Civil Engineering. 2011. No. 7 (25). Pp. 45–51. (rus) DOI: 10.5862/MCE.25.7
- Sokolov, V.A. Kategorii tekhnicheskogo sostoyaniya stroitel'nykh konstruksiy zdaniy pri ikh diagnostike veroyatnostnymi metodami. [Technical condition categories of building structures in their diagnosis by probabilistic methods]. Fundamental'nyye issledovaniya. 2014. No. 6 (6). Pp. 1159–1164. (rus)
- Soldatenko, T.N. Model of identification and prediction of building design defects on the basis of its inspection results. Magazin of Civil Engineering. 2011. No. 7. (25). Pp. 52–60. (rus).
- Badiru, A., Cheung, J. Fuzzy engineering expert systems with neural network applications. John Wiley and Sons. USA. 2002. 289 p.
- Sokolov, V.A. Veroyatnostnyj analiz tekhnicheskogo sostoyaniya (VATS) stroitel'nykh konstrukcij zdaniy staroj gorodskoj zastrojki [Probabilistic analysis of the technical condition (VATS) of building structures of buildings of old urban buildings]. Monografiya. – Saarbrücken, Germany: Izd-vo LAP LAMBERT Academic Publishing is a trademark of: AV Akademikerverlag GmbH & Co. KG. HeinrichBöcking-Str. 6–8, 66121. 2013. 152 p. (rus)

23. Kkaetzel, L.J., Clifton, J.R. Expert Knowledge Based Systems for Materials in the Construction Industry. State-of-the-Art Report, Materials and Structures. 1995. Vol. 28. Pp. 160–174.
24. Kashevarova, G.G., Tonkov, Yu.L. Intellektual'nyye tekhnologii v obsledovanii stroitel'nykh konstruksiy. [Intelligent technology in the survey of building structures]. Academia. Architecture and building. 2018. No. 1. Pp. 92–99. (rus) DOI: 10.22337/2077-9038-2018-1-92-99
25. Smirnov, S.V. Ontologicheskiy analiz v sistemakh komp'yuternogo modelirovaniya: dis. dokt. tekhn. nauk. [Ontological analysis in computer simulation systems]. Ros. akad. nauk., In-t probl. upr. slozh. sistemami. Samara, 2002. 348 p. (rus)
26. Palagin, A.V., Petrenko, N.G., Malakhov, K.S. Metodika proyektirovaniya ontologii PdO [Methods of designing ontology PdO]. Companions, systems and systems. 2011. No. 10. Pp. 5–12. (ukr)
27. Lu, X.; Simmonds, H. KBES for evaluating R.C. framed buildings using fuzzy sets. Automation in Construction. 1997. Vol. 6. Iss. 2. Pp. 121–137.
28. Pomykalski, J.J., Truszkowski, W.F., Brown, D.E. Expert System. Wiley Encyclopedia for Electrical and Electronics Engineering. February, 1999.
29. Zadeh, LA. Fuzzy sets as a basis for a theory of possibility. Fuzzy Sets and Systems. 1999. Vol. 100. Pp. 9–34.
30. Tararushkin, Ye.V. Primeneniye nechetkoy logiki dlya otsenki fizicheskogo iznosa nesushchikh konstruksiy zdaniy. [The use of fuzzy logic to assess the physical deterioration of the supporting structures of buildings]. Vestnik BGTU im. V.G. Shukhova. 2016. No. 10. Pp. 77–82. (rus)
31. Tonkov, Yu.L. Vybor effektivnogo metoda postroyeniya funktsiy prinadlezhnosti dlya otsenki kachestvennykh priznakov tekhnicheskogo sostoyaniya stroitel'nykh konstruksiy [The choice of an effective method of constructing membership functions for assessing the qualitative signs of the technical condition of building structures]. Vestnik PNIPU, Prikladnaya ekologiya. Urbanistika. 2016. No. 3(23). Pp. 126–146. (rus) DOI: 10.15593/2409;5125/2016.03.09
32. Tonkov, Yu.L. Matematicheskie modeli dlya identifikatsii kategorii tekhnicheskogo sostoyaniya stroitel'nykh konstruksiy na osnove nechetkoy logiki [Mathematical models for identifying the category of technical condition of building structures based on fuzzy logic]: dis. ... kand. tekhn. nauk. Perm. nac. issled. politekhn. un-t. Perm. 2018. 208 p. (rus)
33. Saaty, T.L. The Analytic Hierarchy Process. McGraw-Hill, New York. 1980. 287 p.
34. Laarhoven, P.J.M., Pedrycz, W.A. A fuzzy extension of Saaty's priority theory. Fuzzy sets and systems. 1983. Vol. 11. Pp. 229–241.
35. Chang, D.Y. Extent analysis and synthetic decision, optimization techniques and applications. World Scientific. 1992. Vol. 1. Pp. 352–355.

**Contacts:**

*Galina Kashevarova, +7(912)884-38-04; ggkash@mail.ru*  
*Yuriy Tonkov, +7(902)833-38-55; 95081@mail.ru*



DOI: 10.18720/MCE.93.2

## Техническая диагностика железобетонных конструкций с применением интеллектуальных систем

**Г.Г. Кашеварова\*, Ю.Л. Тонков**

*Пермский национальный исследовательский политехнический университет, г. Пермь, Россия*

\* E-mail: [gdkash@mail.ru](mailto:gdkash@mail.ru)

**Ключевые слова:** диагностика зданий и сооружений, железобетонные конструкции, категория технического состояния, экспертная система, нечеткая логика, онтологический анализ

**Аннотация.** Представлены результаты разработки эффективной интеллектуальной системы диагностики технического состояния железобетонных конструкций зданий и сооружений. Категория технического состояния является основным критерием при определении степени аварийности строительного объекта или необходимости принятия мер для его дальнейшей безопасной эксплуатации. Для того, чтобы решить эту проблему, разработана экспертная система, на основе математического аппарата теории нечетких множеств и нечеткой логики, которая может учесть разброс индивидуальных мнений экспертов, значительно сократить время обследования и повысить качество экспертного заключения. Предложена структура организации экспертных знаний для оценки технического состояния строительных конструкций с учетом иерархии знаний, универсальности информации и возможности ее расширения на основе онтологического анализа. Разработана методика формализации экспертной информации с помощью функций принадлежности для входных и выходных параметров управления. Для реализации нечеткого логического вывода разработан алгоритм, адаптированный к данной проблеме. Разработана компьютерная программа, которая реализует метод идентификации категории технического состояния строительных конструкций на основе нечетких баз знаний. Приведены результаты использования этой технологии при обследовании реального промышленного здания. Результаты оценки технического состояния исследуемой структуры, полученные с использованием экспертной системы, подтверждаются экспертными заключениями специалистов, которые не участвовали в создании программы и имеют большой опыт в обследовании строительных конструкций. Настоящая работа мотивирована необходимостью передачи знаний опытных экспертов, и технической книг в предметной области диагностики строительных конструкций, чтобы сделать эти знания и опыт доступными для практикующих инженеров.

### Литература

1. Rucker W., Rohrmann R.G., Hille F. Guidelines for monitoring and assessment – A SAMCO initiative as a basis for the international standardization // Structural Health Monitoring and Intelligent Infrastructure – Proceedings of the 2nd International Conference on Structural Health Monitoring of Intelligent Infrastructure, SHMII. 2005. Vol. 2. Pp. 1671–1676.
2. Jeppsson J. Reliability-Based Assessment Procedures for Existing Concrete Structures. Unpublished doctoral thesis. Lund University, Sweden. 2003. 199 p.
3. Тонков И.Л., Тонков Ю.Л. Актуальные проблемы оценки технического состояния строительных конструкций // Вестник Пермского национального исследовательского политехнического университета. Прикладная экология. Урбанистика. 2017. № 3. С. 94–104.
4. Гроздов В.Т. Признаки аварийного состояния несущих конструкций зданий и сооружений. СПб: Издательский Дом КН+, 2000. 39 с.
5. Гучкин И.С. Диагностика повреждений и восстановление эксплуатационных качеств конструкций. М.: Издательство АСВ, 2001. 171 с.
6. Добромислов А.Н. Диагностика повреждений зданий и инженерных сооружений. М.: МГСУ, 2006. 256 с.
7. Kim Y.M., Kim C.M., Hong S.G. Fuzzy based state assessment for reinforced concrete building structures // Engineering Structures. 2006. Vol. 28. Iss. 9. Pp. 1286–1297.
8. Sasmal S., Ramanjaneyulu K. Condition evaluation of existing reinforced concrete bridges using fuzzy based analytic hierarchy approach // Expert Systems with Applications. 2008. Vol. 35. Pp. 1430–1443.
9. Pakdamar F., Guler K. Fuzzy logic approach in the performance evaluation of reinforced concrete structures (flexible performance). [Электронный ресурс]. System requirements: AdobeAcrobatReader. URL: [http://www.iitk.ac.in/nicee/wcee/article/14\\_05-03-0100.PDF](http://www.iitk.ac.in/nicee/wcee/article/14_05-03-0100.PDF) (дата обращения: 11.08.2016).

10. Zain F.M., Islam M.N., Basri I.H. An expert system for mix design of high performance concrete // *Advances in Engineering Software*. 2005. Vol. 36. No. 5. Pp. 325–337.
11. Moodi F. Integration of knowledge management and Information Technology into the repair of concrete structures: an innovative approach // *International Journal of IT in Architecture // Engineering and Construction*. 2004. Vol. 2. Iss. 3. Pp. 173–190.
12. Khader M. Hamdia. Expert System for Structural Evaluation of Reinforced Concrete Buildings in Gaza Strip Using Fuzzy Logic. A Thesis Submitted in Partial Fulfillment of the Requirement for the Degree of Master of Science in Civil Engineering Rehabilitation and Design of Structure. 2010. 92 p.
13. Sobhani J., Ramezaniapour A.A. Service life of the reinforced concrete bridge deck in corrosive environments: A soft computing system // *Applied Soft Computing Journal*. 2011. Vol. 11 (4). Pp. 3333–3346.
14. Balen K. Learning from damage of masonry structures, expert systems can help // *International Seminar on Historical Constructions*. 2001. November. Pp. 15–27.
15. Pankevich O.D., Shtovba S.D. Application of fuzzy models for diagnostics of constructional structure // *Bulletin of the Vinnytsia Polytechnic Institute*. 2011. No. 4. Pp. 32–36.
16. Shtovba S., Rotshtein A., Pankevich O. Fuzzy rule based system for diagnosis of stone construction cracks of buildings // *Advances in Computational intelligence and learning, methods and applications*. Dordrecht: Kluwer Academic Publisher. 2002. Pp. 401–412.
17. Shtovba S.D., Pankevych O.D. Fuzzy technology-based cause detection of structural cracks of stone buildings // *Proceedings of the 14th International Conference on ICT in Education, Research and Industrial Applications. Integration, Harmonization and Knowledge Transfer*. Kyiv, 2018. Vol. I: Main Conference. Pp. 209–218.
18. Соколов В.А. Оценка технического состояния строительных конструкций зданий на основе многоуровневого вероятностного анализа // *Инженерно-строительный журнал*. 2011. № 7(25). С. 45–51. DOI: 10.5862/МСЕ.25.7
19. Соколов В.А. Категории технического состояния строительных конструкций зданий при их диагностике вероятностными методами // *Фундаментальные исследования*. 2014. № 6(6). С. 1159–1164.
20. Soldatenko T.N. Model of identification and prediction of building design defects on the basis of its inspection results // *Magazin of Civil Engineering*. 2011. No. 7. (25). Pp. 52–60.
21. Badiru A., Cheung J. Fuzzy engineering expert systems with neural network applications. John Wiley and Sons. USA. 2002. 289 p.
22. Соколов В.А. Вероятностный анализ технического состояния (ВАТС) строительных конструкций зданий старой городской застройки. Монография. Саарбрюкен, Германия: Издательство LAP LAMBERT. 2013. 152 с.
23. Kkaetzel L.J., Clifton J.R. Expert Knowledge Based Systems for Materials in the Construction Industry. State-of-the-Art Report // *Materials and Structures*. 1995. Vol. 28. Pp. 160–174.
24. Кашеварова Г.Г., Тонков Ю.Л. Интеллектуальные технологии в обследовании строительных конструкций // *Academia. Архитектура и строительство*. 2018. № 1. С. 92–99. DOI: 10.22337/2077-9038-2018-1-92-99
25. Смирнов С.В. Онтологический анализ в системах компьютерного моделирования: дис... д.т.н. Самара, 2002. 348 с.
26. Palagin A.V., Petrenko N.G., Malakhov K.S. Metodika proyektirovaniya ontologii PdO [Methods of designing ontology PdO] // *Companions, systems and systems*. 2011. No. 10. Pp. 5–12.
27. Lu X.; Simmonds H. KBES for evaluating R.C. framed buildings using fuzzy sets // *Automation in Construction*. 1997. Vol. 6. Iss. 2. Pp. 121–137.
28. Pomykalski J.J., Truszkowski W.F., Brown D.E. Expert System. Wiley Encyclopedia for Electrical and Electronics Engineering. February, 1999.
29. Zadeh LA. Fuzzy sets as a basis for a theory of possibility // *Fuzzy Sets and Systems*. 1999. Vol. 100. Pp. 9–34.
30. Тарарушкин Е.В. Применение нечеткой логики для оценки физического износа несущих конструкций зданий // *Вестник БГТУ им. В.Г. Шухова*. 2016. № 10. С. 77–82.
31. Тонков Ю.Л. Выбор эффективного метода построения функций принадлежности для оценки качественных признаков технического состояния строительных конструкций // *Вестник ПНИПУ. Прикладная экология. Урбанистика*. 2016. № 3(23). С. 126–146. DOI: 10.15593/2409;5125/2016.03.09
32. Тонков Ю.Л. Математические модели для идентификации категорий технического состояния строительных конструкций на основе нечеткой логики // *Ж дисс... к.т.н. Пермский национальный исследовательский политехнический университет*. Пермь, 2018. 208 с.
33. Saaty T.L. The Analytic Hierarchy Process. McGraw-Hill, New York. 1980. 287 p.
34. Laarhoven P.J.M., Pedrycz W.A. A fuzzy extension of Saaty's priority theory // *Fuzzy sets and systems*. 1983. Vol. 11. Pp. 229–241.
35. Chang D.Y. Extent analysis and synthetic decision, optimization techniques and applications // *World Scientific*. 1992. Vol. 1. Pp. 352–355.

### **Контактные данные:**

*Галина Геннадьевна Кашеварова, +7(912)884-38-04; эл. почта: ggkash@mail.ru*

*Юрий Леонидович Тонков, +7(902)833-38-55; эл. почта: 95081@mail.ru*

© Кашеварова Г.Г., Тонков Ю.Л., 2020



DOI: 10.18720/MCE.93.3

## Increased plasticity of nano concrete with steel fibers

V.T. Ngo<sup>a</sup>, T.Q.K. Lam<sup>a\*</sup>, T.M.D. Do<sup>a</sup>, T.C. Nguyen<sup>b</sup>

<sup>a</sup> Mien Tay Construction University, Vinh Long city, Vinh Long province, Vietnam

<sup>b</sup> National Research Moscow State Civil Engineering University, Moscow, Russia

\* E-mail: lamthanhquangkhai@gmail.com

**Keywords:** nano concrete, high strength concrete, steel fibers, plasticity of concrete, increased plasticity

**Abstract.** High strength concrete or nano concrete, it is often brittle, so it is necessary to study the solutions to increase the plasticity to obtain the structure to ensure the bearing capacity. The main advantage of steel fibers concrete is that it makes concrete with high flexibility, high tensile and compressive flexural strength, with bending components such as beams, the tensile area makes the concrete easier to form cracks and makes the structure quickly damaged. In this paper used the experimental method in order to determine the mechanical properties of nano concrete such as the tensile bending strength, the splitting tensile strength, for nano concrete samples with steel fibers and without steel fibers. In addition to the study also identified the deformation stress state of the two types of nano concrete and nano concrete with steel fibers. The use of steel fibers in nano concrete in the experiment made nano concrete increase plasticity, increase tensile bending strength, increase the splitting tensile strength and further enhance the advantages of new materials: steel fibers nano concrete materials.

### 1. Introduction

There are many studies on the effects of nanosilica have been conducted in recent years. The results of these studies have brought a lot of efficiency and encouragement to new researches in the future. In studies [1–5] surveyed for many types of particle size and particle distribution to evaluate the influence on the mechanical properties of concrete from the beginning of hydration to the strength formation. Nanosilica in concrete not only activates strongly with hydrate reactions to produce high-quality C-S-H, but they also fill holes with ultra-fine-sized particles to create increased concrete strength and the reduction of harmful factors of concrete such as permeability and corrosion is significantly improved [6–10].

Similarly, Quercia [11] studied the effect of different types of nanosilica (NS) on the properties of high quality concrete. Two types of NS with surface densities of 200 m<sup>2</sup>/g and 380 m<sup>2</sup>/g were used for the study. There are many factors affecting the quality of concrete were also considered such as the ratio of water/adhesives and the ratio of NS used to the amount of cement. The results show the obvious influence of NS surface area on the mechanical properties of concrete. NS samples with double the C-S-H content had a higher hardness than silica fume samples. The addition of nanoparticles from 5 to 70 nm, formed by sol-gel method with superplasticizer in Portland cement mortar, created compressive strength reaching up to 63.9 MPa and 95.9 MPa after aging during 1 and 28 days, respectively. In addition, studies on cracking and heat in concrete have been studied by many authors [12–17].

Beside studies on nano concrete, studies on the use of fibers dispersed in concrete as inorganic fibers, organic fibers and high strength concrete were also a lot of interest and are studied by many different authors [18–20]. When using fibers in concrete has significantly improved the durability and mechanical properties of concrete, such as flexural strength, impact strength and resistance to fatigue. With these special features, concrete using dispersed fibers has brought many successes in researches as well as in real buildings.

In particular, when adding fibers to concrete has improved the ductility of concrete, the above issue has not been much research mentioned. Plasticity is a very important property of concrete, which represents the strength of concrete structures under the complex effects of load. When the concrete has low plasticity often leads to structures with very high brittle failure, especially for dynamic or fatigue the load. So, parameters can be used to assess the plasticity of concrete such as tensile strength, tensile strength when bending,

Ngo, V.T., Lam, T.Q.K., Do, T.M.D., Nguyen, T.C. Increased plasticity of nano concrete with steel fibers. Magazine of Civil Engineering. 2020. 93(1). Pp. 27–34. DOI: 10.18720/MCE.93.3

Нго В.Т., Лам Т.К.К., До Т.М.Д., Нгуен Ч.Ч. Повышенная пластичности нанобетона со стальными волокнами // Инженерно-строительный журнал. 2020. № 1(93). С. 27–34. DOI: 10.18720/MCE.93.3



the stress-deformation relationship or destructive strength. In particular, steel fibers used in concrete or steel fibers nano concrete were used quite effectively [21–27].

In order to determine the deformation stress state of nano concrete and its destructive properties, it is necessary to study mechanical properties such as compressive strength, tensile strength, separation strength, and elastic modulus. This study focuses on two main issues. The first is the influence of SiO<sub>2</sub> nanoparticles on the mechanical properties concrete. The second is the influence of the dispersed steel fibers on the plasticity of high-strength concrete. To solve the two main problems mentioned above, the paper presented experiments with 36 cylinder samples of 10×20 cm size for compressive strength testing were cast, 3 samples of beams of 10×10×40 cm to determine the tensile bending strength, 3 cylinders of 15×30 cm to determine the elastic modulus and the splitting tensile strength, and 3 cylinders of 15×30 cm size to determine the stress and strain curve diagrams on compression.

## 2. Materials and methods

### 2.1. Materials

Based on the research objectives, the selected mix will continue to be used in subsequent experiments of the study and are given in Table 1.

**Table 1. High strength concrete mixtures.**

Mixtures	Nanosilica, %	Silica, %	Symbol
Mixture 1	0	5	HPC
Mixture 2	0.5	5	HPCN0.5
Mixture 3	1.5	5	HPCN1.5
Mixture 4	3	5	HPCN3.0

So, the aggregates are calculated based on the design of high strength concrete components according to ACI 211, 4R-08. The aggregates are synthesized as a basis for calculating batches to conduct casting samples and presented in Table 2. The number and size of samples for experiment concrete with steel fibers and presented in Table 3.

**Table 2. Aggregate concrete design with compressive strength of 80MPa.**

Ingredient	HPC	HPCN0.5	HPCN1.5	HPCN3.0
Cement, kg	594	594	594	594
Stone, kg	1098	1098	1098	1098
Sand, kg	548	604	592	574
Water, kg	151.8	144.7	146.1	148.5
PG viscocrete, liters	6.53	6.53	6.53	6.53
Nano silic, kg	0	3.15	9.53	19.37
Silica, kg	29.7	29.7	29.7	29.7

The steel fibers content were used in studies varies from 0 to 1.5 % by volume. Recent studies show that, steel fiber to be added in the concrete mix is 1 % by volume was directed to be the optimal result in many of those studies. Based on that basis, the study selected 1 % of steel fibers to add to concrete and serve for experiments of steel fibers nano concrete [21–25]

**Table 3. Number and size of samples used for testing with steel fibers.**

Experimental content	Mixture	Number of samples	Sample shapes	Size, cm
Tensile strength when bending	HPCN1.5 + 1 % steel fibers (78.5 kg/m <sup>3</sup> )	3	Beam samlpe	10×10×40

By some normal steel fibers with flat, a round section. The research has used Dramix steel fibers with round section, technical specifications for steel fibers are given in Figure 1 and Table 4.



**Figure 1. Dramix steel fibers used in research.**

**Table 4. Technical specifications of steel fibers (Dramix).**

No	Technical parameters of steel fibers	Steel fiber type			
		Long, flat 38 mm	Long, flat 52 mm	Round SF-35/0.7 mm	Round SF-35/0.55 mm
1	Shape and cross section of steel fibers	Flat steel fiber section with arc shape		Round steel fiber SF round section	
2	Long, mm	38.00	52.00	35.00	35.00
3	Diameter, mm	1.31	1.31	0.70	0.55
4	Fiber direction rate	29.00	39.70	50.00	65.00
5	Total surface area, cm <sup>2</sup> /kg	5.340	5.340	6.616	8.978
6	Number of fibers, fiber/kg	2.280	1.840	8.600	19.040
7	Tensile strength, daN/cm <sup>2</sup>	10.000			

## 2.2. Experimental plan

After identifying nano concrete mixes with aggregates, it was named HPC, HPCN0.5, HPCN1.5, HPCN3.0 with number and size of samples are given in Table 5.

**Table 5. Sample number and size.**

Content of the experiment	Mixture	Number of samples	Shape	Size, cm
Compressive strength 1day, 7days, 28days	HPC	36	Cylindrical	10x20
	HPCN0.5			
	HPCN1.5			
	HPCN3.0			
The tensile bending strength	Optimized	3	Beam	10x10x40
The elastic modulus and the splitting tensile strength	Optimized	3	Cylindrical	15x30
The stress and strain curve diagrams on compression	Optimized	3	Cylindrical	15x30

## 2.3. Preparation and testing methods

The samples are cast for testing, such as in Tables 3 and 5.

- Cylindrical with 10x20cm and 15x30cm section;
- Beam with 10x10x40cm section;

– Molding process: When the mixture has a hardness of more than 20 seconds or a drop below 4cm, pour the mixture into the mold into two layers. After finishing the first layer, the vibrating table at the frequency of 2800–3000 revolutions/minute, the amplitude of 0.35–0.5 mm then vibrate until all the air bubbles are removed and the cement pool floats evenly. Then poured and swamped like that for the 2nd class.

## 2.4. Moistened samples

Samples are moistened at room temperature until the mold is removed, kept moist in a standard room with a temperature of  $23 \pm 2$  °C, 95–100 % humidity until the day, is shown in Figure 2.

**Figure 2. Moistened the sample after casting.**

## 3. Results and Discussion

### 3.1. Experiment to determine compressive strength (ASTM C39-01).

After preparation of the sample surface, carry out the experiment to determine the compressive strength of the sample. The machine used to test the compressive strength of concrete samples is the TTM2000 electronic compressor with a maximum load of 2000kN, compressing the sample with an increase of 0.3MPa/s as shown in Figure 3.



**Figure 3. The sample is destroyed during the compression.**

The compressive strength of the test samples obtained at the age of 24 hours (1 day), 7 days, 28 days is presented in Tables 6–8.

**Table 6. Experimental results of compressive strength, 24 hours (1 day).**

Experimental results of compressive strength, 24 hours (1 day).							
Type	Sample M1		Sample M2		Sample M3		Medium intensity, MPa
	Force, kN	Intensity, MPa	Force, kN	Intensity, MPa	Force, kN	Intensity, MPa	
HPC	133.9	17.06	138.0	17.58	151.2	19.26	17.97
HPCN0.5	155.8	19.84	152.6	19.44	174.2	22.20	20.49
HPCN1.5	216.2	27.55	206.0	26.25	198.0	25.22	26.34
HPCN3.0	118.6	15.11	103.4	13.17	106.9	13.62	13.97

**Table 7. Experimental results of compressive strength at 7 days.**

Experimental results of compressive strength, 7 days							
Type	Sample M1		Sample M2		Sample M3		Medium intensity, MPa
	Force, kN	Intensity, MPa	Force, kN	Intensity, MPa	Force, kN	Intensity, MPa	
HPC	570.9	72.73	562.8	71.69	547.2	69.71	71.38
HPCN0.5	584.2	74.42	564.1	71.86	590.2	75.18	73.82
HPCN1.5	613.3	78.13	634.9	80.88	619.8	78.96	79.32
HPCN3.0	528.2	67.29	507.5	64.65	545.9	69.54	67.16

**Table 8. Experimental results of compressive strength at 28 days.**

Experimental results of compressive strength at 28 days.							
Type	Sample M1		Sample M2		Sample M3		Medium intensity, MPa
	Force, kN	Intensity, MPa	Force, kN	Intensity, MPa	Force, kN	Intensity, MPa	
HPC	748.3	95.33	718.3	91.50	722.0	91.97	92.93
HPCN0.5	714.2	90.98	711.6	90.65	702.3	89.46	90.36
HPCN1.5	729.5	92.93	714.3	91.00	755.7	96.27	93.40
HPCN3.0	642.6	81.86	618.2	78.75	648.2	82.58	81.06

Figure 4 shows that the highest compressive strength of HPCN1.5 concrete samples at 24 hours, 7 days, 28 days with the highest results. If compared with concrete using only siliceous soot (HPC), the compressive strength of HPCN1.5 grows faster in 24 hours and 7 days with the results increasing respectively 46.58 % and 11.12 %.

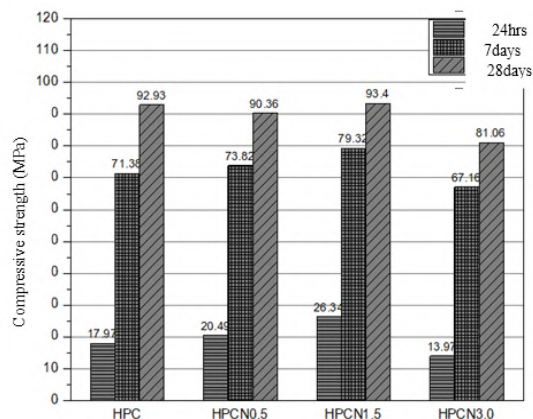


**Figure 4. Compressive strength of nano concrete.**

With the results of the compressive strength test of HPCN1.5 aggregate, the authors decided to use this aggregate to conduct experiments to determine some other mechanical properties of nano concrete.

The use of nano concrete with steel fibers has increased the compressive strength of nano concrete, especially in the early age (7 hrs – 24 days).

The effect of nano SiO<sub>2</sub> on the strength of high-strength concrete was investigated through different ratio of using NS. As the results shown, with the ratio of 1.5 % nano SiO<sub>2</sub> created concrete samples with the most optimal strength in experiments. When nano SiO<sub>2</sub> was added to the concrete mixture, the compressive strength at 28 days was not significantly different among the ratios. However, the strength of the samples at the early age (24h and 7 days) is very different due to the activation effect of the rate of SiO<sub>2</sub> nanoparticles. Increasing the ratio of SiO<sub>2</sub> nano to 3 % gives the concrete sample a reduction in strength compared to the rate of 1.5 %, the reason is that the dispersion of SiO<sub>2</sub> nano ultrafine particles is uneven in the mixture and forms local weakness areas.

### 3.2. The experiment determines the tensile bending strength (ASTM C78-02).

Tensile strength is determined on 10×10×40cm size samples. The test is carried out according to ASTM C78-02 with 4-point bending method is displayed in Figure 5. Table 9 presents the results of experimental results of tensile strength when bending at 28 days.

**Table 9. Experimental results of the tensile bending strength at 28 days.**

Sign	Force, kN	Tensile strength when bending, MPa	Medium, MPa
M1	26.9	8.07	
M2	25.1	7.53	7.99
M3	27.9	8.37	

### 3.3. Elastic modulus (ASTM C469-02)

Elastic modulus of nano concrete is tested according to ASTM C469-02. Sample with diameter of 150mm, height of 300 mm is shown in Figure 6.



**Figure 5. Tensile strength test when bending.**



**Figure 6. Elastic modulus of nano concrete.**

**Table 10. Experimental results of elastic modulus (HPCN1.5).**

Sign	Deformation 1	Deformation 1	Stress 1	Stress 2	Elastic modul	Elastic modul medium
	$\varepsilon_1$	$\varepsilon_2$	$\sigma_1$ , MPa	$\sigma_2$ , MPa	$E$ , MPa	$E_{tb}$ , MPa
M1	0.00005	0.00075	1.6	36.8	50286	
M2	0.00005	0.00079	1.9	38.2	49054	50036
M3	0.00005	0.0007	2.9	35.9	50769	

### 3.4. The experiment determines the tensile strength when splitting (ASTM C496-04).

The strength of splitting of nano concrete is tested according to ASTM C496-04. The cylinder is 150 mm in diameter and 300 mm in height. The experiment was carried out on 3 samples after performing experiments to determine the elastic modulus. Loading speed is 1MPa/s.



**Figure 7. Test strength of splitting.**

**Table 11. Experimental results of splitting.**

Sign	Force, kN	Tensile strength when bending, MPa	Medium, MPa
M1	343.1	4.86	
M2	350.8	4.97	4.97
M3	360.5	5.10	

**3.5. Experiment to determine the stress and strain diagram.**

Determining the stress deformation relationship of nano concrete is carried out to compress the center directly on cylindrical sample size 150x300 mm.

On each specimen tested and two resistors of 60 mm length are pasted along both sides of the cylinder to measure the deformation of the sample. The compression force is measured by Loadcell type 2000KN placed under the test sample is shown in Figure 8.

Figure 9 shows the relationship between stress and strain for 3 test samples M1, M2 and M3.



**Figure 8. Experiment to determine stress – deformation.**

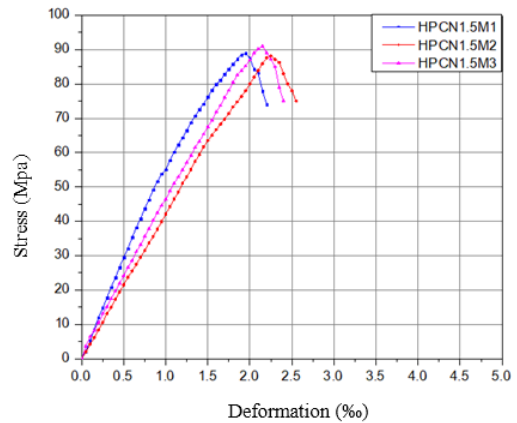


**Figure 9. The diagram of stress-strain for HPCN1.5 nano concrete.**

When the stress reaches the maximum, the material is damaged, the stress value decreases rapidly compared to the deformation of the material. Based on the graph of Figure 9, the slope of the stress strain line after the top is large, the concrete is suddenly destroyed when the deformation is still very small. From the results in Figure 9 show that the concrete in the study is very brittle.

**Nano concrete experiments added steel fibers.** The steps of mixing the mixture, casting the nano concrete and Dramix fibers are carried out similarly to the nano concrete without the fibers, Dramix fibers will be added to the mixture at the end-stage is shown in Figure 10. And Figure 11 shows the tensile strength test when bending of nano fiber concrete with steel fibers.



**Figure 10. Mixing nano-concrete mixture with steel fibers.**



**Figure 11. 4-point bending test and sample after destructive.**

Tables 12–13 are presented results of the tensile bending strength and tensile strength test when splitting.

**Table 12. Experimental results of the tensile bending strength.**

Sample	Force, kN	Tensile strength when bending, MPa	Medium, MPa
M1	55.2	16.56	16.93
M2	58.9	17.67	
M3	55.2	16.56	

**Table 13. Results of tensile strength test when splitting.**

Sign	Force, kN	Tensile strength test when splitting, MPa	Medium, MPa
M1	466.9	6.61	6.43
M2	453.4	6.42	
M3	441.5	6.25	

The relationship between stress and deformation of concrete samples with steel fibers is shown in Figure 12.

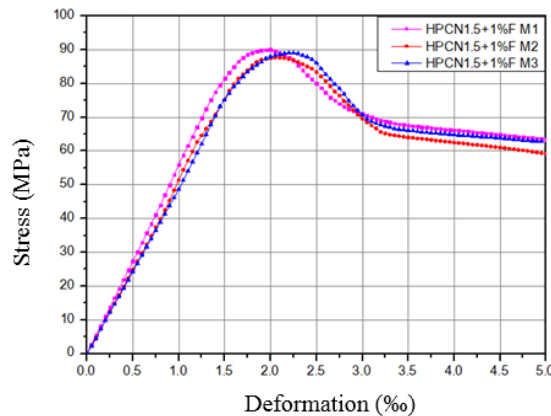


**Figure 12. Stress – deformation when compressing of nano concrete with steel fibers.**

Based on the test results of the tensile bending strength and tensile strength when splitting (Tables 12, 13) of nano-fiber concrete, the difference can be quite large. When adding steel fibers to the concrete mixture, the tensile bending strength and the splitting tensile strength increased compared to when the concrete without steel fibers was 111.8 % and 29.3 %, respectively.

From Figure 12, the stress-strain curve shows that when the deformation reaches a maximum value, the stress decreases slowly, the area under the curve (destruction energy) increases. It can be seen that the peak load of steel fibers concrete is approximately the same as that of non-steel fibers. However, there is a difference, nano-fiber concrete after cracking appears, stress drops suddenly, but then stabilizes and slows down.

The mechanical properties change, such as the tensile bending strength, the splitting tensile strength and stress deformation relations show that the steel fibers nano concrete are more flexible. The amount of fibers added to a concrete mix has limited the appearance of cracks and after the cracks were stabilized. The steel fibers that link cracks like a thread stitching the surface of cracks, this phenomenon is exacerbated when the base material (concrete) has high strength, can create great adhesion to steel fibers.

## 4. Conclusions

Based on the results of the study lead to the following conclusions:

1. The effect of nano SiO<sub>2</sub> on the strength of high-strength concrete was investigated through the different ratios of using NS. The results shown with the ratio of 1.5 % nano SiO<sub>2</sub> created concrete samples with the optimal strength in the components in experiments. When nano SiO<sub>2</sub> was added to the concrete, the compressive strength of the sample at 28 days was not significantly different between the ratios. However, the strength of the samples at an early age (24h and 7 days) is very different due to the activation effect of the rate of SiO<sub>2</sub> nanoparticles. Increasing the ratio of SiO<sub>2</sub> nano to 3 % gives the concrete sample a reduction in strength compared to the rate of 1.5 %, the reason is that the dispersion of SiO<sub>2</sub> nano ultrafine particles is uneven in the mixture and forms local weakness areas.

2. Study of the stress-strain state for nano concrete without steel fibers, when the stress reaches the maximum, the material is damaged, the stress value decreases rapidly compared to the deformation of the material. The slope of the stress-strain curve at the post-peak stage is large, the concrete is suddenly destroyed when the deformation is still very small.

3. When adding steel fibers Dramix with a ratio of 1 % to enhance plasticity, bending strength of nano concrete using steel fibers increased by more than 110 % compared to nano concrete don't use steel fibers. Stress-strain relationship curve varies significantly compared to the type without steel fibers. The stress after the peak decreases slowly, the curve becomes less slope, the area under the curve is also much larger. The above results have confirmed the improvement of mechanical properties, especially the flexibility of nano concrete when adding steel fibers.

## References

1. Khaloo, A., Mobini, M.H., Hosseini, P. Influence of different types of nano-SiO<sub>2</sub> particles on properties of high-performance concrete. *Construction and Building Materials*. 2016. 113. Pp. 188–201
2. Bagheri, A., Parhizkar, T., Madani, H., Raisghasemi, A. The influence of pyrogenic nanosilicas with different surface areas and aggregation states on cement hydration. *Asian J. Civ. Eng.* 2013. 14. Pp. 783–796.
3. Berra, M., Carassiti, F., Mangialardi, T., Paolini, A.E., Sebastiani, M. Effects of nanosilica addition on workability and compressive strength of Portland cement pastes. *Constr. Build. Mater.* 2012. 35. Pp. 666–675.
4. Land, G., Stephan, D. The influence of nano-silica on the hydration of ordinary Portland cement. *J. Mater. Sci.* 2012. 47. Pp. 1011–1017.
5. Hosseini, P., Booshehrian, A., Farshchi, S. Influence of nano-SiO<sub>2</sub> addition on microstructure and mechanical properties of cement mortars for ferrocement. *J. Trans. Res. Rec.* 2010. 2141. Pp. 15–20.
6. Bahadori, H., Hosseini, P. Reduction of cement consumption by the aid of silica nano-particles (investigation on concrete properties). *J. Civ. Eng. Manage.* 2012. 18(3). Pp. 416–425
7. Baomin, W., Lijiu, W., Lai, F.C. Freezing resistance of HPC with nano-SiO<sub>2</sub>. *J. Wuhan Univ. Technol. Mater. Sci. Ed.* 2008. 23. Pp. 85–88
8. Sobolev, K., Flores, I., Torres-Martinez, L.M., Valdez, P.L., Zarazua, E., Cuellar, E.L. Engineering of SiO<sub>2</sub> Nanoparticles for Optimal Performance in Nano Cement-Based Materials. *Nanotechnology in Construction*. 2009. Vol. 3. Pp. 139–148.
9. Senff, L., Hotza, D., Repette, W.L., Ferreira, V.M., Labrincha, J.A. Mortars with nano-SiO<sub>2</sub> and micro-SiO<sub>2</sub> investigated by experimental design. *Constr. Build. Mater.* 2010. 24. Pp. 1432–1437
10. Min-Hong, Zhang, Jahidul, Islam. Use of nano-silica to reduce setting time and increase early strength of concretes with high volumes of fly ash or slag. *Construction and Building Materials*. 2012.
11. Quercia Bianchi, G. Application of nano-silica in concrete. Eindhoven: Technische Universiteit Eindhoven, 2014.
12. Van Lam, T., Nguyen, C.C., Bulgakov, B.I., Anh, P.N. Composition calculation and cracking estimation of concrete at early ages. *Magazine of Civil Engineering*. 2018. 82(6). Pp. 136–148. doi: 10.18720/MCE.82.13
13. Do, T.M.D., Lam, T.Q.K. Solutions to improve the quality of mass concrete construction in climate conditions of Southern Vietnam. *International Journal of Innovative Technology and Exploring Engineering*. 2019. Vol. 8. No. 6C2. Pp. 188–192.
14. Do, T.M.D., Lam, T.Q.K. Analysis of Risk Problems in Construction by R software. *International Journal of Engineering and Advanced Technology*. 2019. Vol. 8. No. 5. Pp. 1872–1875.
15. Chuc, N.T., Bach L.X. Reducing temperature difference in mass concrete by surface insulation. *Magazine of Civil Engineering*. 88(4). 2019. Pp. 70–79. DOI: 10.18720/MCE.88.7
16. Aniskin, N., Nguyen T.-C. Influence factors on the temperature field in a mass concrete. *E3S Web of Conferences*. 2019. 97. DOI: 10.1051/e3sconf/20199705021
17. Chuc, N.T., Thuan, P.V., Kiet, B.A. The effects of insulation thickness on temperature field and evaluating cracking in the mass concrete. *Electronic Journal of Structural Engineering*. 2018. 18(2)
18. Klyuev, S.V., Klyuev, A.V., Vatin, N.I. Fiber concrete for the construction industry. *Magazine of Civil Engineering*. 2018. 84(8). Pp. 41–47. doi: 10.18720/MCE.84.4
19. Kiyanev, A.V. Concrete with recycled polyethylene terephthalate fiber. *Magazine of Civil Engineering*. 2018. 84(8). Pp. 109–118.
20. Li, C.Y., Chou, T.W. Modeling of damage sensing in fiber composites using carbon nano-tube networks. *Nanotechnology in Construction*. 2008. Vol. 68. Pp. 3373–3379.
21. Lam, T.Q.K. Research the stress-deformation of double-layer reinforced concrete shell by experiment. *Vietnam Journal of Construction*. 2018. Vol. 3. Pp. 58–61.
22. Lam, T.Q.K., Do, T.M.D. Effect of each shell thickness on deformation stress and the ability for causing the cracks in the multilayer doubly curved shell roof. *International Journal of Innovative Technology and Exploring Engineering*. 2019. 8(6C2). Pp. 215–220.
23. Lam, T.Q.K., Do, T.M.D. Stress-strain in multi-layer reinforced concrete doubly curved shell roof. *International Journal of Innovative Technology and Exploring Engineering*. 2019. 8(4S2). Pp. 419–424.
24. Nguyen Ngoc Long. Study the selection and design of steel fiber concrete components suitable for the use of bridge structures in Vietnam. Ministry-level scientific research topic. 2005.
25. Lam, T.Q.K., Do, T.M.D. Sliding between layers in 2-layer reinforced concrete beams and shell. *International Journal of Engineering and Advanced Technology*. 2019. Vol. 8. No. 5. Pp. 1867–1871.
26. Ngo, V.T., Lam, T.Q.K., Do, T.M.D., Nguyen, T.C. Nano concrete aggregation with steel fibers: A problem to enhance the tensile strength of concrete. *E3S Web of Conf.* 2019. 135. DOI: 10.1051/e3sconf/201913503001
27. Tran, H.Q., Lam, T.Q.K., Do, T.M.D. Model of prefabricated concrete frame in the condition of southern Vietnam. *E3S Web of Conf.* 2019. 135. DOI: 10.1051/e3sconf/201913503043

## Contacts:

*Van Thuc Ngo, +84939423461; nvthuc34@gmail.com*

*Thanh Quang Khai Lam, +84909563055; lamthanhquangkhai@gmail.com*

*Thi My Dung Do, +84982191146; dothimydung1983@gmail.com*

*Trong Chuc Nguyen, +7(966)3319199; ntchuc.mta198@gmail.com*

© Ngo, V.T., Lam, T.Q.K., Do, T.M.D., Nguyen, T.C., 2020



DOI: 10.18720/MCE.93.4

## Long span bridges buffeting response to wind turbulence

R.N. Guzeev<sup>a</sup>, A. Domaingo<sup>b</sup>

<sup>a</sup> St. Petersburg State University of Architecture and Civil Engineering, St. Petersburg, Russia

<sup>b</sup> ALLPLAN Infrastructure GmbH, Graz, Austria

\* E-mail: [guzeev.roman@gmail.com](mailto:guzeev.roman@gmail.com)

**Keywords:** cable stayed and suspension bridges, buffeting response, turbulence model, bridge deck, structural design, coherence, random vibration, numerical models.

**Abstract.** The buffeting response of the cable-supported bridges is studied. Several wind turbulence models are summarized and wind field models for practical application in bridge and structural engineering is proposed. The wind turbulence model comprises the mean wind and turbulence intensity profile, power spectral density and coherence functions. The dynamic response of the structure is governed by random vibration theory of stationary random process. The simplified method of analysis using the mode decomposition method is proposed where the only main modes are considered and the aerodynamic damping is introduced by means of flutter derivatives. The method of cable system coherence analysis is presented. The calculation procedure of generalized power spectral densities of wind turbulence load for different structural component is proposed. This procedure takes into account the effects of all three orthogonal components of wind turbulence. The contribution of the wind velocity components into total dynamic response and their correlation for different structural elements is studied.

### 1. Introduction

Slender cable-stayed structures, especially bridges are vulnerable to wind action and prone to significant dynamic response to natural wind turbulence. Wind turbulence near the ground is produced by the boundary layer of wind flow at the height 300-400 m [1, 2]. This is a layer where the structure has to be built.

The cable-stayed or suspension bridge has three main structural components such as the bridge deck girder, pylons and cables. All of them have different interaction with the wind flow. At every structural element six component forces are acting which consist of three steady state forces and three moments.

The bridge deck can be considered as a prismatic 2D body with specific cross-section. For example, the cross-section can be a monobox girder (Golden Horn Bay Bridge, Russky Island Bridge, Russia) or a double deck girder (Stonecutters Bridge, China and bridge over Peter The Grate Channel, Russia). Steady state aerodynamic forces can be reduced to drag  $D$  and lift  $L$  forces and torsion (pitch) moment  $M$  (Figure 1). Torsional and vertical frequency of the cable-stayed bridge deck are well separated. Usually torsional frequency is 1.5–3.0 times higher than vertical one.

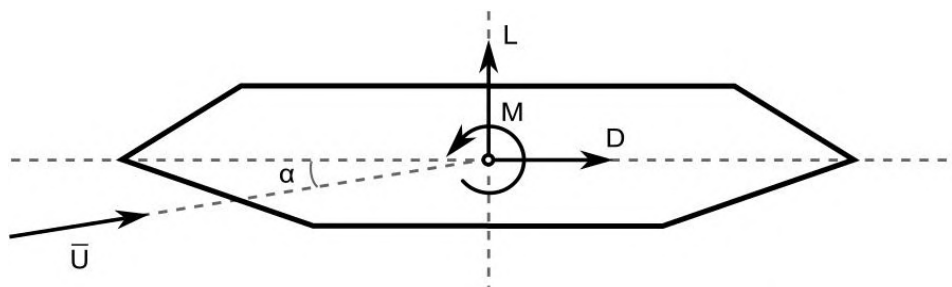


Figure 1. Aerodynamic forces.

Guzeev, R.N., Domaingo, A. Long span bridges buffeting response to wind turbulence. Magazine of Civil Engineering. 2020. 93(1). Pp. 35–49. DOI: 10.18720/MCE.93.4

Гузев Р.Н., Доминго А. Реакция большепролетных мостов на турбулентный ветровой поток // Инженерно-строительный журнал. 2020. № 1(93). С. 35–49. DOI: 10.18720/MCE.93.4



This work is licensed under a CC BY-NC 4.0

Aerodynamic forces acting on the pylon can be described by only drag and lift forces. The torsional moment can be neglected due to the relatively high torsional stiffness. For symmetric cross sections, the lift forces do not produce significant effect on wind response. For non-symmetrical cross-sections, the lift force must be considered as well as the drag force. Besides, first derivatives of aerodynamic coefficients by the angle of incidence significantly influence the static and dynamic stability of the structure, e.g. torsional divergence and across wind galloping, respectively [3].

In order to linearize the problem fluctuation components are considered as small values and only linear terms remain in the expression for wind pressure, effective angle of incidence and wind load coefficients expansion. In the most general case, also the relative velocity due to the moving structure must be considered. In the present study the effect of moving structure is considered only in terms of aerodynamic damping and evaluated by the means of the flutter derivatives.

The conventional approach to the turbulence wind action such as that in chimneys, truss towers, masts and simple buildings considers only along wind component of the wind fluctuation velocity [4, 5]. Turbulence action on cable-stayed bridges requires consideration of all three components. The vertical component for the bridge deck and the transversal component for pylons produce changes in the mean wind angle of incidence. This subsequently causes dynamic response because the aerodynamic coefficients, particularly lift coefficient, strongly depend on the angle of incidence [6, 7].

For cables with circular symmetrical cross-section it is enough to take into account only the drag force.

Steady-state forces can be described by the means of steady-state aerodynamic coefficients which can be obtained through wind tunnel tests or CFD analysis [6, 7]. The most reliable aerodynamic properties are given by wind tunnel cross section tests at the fine scale. CFD analysis also gives good results but requires highly professional approach and adjustment of the wind flow model to the specific purpose.

Wind velocity comprises the mean wind velocity vector and three orthogonal fluctuation components.

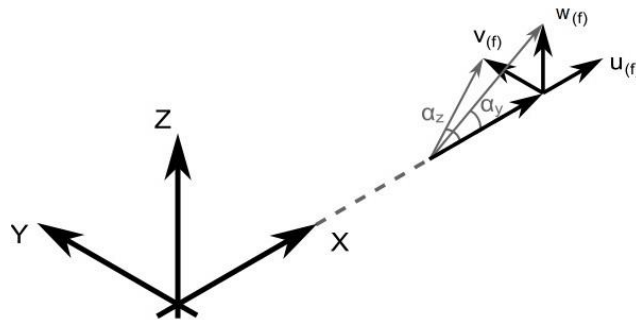


**Figure 2. Orthogonal fluctuation components of wind flow.**

Pylons with two or more legs with transversal wind direction produce a shadow effect for the downwind leg. Reduction in the wind force for the downwind leg can be taken into account by introducing the shadow coefficient. The value of such coefficient as estimated by CFD analyses and wind tunnel tests for common pylon structures with A-shaped pylons is about 0.6–0.7.

The wind turbulence fluctuation velocity is considered to be a stationary ergodic random process. The full model of the wind field sufficient to calculate the structural response should include the mean wind velocity profile, turbulence intensity profile, power spectral density and root coherence function. This metrological data should be derived through long-term monitoring in several points on site [8, 9] or numerical modeling [10]. However, it is acceptable to use generalized models such as [1, 2, 4, 5].

The buffeting analysis basics for line-like slender structures was established by Davenport 1960's [11]. The proposed method is employed idea that variance of response can be represented by background and resonance response. The authors [12] modified Davenport's method and took into account only the deck of the bridge and coherence along the bridge axis for cable stayed bridge with main span 400 m where effect of cables is moderate. The cable-stayed bridges buffeting response taking into account heave, pitch and torsional modes was studied in [7]. The buffeting response of the extremely long Stonecutters cable-stayed bridge is studied in [13, 14], taking into account the deck aerodynamic properties and coherence along the bridge.

Experimental and analytical studies of buffeting response and wind field at bridge sites are given in [8, 9, 15–17]. The authors [5, 18] and national codes [1, 2, 4] proposed different approach for analytical description of wind turbulent flow.

For the extremely long cable-stayed bridges, the cables assume a significant amount of the wind load because the cables system for such bridges form a sort of 3D "sails" and spatial coherence shall be analyzed. The wind load affect both the pylons and the deck. Consideration all components of wind turbulence is crucial for long span cable-stayed bridges buffeting analysis.

This paper is devoted to comprehensive study of buffeting response for long span cable-stayed bridges and comprises turbulence model for practical application, analytical description of aerodynamic interaction between wind flow and structural elements, consideration of three components of wind turbulence and spatial coherence for cable system, deck and pylons.

This paper is dedicated to the analysis of dynamic response to the wind natural turbulence. Other aeroelastic phenomena is out of scope. The flutter critical wind velocity for the bridge structure must be much higher than the design wind velocity. In contrary, vortex shedding lock-in vibration usually occurs for the relatively low wind velocity where the effect of wind turbulence could be neglected. The negative aerodynamic damping is not allowed for the bridge structures within design wind speed. Thus, galloping and other aerodynamic instability caused by negative damping is not considered in the article.

## 2. Methods

### 2.1. Wind turbulence model

The mean wind profile is described by logarithmic or power law. Both profiles depend on the type of the surrounding terrain. The logarithmic law uses the parameter of terrain roughness. The power law takes into account the terrain effect by introducing different exponents. We can obtain the mean wind velocity by multiplying the wind profile coefficient by the base wind velocity at the height of 10 m. The base wind velocity is available, for example, in [5, 18] or using local measurement.

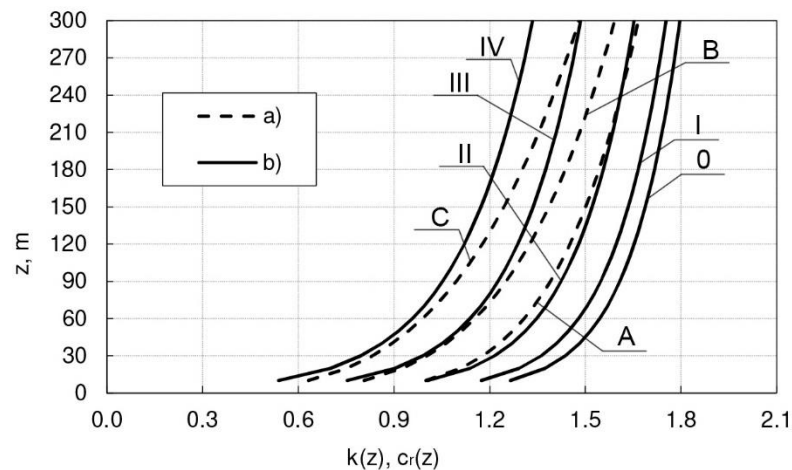


**Figure 3. Mean wind velocity coefficient profile:**  
**a) the power law for terrain A, B, C [8]; b) the logarithmic law for terrain 0-IV [6].**

To be on the safe side, the logarithmic law is more preferable for structures located on the regular terrain covered with vegetation and buildings. Meanwhile, for the open terrain both profiles are very close (Figure 2). This kind of terrain such as rivers, lakes and sea shore correspond to the typical location of a bridge site. However, for bridges in the city surrounded by buildings or high hills the local terrain must be considered [15–17]. Therefore, the logarithmic expression for the mean velocity profile is employed in the present study.

$$c_r = k_r \ln(z / z_0), \quad (1)$$

where  $z$  is elevation above ground or water surface;

$z_0$  is the roughness length;

$k_r$  is the terrain factor.

The values for  $z_0$  and  $k_r$  refer to [6].

The most important parameter of wind turbulence is the normalized non-dimension power spectral density of wind fluctuation velocity. The European standard on wind action uses the Kaimal spectrum of along wind component [6]. The American standard slightly modifies the Kaimal spectrum. This spectrum has limitation of application with height 200 m. Russian, Chinese and Canadian codes use the Davenport spectrum for this component [5]. The Davenport spectrum has significant disadvantages because it does not depend on the height and turbulence length scale is constant. However, applying the Davenport spectrum is much easier for dynamic structural analysis. In this case, for simple structures with the simple mode shape, calculation can be made by hand. The Karman spectrum is also widely used in structural analysis and national wind engineering standards. The Australian and Japanese documents have adopted the Karman spectrum. The Karman spectrum with modification in high frequency range is given in Engineering Science Data Unit (ESDU) [1, 2]. Besides, the new

Karman spectra are given there for the full range of frequencies. However, for cable-stayed structures with relatively low natural frequencies the Karman spectrum Equation (2) can be used.

$$\frac{fS_{uu}(f)}{\sigma_u^2} = \frac{4n_u}{(1+70.8n_u^2)^{5/6}}, \quad (2)$$

where  $S_{uu}(f)$  is the PSD function of along wind component;

$\sigma_u$  is the standard deviation of along wind component;

$f$  is the frequency in Hz;

$n_u$  is the non-dimensional frequency.

The non-dimensional form of spectral density requires non-dimensional frequency normalized by the wind velocity and integral turbulence length scale  $n_u = fL_u / \bar{U}(z)$ . The integral turbulence length scale represents the average size of turbulence eddies.

The sophisticated expression for the modified and Karman spectra and the turbulence length scale is given in [1, 2].

For practical application the power Counihan turbulence length scale can be employed [19].

$$L_u = 300(z/300)^{0.46+0.074\ln(z_0)}. \quad (3)$$

The Davenport spectrum for along wind component uses the constant integral length scale and it is equal to 1200 m.

From many field measurements [20], the turbulence length scale for along wind component corresponds to the length scale for vertical and transversal components in the following ratio:

$$L_v \approx L_u / 3; \quad L_w \approx L_u / 9. \quad (4)$$

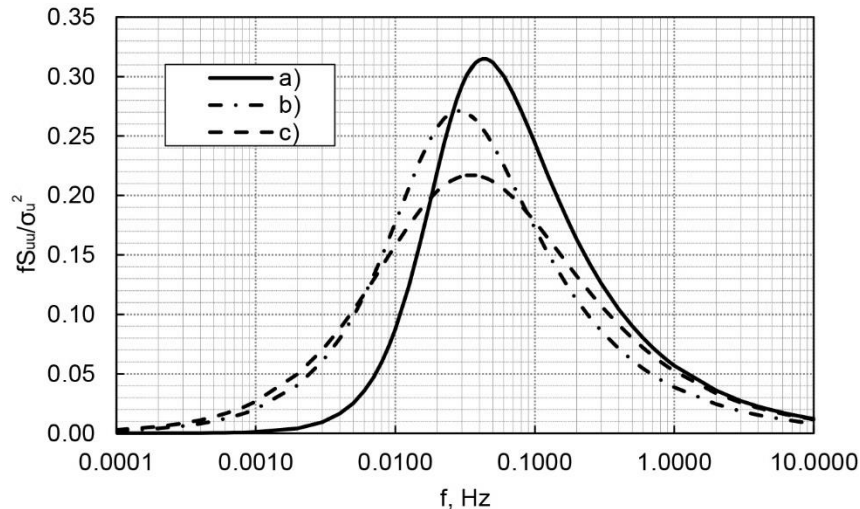


**Figure 4. Normalized PSD spectrum of longitudinal component:**  
a) the Davenport spectra, b) the Karman spectra, c) the Kaimal spectrum.

The vertical and transversal components as it was mentioned above, are important as well as the along wind component. For these components there exists the various representation of the spectrum. For practical application the Karman spectra [1] give a good approximation in the absence of field measurements and monitoring.

$$\frac{fS_{ii}(f)}{\sigma_i^2} = \frac{4n_i(1+755.2n_i^2)}{(1+283.2n_i^2)^{11/6}}, \quad (5)$$

where  $I = v, w$  is the notation of the turbulence components direction;

$S_{ii}(f)$  is the PSD function for vertical and transversal components;

$n_i$  is the non-dimensional frequency.

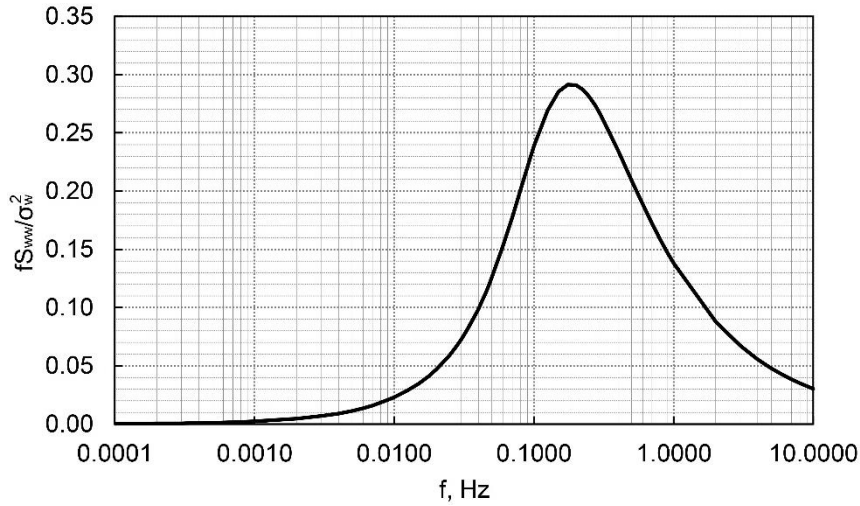


**Figure 5. Normalized PSD spectrum of vertical component.**

We have to complete the description of wind velocity component power spectral densities with the cross spectra of along wind and vertical components and the vertical and transversal component. Actually, this component has complex value. For simplified analysis, the cross spectra can be neglected in the assumption of the statistically independent along wind and vertical component as well as the transversal component but this assumption seems to be incorrect because the structure is located in the anisotropic turbulence boundary layer. The imaginary part can be neglected because it contributes nothing to the maximal structural response. Because of the turbulence eddies moving pattern, the real part of the cross spectrum has to be negative. In this study we employ the following expression for the cross spectrum [12].

$$\frac{fS_{uv}(f)}{u_*^2} = -\frac{14fz/\bar{U}(z)}{(1+9.6fz/\bar{U}(z))^{2.4}} \tag{6}$$

The standard deviation of wind fluctuation velocity is described by the turbulence intensity profile. Turbulence intensity is the ratio of the standard deviation to the mean wind velocity. Sophisticated expressions of the turbulence intensity based on the field measurement refer to [1]. The formulation of the turbulence intensity is closely related to the power spectral density shape. Eurocode [4] uses the logarithmic expression, meanwhile the Davenport spectrum uses the power law for turbulence intensity [5]. In the present study for the purposes of structural analysis of cable supported structures we use the logarithmic law.

$$I_u(z) = \frac{\sigma_u}{\bar{U}(z)} = \frac{1}{\ln(z/z_0)} \tag{7}$$

For relatively small terrain roughness, the power law and logarithmic law are barely different. However, for significant roughness, the difference in turbulence intensity profiles is significant and the logarithmic law is more conservative in terms of structural response.

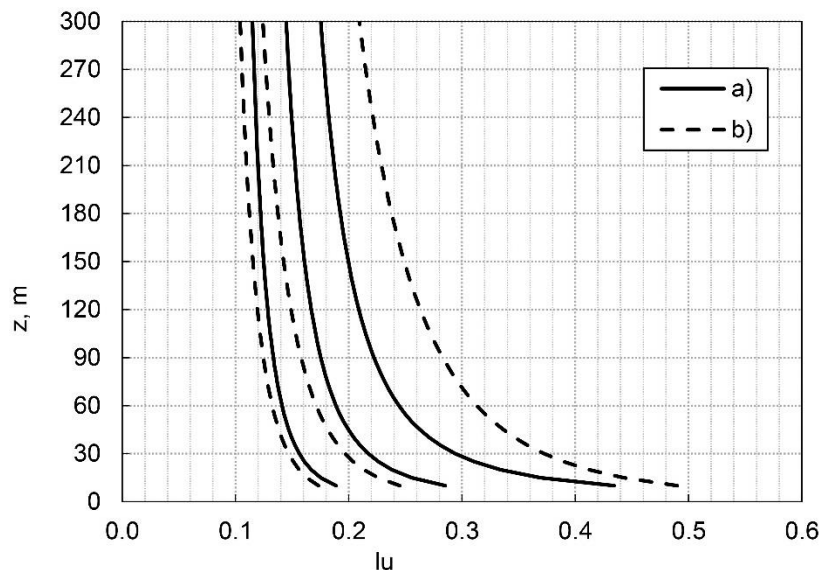


**Figure 6. Turbulence intensity profile: a) logarithmic low [7]; b) power low [8].**

Based on the observations the known relation between turbulence intensity components is employed in this study [20]:

$$I_v = 0.5I_u; \quad I_w = 0.75I_u. \quad (8)$$

For continuous structures such as the bridge deck, it is important to take into account the correlation of the turbulence eddies between two points  $i$  and  $j$  in the space. This is done by means of the root coherence function  $\chi(\omega)$  [21].

$$S(\omega)_{ij} = \sqrt{S(\omega)_{ii}S(\omega)_{jj}} \chi(\omega). \quad (9)$$

It is a common approach to use the exponential decay function (Equation (10)).

$$\chi_{ii}(\omega)_{ij} = \exp\left(-\frac{\omega \sqrt{C_{l,x}^2(x_i - x_j)^2 + C_{l,y}^2(y_i - y_j)^2 + C_{l,z}^2(z_i - z_j)^2}}{\pi(\bar{U}_i + \bar{U}_j)}\right). \quad (10)$$

This idea was first proposed by Davenport. Later, numerous approaches were suggested to estimate the decay coefficients  $C_l$ . The present study uses values proposed in [20] and given in the Table 1. The study [5] uses the similar coefficients but instead of the average of mean wind velocity for two points they use the mean wind velocity at the height 10 m. This approach significantly simplifies the structural analysis. Such assumption seems to be artificial from the theoretical point of view and coherence should depend on the value of mean velocity at the points in question. In the present study is employed the general relation for two points (Equation (10)).

**Table 1. Root coherence function decay coefficients**

Component	$x$	$y$	$z$
$u$	3.0	10.0	10.0
$v$	3.0	6.5	6.5
$w$	0.5	6.5	3.0

For the cross spectrum we introduce the following coherence function in the form proposed in [22].

$$\chi_{uw} = \sqrt{|\chi_{uu}| |\chi_{ww}|}. \quad (11)$$

## 2.2. Turbulence wind load in the frequency domain

The general wind distributed load on a structural element is calculated using the steady state wind load coefficients, which is expressed as

$$\begin{Bmatrix} D \\ L \\ M \end{Bmatrix} = 1/2\rho B U(t)^2 \begin{Bmatrix} C_D(\alpha(t)) \\ C_L(\alpha(t)) \\ BC_M(\alpha(t)) \end{Bmatrix} \approx 1/2\rho B (\bar{U} + 2\bar{U}u(t) + u(t)^2) \begin{Bmatrix} C_D(\bar{\alpha}) + \frac{\partial C_D}{\partial \alpha} \alpha \\ C_L(\bar{\alpha}) + \frac{\partial C_L}{\partial \alpha} \alpha \\ BC_L(\bar{\alpha}) + B \frac{\partial C_L}{\partial \alpha} \alpha \end{Bmatrix} \quad (12)$$

$D, L, M$  are the drag, lift and pitch moment forces corresponding to the aerodynamic steady state aerodynamic coefficients  $C_D, C_L, C_M$ ;

$\rho = 1.225 \text{ kg/m}^3$  is the air density at the average temperature and pressure;

$\bar{U}$  is the mean wind velocity at the element height;

$u(t)$  is along wind turbulence component;

$\alpha(t)$  is the angle of incidence or angle of attack;

$\frac{\partial C_D}{\partial \alpha}, \frac{\partial C_L}{\partial \alpha}, \frac{\partial C_M}{\partial \alpha}$  are first derivatives of the steady state coefficients by angle of incidence.

It should be pointed out, that expression (12) neglects any response of the structure and the vertical fluctuating wind component is not considered for instantaneous wind velocity.

The angle of attack for the turbulence air flow is not constant and depends on the fluctuation velocity. Thus, it can be expressed in the following way:

The tangent of incidence angle can be obtained using a simple geometrical relation:

$$\tan(\alpha_y) = \frac{w(t)}{\bar{U} + u(t)}; \quad \tan(\alpha_z) = \frac{v(t)}{\bar{U} + u(t)}.$$

The assumption about the smallness of pulsation components allows us to change the tangent of angle incidence by its value and expression for angles of incidence can be written down as:

$$\alpha_y = \frac{w(t)}{\bar{U}}; \quad \alpha_z = \frac{v(t)}{\bar{U}}.$$

The wind load for every structural element now takes the following form

$$\begin{Bmatrix} D \\ L \\ M \end{Bmatrix} = \bar{F}_{ae} + \rho \bar{U} B \begin{bmatrix} C_D & \frac{1}{2} \partial C_D / \partial \alpha \\ C_L & \frac{1}{2} \partial C_L / \partial \alpha \\ BC_M & \frac{1}{2} B \partial C_M / \partial \alpha \end{bmatrix} C_{ae} \begin{Bmatrix} u(t) \\ v(t) \\ w(t) \end{Bmatrix}, \quad (13)$$

where  $\bar{F}_{ae}$  is the static wind response to mean wind velocity;

$C_{ae}$  is the matrix that convert the turbulence components from the main coordinate system into the local coordinate system of the structural element where steady state coefficients have been determined.

Thus, transfer matrix function between wind turbulence components can be written in the following form

$$H_b(i\omega) = \rho \bar{U} B \begin{bmatrix} C_D & \frac{1}{2} \partial C_D / \partial \alpha \\ C_L & \frac{1}{2} \partial C_L / \partial \alpha \\ BC_M & \frac{1}{2} B \partial C_M / \partial \alpha \end{bmatrix} C_{ae}. \quad (14)$$

It is known from the analytical solution for a thin plate in potential flow that the response to fluctuation velocity is frequency dependent. Therefore for the stream lined deck we have to introduce frequency dependent admittance functions. For thin and streamlined decks, the theoretical Sears  $Q_w(k)$  [23] and Horlock  $Q_u(k)$  [24] functions can be used that are defined through the Theodorsen function and depends on reduced frequency  $k = B\omega / 2\bar{U}$ . These functions have complex value and they are shown on the complex plane (Figure 6). For the vertical component, introducing  $Q_w(k)$  is justified but for along wind component, it is not. To be on the safe side, in the present study  $Q_u(k)$  is neglected and the final transfer matrix is given in the form:

$$H_b(i\omega) = \rho \bar{U} B \begin{bmatrix} C_D & \frac{1}{2} \partial C_D / \partial \alpha \\ C_L Q_w(k) & \frac{1}{2} \partial C_L / \partial \alpha Q_w(k) \\ BC_M Q_w(k) & \frac{1}{2} B \partial C_M / \partial \alpha Q_w(k) \end{bmatrix} C_{ae}. \quad (15)$$

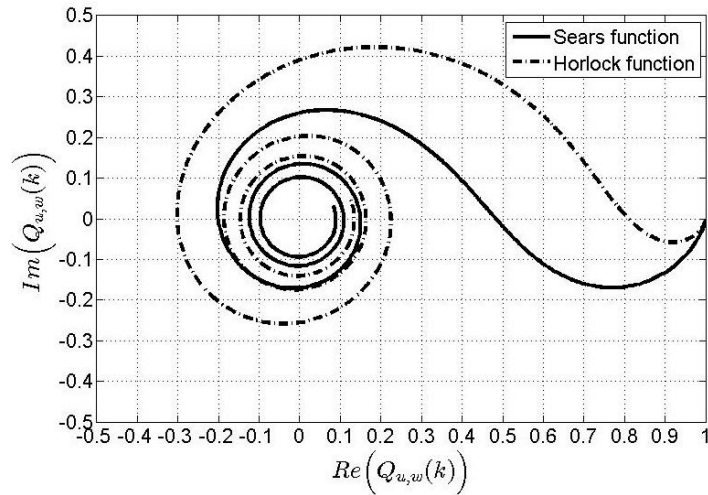


**Figure 7. Sears and Horlock function of reduced frequency on complex plain.**

Finally, the spectral density of aeroelastic forces for points  $i$  and  $j$ , the owing relations of stationary random process theory can be written down as following:

$$S_i(\omega)_{ij} = H_b(i\omega) \begin{bmatrix} \chi_{uu}(\omega)S_{uu}(\omega) & \chi_{uv}(\omega)S_{uv}(\omega) & \chi_{uw}(\omega)S_{uw}(\omega) \\ \chi_{uv}(\omega)S_{uv}(\omega) & \chi_{vv}(\omega)S_{vv}(\omega) & 0 \\ \chi_{uw}(\omega)S_{uw}(\omega) & 0 & \chi(\omega)S_{ww}(\omega) \end{bmatrix} \left( H_b(i\omega)^* \right)^T \quad (16)$$

Here the symbol \* marks complex conjugate value.

It is known from wind tunnel tests and CFD analysis that aerodynamic admittance functions for the real bridge deck are quite different from the airfoil admittance function [25, 26]. The admittance function usually reduces the dynamic response of the bridge in turbulent flow [25].

At the next step we have to perform the structural analysis in the frequency domain and find the standard deviation and peak response in terms of displacement, acceleration and velocity.

### 3. Results and Discussion

In the present study the following approach is used for dynamic response analysis. The mean wind velocity and PSD functions for the pylon are defined at the 0.7 H of the pylon height. The wind turbulence parameter for the deck is assumed to be constant and is defined at the deck level.

We are employing natural mode decomposition method and consider only the first lateral, vertical and pitch modes (Figure 6). All these modes we assume to be statistically independent and we neglect correlation between the modal responses. This assumption is valid if the natural frequencies are separated widely enough from each other.

Therefore for each mode the power density of the generalized turbulence load is written down assuming that there is no coupling between deck cables and pylons

$$\begin{aligned} S_{q,x}(\omega) &= S_{x,u}^d(\omega) + S_{x,w}^d(\omega) + S_{x,uw}^d(\omega) + S_{x,u}^p(\omega) + S_{x,u}^c(\omega); \\ S_{q,z}(\omega) &= S_{z,u}^d(\omega) + S_{z,w}^d(\omega) + S_{z,uw}^d(\omega); \\ S_{q,\varphi}(\omega) &= S_{\varphi,u}^d(\omega) + S_{\varphi,w}^d(\omega) + S_{\varphi,uw}^d(\omega), \end{aligned} \quad (17)$$

where  $S_{x,u}^d(\omega) = S_u(\omega)(\rho\bar{U}B)^2 C_j^2 \int_0^L \varphi(x') \int_0^L \exp\left(-\frac{C_{uy}f|x-x'|}{\bar{U}}\right) \varphi(x) dx dx'$  is the spectrum caused by the action of longitudinal component at bridge deck and  $j$  corresponds to the drag, lift forces and pitch moment;

$S_{x,w}^d(\omega) = S_w(\omega) \left(\frac{1}{2} \rho\bar{U}B\right)^2 \left(\frac{\partial C_j}{\partial \alpha}\right)^2 \int_0^L \varphi(x') \int_0^L \exp\left(-\frac{C_{wy}f|x-x'|}{\bar{U}}\right) \varphi(x) dx dx'$  is spectra caused by the action of the vertical component at bridge deck;

$S_{x,u}^d(\omega) = S_{uw}(\omega)(\rho\bar{U}B)C_j \frac{\partial C_j}{\partial \alpha} \int_0^L \varphi(x') \int_0^L \exp\left(-\frac{C_{wy}f|x-x'|}{\bar{U}}\right) \varphi(x) dx dx'$  is spectra caused by cross power spectral density of the longitudinal and vertical components.

We can obtain in the same manner PSD  $S_{x,u}^p(\omega)$  of the wind load on the pylon with integration over the pylon height.

More complicated procedure to calculate participation of cable-stays is presented. The cable-stays have different outer diameter and length. Besides, they are separated in three directions and more precise evaluation of coherence is required.

The modal wind spectral load on the cable system can be evaluated using general approach. The expression for the modal spectrum  $S_{x,u}^c$  in the general case,

$$S_{x,u}^c = C_D^2 \iint_G \int_G S_u(r, r', \omega) D(r) D(r') \varphi(r) \varphi(r') ds ds', \quad (18)$$

where  $G$  is the set of line segments that represent cables system;

$D(r)$  is the cable duct outer diameter;

$\varphi(r)$  is the mode shape along cables system;

The integral in the Equation (18) can be replaced by the sum of integrals over every single cable

$$\begin{aligned} S_{x,u}^c &= C_D^2 \int_G \left( \int_{l_1} S_{uu}(r, r', \omega) D(r) D(r') \varphi(r) \varphi(r') ds + \dots + \int_{l_n} S_{uu}(r, r', \omega) D(r) D(r') \varphi(r) \varphi(r') ds \right) ds' = \\ &= C_D^2 \sum_{\alpha=1}^n \sum_{\beta=1}^n \int_{l_\alpha} \int_{l_\beta} D_\alpha \varphi(r) S_{uu}(r, r', \omega) D_\beta \varphi(r') ds ds'. \end{aligned} \quad (19)$$

In this approach the mode shape is considered constant over cable length and determine in the cable mid node. The cable duct diameter is constant for every single cable. Now we use cross spectrum between points  $r(x, y, z)$  and  $r'(x', y', z')$  in the form of Equation (9) and (10). Therefore the Equation (19) can be written in matrix form

$$S_{x,u}^c = C_D^2 S_{uu}^c(\omega) \Phi^T J \Phi, \quad (20)$$

where  $S_{uu}^c(\omega)$  is PSD spectrum of the longitudinal wind component determined at the average cable height;

$\Phi$  is vector of product mode shape  $\varphi$  at cable mid node and their duct diameter;

$J$  is the coherence matrix between cables.

Every element of matrix  $J$  can be determined using numerical integration over the cable length as it was done for the bridge deck as following

$$J_{ij} = \int_0^{l_i} \int_0^{l_j} \exp\left(-f \sqrt{C_{xu}(x-x')^2 + C_{yu}(y-y')^2 + C_{zu}(z-z')^2} / \bar{U}\right) ds ds'. \quad (21)$$

Finally, the spectra of modal response and corresponding standard deviation can be now determined using transfer functions

$$S_i(\omega) = |F(i\omega)|^2 S_{q,i}(\omega); \quad (22)$$

$$\sigma_i^2 = \int_0^\infty |F(i\omega)|^2 S_{q,i}(\omega) d\omega = \int_0^\infty \frac{1}{|M(-\omega^2 + 2i\xi_i\omega_i\omega + \omega_i^2)|^2} S_{q,i}(\omega) d\omega, \quad (23)$$

where  $i = x, z, \varphi$  is the index of response direction;

$\omega_i, \xi_i$  – are the natural cyclic frequency and damping ratio of lateral, vertical and torsional modes;

$M$  is the generalized modal mass.

Let us consider a cable stayed bridge with the main span 1100 m. The results of eigenvalue analysis and the natural frequency are shown on the Figure 8 and Table 2.

**Table 2. Natural frequency for basic mode shapes.**

Mode shape	Frequency, Hz
Lateral	0.076
Vertical	0.174
Torsional	0.479

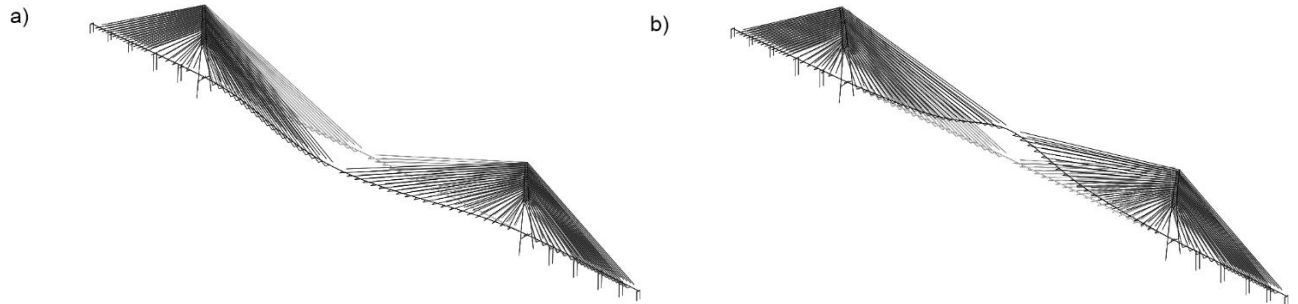


**Figure 8. Lateral (a) and vertical (b) mode shapes.**

The height of the bridge above water level is 70 m. The design wind mean velocity at the height 10 m is 38 m/s. The roughness of the terrain is  $z_0 = 0.01$ . The mean wind velocity and turbulence intensity profile are obtained according equation (1) and (7). The PSD function for the wind velocity fluctuation components is described by the expressions (2), (5) and (6).

The steady state coefficients are obtained through the wind tunnel test  $C_D = 0.069$ ;  $\partial C_D / \partial \alpha = -0.154$ ;  $C_L = 0.13$   $\partial C_L / \partial \alpha = 3.05$ ;  $C_M = 0.046$ ;  $\partial C_M / \partial \alpha = 0.89$ .

The drag coefficient for the pylon is taken equal to 1.70 for upwind leg and 1.02 for downwind leg for mean pylon width of 9 m.

The drag coefficient 0.6 for cables in strong wind is provided by the cable manufacturer.

The damping ratio takes into account structural and aerodynamic damping. The aerodynamic damping for lateral response uses steady state approximation, while for vertical and torsional modes the damping ratio is evaluated by means of flutter derivatives [5], obtained in the cross section wind tunnel test.

$$\begin{aligned}\xi_x &= \xi_s + \frac{2C_D \rho U B}{2\omega_x m}; \\ \xi_z &= \xi_s - \frac{\rho B^2}{2H_1^* m}; \\ \xi_\varphi &= \xi_s - \frac{\rho B^4}{2A_2^* I_p},\end{aligned}\tag{24}$$

where  $m$  and  $I_p$  are the mass and mass moment of inertia per unit length of the deck;

All three values of the damping ratio is mode dependent and have different value.

$H_1^* = -3.276$ ,  $A_2^* = -0.062$  are flutter derivatives for the vertical and torsional bridge deck displacements obtained for the natural frequencies;

$\xi_s = 0.05$  is the structural damping ratio.

The deck and cables have almost equal drag resistance to mean wind flow and added mass from cables much less then deck mass. For that reason we introduce additional factor 2.0 for  $\xi_x$  in Equation (24).

Figure 9 shows the graphs of standard deviation response versus mean wind velocity at the height of 10 m.

We can see that the vertical displacement has almost the same order as the lateral one. The vertical vibrations also produce significant vertical inertia loads and shall be taken into account in design checks.

Aerodynamic admittance noticeably reduces the structural response by 26 % for vertical response and 40 % for rotating angle. Hereby, are used Sears functions, but they can underestimate admittance effect on response. Therefore, wind tunnel and CFD study shall be performed for extreme long bridges.

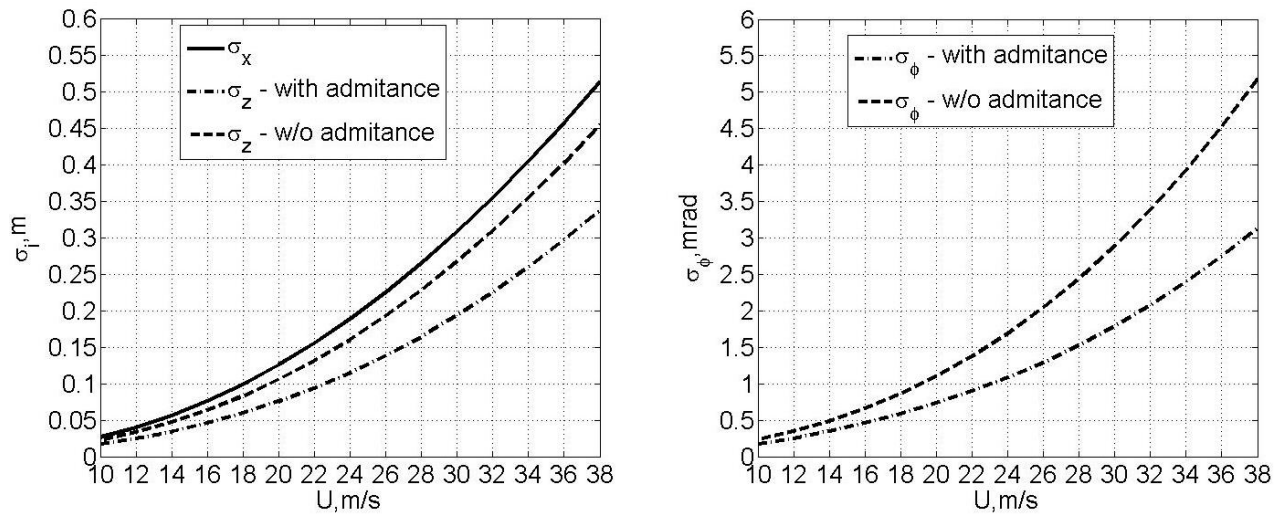


**Figure 9. Standard deviation of lateral –  $u$ , vertical –  $w$  displacements and torsional  $\phi$  rotation at the mid span.**

Actually, the bridge buffeting response depends on type of bridge structural system, length of the main span, bridge deck aerodynamic properties and climate conditions.

The measured on site standard deviation for Lysefjord suspension bridge with 446 m main span are 0.1 m for lateral motion and 0.05 m at the middle of span for mean wind velocity 17.7 m/s [16]. The measured displacements are slightly less than analytical one. The response standard deviation derived from direct measuring in terms of acceleration for Norway Hardanger suspension bridge with span 1336 m is given in [17]. The most suitable values for comparison is data published in for Stonecutters bridge with main span 1018 m [13, 14]. The peak lateral buffeting response is 0.75 m and peak vertical response is 1.4 m for ocean exposure with wind velocity 52 m/s at the deck level. If we take peak factor equal to 3.5 we get standard deviation 0.21 m and 0.4 m for lateral and vertical response respectively. The Stonecutter bridge deck is 1.8 times wider than in the example. That is why the lateral response of Stonecutter bridge less than in the example.

Table 3 shows the results for the middle of the central span for design wind velocity 38 m/s at the 10 m height. After integrating Equation (17) according to Equation (22) we obtain the response variance. The variance has contribution of different parts of the structure and depends on correlation of turbulence components. The Table 3 explains the results as the ratio of each term in Equation (17) to the total response variance.

**Table 3. Contribution of different structural elements and correlation of turbulence components into total response.**

Response	Deck			Pylons $u, u$	Cables $u, u$
	$u, u$	$w, w$	$u, w$		
Lateral	0.391	0.161	0.151	0.084	0.295
Vertical	0.039	0.870	0.090	–	–
Torsional	0.101	1.073	–0.174	–	–

The main lateral response for long span bridges is the result of the deck and cable interaction with wind. It should be emphasized that the cables and the deck makes almost the same contribution into this response. Therefore, reducing the cable diameter and resistance to air flow is the main problem to be solved by the designer. Also noticeable contribution to the lateral response is given by the cross spectrum. The product sign of the drag coefficient and its slope is negative and the sign of the cross spectrum is also negative as it was mentioned above. This fact increases total lateral response. On the contrary, the torsional response is reduced due to the positive product of the pitch coefficient and its slope while covariance between longitudinal and vertical turbulence components is negative. If we compare the total response neglecting the cross spectrum with the total response, we find the lateral response increased by 8 % and the torsional response decreased by 8 %. However, vertical and torsional responses are marginally caused by derivatives of the steady state

aerodynamic coefficients. Thus, the deck shape options shall be consider carefully in terms of the steady state coefficients and their slopes. Besides, the steady state coefficients help the designer to assess the aerodynamic stability.

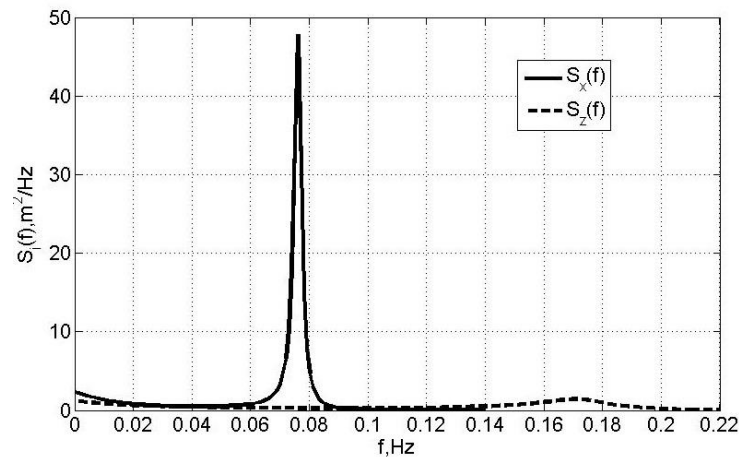


**Figure 10. Power spectral density of the lateral –  $x$ , vertical –  $z$  displacements at the mid span.**

The Van der Hoven spectra is represented by synoptic and turbulent parts. The synoptic part is considered as static wind load. The turbulent part is considered as dynamic wind action with peak around 0.02 Hz. The dynamic part with turbulent peak is described by power spectral density. According to Davenport the structural response can be represented as a sum of background and resonance components. The natural frequencies of the real bridges are quite separated from the turbulent spectral peak. The frequencies around 0.02 Hz contribute mostly to the background part of the total response. For the given example, (Figure 10) background part is 4 % of total dynamic response for lateral motion and include wind action within peak spectral frequency range.

On the Figure 10 is shown the power spectral density function of the lateral and vertical response. The response is divided into background response within range up to 0.02 Hz and the resonance response near the natural frequency. The lateral response has sharp resonance peak while the vertical one is shallow and wide due to significantly higher aerodynamic damping.

The general procedure for power law and logarithmic law is the same and using one of them depends on local climate condition and design code. The difference for both laws for the open terrain is very small. For the given example the difference in turbulent dynamic response is 7 % and 9 % in mean static response.

The real bridge structures within synoptic region about 0.02 Hz are hardly possible. For the given example, with lateral frequency 0.076 Hz the ratio of total response to the peak buffeting response is 1.89 for mid span.

#### 4. Conclusion

1. The three component of wind velocity fluctuation as well as three aerodynamics forces shall be considered for long span cable stay analysis of structural response to turbulence wind flow.
2. The turbulence wind models for practical use in the absence of detailed site measurement proposed.
3. Analysis of structural response is based on the random stationary vibration theory under the assumption of small fluctuation velocities using steady state aerodynamic coefficients.
4. The simplified method of analysis using three main lateral, vertical and torsional modes is proposed. The method of cable system coherence analysis is presented.
5. The cable stay bridge with the main span of 1100 m is considered with the design wind velocity at the height of 10 m is considered. The power spectral density and the standard deviation response versus the wind velocity is obtained.
6. For the bridge deck shape in question the cross spectrum of the vertical component increases lateral response and reduce torsional one. The lateral response is caused mainly by the deck and cables. The deck and cables have almost equal contribution in the total response for the extremely long bridges.
7. The steady state coefficients shall be carefully considered when choosing the deck shape options.

8. The proposed method can be used for any dynamic excitation, which can be represented, by spectral densities and coherence and correlation functions. The linear resonance response can be analyzed by the methods of structural dynamic if excitation force is deterministic and known before calculation.

## References

1. ESDU 85020. Characteristics of Atmospheric Turbulence Near the Ground – 2. Single Point Data for Strong Winds (Neutral Atmosphere). 2001.
2. ESDU 86010. Characteristics of Atmospheric Turbulence Near the Ground – 3. Variations in Space and Time for Strong Winds (Neutral Atmosphere). ESDU Data Items. 2001.
3. Simiu, E., Scanlan, R.H. Wind effects on structures : an introduction to wind engineering. New York, 1986.
4. EN 1991-1-4. Eurocode 1: Actions on structures – Part 1–4: General actions -Wind actions. European Committee for Standardization. 2005. DOI: ICS 91.010.30; 93.040.
5. Popov, N.A. Tornadoes and severe storms in Russia. Proceedings of the Conference on Natural Disaster Reduction. ASCE. Washington, D.C., 1996. Pp. 301–307.
6. Koljushev, I., Guzeev, R., Maslov, D. Engineering solutions for Golden Horn Bay bridge with V-shaped pylons. Long Span Bridges and Roofs – Development, Design and Implementation: 36th IABSE symposiumKolkata, 2013. Pp. 188–189.
7. Larsen, A. Advances in aeroelastic analyses of suspension and cable-stayed bridges. Journal of Wind Engineering and Industrial Aerodynamics. 1998. DOI: 10.1016/S0167-6105(98)00007-5.
8. Hui, M.C.H., Larsen, A., Xiang, H.F. Wind turbulence characteristics study at the Stonecutters Bridge site: Part I—Mean wind and turbulence intensities. Journal of Wind Engineering and Industrial Aerodynamics. 2009. 97(1). Pp. 22–36. DOI: 10.1016/J.JWEIA.2008.11.002.
9. Hui, M.C.H., Larsen, A., Xiang, H.F. Wind turbulence characteristics study at the Stonecutters Bridge site: Part II: Wind power spectra, integral length scales and coherences. Journal of Wind Engineering and Industrial Aerodynamics. 2009. 97(1). Pp. 48–59. DOI: 10.1016/J.JWEIA.2008.11.003.
10. Zhu, J., Zhang, W. Numerical simulation of wind and wave fields for coastal slender bridges. Journal of Bridge Engineering. 2017. 22(3). Pp. 1–17. DOI: 10.1061/(ASCE)BE.1943-5592.0001002.
11. Davenport, A.G. Buffeting of a suspension bridge by storm winds. Journal of the Structural Division. 1962. Vol. 88. Iss. 3. Pp. 233–270.
12. Jain, A., Jones, N.P., Scanlan, R.H. Coupled flutter and buffeting analysis of long-span bridges. Journal of Structural Engineering. 1996. 122(7). Pp. 716–725. DOI: 10.1061/(ASCE)0733-9445(1996)122:7(716).
13. Falbe-Hansen, K., Vejrum, T., Carter, M. Stonecutters Bridge – Design of the Steel Superstructure. Steelbridge 2004, Steel bridges extend structural limits. (June 2004)Millau, 2004. Pp. 1–18.
14. Hui, M.C.H., Ding, Q.S., Xu, Y.L. Buffeting Response Analysis of Stonecutters Bridge. HKIE Transactions. 2005. 12(2). Pp. 8–21. DOI: 10.1080/1023697X.2005.10667998.
15. Fenerci, A., Øiseth, O., Rønquist, A. Long-term monitoring of wind field characteristics and dynamic response of a long-span suspension bridge in complex terrain. Engineering Structures. 2017. DOI: 10.1016/j.engstruct.2017.05.070.
16. Cheynet, E., Jakobsen, J.B., Snæbjörnsson, J. Buffeting response of a suspension bridge in complex terrain. Engineering Structures. 2016. 128. Pp. 474–487. DOI: 10.1016/J.ENGSTRUCT.2016.09.060.
17. Fenerci A., Øiseth, O. Full-Scale Measurements on the Hardanger Bridge During Strong Winds. Dynamics of Civil Structures, Volume 2. Conference Proceedings of the Society for Experimental Mechanics Series. Springer. Cham, 2016.
18. Khrapunov, E.F., Solovov, S.Y. Modeling of the mean wind loads on structures. Magazine of Civil Engineering 2019. 88(4). Pp. 42–51. DOI: 10.18720/MCE.88.4.
19. Lingu, D., Gelder, P. Characteristics of Wind Turbulence With. 2nd European & African Conference on Wind Engineering. Vol. 2Genova, 1997. Pp. 1271–1277.
20. Solari, G., Piccardo, G. Probabilistic 3-D turbulence modeling for gust buffeting of structures. Probabilistic Engineering Mechanics. 2001. 16(1). Pp. 73–86. DOI: 10.1016/S0266-8920(00)00010-2.
21. Yan, L., Zhu, L.D., Flay, R.G.J. Span-wise correlation of wind-induced fluctuating forces on a motionless flat-box bridge deck. Journal of Wind Engineering and Industrial Aerodynamics. 2016. 156. Pp. 115–128. DOI: 10.1016/J.JWEIA.2016.07.004.
22. Katsuchi, B.H., Jones, N.P., Scanlan, R.H., Member, H. Multimode Coupled Flutter and Buffeting Analysis of the Akashi-Kaikyo Bridge. Journal of Structural Engineering. 1999. Pp. 60–70. DOI: 10.1061/(asce)0733-9445(1999)125:1(60).
23. Fung, Y.C. An Introduction to the Theory of Aeroelasticity. Dover. New York, 1969.
24. Horlock, J.H. Fluctuating Lift Forces on Aerofoils Moving Through Transverse and Chordwise Gusts. Journal of Basic Engineering. 1968. 90. Pp. 494–500. DOI: 10.1115/1.3605173.
25. Hejlesen, M.M., Rasmussen, J.T., Larsen, A., Walther, J.H. On estimating the aerodynamic admittance of bridge sections by a mesh-free vortex method. Journal of Wind Engineering and Industrial Aerodynamics. 2015. 146. Pp. 117–127. DOI: 10.1016/j.jweia.2015.08.003.
26. Zhao, L., Ge, Y. Cross-spectral recognition method of bridge deck aerodynamic admittance function. Earthquake Engineering and Engineering Vibration. 2015. 14(4). Pp. 595–609. DOI: 10.1007/s11803-015-0048-8.

## Contacts:

Roman Guzeev, +78124980925; guzeev.roman@gmail.com

Andreas Domaingo, +4331626978636; adomaingo@allplan-infra.com



DOI: 10.18720/MCE.93.4

## Реакция большепролетных мостов на турбулентный ветровой поток

**Р.Н. Гузеев<sup>a\*</sup>, А. Доминго<sup>b</sup>**

<sup>a</sup> Санкт-Петербургский государственный архитектурно-строительный университет, Санкт-Петербург, Россия

<sup>b</sup> ALLPLAN Infrastructure GmbH, Грац, Австрия

\* E-mail: [guzeev.roman@gmail.com](mailto:guzeev.roman@gmail.com)

**Ключевые слова:** вантовые и висячие мосты, динамический отклик, модели турбулентности, пролетное строение моста, проектирование конструкций, когерентность, случайные колебания, численные модели.

**Аннотация.** Изучен отклик вантовых мостов на воздействие пульсационной ветровой нагрузки. Обобщены несколько моделей ветрового потока и предложены модели для практического применения. Модель ветрового потока включает в себя профили средней скорости и интенсивности турбулентности, энергетические спектры и функции пространственной когерентности. Динамический отклик конструкции определяется теорией случайных колебаний для стационарного случайного процесса. Предложен упрощенный метод расчета, используя разложение по собственным формам колебаний с учетом только основных форм. Аэродинамическое демпфирование вычисляется с использованием производных флаттера. Разработан метод учета пространственной когерентности ветровой нагрузки для вантовой системы. Предложена процедура вычисления обобщенной спектральной плотности пульсационной ветровой нагрузки для различных конструктивных элементов, которая учитывает влияние трех компонент пульсаций скорости ветра. Проанализирован вклад различных компонент пульсаций скорости ветра и их корреляция в полный динамический отклик различных элементов конструкции.

### Литература

- ESDU 85020. Characteristics of Atmospheric Turbulence Near the Ground – 2. Single Point Data for Strong Winds (Neutral Atmosphere). 2001.
- ESDU 86010. Characteristics of Atmospheric Turbulence Near the Ground – 3. Variations in Space and Time for Strong Winds (Neutral Atmosphere). ESDU Data Items. 2001.
- Simiu E., Scanlan R.H. Wind effects on structures : an introduction to wind engineering. New York, 1986.
- EN 1991-1-4. Eurocode 1: Actions on structures – Part 1–4: General actions -Wind actions. European Committee for Standardization. 2005. DOI: ICS 91.010.30; 93.040.
- Popov N.A. Tornadoes and severe storms in Russia. Proceedings of the Conference on Natural Disaster Reduction. ASCE. Washington, D.C., 1996. Pp. 301–307.
- Koljushev I., Guzeev R., Maslov D. Engineering solutions for Golden Horn Bay bridge with V-shaped pylons // Long Span Bridges and Roofs – Development, Design and Implementation: 36th IABSE symposium Kolkata, 2013. Pp. 188–189.
- Larsen A. Advances in aeroelastic analyses of suspension and cable-stayed bridges // Journal of Wind Engineering and Industrial Aerodynamics. 1998. DOI: 10.1016/S0167-6105(98)00007-5.
- Hui M.C.H., Larsen A., Xiang H.F. Wind turbulence characteristics study at the Stonecutters Bridge site: Part I—Mean wind and turbulence intensities // Journal of Wind Engineering and Industrial Aerodynamics. 2009. 97(1). Pp. 22–36. DOI: 10.1016/J.JWEIA.2008.11.002.
- Hui M.C.H., Larsen A., Xiang H.F. Wind turbulence characteristics study at the Stonecutters Bridge site: Part II: Wind power spectra, integral length scales and coherences // Journal of Wind Engineering and Industrial Aerodynamics. 2009. 97(1). Pp. 48–59. DOI: 10.1016/J.JWEIA.2008.11.003.
- Zhu J., Zhang W. Numerical simulation of wind and wave fields for coastal slender bridges // Journal of Bridge Engineering. 2017. 22(3). Pp. 1–17. DOI: 10.1061/(ASCE)BE.1943-5592.0001002.
- Davenport A.G. Buffeting of a suspension bridge by storm winds // Journal of the Structural Division. 1962. Vol. 88(Issue 3). Pp. 233–270.
- Jain A., Jones N.P., Scanlan R.H. Coupled flutter and buffeting analysis of long-span bridges // Journal of Structural Engineering. 1996. 122(7). Pp. 716–725. DOI: 10.1061/(ASCE)0733-9445(1996)122:7(716).
- Falbe-Hansen K., Vejrum T., Carter M. Stonecutters Bridge – Design of the Steel Superstructure // Steelbridge 2004, Steel bridges extend structural limits. (June 2004) Millau, 2004. Pp. 1–18.
- Hui M.C.H., Ding Q.S., Xu Y.L. Buffeting Response Analysis of Stonecutters Bridge // HKIE Transactions. 2005. 12(2). Pp. 8–21. DOI: 10.1080/1023697X.2005.10667998.

15. Fenerci A., Øiseth O., Rønquist A. Long-term monitoring of wind field characteristics and dynamic response of a long-span suspension bridge in complex terrain // *Engineering Structures*. 2017. DOI: 10.1016/j.engstruct.2017.05.070.
16. Cheynet E., Jakobsen J.B., Snæbjörnsson J. Buffeting response of a suspension bridge in complex terrain // *Engineering Structures*. 2016. 128. Pp. 474–487. DOI: 10.1016/J.ENGSTRUCT.2016.09.060.
17. Fenerci A., Øiseth O. Full-Scale Measurements on the Hardanger Bridge During Strong Winds // *Dynamics of Civil Structures*. Vol. 2. Conference Proceedings of the Society for Experimental Mechanics Series. Springer. Cham, 2016.
18. Соловьев С.Ю., Храпунов Е.Ф. Моделирование средних ветровых нагрузок на сооружения // *Инженерно-строительный журнал*. 2019. № 4(88). С. 42–51. DOI: 10.18720/MCE.88.4
19. Lingu D., Gelder P. Characteristics of Wind Turbulence With // *2nd European & African Conference on Wind Engineering*. Vol. 2Genova, 1997. Pp. 1271–1277.
20. Solari G., Piccardo G. Probabilistic 3-D turbulence modeling for gust buffeting of structures // *Probabilistic Engineering Mechanics*. 2001. 16(1). Pp. 73–86. DOI: 10.1016/S0266-8920(00)00010-2.
21. Yan L., Zhu L.D., Flay R.G.J. Span-wise correlation of wind-induced fluctuating forces on a motionless flat-box bridge deck // *Journal of Wind Engineering and Industrial Aerodynamics*. 2016. 156. Pp. 115–128. DOI: 10.1016/J.JWEIA.2016.07.004.
22. Katsuchi B.H., Jones N.P., Scanlan R.H., Member H. Multimode Coupled Flutter and Buffeting Analysis of the Akashi-Kaikyo Bridge // *Journal of Structural Engineering*. 1999. Pp. 60–70. DOI: 10.1061/(asce)0733-9445(1999)125:1(60).
23. Fung Y.C. *An Introduction to the Theory of Aeroelasticity*. Dover. New York, 1969.
24. Horlock J.H. Fluctuating Lift Forces on Aerofoils Moving Through Transverse and Chordwise Gusts // *Journal of Basic Engineering*. 1968. 90. Pp. 494–500. DOI: 10.1115/1.3605173.
25. Hejlesen M.M., Rasmussen J.T., Larsen A., Walther J.H. On estimating the aerodynamic admittance of bridge sections by a mesh-free vortex method // *Journal of Wind Engineering and Industrial Aerodynamics*. 2015. 146. Pp. 117–127. DOI: 10.1016/j.jweia.2015.08.003.
26. Zhao L., Ge Y. Cross-spectral recognition method of bridge deck aerodynamic admittance function // *Earthquake Engineering and Engineering Vibration*. 2015. 14(4). Pp. 595–609. DOI: 10.1007/s11803-015-0048-8.

**Контактные данные:**

*Роман Николаевич Гузеев, +78124980925; эл. почта: guzeev.roman@gmail.com*

*Андреас Доминго, +4331626978636; эл. почта: adomaingo@allplan-infra.com*



DOI: 10.18720/MCE.93.5

## Earthquake resistance of buildings on thawing permafrost grounds

**T.A. Belash<sup>a</sup>, T.V. Ivanova<sup>b</sup>**

<sup>a</sup> *Petersburg State Transport University, St. Petersburg, Russia*

<sup>b</sup> *«B.E. Vedeneev VNIIG», JSC, St. Petersburg, Russia*

\* *E-mail: belashta@mail.ru*

**Keywords:** thawing permafrost ground, seismic survey, stresses, strains, settlement, foundation platform

**Abstract.** A feature of the structural solution of the building is the presence of a solid underground foundation in the form of a three-dimensional rigid reinforced concrete platform. The building will be erected on thawing grounds; thawing takes place during the entire period of operation. Theoretical analysis of stress-strained building structures exposed to static and seismic loads has been carried out. Seismic load was determined by a specified response spectrum method. The calculation was carried out taking into account the presence of a thawing basin under the foundation with the size of the bowl varying from 6 m to 27 m. It was found that the building structures exposed to a seismic load are subject to increased stress and strain as compared with the static load exposure. Evaluation of the obtained values has shown that they did not exceed the permissible limits for the accepted strength properties of structural materials even in conditions of a maximum thawing basin. Foundation settlement is gradual. The adopted foundation structure design ensures the required earthquake resistance of the building in the given construction conditions.

### 1. Introduction

Currently, active development takes place in the northern and eastern regions of the Russian Federation. A characteristic feature of these regions are severe climatic conditions, complicated engineering and geological conditions: permafrost occurrence in its various manifestations, seismic activity of magnitude 6 and above in many regions, lack of developed infrastructure, etc. As you know, these territories are rich in deposits of gas, oil, coal, various materials and other minerals. In addition, coastal areas provide access to seas and oceans, and majestic woodlands extend for many kilometers in the eastern part. Active development is underway in these areas: workers' urban-type settlements near production areas, research centers, transportation buildings and facilities, woodworking plants, metalwork plants, etc., are currently being built. Their trouble-free functioning under conditions of simultaneous manifestation of various kinds of natural, climatic and seismic impacts is a complicated engineering task, the solution of which is of great national importance. In this case, the most dangerous situation arises when the complex properties of permafrost soils and high seismic activity are manifested, which can cause the collapse of buildings and structures, as was observed, for example, in Anchorage after the earthquake in 1964 and in 2018. In this regard, the issues under consideration for assessing the earthquake resistance of buildings in conditions of thawing permafrost soils are relevant and of great practical importance.

The practice of construction on permafrost grounds includes two principles of their application as bases with their frozen condition preserved (principle I) during construction and throughout operation period and principle II, when grounds are used in thawed or thawing condition. The aspects of use of permafrost ground as building foundation bases have been studied in extensive literature sources referenced in [1–10], as well as in various regulations. The need to make a choice of the principle of using permafrost soils of the base, as well as the means by which the state of the base (frozen or thawed) is achieved, should be made on the basis of technical and economic comparison of options taking into account the engineering and geocryological conditions of the construction site, space-planning and structural solutions of the building, etc. However, the seismic activity in the region can also have a significant influence on the decision to use permafrost ground as a foundation base. The studies described in the publications of V.P. Solonenko, E.N. Chemezov, S.I. Grib

Belash, T.A., Ivanova, T.V. Earthquake resistance of buildings on thawing permafrost grounds. Magazine of Civil Engineering. 2020. 93(1). Pp. 50–59. DOI: 10.18720/MCE.93.5

Белаш Т.А., Иванова Т.В. Сейсмостойкость здания на оттаивающих вечномёрзлых основаниях // Инженерно-строительный журнал. 2020. № 1(93). С. 50–59. DOI: 10.18720/MCE.93.5



[11–15] and other Russian and foreign authors [16–34] were carried out to investigate seismic resistance of buildings on permafrost ground using various construction principles. These studies investigated the seismic properties of frozen soils. The influence of moisture content and temperature conditions of soil on seismic wave parameters was demonstrated. It was found that any upward variation of soil temperature entails an increase in the oscillation period and, vice versa, it decreases as temperature decreases. The studies have shown that for frozen soils, the seismic rating can decrease by magnitude 1, and for thawed soils, it increases by magnitude 1, this circumstance was reflected in construction objects.

It is shown that the effect of seismic impact is influenced not only by the strength of the earthquake, but also by the dynamic parameters of the construction object as a whole and its individual structural elements. The essential point in this case is the correct assessment of the nature and intensity of the transmission of vibrations of the Foundation structure from the ground base to the building. According to the results of studies, it was found that the flexibility of the Foundation has a significant impact on the shear forces that appear during seismic action on the soil surface. In addition, while transmitting vibrations to the building, the ground itself is involved in joint oscillations with the building in the form of apparent soil masses. The degree of soil setting at the bottom of foundation is a factor that determines the design solution reliability and is crucial for determining the earthquake resistance of the building. Earthquake resistance assessment of the building shall include the loads not only on the building itself, but also on the ground, as well as their combined action.

Based on the foregoing, a particularly important circumstance is the decision on the choice of foundation structures. To implement principle I, as known, pile or pier type foundations, strip foundations, as well as special design solutions aimed at natural cooling of soil surface can be used to minimize the impact of heat energy released by the building. This foundation option is applicable only to hard frozen and plastic frozen soils, it is preferred for permafrost areas with relatively constant negative temperatures of earth stratum. In the southern permafrost areas, the average annual air temperature variations are significant, which obviously affects the temperature condition of frozen ground. The probability of their transition to thawed state, and, consequently, loss of bearing capacity make it difficult to build foundations according to principle I. In this case, the most preferable and efficient solution is to apply principle II. Particular care is required for building foundations using permafrost ground according to principle II, because in the event of uneven precipitation, the foundations must not only absorb the load from the aboveground portion, but also be strong and resistant to unacceptable deformations and failure. Solid and rigid foundation structures are preferred for such grounds. Currently, there are various foundation solutions designed for combined operation of principle II and seismic conditions. The proposed solutions are based on the foundation design in the form of a rigid three-dimensional platform. Some examples of its execution, developed by Russian specialists, are presented in Figures 1–3. A distinctive feature of these structures is the ability to accommodate deformations caused by uneven setting of ground and seismic load due to the three-dimensional action of the design solution, which is achieved by rigid connection of the top and bottom slabs, a system of braced cross beams, trusses or ribs. In some cases, it is additionally proposed to arrange a sliding layer between the bottom of the foundation and subsoil [35–37]. Structural assessment of the proposed decisions indicates their applicability for the implementation of principle II. Further introduction of these foundations into construction practice requires additional research taking into account the special manifestation of permafrost soil properties of the base and seismic activity. In this regard, the purpose of the present study is to estimate the seismic stability of the building on a massive platform-type foundation under permafrost soil conditions according to principle II, taking into account their thawing during operation. The study was carried out on the example of a transport facility (station complex). The task of the study was to determine the stress-strain state of the construction object taking into account the expected deformations and compliance of the base itself.

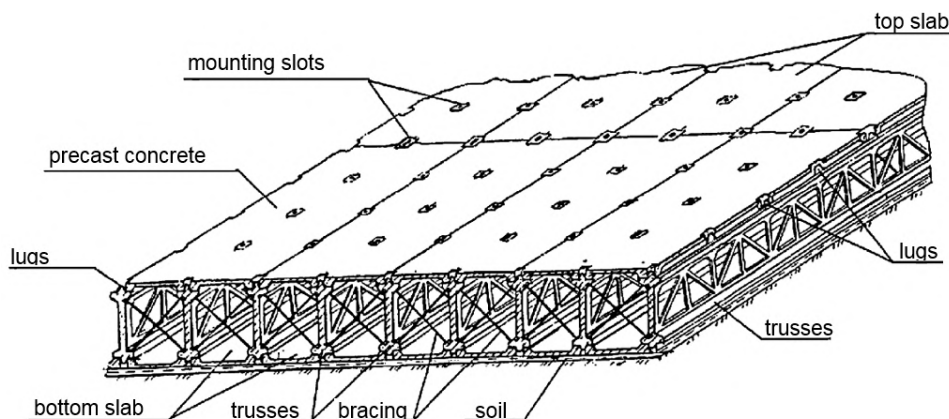


Figure 1. Precast concrete foundation platform [35].

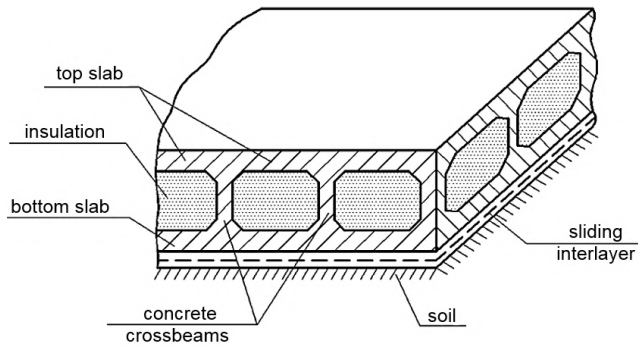


Figure 2. Cast-in-place foundation platform [36].

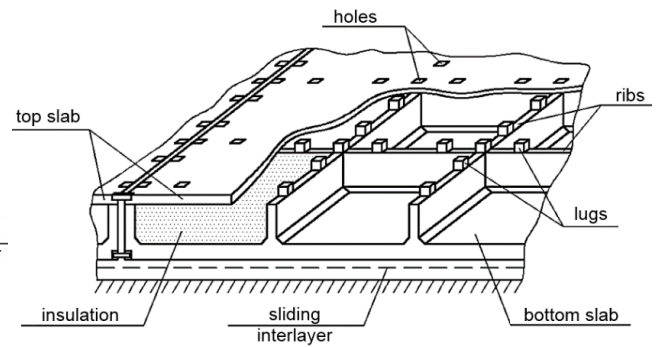


Figure 3. Precast concrete foundation platform for low-rise buildings [37].

These aspects are being studied at the Emperor Alexander I St. Petersburg State Transport University, the Department of Buildings, and some findings have been published in [38]. Subsequent studies have provided a final assessment of the building behavior in combined permafrost and earthquake conditions using the second construction principle. The findings of these studies are described herein.

## 2. Design Analysis Method

The design analysis method was developed and described in [38]. The building under consideration is a transportation facility and has a foundation designed in the form of a three-dimension solid platform (Figure 8 in [38]). Some space-planning and structural features of the building shall be pointed out such as the building is rectangular in plan its dimensions are 55 m  $\times$  27 m. The structure of the building is of framework type with transverse crossbars. Columns are solid, concrete cross section 400 mm  $\times$  400 mm, concrete class B30. Column spacing in the longitudinal and transverse directions is 6 m and 3 m. Crossbars are solid T-sections, cross section 400 mm  $\times$  450 mm, concrete class B25. External walls – hinged lightweight concrete panels. The three-dimension foundation design is shown in Figure 4. Three-dimension units consist of two parts – bottom (box-shaped) part consisting of a 300 mm thick slab and 200 mm thick ribs with 1500 mm  $\times$  1800 mm holes and a 200 mm top cast-in-place slab which is cast at the construction site after the box-shaped unit installation.

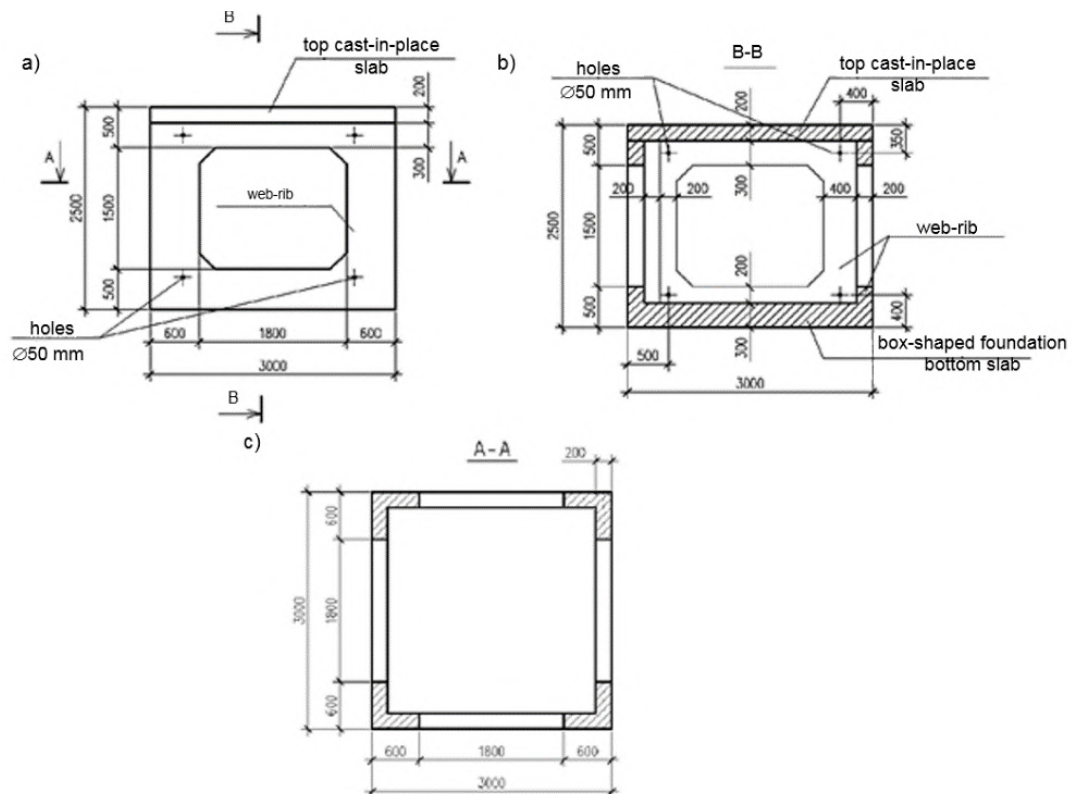


Figure 4. Three-dimension foundation: a – elevation; b – section A-A; c – section B-B.

As was noted in [38], a building model was built for the study based on the specific soil conditions of the foundation in question; for this a soil body was made from solid finite elements. Various development stages of the thawing basin shown in Figure 5 and Table 1 were assigned to the final elements (FE). The calculations were carried out for full static and seismic loads. Seismic design of the building under consideration was carried out according to the spectral method taking into account the recommendations from the applicable regulations.

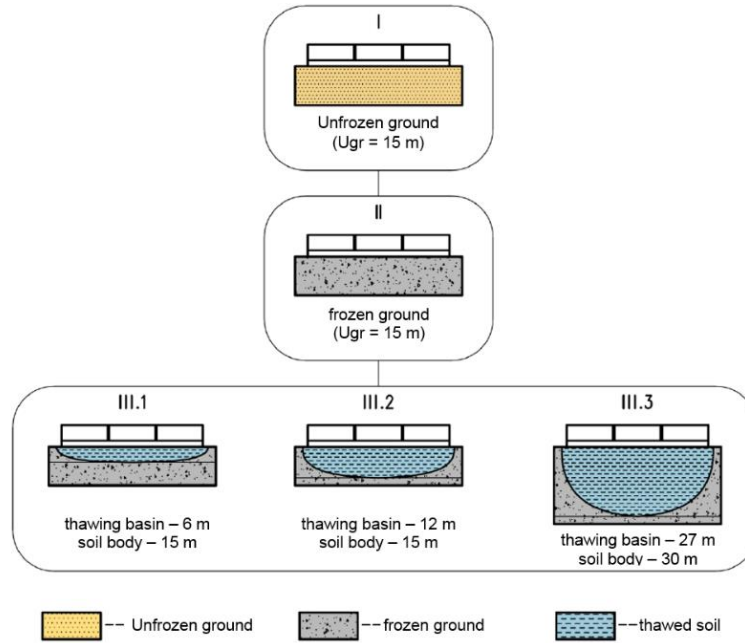


Figure 5. Design options for a building model with a soil body.

Table 1. Stiffness parameters for solid FE that simulate soil conditions for all design model options.

Number in the diagram, type of FE and name of layer	Modulus of deformation, kN/cm <sup>2</sup>	Bulk density, T/m <sup>3</sup>	Quantity FE
Option I			
1  Unfrozen ground	80	1.8	23520
Option II			
1  frozen ground	150	1.8	23520
Option III.1			
1  frozen ground	150	2.0	1658
2  layer 1 – MELT soil	50	1.5	4418
3  layer 2 – MELT soil	70	1.7	3444
Option III.2			
1  frozen ground	150	2.0	9546
2  layer 1 – THAWED soil	50	1.5	4418
3  layer 2 – THAWED soil	60	1.6	4230
4  layer 3 – THAWED soil	70	1.7	3280
5  layer 4 – THAWED soil	80	1.8	2046
Option III.3			
1  frozen soil – 1	150	2.0	1753
2  frozen soil – 2	170	2.1	10292
3  layer 1 – THAWED soil	50	1.5	4418
4  layer 2 – THAWED soil	55	1.55	4418
5  layer 3 – THAWED soil	60	1.6	4418
6  layer 4 – THAWED soil	65	1.65	4418
7  layer 5 – THAWED soil	70	1.7	4095
8  layer 6 – THAWED soil	75	1.75	2520
9  layer 7 – THAWED soil	80	1.8	1300

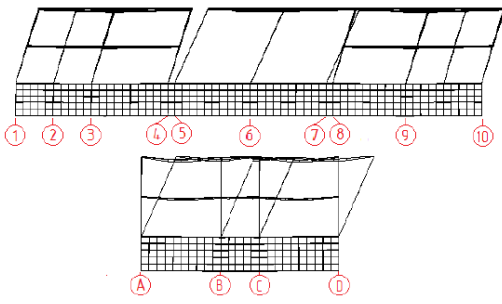
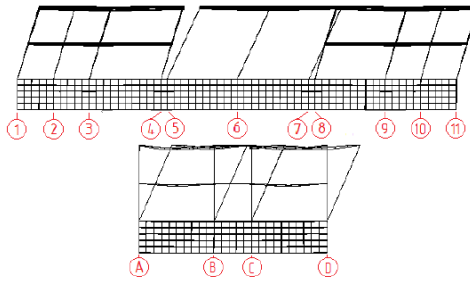
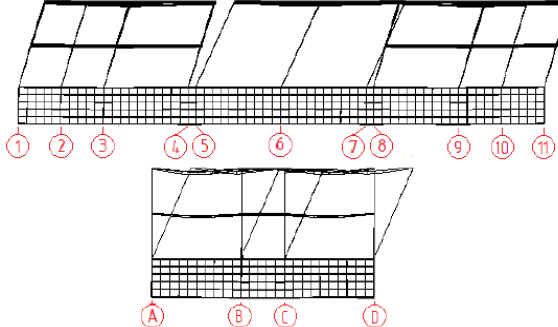
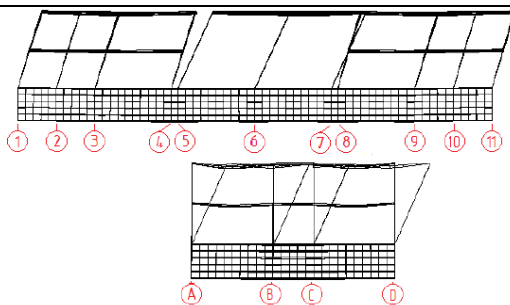
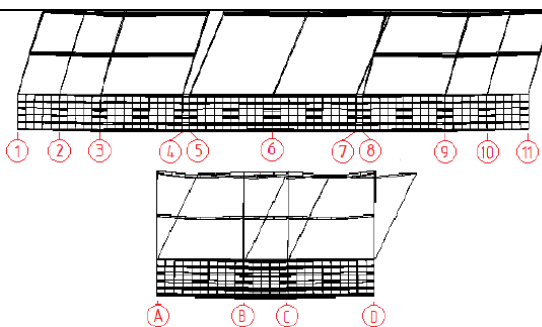
Note:

1. The total number of solid elements (options B 1.0.0 – B 1.2) is 23520;
2. The total number of solid elements (option B 1.3) is 37632.

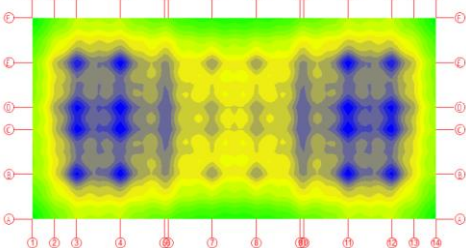
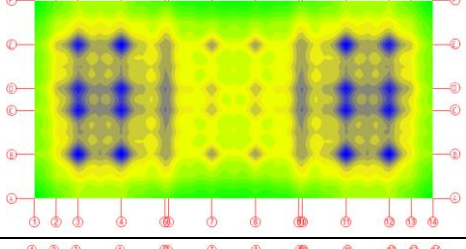
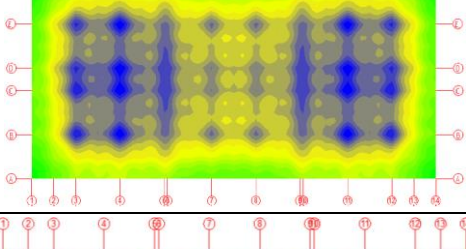
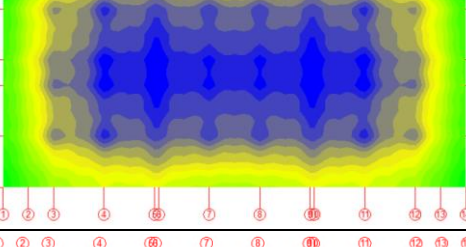
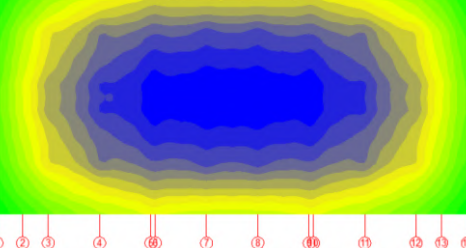
### 3. Results and Discussion

The seismic design of the building under full earthquake load is summarized in Tables 2 and 3 (the full static load calculation results are listed in [38]).

**Table 2. Stress-strain condition parameters of the model options exposed to the total earthquake load.**

Building deformations (longitudinal and transverse)		Maximum parameter values			
1		2			
Option I					
	unfrozen soil (Ugr = 15 m)	Design	$\Delta z_{max}$ , mm	$\sigma_x$ , kN/m <sup>2</sup>	$\sigma_y$ , kN/m <sup>2</sup>
		Top slabs	-4.49	-7187.34	-4514.84
		Foundation	-2.7	-6864.6	-4,514.84
				6738.65	11022.51
		Design	$N$ , kN	$M$ , kNm	$Q$ , kN
		Columns	-601.18	-148.04	-50.85
		Door bolt	-8.31	-90.12	-80.38
				47.89	60.38
Option II					
	frozen ground (Ugr = 15 m)	Design	$\Delta z_{max}$ , mm	$\sigma_x$ , kN/m <sup>2</sup>	$\sigma_y$ , kN/m <sup>2</sup>
		Top slabs	-3.3	-6720.26	-4215.33
		Foundation	-1.46	-6403.1	-4215.33
				6284.34	10730.51
		Design	$N$ , kN	$M$ , kNm	$Q$ , kN
		Columns	-601	-140.18	-47.99
		Door bolt	-7.74	-88.69	-78.92
				46.91	58.81
	thawing basin - 6 m; soil body - 15 m	Design	$\Delta z_{max}$ , mm	$\sigma_x$ , kN/m <sup>2</sup>	$\sigma_y$ , kN/m <sup>2</sup>
		Top slabs	-3.54	-6795.44	-4226.72
		Foundation	-1.76	-6531.58	-4226.72
				6344.86	10832.68
		Design	$N$ , kN	$M$ , kNm	$Q$ , kN
		Columns	-600.36	-141.67	-48.8
		Door bolt	-7.91	-88.74	-78.98
				47.11	58.96
Option III.2					
	thawing basin - 12 m; soil body - 15 m	Design	$\Delta z_{max}$ , mm	$\sigma_x$ , kN/m <sup>2</sup>	$\sigma_y$ , kN/m <sup>2</sup>
		Top slabs	-3.9	-6880.71	-4229.83
		Foundation	-2.25	-6614.13	-4229.83
				6486.82	10913.02
		Design	$N$ , kN	$M$ , kNm	$Q$ , kN
		Columns	-599.14	-144.42	-49.85
		Door bolt	-8.12	-88.85	-79.37
				47.28	59.05
Option III.3					
	thawing basin - 27 m; soil body - 30 m	Design	$\Delta z_{max}$ , mm	$\sigma_x$ , kN/m <sup>2</sup>	$\sigma_y$ , kN/m <sup>2</sup>
		Top slabs	-8.97	-7625.67	-4975.84
		Foundation	-7.6	-7625.67	-4975.84
				7732.81	11294.93
		Design	$N$ , kN	$M$ , kNm	$Q$ , kN
		Columns	-596.3	-157.58	-59.62
		Door bolt	-10.01	-94.85	-81.34
				50.18	61.74

**Table 3. Vertical displacement isofields at the foundation bottom level under the combined action of full static load and total earthquake load.**

Vertical displacement isofields	Design option number and displacement parameters	
1	2	
	Option I	
	Displacements $\Delta z$ , mm	
	max	min
	-2.7	-2.38
	Option II	
	Displacements $\Delta z$ , mm	
	max	min
	-1.46	-1.27
	Option III.1	
	Displacements $\Delta z$ , mm	
	max	min
	-1.76	-1.4
	Option III.2	
	Displacements $\Delta z$ , mm	
	max	min
	-2.25	-1.59
	Option III.3	
	Displacements $\Delta z$ , mm	
	max	min
	-7.6	-5.88

Note:

1. In the Figures maximum values are shown in blue and minimum values are shown in green.

The stress-strain data analysis of the building bearing structures has shown that under both static and earthquake load the settlement the foundation structure does not exceed  $\approx 7.6$  mm at the maximum depth of the thawing basin. At the same time, stresses and forces in structures exposed to earthquake load as compared with static load increase significantly, but their maximum values do not exceed the maximum allowable compressive and tensile values taking into account the strength characteristics of concrete and reinforcement adopted in the design. As a result of calculation and theoretical research it is established that seismic resistance of the building with the accepted type of the base on thawing bases is provided. The sediment in the level of the sole of the foundation has a uniform distribution. The results obtained relate to a specific type of foundation – the foundation of the platform type, working in conditions of high seismic activity

and the presence of thawing permafrost soils. The studies were carried out taking into account the peculiarities of seismic impact of different intensity and frequency composition.

The presented results are of great importance for the implementation in practice of construction of the considered foundation structure and allow to draw a conclusion about its high efficiency in comparison with other structures, for example, pile foundations [30]. Currently, in the world practice of construction there are no recommendations for the use of this design in permafrost and high seismic activity.

#### 4. Conclusions:

1. Assessment of the seismic resistance of buildings in permafrost areas is one of the most challenging engineering task, the successful solution of which substantially depends on the accepted foundation designs of these buildings.

2. The studies has shown that platform-type solid foundations that provide uniform settlement of the building even with a significant depth of thawing basin are one of the most reasonable design solutions for thawing permafrost soils during earthquake impacts. Foundation design may be developed using various proposals wide range of which is given in patent literature.

3. The maximum stresses and strains in load-bearing structures of the building on the accepted type of foundation exposed to earthquake load are significantly higher than when exposed to static load, but they do not exceed the maximum permissible limits.

The use of the type of foundation under consideration is possible in various structural solutions of buildings, in particular, in high-rise buildings, and in buildings using other materials and structures.

Safe operation of facilities with the type of foundation under consideration for a long period of time is guaranteed with full compliance with the requirements of the norms and rules of operation of buildings in permafrost and seismic areas.

#### 5. Acknowledgements

When carrying out the study, the staff of the Department of the Buildings of Emperor Alexander I St. Petersburg State Transport University, Candidate of Engineering Sciences Nudga I.B., Chirkst T.M. took part.

#### References

1. Vylov, S.S., Sheinkman, D.R., Dokuchaev, V.V. Podzemnye l'dy i sil'nol'distye grunty kak osnovaniya sooruzhenij [Underground ice and highly wet permafrost soils as building foundations]. Leningrad:Stroyizdat. Leningradskoe otd-nie, 1976. 167 p. (rus)
2. Kudryavtsev, S.A., Sakharov, I.I., Paramonov V.N. Promerzanie i ottaivanie gruntov (prakticheskie primery i konechnoelementnye raschety) [Freezing and thawing of soils (practical examples and finite element calculations)]. SPb.: Georekonstrukciya, 2014. 248 p. (rus)
3. Allard, M., Lemay, M. Nunavik and Nunatsiavut: From science to policy. An Integrated Regional Impact Study (IRIS) of climate change and modernization. ArcticNet Inc. Quebec City, Canada, 2012. 303 p.
4. Ran, Y., Li, X., Cheng, G. Climate warming over the past half century has led to thermal degradation of permafrost on the Qinghai-Tibet Plateau. *Cryosphere*. 2018. 12(2). Pp. 595–608. DOI: 10.5194/tc-12-595-2018.
5. Inzhutov, I.S., Zhadanov, V.I., Nazirov, R.A., Servatinskii, V.V., Semenov, M.Y., Amelchugov, S.P., Archipov, I.N., Goncharov, Y.M., Chaikin, E.A. Research of permafrost soil thawing under the structural foundation platform. IOP Conference Series: Materials Science and Engineering. Novosibirsk, Russia. 2018. 456(1). DOI: 10.1088/1757-899X/456/1/012046.
6. Crowther, G.S. Lateral pile analysis frozen soil strength criteria. *Journal of Cold Regions Engineering*. 2015. 29(2). Pp. 1–15. DOI: 10.1061/(ASCE)CR.1943-5495.0000078.
7. Rotta Loria, A.F., Frigo, B., Chiaia, B. A non-linear constitutive model for describing the mechanical behaviour of frozen ground and permafrost. *Cold Regions Science and Technology*. 2017. No. 133. Pp. 63–69. DOI: 10.1016/j.coldregions.2016.10.010.
8. Wenping Fei, Yang, Z.J., Sun, T. Ground freezing impact on laterally loaded pile foundations considering strain rate effect. *Cold Regions Science and Technology*. 2019. No. 157. Pp. 53–63. DOI: 10.1016/j.coldregions.2018.09.006.
9. Wotherspoon, L.M., Sriharan, S., Pender, M.J. Modelling the response of cyclically loaded bridge columns embedded in warm and seasonally frozen soils. *Engineering Structures*. 2010. 32(4). Pp. 933–943. DOI: 10.1016/j.engstruct.2009.12.019.
10. Yang, Z.J., Still, B., Ge, X. Mechanical properties of seasonally frozen and permafrost soils at high strain rate. *Cold Regions Science and Technology*. 2015. No. 113. Pp. 12–19. DOI: 10.1016/j.coldregions.2015.02.008.
11. Solonenko, V.P. Zemletryaseniya i vulkany Stanovogo nadgor'ya [Earthquakes and volcanoes of Stanovoy Highlands]. *Priroda*. 1964. No. 9. Pp. 102–110. (rus)
12. Chemezov, E.N., Petrov, A.F., Blinova, T.E. O seismoopasnosti territorii Yakutska [On the seismic hazard in Yakutsk area]. *Vestnik Severo-vostochnogo federal'nogo universiteta im. M.K. Ammosova*. 2007. 4(3). Pp. 33–38. (rus)
13. Solonenko, V.P. Seismogeologiya i seismicheskoe rajonirovanie trassy BAM i zony ee ekonomicheskogo vliyaniya [Seismic geology and seismic zoning of the Baikal-Amur Mainline and its economic influence zones]. Novosibirsk: Nauka, Sib. otd-nie, 1979. 69 p. (rus)
14. Solonenko, V.P. Seismogeologicheskie usloviya zony stroitel'stva BAM [Seismic geological conditions of the Baikal-Amur Mainline construction zone]. *Irkutsk: Irkutskaya oblastnaya tipografiya No. 1*, 1981. 48 p. (rus)
15. Grib, S.I. Svajnye fundamenti na vechnomerzlyh gruntah v seismicheskikh rajonah [Pile foundations on permafrost grounds in seismic areas]. Leningrad: Stroyizdat, Leningradskoe otd-nie., 1983. 152 p. (rus)
16. Kharitonov, V.A. Sejsmostojkoe stroitel'stvo na vechnomerzlyh gruntah [Earthquake-resistant construction on permafrost ground]. Moscow: Stroyizdat, 1980. 77 p. (rus)

17. Yang, Z.J., Dutta, U. Numerical analysis of permafrost effects on the seismic site response. *Soil Dynamics and Earthquake Engineering*. 2011. 31(3). Pp. 282–290.
18. Yang, Z.J., Li, Q. Seasonally frozen soil effects on the dynamic behavior of highway bridges. *Sciences in Cold and Arid Regions*. 2012. 4(1). Pp. 13–20.
19. Chen, G.S., Davis, D., Hulse, J.L. Measurement of frozen soil-pile dynamic properties: a system identification approach. *Cold Regions Science and Technology*. 2012. No. 70. Pp. 98–106.
20. Wotherspoon, L.M., Sritharan, S., Pender, M.J., Carr, A.J. Investigation on the impact of seasonally frozen soil on seismic response of bridge columns. *Journal of Bridge Engineering*. 2010. 15(5). Pp. 473–481. DOI: 10.1061/(ASCE)BE.1943-5592.0000075.
21. Gu, Q., Yang, Z., Peng, Y. Parameters affecting laterally loaded piles in frozen soils by an efficient sensitivity analysis method. *Cold Regions Science and Technology*. 2016. No. 121. Pp. 42–51. DOI: 10.1016/j.coldregions.2015.10.006.
22. Shelman, A., Tantalla, J., Sritharan, S., Nikolaou, S., Lacy, H. Characterization of seasonally frozen soils for seismic design of foundations. *Journal of Geotechnical and Geoenvironmental Engineering*. 2014. 140(7). Pp. 1–10. DOI: 10.1061/(ASCE)GT.1943-5606.0001065.
23. James, S.R., Knox, H.A., Abbott, R.E., Panning, M.P., Screaton, E.J. Insights Into Permafrost and Seasonal Active-Layer Dynamics From Ambient Seismic Noise Monitoring. *Journal of Geophysical Research: Earth Surface*. 2019. Pp. 1–19. DOI: 10.1029/2019JF005051.
24. Matson, R., Wolf, K., Yancey, D. Influence of permafrost on seismic imaging in Alaska. *SPE Arctic and Extreme Environments Conference and Exhibition (AEE 2013)*. Moscow, 2013. Pp. 76–103. DOI: 10.2118/166821-MS.
25. Skvortsov, A.G., Sadurtdinov, M.R., Tsarev, A.M. Methods for permafrost studies seismic criteria for indentifying frozen soil. *Scientific journal earth's cryosphere*. 2014. XVIII(2). Pp. 75–80.
26. Skvortsov, A.G., Tsarev, A.M., Sadurtdinov, M.R. Methods of permafrost studies seismic studies in frozen ground. *Scientific journal earth's cryosphere*. 2011. XV(4). Pp. 96–98.
27. Krautblatter, M., Draebing, D. Pseudo 3-D P wave refraction seismic monitoring of permafrost in steep unstable bedrock. *Journal of Geophysical Research: Earth Surface*. 2014. 119(2). Pp. 287–299. DOI: 10.1002/2012JF002638.
28. Che, A.L., Wu, Z.J., Wang, P. Stability of pile foundations base on warming effects on the permafrost under earthquake motions. *Soils and Foundations*. 2014. 54(4). Pp. 639–647. DOI: 10.1016/j.sandf.2014.06.006.
29. Wu, Z.J., Che, A.L., Ghen, T. Warming effects on permafrost under earthquake motions and seismic stability of pile foundation of dry bridge. *Materials Research Innovations*. 2011. 15(Suppl. 1). DOI: 10.1179/143307511X12858957676957.
30. Edwin, S. Clarke. *Permafrost Foundation: State of the Practice*. American Society of Civil Engineers. 2007. 94 p.
31. Weber, S., Fäh, D., Beutel, J., Faillettaz, J., Gruber, S., Vieli, A. Ambient seismic vibrations in steep bedrock permafrost used to infer variations of ice-fill in fractures. *Earth and Planetary Science Letters*. 2018. No. 501. Pp. 119–127. DOI: 10.1016/j.epsl.2018.08.042.
32. Draebing, D. Application of refraction seismics in alpine permafrost studies: A review. *Earth-Science Reviews*. 2016. No. 155. Pp. 136–152. DOI: 10.1016/j.earscirev.2016.02.006.
33. Melnikov, V.P., Skvortsov, A.G., Malkova, G. V., Drozdov, D.S., Ponomareva, O.E., Sadurtdinov, M.R., Tsarev, A.M., Dubrovin, V.A. Seismic studies of frozen ground in Arctic areas. *Russian Geology and Geophysics*. 2010. 51(1). Pp. 136–142. DOI: 10.1016/j.rgg.2009.12.011.
34. Belash, T.A., Mitrofanova, M.N. Pile foundations for areas with a joint manifestation of permafrost and high seismic activity. *IOP Conference Series: Materials Science and Engineering*. Novosibirsk, Russia. 2018. No. 463. DOI: 10.1088/1757-899X/463/2/022076.
35. Abovsky, N.P., Abovskaya, S.N., Matyushenko, V.A., Sapkalov, V.I., Morozov, S.V., Pishutina, G.V., Temerova, A.S. Sbornaya prostranstvennaya zhelezobetonnyaya fundamentnaya platforma dlya stroitel'stva mnogoetazhnykh zdaniy v osobykh gruntovykh usloviyakh i sejsmichnosti [Precast three-dimension concrete foundation platform for the construction of multi-storey buildings in specific soil and earthquake conditions]. Utility patent Russia no. 2004107322/22, 2004. (rus)
36. Abovsky N.P., Sapkalov V.I., Sidelev V.A. Monolitnaya prostranstvennaya fundamentnaya platforma [Precast three-dimension foundation platform]. Utility patent Russia no. 2004135990/22, 2005. (rus)
37. Sidelev, V.A., Abovsky, N.P., Popovich, A.P., Sapkalov, V.I., Karasev, D.V. Prostranstvennaya zhelezobetonnyaya fundamentnaya platforma dlya maloetazhnykh zdaniy dlya stroitel'stva v osobykh gruntovykh usloviyakh i sejsmichnosti v sbornom i monolitnom variantah [Three-dimension concrete foundation platform for low-rise buildings to be built in specific soil conditions and seismic activity in precast and cast-in-place versions Utility patent Russia no. 2006113951/22, 2006. (rus)
38. Belash, T.A. Design peculiarities of foundation structures in permafrost and seismically active areas. *Proceedings of the international conference on geotechnics fundamentals and applications in construction: new materials, structures, technologies and calculations (GFAC 2019)*. Saint Petersburg, 2019. No. 2. Pp. 36–44. DOI: 10.1201/9780429058882-8.

### Contacts:

*Tatiana Belash, +7(921)9910115; belashta@mail.ru*

*Tatiana Ivanova, +7(812)4939363; IvanovaTV@vniig.ru*

© Belash, T.A., Ivanova, T.V., 2020



DOI: 10.18720/MCE.93.5

## Сейсмостойкость здания на оттаивающих вечномерзлых основаниях

Т.А. Белаш<sup>а\*</sup>, Т.В. Иванова<sup>б</sup><sup>а</sup> *Петербургский государственный университет путей сообщения Императора Александра I, Санкт-Петербург, Россия*<sup>б</sup> *АО «ВНИИГ им. Б.Е. Веденеева», Санкт-Петербург, Россия*\* E-mail: [belashta@mail.ru](mailto:belashta@mail.ru)

**Ключевые слова:** вечномерзлое оттаивающее основание, сейсмика, напряжения, деформации, осадка, фундамент-платформа

**Аннотация.** Особенностью конструктивного решения здания, является наличие в подземной части массивного фундамента, выполненного в виде пространственной жесткой железобетонной платформы. Здание возводится на протаивающих основаниях, оттаивание происходит в течение всего срока эксплуатации. Выполнен расчетно-теоретический анализ напряженно-деформируемого состояния строительных конструкций здания на действия статической и сейсмической нагрузок. Сейсмическая нагрузка определялась по нормативной, линейно-спектральной методике. Расчетное исследование выполнялось с учетом наличия под фундаментной конструкцией чаши оттаивания, величина которой изменялась от 6 до 27 м. Установлено, что в конструкциях здания в случае возникновения сейсмической нагрузки в них наблюдается рост напряжений и деформаций, по сравнению с действием статической нагрузки. Оценка полученных значений показывает, что они не превышают предельно допустимые показатели при принятых прочностных характеристиках материалов конструкций даже в условиях максимальной чаши оттаивания. Осадка фундамента равномерная. Принятое решение фундаментной конструкции обеспечивает сейсмостойкость здания в рассматриваемых условиях строительства.

### Литература

1. Вялов С.С., Шейнкман Д.Р., Докучаев В.В. Подземные льды и сильнольдистые грунты как основания сооружений. Ленинград: Стройиздат. Ленингр. отд-ние, 1976. 167 с.
2. Кудрявцев С.А., Сахаров И.И., Парамонов В.Н. Промерзание и оттаивание грунтов (практические примеры и конечноэлементные расчеты). СПб.: Геореконструкция, 2014. 248 с.
3. Allard M., Lemay M. Nunavik and Nunatsiavut: From science to policy. An Integrated Regional Impact Study (IRIS) of climate change and modernization. Quebec City, Canada: ArcticNet Inc., 2012. 303 p.
4. Ran Y., Li X., Cheng G. Climate warming over the past half century has led to thermal degradation of permafrost on the Qinghai-Tibet Plateau // *Cryosphere*. 2018. No. 2(12). Pp. 595–608. DOI: 10.5194/tc-12-595-2018.
5. Inzhutov I.S., Zhadanov V.I., Nazirov R.A., Servatinskii V. V., Semenov M.Y., Amelchugov S.P., Archipov I.N., Goncharov Y.M., Chaikin E.A. Research of permafrost soil thawing under the structural foundation platform // *IOP Conference Series: Materials Science and Engineering*. Novosibirsk, Russia. 2018. No. 1(456). DOI: 10.1088/1757-899X/456/1/012046.
6. Crowther G.S. Lateral pile analysis frozen soil strength criteria // *Journal of Cold Regions Engineering*. 2015. No. 29(2). Pp. 1–15. DOI: 10.1061/(ASCE)CR.1943-5495.0000078.
7. Rotta Loria A.F., Frigo B., Chiaia B. A non-linear constitutive model for describing the mechanical behaviour of frozen ground and permafrost // *Cold Regions Science and Technology*. 2017. 133. Pp. 63–69. DOI: 10.1016/j.coldregions.2016.10.010.
8. Wenping Fei, Yang Z.J., Sun T. Ground freezing impact on laterally loaded pile foundations considering strain rate effect // *Cold Regions Science and Technology*. 2019. 157. Pp. 53–63. DOI: 10.1016/j.coldregions.2018.09.006.
9. Wotherspoon L.M., Sritharan S., Pender M.J. Modelling the response of cyclically loaded bridge columns embedded in warm and seasonally frozen soils // *Engineering Structures*. 2010. No. 4(32). Pp. 933–943. DOI: 10.1016/j.engstruct.2009.12.019.
10. Yang Z.J., Still B., Ge X. Mechanical properties of seasonally frozen and permafrost soils at high strain rate // *Cold Regions Science and Technology*. 2015. 113. Pp. 12–19. DOI: 10.1016/j.coldregions.2015.02.008.
11. Солоненко В.П. Землетрясения и вулканы Станового надгорья // *Природа*. 1964. № 9. С. 102–110.
12. Чemezov Е.Н., Петров А.Ф., Блинова Т.Е. О сейсмоопасности территории Якутска // *Вестник Северо-восточного федерального университета им. М.К. Аммосова*. 2007. № 4(3). С. 33–38.
13. Солоненко В.П. Сейсмогеология и сейсмическое районирование трассы БАМ и зоны ее экономического влияния. Новосибирск: Наука, Сиб. отд-ние, 1979. 69 с.
14. Солоненко В.П. Сейсмогеологические условия зоны строительства БАМ. Иркутск: Иркутская областная типография №1, 1981. 48 с.

15. Гриб С.И. Свайные фундаменты на вечномёрзлых грунтах в сейсмических районах. Л.: Стройиздат, Ленингр. отд-е, 1983. 152 с.
16. Харитонов В.А. Сейсмостойкое строительство на вечномёрзлых грунтах. М.: Стройиздат, 1980. 77 с.
17. Yang Z.J., Dutta U. Numerical analysis of permafrost effects on the seismic site response // *Soil Dynamics and Earthquake Engineering*. 2011. No. 31(3). Pp. 282–290.
18. Yang Z.J., Li Q. Seasonally frozen soil effects on the dynamic behavior of highway bridges // *Sciences in Cold and Arid Regions*. 2012. No. 4(1). Pp. 13–20.
19. Chen G.S., Davis D., Hulseley J.L. Measurement of frozen soil-pile dynamic properties: a system identification approach // *Cold Regions Science and Technology*. 2012. 70. Pp. 98–106.
20. Wotherspoon L.M., Sritharan S., Pender M.J., Carr A.J. Investigation on the impact of seasonally frozen soil on seismic response of bridge columns // *Journal of Bridge Engineering*. 2010. No. 5(15). Pp. 473–481. DOI: 10.1061/(ASCE)BE.1943-5592.0000075.
21. Gu Q., Yang Z., Peng Y. Parameters affecting laterally loaded piles in frozen soils by an efficient sensitivity analysis method // *Cold Regions Science and Technology*. 2016. 121. Pp. 42–51. DOI: 10.1016/j.coldregions.2015.10.006.
22. Shelman A., Tantalla J., Sritharan S., Nikolaou S., Lacy H. Characterization of seasonally frozen soils for seismic design of foundations // *Journal of Geotechnical and Geoenvironmental Engineering*. 2014. No. 7(140). Pp. 1–10. DOI: 10.1061/(ASCE)GT.1943-5606.0001065.
23. James S.R., Knox H.A., Abbott R.E., Panning M.P., Screamon E.J. Insights Into Permafrost and Seasonal Active-Layer Dynamics From Ambient Seismic Noise Monitoring // *Journal of Geophysical Research: Earth Surface*. 2019. Pp. 1–19. DOI: 10.1029/2019JF005051.
24. Matson R., Wolf K., Yancey D. Influence of Permafrost on Seismic Imaging in Alaska // *SPE Arctic and Extreme Environments Conference and Exhibition (AEE 2013)*. Moscow, 2013. Pp. 76–103. DOI: 10.2118/166821-MS.
25. Skvortsov A.G., Sadurtdinov M.R., Tsarev A.M. Methods for permafrost studies seismic criteria for indentifying frozen soil // *Scientific journal earth's cryosphere*. 2014. No. XVIII(2). Pp. 75–80.
26. Skvortsov A.G., Tsarev A.M., Sadurtdinov M.R. Methods of permafrost studies seismic studies in frozen ground // *Scientific journal earth's cryosphere*. 2011. No. XV (4). Pp. 96–98.
27. Krautblatter M., Draebing D. Pseudo 3-D P wave refraction seismic monitoring of permafrost in steep unstable bedrock // *Journal of Geophysical Research: Earth Surface*. 2014. No. 2(119). Pp. 287–299. DOI: 10.1002/2012JF002638.
28. Che A.L., Wu Z.J., Wang P. Stability of pile foundations base on warming effects on the permafrost under earthquake motions // *Soils and Foundations*. 2014. No. 4(54). Pp. 639–647. DOI: 10.1016/j.sandf.2014.06.006.
29. Wu Z.J., Che A.L., Ghen T. Warming effects on permafrost under earthquake motions and seismic stability of pile foundation of dry bridge // *Materials Research Innovations*. 2011. No. Suppl. 1(15). Pp. 586–589. DOI: 10.1179/143307511X12858957676957.
30. Edwin S. Clarke. Permafrost Foundation: State of the Practice. American Society of Civil Engineers, 2007. 94 p.
31. Weber S., Fäh D., Beutel J., Failletaz J., Gruber S., Vieli A. Ambient seismic vibrations in steep bedrock permafrost used to infer variations of ice-fill in fractures // *Earth and Planetary Science Letters*. 2018. 501. Pp. 119–127. DOI: 10.1016/j.epsl.2018.08.042.
32. Draebing D. Application of refraction seismics in alpine permafrost studies: A review // *Earth-Science Reviews*. 2016. 155. Pp. 136–152. DOI: 10.1016/j.earscirev.2016.02.006.
33. Melnikov V.P., Skvortsov A.G., Malkova G. V., Drozdov D.S., Ponomareva O.E., Sadurtdinov M.R., Tsarev A.M., Dubrovin V.A. Seismic studies of frozen ground in Arctic areas // *Russian Geology and Geophysics*. 2010. No. 1(51). Pp. 136–142. DOI: 10.1016/j.rgg.2009.12.011.
34. Belash T.A., Mitrofanova M.N. Pile foundations for areas with a joint manifestation of permafrost and high seismic activity // *IOP Conference Series: Materials Science and Engineering*. Novosibirsk, Russia. 2018. No. 1 (463). DOI: 10.1088/1757-899X/463/2/022076.
35. Пат. на полезную модель 38789 РФ, МКП E02D 27/32, E02D 27/34, E02D 27/35, Сборная пространственная железобетонная фундаментная платформа для строительства многоэтажных зданий в особых грунтовых условиях и сейсмичности / Абовский Н.П., Абовская С.Н., Матюшенко В.А., Сапкалов В.И., Морозов С.В., Пишутин Г.В., Темерова А.С.; заявитель и патентообладатель Красноярская государственная архитектурно-строительная академия – № 2004107322/22; заявл. 11.03.2004; опубл. 10.07.2004.
36. Пат. на полезную модель 45410 РФ, МКП E02D 27/32, E02D 27/34, E02D 27/35, Монолитная пространственная фундаментная платформа / Абовский Н.П., Сапкалов В.И., Сиделев В.А.; заявитель и патентообладатель Красноярская государственная архитектурно-строительная академия – № 2004135990/22; заявл. 08.12.2004; опубл. 10.05.2005.
37. Пат. на полезную модель 45410 РФ, E02D 27/34, Пространственная железобетонная фундаментная платформа для малоэтажных зданий для строительства в особых грунтовых условиях и сейсмичности в сборном и монолитном вариантах / Сиделев В.А., Абовский Н.П., Попович А.П., Сапкалов В.И., Карасев Д.В.; заявитель и патентообладатель Красноярская государственная архитектурно-строительная академия – № 2006113951/22; заявл. 24.04.2006; опубл. 10.08.2006.
38. Belash T.A. Design peculiarities of foundation structures in permafrost and seismically active areas // *Proceedings of the international conference on geotechnics fundamentals and applications in construction: new materials, structures, technologies and calculations (GFAC 2019)*. Saint Petersburg, 2019. 2. Pp. 36–44. DOI: 10.1201/9780429058882-8.

### **Контактные данные:**

*Татьяна Александровна Белаш, +7(921)9910115; эл. почта: belashta@mail.ru*

*Татьяна Викторовна Иванова, +7(812)4939363; эл. почта: IvanovaTV@vniig.ru*



DOI: 10.18720/MCE.93.6

## Load-carrying capacity of timber-concrete composite panels

R. Vasiljevs<sup>a</sup>, D. Serdjuks<sup>a\*</sup>, K. Buka-Vaivade<sup>a</sup>, A. Podkoritovs<sup>a</sup>, N. Vatin<sup>b</sup>

<sup>a</sup> Riga Technical University, Riga, Latvia

<sup>b</sup> South Ural State University, Chelyabinsk, Russia

\* E-mail: [Dmitrijs.Serdjuks@rtu.lv](mailto:Dmitrijs.Serdjuks@rtu.lv)

**Keywords:** rigid timber to concrete joint, bending test, composite structures, structural analysis, timber, fasteners, fiber-reinforced materials, failure(mechanical)

**Abstract.** Timber-concrete composite panels, due to its benefits, are one of the most popular alternatives to common slabs of pure timber or concrete. In the analyse of load-carrying capacity for timber-concrete composite panels, subjected to flexure, the important component is connection system between concrete layer and timber, which affects the stress distribution and the deformations of the structure. Possibility to increase effectiveness of structural materials use and load-carrying capacity of the timber-concrete composite structural members, with the rigid timber to concrete joint, was evaluated in this research. Consequently, possibility to develop rigid timber to concrete joint by the using of the crushed granite pieces as the keys was checked by the experiment. Development of rigid timber to concrete joint enables to increase effectiveness of the structural materials use in timber-concrete composite panels in comparison with the compliant once. Behavior of the timber-concrete composite panels were analysed by the transformed section method, finite element method and by experiment for the purpose of this study. Four timber-concrete composite panels were statically loaded till the failure by the scheme of three-point bending. Variants of composite panels with the rigid and combined timber-concrete joints were investigated. The rigid timber-concrete joint was provided by the pieces of crushed granite, which were strengthened on the surface of the timber boards by epoxy glue. Dimensions of the crushed granite pieces changes within the limits from 16 to 25 mm. Moreover, the combined timber-concrete joint was provided by the screws and by the crushed granite pieces. The screws were placed under the angles equal to 45 degrees relatively to the direction of fibres of the timber layers in accordance with the literature recommendations. As a result, it was stated, that load-carrying capacity of timber-concrete composite panels is up to 1.9 times higher than the same of cross-laminated timber panels. The maximum load-carrying capacity in 43 kN was obtained for the variant of timber-concrete composite panel with the rigid timber to concrete joint at the same time.

### 1. Introduction

Timber-concrete composite structures become enough popular during the last years as an alternative to reinforced concrete structures. Timber-concrete composite structures are mainly subjected to flexure and combine advantages of pure timber and pure concrete structures [1–13]. It can be beams, panels or slabs of floors and roofs mainly. Timber-composite structures cause interest of researchers during the last years. Different variants of concrete to timber joints so as several variants of structural solutions, which enables to increase the load-carrying capacity of timber-concrete composite structure are the major directions of the investigations at the present moment [14–17].

Timber-concrete composite structures possess the following advantages in comparison with the pure timber structures:

- Increased stiffness;
- Increased load carrying capacity;
- Increased fire resistance;

Vasiljevs, R., Serdjuks, D., Buka-Vaivade, K., Podkoritovs, A., Vatin, N. Load-carrying capacity of timber-concrete composite panels. Magazine of Civil Engineering. 2020. 93(1). Pp. 60–70. DOI: 10.18720/MCE.93.6

Васильев Р., Сердюк Д.О., Бука-Вайваде К., Подкорытов А., Ватин Н.И. Несущая способность деревобетонных композитных панелей // Инженерно-строительный журнал. 2020. № 1(93). С. 60–70. DOI: 10.18720/MCE.93.6



- Improved sound insulation;
- Reduced sensitivity concerning vibrations;
- Simplified possibility to realize the horizontal bracing of the structure [13].

Load-carrying capacity of structural members grows also so as protective or finishing layers of concrete or another cement-base composite are involved into common work with the timber members and take up a part of the applied load. The fire resistance grows so as concrete layer plays a role of protective covering [10, 11]. Sound absorption of timber-concrete composite structures grows so as timber has approximately three-time higher sound absorption coefficient in comparison with the concrete.

Timber-concrete composite structures possess the following advantages in comparison with the pure concrete structures:

- Reduced dead load;
- Increase of re-growing materials and therefore less CO<sub>2</sub> emissions;
- Increase of prefabricated elements leading to a faster erection of the structure and therefore, to a lower influence of the surrounding conditions during the erection phase;
- Reduced volume of concrete, which leads to a faster building process and less volume to be transported on site;
- Reduced effort for the props/formwork since the load carrying capacity and the stiffness of the timber cross section is higher than the related properties of the prefabricated concrete elements [13].

Behaviour of timber-concrete composite structural members strongly dependent from the type of timber to concrete joint. Compliant and rigid once are two types of timber to concrete joints in timber-concrete composite structures existing now. Investigations of behaviour of timber to concrete joints indicates, that the timber-concrete composite structural members realized by the compliant and rigid timber to concrete joints, are characterized by the comparable load-carrying capacity [4, 5]. Studies shows, that the adhesive composite connection of the timber-concrete structural members is very effective, it provides higher bending stiffness [4] and leads to smaller deflections and a better composite behaviour [18] in comparison with mechanical fasteners. Theoretically timber-concrete composite structural members realized by the rigid timber to concrete joints, possess a potential for increase of it load-carrying capacity in comparison with the analogous members realized by the compliant joints due to the more rational structural materials use in the first case [5]. More rational materials use and probable increase of the load-carrying capacity in timber-concrete composite structural members is joined with the normal stresses distribution between the joined layers caused by the different compliances of the joints in the both mentioned above cases [5].

So, aim of the current study is analyse of load-carrying capacity for timber-concrete composite members subjected to flexure. Possibility to increase load-carrying capacity of the timber-concrete composite structural members subjected to flexure with the rigid timber to concrete joint in comparison with the pure timber member should be evaluated for the purpose. Behaviour of timber to concrete joints in timber-concrete composite members subjected to flexure should be investigated.

## 2. Methods

### 2.1. Realization of rigid timber to concrete joint

A hypothesis that using of the pieces of the crushed granite joined with the timber by the epoxy glue as the keys, enables to obtain a rigid timber-to concrete joint, was checked by experiment. The suggested type of timber-to concrete joint is close to grooved joint with the using of epoxy adhesives [4, 5]. However, suggested timber-to concrete joint enables to avoid deformations of the timber keys working in grooved joint in local compression in zones of contacts with the concrete. Additional rigidity of the suggested timber-to concrete joint should be provided as a result. The suggested timber-to concrete joint is characterized by the decreased workability and is simpler in realisation in comparison with the grooved joint.

Two groups of small-scale timber-concrete composite specimens were prepared and tested in laboratorian conditions. The first group include twelve small-scale timber-concrete composite specimens where the rigid timber-concrete joint was provided by the pieces of crushed granite, which were strengthened on the surface of the timber boards by epoxy glue Sica Dur 330. The epoxy glue Sica Dur 330 has modules of elasticity and shear strength equal to 12800 and 15 MPa, correspondingly. Dimensions of the crushed granite pieces changes within the limits from 2 to 25 mm. Three sub-groups by the four specimens in the each were prepared within the first group with the different dimensions of the pieces of crushed granite, which are shown in Figure 1.



**Figure 1. Granite pieces with different dimensions joined with the timber board by the epoxy glue: (a) 2-5 mm; (b) 5-8 mm; (c) 16-25 mm [19]**

The pieces of crushed granite were joined with the surface of the timber by the glue, as it is shown on Figure 1. The hardening of the glue was provided in course of two days and then the cement base finishing mass was casted into the moulds. So, the pieces of crushed granite work as a dowel, which are involved into the layer of the cement composite. Geometrical parameters of hybrid timber-concrete composite specimens with rigid timber to concrete joint are the same as for the specimens with the compliant joints, which were explained above [19]. Specimens have the length, width and thickness equal to 400, 95 and 43 mm, correspondingly. The small-scale hybrid timber-concrete composite specimens consists from the layers of cement base finishing mass Sacret BAM and timber boards of strength class C24 with thicknesses equal to 25 and 18 mm, correspondingly. Thickness of cement base finishing mass layer was equal to 25 mm so as it is a maximum size of the crushed granite pieces used for the specimens with the rigid timber to concrete joint. The cement base finishing mass Sacret BAM has modulus of elasticity and density equal to 30000 MPa and 20 kN/m<sup>3</sup>, correspondingly. Its strength class is C20. The timber-concrete composite specimens were tested after twenty-eight days from the specimen's formation.

Second group include twelve small scale hybrid timber-concrete specimens, which were prepared with compliant timber to concrete joint provided by the screws with length and diameter equal to 40 and 4 mm, correspondingly. Three variants of the screw's placement were considered. The screws were placed under the angles 90° and 45° relatively to longitudinal axis of the specimens, correspondingly, for the two first variants. Two screws were placed in each point under the angle 45° relatively to longitudinal axis of the specimens, for the third variant [19]. So, third variant of the screw's placement is characterized by the two times increased amount of screws in comparison with the two first variants. Three sub-groups by the four specimens in the each were prepared within the second group with the three variants of the screw's placement, which are shown in Figure 2.

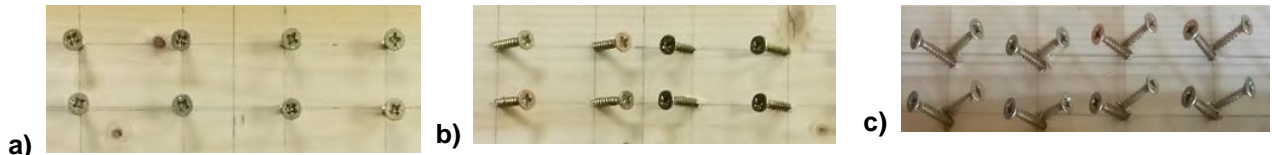


**Figure 2. Considered variants of screws placement: (a) screws were placed under the angle 90° relatively to longitudinal axis of the specimens; (b) screws were placed under the angles 45°; (c) two screws were placed in each point under the angle 45° [19]**

Intensity of the concentrated force applied in the middle of the specimen's span and maximum vertical displacements are two parameters, which were taken under the control during the experiment. The expected load-carrying capacities of the timber-concrete composite specimens were previously determined by the transformed section method [16]. The maximum vertical displacements were measured by two mechanical indicators placed in the middle of the span (Figure, 3(a)).

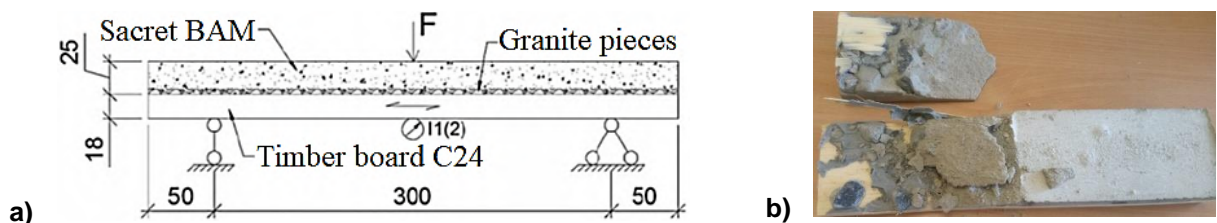


**Figure 3. Testing of timber-concrete composite specimens: (a) scheme of the specimens testing; (b) failure mode of the specimen with the rigid timber to concrete joint and granite pieces dimensions changing within the limits from 16 to 25 mm [19]**

Precision of the maximum vertical displacements measurements was equal to 0.01.mm. All the specimens were loaded until the failure to determine their load-carrying capacities. The vertical load was applied with the steps equal to 2 kN with the speed equal to 2 mm/min [19].

## 2.2. Approach for the load-carrying capacity analyse for timber-concrete composite panels

### 2.2.1 Experimental analyze of load-carrying capacity for timber-concrete composite panels

Four timber-concrete composite panels with the different timber to concrete joints were analysed analytically and by experiment. Two panels were prepared with the combined timber to concrete joint, which is provided by the granite pieces with dimensions changing within the limits from 16 to 25 mm and by the couples of screws, which are placed under the angles in 45° relatively the longitudinal axes of the panels. The diameters and lengths of the screws were equal to 4 and 40 mm, correspondingly (Figure 4(a)). Adding of the screws enables to increase reliability of the panels and provide a common work of the layers in case of defects of the glued joint [5].

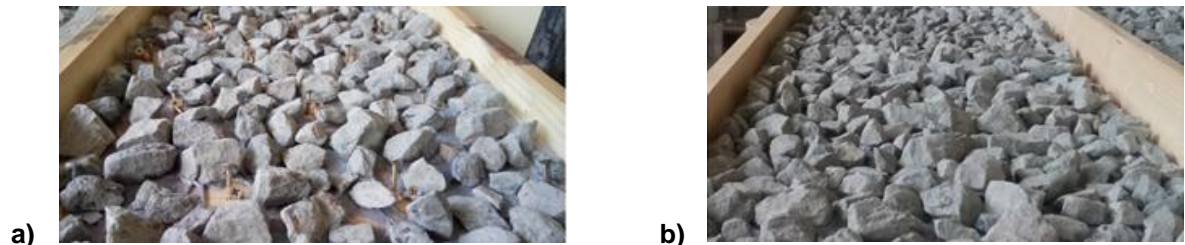


**Figure 4. Placement of the granite pieces and screws, providing timber to concrete joint in the timber-concrete composite panels: (a) granite pieces and screws; (b) granite pieces only [19]**

The screws were placed in accordance with the requirements of EN 1995-1-1 [20]. Timber to concrete joint in another two panels was provided by the granite pieces with dimensions changing within the limits from 16 to 25 mm only (Fig.3. (b)). The granite pieces were joined to the surface of the timber by the epoxy glue Sica Dur 330. Timber-concrete composite panels consist from the cross-laminated timber (CLT) components, which are strengthened by the carbon fiber reinforced plastic tape in the tensioned zone and with the layer of finishing mass Sacret BAM with thickness in 30 mm in compressed zone. Shrinkage of the finishing mass was not taken into account so as it was equal for all the specimens. The cross-laminated timber base consists from the three layers of strength class C24 timber boards with thickness in 20 mm. Fibers of outer layers are oriented parallel to the longitudinal axis of the panels. The panels have length, width and thickness equal to 2000, 350 and 60 mm, correspondingly (Fig.5. (b)). The panels were produced by the Sconto enterprise, Ltd, Jelgava, Latvia.

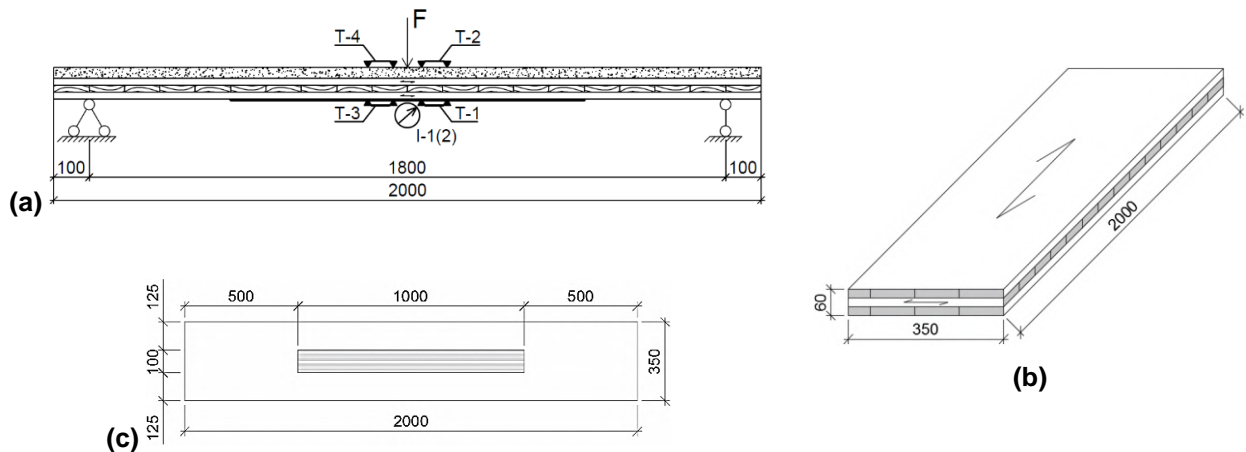


**Figure 5. The design scheme and measuring devices placement for the timber-concrete composite panels (a); cross-laminated timber component of the timber-concrete composite panels (b); placement of the carbon fiber reinforced tape on it surface in the tensioned zone (c) [19]**

The carbon fiber reinforced tape Mapei Carboplate E250 has the modulus of elasticity, tensile strength and thickness equal to 250000 MPa, 2500 MPa and 1.4 mm, correspondingly [21]. The carbon fiber reinforced tape was strengthened to the surface of the cross-laminated timber panel by the epoxy glue Sica Dur 330 (Figure 4(c)). The design scheme and apparatus placement for the timber-concrete composite panels is shown on the Figure 4 (a). Two couples of strain measuring devices and one couple of deflectometers were used during the static loading of the timber-concrete composite panels. Strain measuring devices T-2 and T-4 were placed on the surface of the finishing mass Sacret BAM in compressed zone. Strain measuring devices T-1 and T-3 were placed in tensioned zone on the surface of the cross-laminated timber. A couple of the deflectometers I-1 and I-2 were placed in the middle of the span. Precision of the maximum vertical displacements and absolute deformations measurements was equal to 0.01.mm and 0.001 mm, correspondingly. All the specimens were loaded until the failure to determine their load-carrying capacities.

The process of loading of each panel takes up until 20 minutes and the loading can be classified as the short-term once. The vertical load was applied with the steps equal to 2 kN with the speed equal to 2 mm/min [19].

### 2.2.2 Analytical analyze of load-carrying capacity for timber-concrete composite panels

Load-carrying capacity of timber-concrete composite panels was carried out analytically by the transformed section method and by the FEM [22], which was realized by the software RFEM 5.13. The plate finite elements were used to develop the FEM model of the timber-concrete composite panels.

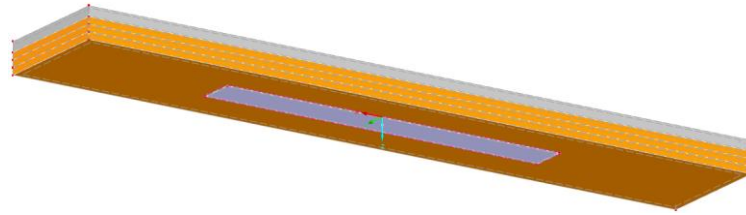


**Figure 6. The FEM model of the timber-concrete composite panel developed by the software RFEM 5.13 [19]**

The model was divided into the finite elements by the rectangular mesh (Figure 6). Timber-concrete panels analyze by the software RFEM 5.13 include following stages: development of the model, applying of loads, solution of the task and analyze of obtained results. Analyzed timber-concrete panels were considered as the structural members made of orthotropic structural material and the dependence between the internal forces and deformations has the following shape [23]:

$$\begin{Bmatrix} m_x \\ m_y \\ m_{xy} \\ v_x \\ v_y \\ n_x \\ n_y \\ n_{xy} \end{Bmatrix} = \begin{bmatrix} D_{11} & D_{12} & D_{13} & 0 & 0 & D_{16} & D_{17} & D_{18} \\ D_{21} & D_{22} & D_{23} & 0 & 0 & D_{26} & D_{27} & D_{28} \\ D_{31} & D_{32} & D_{33} & 0 & 0 & D_{36} & D_{37} & D_{38} \\ 0 & 0 & 0 & D_{44} & D_{45} & 0 & 0 & 0 \\ 0 & 0 & 0 & D_{54} & D_{55} & 0 & 0 & 0 \\ D_{61} & D_{62} & D_{63} & 0 & 0 & D_{66} & D_{67} & D_{68} \\ D_{71} & D_{72} & D_{73} & 0 & 0 & D_{76} & D_{77} & D_{78} \\ D_{81} & D_{82} & D_{83} & 0 & 0 & D_{86} & D_{87} & D_{88} \end{bmatrix} \begin{Bmatrix} k_x \\ k_y \\ k_{xy} \\ \gamma_{xz} \\ \gamma_{yz} \\ \varepsilon_x \\ \varepsilon_y \\ \gamma_{xy} \end{Bmatrix} \quad (1)$$

where:  $m_x, m_y$  are bending moment that creates stresses in direction of the local axis x and y, correspondingly;  $m_{xy}$  is torsional moment;  $v_x, v_y$  are shear force acting relatively axis x and y, correspondingly;  $n_x, n_y$  are axial force in direction of the local axis x and y, correspondingly;  $n_{xy}$  is shear flow; stiffness matrix elements:  $D_{11} - D_{33}$  are bending and torsion,  $D_{16} - D_{38}$ ,  $D_{61} - D_{83}$  are eccentric effects,  $D_{44} - D_{55}$  are shear,  $D_{66} - D_{88}$  are membrane;  $k_x, k_y$  are bending about the local member axis x and y, correspondingly;  $k_{xy}$  is torsional deformation in plane  $xy$ ;  $\varepsilon_x, \varepsilon_y$  are strain in direction of the member axis x and y, correspondingly;  $\gamma_{xz}, \gamma_{yz}, \gamma_{xy}$  are shear deformation in plane  $xz, yz$  and  $xy$ , correspondingly.

Transformed section method was chosen for analytical analyze of load-carrying capacity for timber-concrete composite panels so as it is characterized by the simplified design procedure and comparable precision in comparison with the k-method, gamma method and shear analogy method. Transformed cross-section method is joined with the replacement of the real cross-section of element by the equivalent transformed cross-section [24–26]. Transformation of cross – section is based on the ratios of moduli of elasticity of the layers to the modulus of elasticity of the outer layers of CLT panels, which were oriented in the longitudinal direction. The widths of the internal layer of the CLT panels, layer of finishing mass Sacret BAM and carbon fiber reinforced tape Mapei Carboplate E250 must be multiplied by the relations of modulus of elasticities. Obtained transformed cross-section then is considered as glued homogenous cross-section. Checks of ultimate limit state (ULS) and serviceability limit state (SLS) must be conducted based on the recommendations of [20].

## 3. Results and Discussions

### 3.1. Behaviour of rigid timber to concrete joint

Two groups of small-scale timber-concrete composite specimens, explained in detail before, were tested by the experiment. The dependences of the maximum vertical displacements of the hybrid timber-concrete specimens subjected to flexure on the intensity of the vertical applied load were obtained together with the load-carrying capacities for all the specimens of six sub-groups. The maximum vertical displacements as a function from the vertical load for six sub-groups of tested specimens are shown on Figure 7.

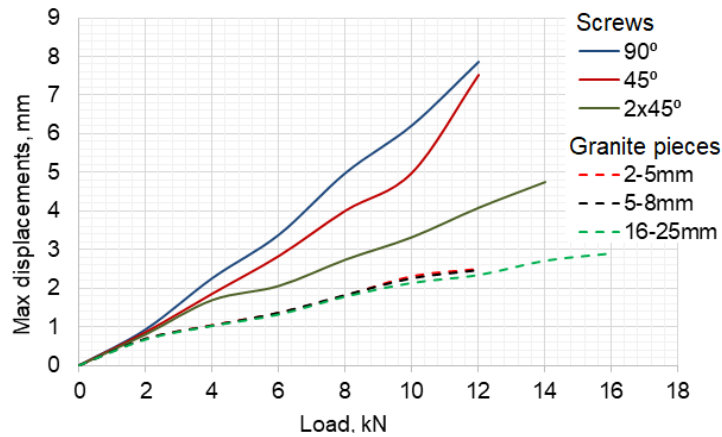


**Figure 7. The maximum vertical displacements as a function from the vertical load for six sub-groups of tested small-scale timber-concrete composite specimens [19].**

The maximum mean load-carrying capacities for small-scale timber-composite specimens of the first group with the dimensions of crushed granite pieces changing within the limits from 2 to 5 mm, from 5 to 8 mm and from 16 to 25 mm are equal to 12.1, 12.9 and 16.2 kN. The maximum mean load-carrying capacities for small-scale timber-composite specimens of the second group where the screws were placed under the angle  $90^\circ$  and  $45^\circ$  relatively to longitudinal axis of the specimens so as for the sub-group, where two screws were placed in each point under the angle  $45^\circ$ , are equal to 10.8, 11.00 and 13.2 kN. The values of load-carrying capacities of the first and second groups of small-scale specimens, obtained by the transformed section method, were equal to 10 and 12 kN, correspondingly [19].

The values of maximum load-carrying capacities of twelve tested small-scale timber-concrete composite specimens of the first group are 25.92 % bigger than the values, obtained by the transformed section method and 18.52 % than the maximum load-carrying capacities of twelve tested specimens of the second group. It enables to make a conclusion, that the using of the pieces of the crushed granite joined with the timber by the epoxy glue as the keys, enables to obtain a rigid timber-to concrete joint.

The obtained results enable to conclude, that using of the rigid timber to concrete joint instead of compliant ones, enables to increase the load-carrying capacity of the small-scale timber-concrete composite specimens subjected to flexure from 16.55 to 50 %. Increase of the crushed granite pieces from 2–5 to 16–25 mm enables to increase load-carrying capacity of considered specimens by 33.88 % [19].

### 3.2. Behaviour of timber-concrete composite panels

The stresses, acting in the outer top and bottom fibers of the four timber-concrete composite panels, explained before, its maximum vertical displacements and load-carrying capacities were evaluated by the experiment and analytically by FEM. Maximum vertical displacements of the timber-concrete composite panels were evaluated by the transformed section method also. Four timber-concrete composite panels were divided in to two sub-groups. The first sub-group include the specimens, which were created with the combined timber to concrete joint, which is provided by the granite pieces and by the couples of screws, as it was explained before. These specimens will be mentioned next as first and second once. The second sub-group include the specimens, which were created with the timber to concrete joint, which is provided by the granite pieces only. These specimens will be mentioned next as third and fourth once. The failure mode for the specimens from the first and second sub-groups is shown on Figure 8.



**Figure 8. The failure mode for the specimens from the first and second sub-groups: (a) second specimen; (b) fourth specimen [19]**

The failure of all four specimens starts from the timber in the contact zone with the carbon fiber reinforced tape in the tensioned zone of the specimen. Then occur breaking of cement composite in compressed zone and cross-laminated timber base. The maximum load-carrying capacities of all four specimens are equal to 33, 38, 43 and 39 kN, correspondingly. It was shown, that adding of the screws did not effects on the load-carrying capacities of the timber-concrete composite panels. The load-carrying capacity decrease for the first specimen can be explained by the defects – knots in the contact zone of cross-laminated timber base with the carbon fiber reinforced tape in the tensioned zone of the specimen. But existence of the defects did not effects on the failure mode of the first specimen (Figure 9).

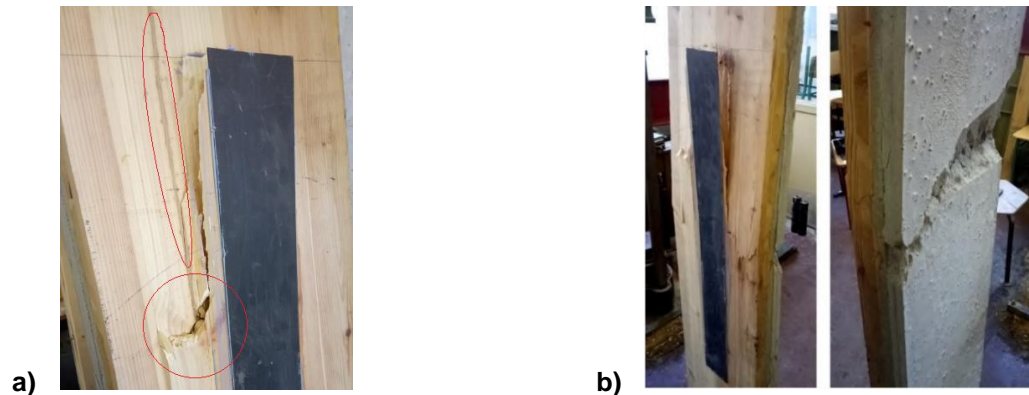


**Figure 9. Defects and failure mode of the first specimen: (a) knots in the contact zone of cross-laminated timber base with the carbon fiber reinforced tape in the tensioned zone of the first specimen; (b) failure mode of the first specimen [19]**

The dependences of the maximum vertical displacements of the specimens on the intensity of applied vertical load were obtained by the transformed section method, by the FEM, which was realized by the software RFEM 5.13. and by the experiment for the both sub-groups of the specimens. The dependences for the second and fourth specimens are shown on the Figure 10. The dependences obtained for the first and third specimens, have the similar shapes.

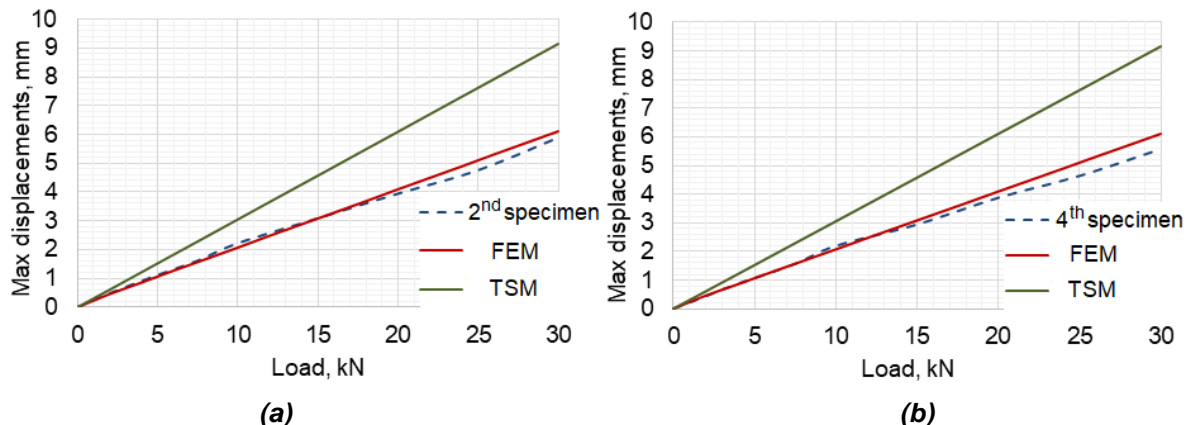


**Figure 10. The dependences of the maximum vertical displacements of the specimens on the intensity of applied vertical load: (a) second specimen; (b) fourth specimen; FEM – dependence, which is obtained by the finite element method; TSM – dependence, which is obtained by the transformed section method [19]**

The obtained dependences are linear for the both sub-groups of the specimens and existence of the screws as the members providing additional bonds between the cross-laminated timber base and the layer of cement composite did not effect on the behaviours of the specimens. So, the maximum experimental vertical displacements of the first and second sub-groups of the specimens obtained at the vertical load equal to 30 kN are equal to 6.71, 5.87, 5.37 and 5.56 mm, correspondingly. Maximum vertical displacements, observed for the first specimen, can be explained by the defects of it cross-laminated timber base. The maximum differences obtained between the results, got by the experiment, FEM and TSM were equal to 11.96 and 41.31%, correspondingly [19].

The dependences of the maximum normal stresses acting in the compressed and tensioned zones of the specimens on the intensity of applied vertical load were obtained by the by the FEM and by the experiment for the both sub-groups of the specimens. The dependence for the second and fourth specimens are shown on the Figure 11. The dependences, obtained for the first and third specimens, have the similar shapes.

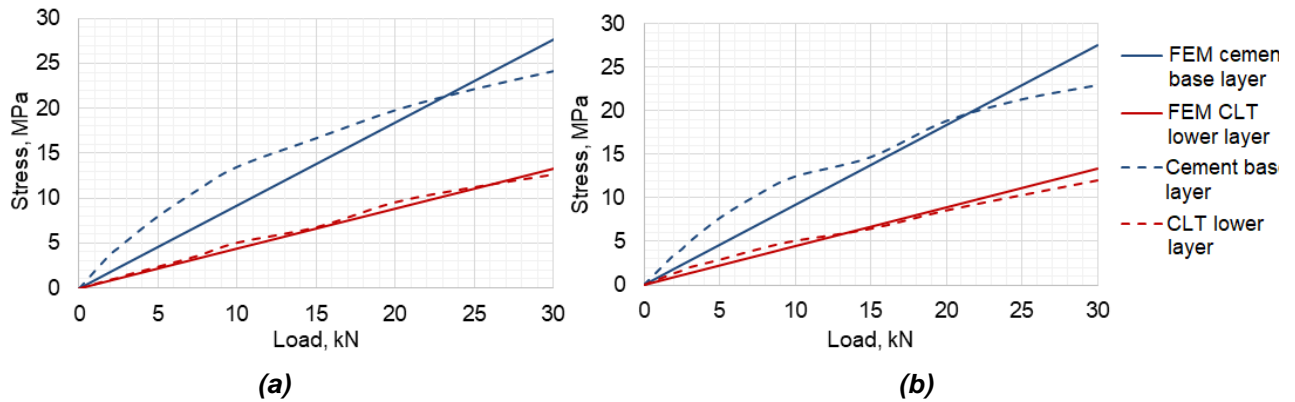


**Figure 11. The dependences of the maximum normal stresses acting in the compressed and tensioned zones of the specimens on the intensity of applied vertical load: (a) second specimen; (b) fourth specimen, other designations as on Figure 10 [19]**

The dependences obtained by the experiment are characterized by the shapes, which is closed to linear. The values of the maximum normal stresses, obtained by the experiment in the cement base finishing mass layer at the value of the vertical load in 30 kN, were equal to 27.70, 24.13, 21.05 and 22.90 MPa for the first, second, third and fourth specimens, correspondingly. The values of maximum normal stresses, obtained by the experiment in the cross-laminated timber base, were equal to 13.29, 12.60, 11.43 and 12.04 MPa for the first, second, third and fourth specimens, correspondingly. The difference between the maximum normal stresses obtained by the experiment and by FEM, which was realized by the software RFEM 5.13., exceed 9.54 % for the cement base finishing mass layer, placed in the compressed zone and 17.06 % for the cross-laminated timber base, placed in tensioned zone [19].

It can be concluded, that involving of the layer of cement-based finishing mass into the common work with the cross-laminated timber panel by the development of the rigid timber to concrete joint enables to obtain timber-concrete composite panel with increased load-carrying capacity. Load-carrying capacity of the cross-laminated timber panel, considered as the base of the timber-concrete composite panel, which was investigated in the current work, is equal to 22.60 kN in case, if the panel is loaded by the scheme, which is shown on the Figure 5 [24]. So, involving of the layer of cement-based finishing mass into the common work with the cross-laminated timber panel by the development of the rigid timber to concrete joint enables to increase the load-carrying capacity of the panel from 1.46 till 1.90 times.

#### 4. Conclusions

Load-bearing capacity of timber-concrete composite panels subjected to flexure was study. The improvement of load-bearing capacity from the common work of the layer of cement-based finishing mass and CLT panel which is provided by the development of the rigid timber to concrete joint was analysed analytically and by experiment. Possibility to develop rigid timber to concrete joint by the using of the crushed granite pieces as the keys was checked by small-scale timber-concrete composite specimens subjected to flexure.

The results showed that:

1. The common work of timber-concrete panels provided by rigid joints enables to obtain composite panel with increased up to 1.9 times load-bearing capacity in comparison with CLT panel;
2. The using of the rigid timber to concrete joint instead of compliant ones enables to increase the load-bearing capacity of the small-scale from 16.55 to 50 %;
3. The increase of the crushed granite pieces from 2–5 to 16–25 mm enables to increase load-carrying capacity of considered specimens by 33.88%.

#### 5. Acknowledgement

The authors staff reflect gratitude to Sconto enterprise, Ltd, Jelgava, Latvia which provide CLT specimens for laboratorian experiments.

#### References

1. Goremikins, V., Serdjuks, D., Buka-Vaivade, K., Pakrastins, L., Vatin, N.I. Prediction of behaviour of prestressed suspension bridge with timber deck panels. *The Baltic Journal of Road and Bridge Engineering*. 2017. 12(4). Pp. 234–240. doi: 10.3846/bjrbe.2017.29
2. Timber concrete composites. KLH Massivholz GmbH, 2018. 12 p.
3. Al Ali, M., Bajzecerova, V., Kvocak, V. Design methods of timber-concrete composite ceiling structure. *Magazine of Civil Engineering*. 2017. 73(5). Pp. 88–95. doi: 10.18720/MCE.73.8.
4. Kanocz, J., Bajzecerova, V. Timber – concrete composite elements with various composite connections. Part 3: adhesive connection *Wood Research*. 2015. 60. Pp. 939–952.

5. Kanocz, J., Bajzecerova, V., Steller, S. Timber – concrete composite elements with various composite connections. Part 1: screwed connection Wood Research. 2013. 58. Pp. 555–570.
6. Miotto, J.L., Dias, A.A. Structural efficiency of full-scale timber–concrete composite beams strengthened with fiberglass reinforced polymer. Composite Structures. 2015. 128. Pp. 145–154. doi: 10.1016/j.compstruct.2015.03.054
7. Brunner, M., Schnüriger, M. Adhesive connection for timber-concrete-composite. 9th World Conference on Timber Engineering, WCTE 2006, Portland, USA, 2006. Pp. 171.
8. Brunner, M., Romer, M., Schnüriger, M. Timber-concrete-composite with an adhesive connector (wet on wet process). Materials and Structures. 2007. 40. Pp. 119–126. doi: 10.1617/s11527-006-9154-4
9. Crews, K., Gerber, C. Development of design procedures for timber concrete composite floors in Australia and New Zealand. CIB-W18/43-7-5, Nelson, New Zealand, Nelson, August 22-26, 2010. Pp. 1–4.
10. Ceccotti, A. Composite concrete-timber structures. Progress in structural engineering and materials. 2002. 4(3). Pp. 264–275. doi: 10.1002/pse.126
11. Gravit, M.V., Serdjus, D., Bardin, A.V., Prusakov, V., Buka-Vaivade, K. Fire Design Methods for Structures with Timber Framework. Magazine of Civil Engineering. 2019. 85(1). Pp. 92–106. doi: 10.18720/MCE.85.8
12. Gravit, M.V., Nedryshkin, O.V., Ogidan, O.T. Transformable fire barriers in buildings and structures. Magazine of Civil Engineering. 2018. 77(1). Pp. 38–46. doi: 10.18720/MCE.77.4
13. Dias, A., Schänzlin, J., Dietsch, P. (eds.) Design of timber-concrete composite structures: Shaker Verlag GmbH. Aachen, 2018. 228 p.
14. Holschemacher, K., Selle, R., Schmidt, J., Kieslich, H. Holz-Beton-Verbund. Betonkalender 2013. Ernst & Sohn. Berlin, 2013. Pp. 241–287.
15. Postulka, J. Holz-Beton-Verbunddecken 36 Jahre Erfahrung. Bautechnik. 1997. 74. Pp. 478–480.
16. Rautenstrauch, K. Entwicklung der Holz-Beton-Verbundbauweise. König, G., Holschemacher, K., Dehn, F. (eds): Innovationen im Bauwesen, Holz-Beton-Verbund. Bauwerk Verlag. Berlin, 2004. Pp. 1–22.
17. Yeoh, D., Fragiaco, M., De Franceschi, M., Boon, K. H. State of the Art on Timber-Concrete Composite Structures: Literature Review. Journal of Structural Engineering. 2011. Pp. 1085–1095.
18. Negrao, J.H., Oliveira, F.M., Oliveira, C.L. Investigation on Timber-Concrete Glued Composites. Conference: 9th World Conference on Timber Engineering (9 WCTE), Portland, U.S.A, 2006.
19. Vasiljev, R. Load-carrying Capacity Analyse for Hybrid Composite Member. M.S. thesis. Riga Technical university. Riga, 2018. 114 p.
20. Eurocode 5: Design of timber structures – Part 1-1: General-Common rules and rules for buildings.
21. Carboplate. Mapei. 2008. 4 p.
22. Auclair, S., Sorelli, L., Salenikov, A. Simplified nonlinear model for timber-concrete composite beams. International Journal of Mechanical Sciences. 2016. 117. Pp. 30–42. doi: 10.1016/j.ijmecsci.2016.07.019
23. RFEM 5 user manual. Dlubal Software. 2018. 647 p.
24. Buka-Vaivade K., Serdjus D., Goremikins V., Vilguts A., Pakrastins L. Experimental Verification of Design Procedure for Elements from Cross-laminated Timber. Proceedings of 12 th International Conference Modern Building Materials Structures and Techniques, MBMST 2016, Vilnius, Lithuania, May 26–27, 2016. 172. Pp. 1212–1219. doi: 10.1016/j.proeng.2017.02.142
25. Buka-Vaivade, K., Serdjus, D., Goremikins, V., Pakrastins, L., Vatin, N.I. Suspension structure with cross-laminated timber deck panels. Magazine of Civil Engineering. 2018. 83(7). Pp. 126–135. doi: 10.18720/MCE.83.12.
26. Murnieks, J., Serdjus, D., Buka-Vaivade, K. Load-Carrying Capacity Increase of Arch-Type Timber Roof. Proceedings of the 12th International Scientific and Practical Conference: Environment. Technology. Resources. Rezekne, Latvia, 2019. 1. Pp. 175–179. doi: 10.17770/etr2019vol1.4056

### **Contacts:**

*Romans Vasiljevs, +37167089145; rominz@bk.ru*

*Dmitrijs Serdjus, +37126353082; Dmitrijs.Serdjus@rtu.lv*

*Karina Buka-Vaivade, +37126353082; karina.buka.vaivade@gmail.com*

*Andrejs Podkoritovs, +37167089145; andrew-next@inbox.lv*

*Nikolai Vatin, +79219643762; vatin@mail.ru*

© Vasiljevs, R., Serdjus, D., Buka-Vaivade, K., Podkoritovs, A., Vatin, N., 2020



DOI: 10.18720/MCE.93.6

## Несущая способность деревобетонных композитных панелей

**Р. Васильев<sup>а</sup>, Д.О. Сердюк<sup>а\*</sup>, К. Бука-Вайваде<sup>а</sup>, А. Подкорытов<sup>а</sup>, Н.И. Ватин<sup>б</sup>**

<sup>а</sup> Рижский технический университет, Рига, Латвия

<sup>б</sup> Южно-Уральский государственный университет, г. Челябинск, Россия

\* E-mail: [Dmitrijs.Serdjuks@rtu.lv](mailto:Dmitrijs.Serdjuks@rtu.lv)

**Ключевые слова:** жесткое соединение бетона с древесиной, испытание на изгиб, композитные конструкции, расчет конструкции, элемент крепления, материалы, армированные волокном, разрушение (механическое)

**Аннотация.** Деревобетонные композитные панели, благодаря своим преимуществам, являются одной из самых популярных альтернатив обычным плитам из чистого дерева или бетона. При анализе несущей способности деревобетонных композитных панелей, подверженных изгибу, важным компонентом является система соединения между слоем бетона и древесиной, которая влияет на распределение напряжений и деформации конструкции. Данное исследование включает в себя проверку возможности увеличения эффективности использования бетона и древесины, а также увеличения несущей способности деревобетонных композитных панелей путем создания жесткого соединения древесины с бетоном. Экспериментально проверена возможность образования жесткого соединения древесины с бетоном при использовании гранитного щебня в качестве шпонок. Работа под нагрузкой деревобетонных композитных панелей исследована при помощи метода приведенных сечений и метода конечных элементов, а также экспериментально. Четыре деревобетонные композитные панели были загружены статической нагрузкой до разрушения по схеме трехточечного изгиба. Варианты панелей с жестким и комбинированным соединениями древесины с бетоном были рассмотрены. Жесткое соединение бетона с древесиной было обеспечено при использовании гранитного щебня, приклеенного на поверхности поперечно ламинированных деревянных панелей при помощи эпоксидного клея. Размер частиц гранитного щебня менялся в пределах от 16 до 25 мм. Комбинированное соединение бетона с древесиной было обеспечено при использовании шурупов и гранитного щебня. Шурупы были размещены под углом 45 градусов относительно продольных осей поперечно ламинированных деревянных панелей, направление которых совпадает с направлениями волокон наружных слоев. Показано, что несущая способность деревобетонных композитных панелей в 1,9 раз превышает таковую для поперечно ламинированных деревянных панелей, использованных в качестве основы. Наибольшая несущая способность в 43 кН была получена для деревобетонной композитной панели с жестким соединением древесины с бетоном.

### Литература

- Goremikins V., Serdjus D., Buka-Vaivade K., Pakrastins L., Vatin N.I. Prediction of behaviour of prestressed suspension bridge with timber deck panels. *The Baltic Journal of Road and Bridge Engineering*. 2017. 12(4). Pp. 234–240. doi: 10.3846/bjrbe.2017.29
- Timber concrete composites. KLH Massivholz GmbH, 2018. 12 p.
- Ал Али М., Байзечерова В., Квочак В. Методы проектирования деревожелезобетонной композитной потолочной конструкции // *Инженерно-строительный журнал*. 2017. № 5(73). С. 88–95. doi: 10.18720/MCE.73.8
- Kanocz J., Bajzecerova V. Timber – concrete composite elements with various composite connections. Part 3: adhesive connection *Wood Research*. 2015. 60. Pp. 939–952.
- Kanocz J., Bajzecerova V., Steller S. Timber – concrete composite elements with various composite connections. Part 1: screwed connection *Wood Research*. 2013. 58. Pp. 555–570.
- Miotto J.L., Dias A.A. Structural efficiency of full-scale timber–concrete composite beams strengthened with fiberglass reinforced polymer. *Composite Structures*. 2015. 128. Pp. 145–154. doi: 10.1016/j.compstruct.2015.03.054
- Brunner M., Schnüriger M. Adhesive connection for timber-concrete-composite. 9th World Conference on Timber Engineering, WCTE 2006, Portland, USA, 2006. Pp. 171.
- Brunner M., Romer M., Schnüriger M. Timber-concrete-composite with an adhesive connector (wet on wet process). *Materials and Structures*. 2007. 40. Pp. 119–126. doi: 10.1617/s11527-006-9154-4
- Crews K., Gerber C. Development of design procedures for timber concrete composite floors in Australia and New Zealand. CIB-W18/43-7-5, Nelson, New Zealand, Nelson, August 22-26, 2010. Pp. 1–4.
- Seccotti A. Composite concrete-timber structures. *Progress in structural engineering and materials*. 2002. 4(3). Pp. 264–275. doi: 10.1002/pse.126

11. Гравит М.В., Сердюк Д.О., Бардин А.В., Прусаков В.А., Бука-Вайваде К. Методы определения огнестойкости конструкций деревянного каркаса // Инженерно-строительный журнал. 2019. № 1(85). С. 92–106. DOI: 10.18720/MCE.85.8
12. Гравит М.В., Недрышкин О.В., Огидан О.Т. Трансформируемые противопожарные преграды в сооружениях и строениях // Инженерно-строительный журнал. 2018. № 1(77). С. 38–46. doi: 10.18720/MCE.77.4
13. Dias A., Schänzlin J., Dietsch P. (eds.) Design of timber-concrete composite structures: Shaker Verlag GmbH. Aachen, 2018. 228 p.
14. Holschemacher K., Selle R., Schmidt J., Kieslich H. Holz-Beton-Verbund. Betonkalender 2013. Ernst & Sohn. Berlin, 2013. Pp. 241–287.
15. Postulka J. Holz-Beton-Verbunddecken 36 Jahre Erfahrung. Bautechnik. 1997. 74. Pp. 478–480.
16. Rautenstrauch K. Entwicklung der Holz-Beton-Verbundbauweise. König, G., Holschemacher, K., Dehn, F. (eds): Innovationen im Bauwesen, Holz-Beton-Verbund. Bauwerk Verlag. Berlin, 2004. Pp. 1–22.
17. Yeoh D., Fragiaco M., De Franceschi M., Boon K.H. State of the Art on Timber-Concrete Composite Structures: Literature Review. Journal of Structural Engineering. 2011. Pp. 1085–1095.
18. Negrao J.H., Oliveira F.M., Oliveira C.L. Investigation on Timber-Concrete Glued Composites. Conference: 9th World Conference on Timber Engineering (9 WCTE), Portland, U.S.A, 2006.
19. Vasiljev R. Load-carrying Capacity Analyse for Hybrid Composite Member. M.S. thesis. Riga Technical university. Riga, 2018. 114 p.
20. Eurocode 5: Design of timber structures – Part 1-1: General-Common rules and rules for buildings.
21. Carboplate. Mapei. 2008. 4 p.
22. Auclair S., Sorelli L., Salenikov A. Simplified nonlinear model for timber-concrete composite beams. International Journal of Mechanical Sciences. 2016. 117. Pp. 30–42. doi: 10.1016/j.ijmecsci.2016.07.019
23. RFEM 5 user manual. Dlubal Software. 2018. 647 p.
24. Buka-Vaivade K., Serdjus D., Goremikins V., Vilguts A., Pakrastins L. Experimental Verification of Design Procedure for Elements from Cross-laminated Timber. Proceedings of 12 th International Conference Modern Building Materials Structures and Techniques, MBMST 2016, Vilnius, Lithuania, May 26-27, 2016. 172. Pp. 1212–1219. doi: 10.1016/j.proeng.2017.02.142
25. Бука-Вайваде К., Сердюк Д.О., Горемыкин В.В., Пакрастиньш Л., Ватин Н.И. Подвесная конструкция с настилом из поперечно ламинированных деревянных панелей // Инженерно-строительный журнал. 2018. № 7(83). С. 126–135. doi: 10.18720/MCE.83.12
26. Murnieks J., Serdjus D., Buka-Vaivade K. Load-Carrying Capacity Increase of Arch-Type Timber Roof. Proceedings of the 12th International Scientific and Practical Conference: Environment. Technology. Resources. Rezekne, Latvia, 2019. 1. Pp. 175–179. doi: 10.17770/etr2019vol1.4056

**Контактные данные:**

*Роман Васильев, +37167089145; rominz@bk.ru*

*Дмитрий Олегович Сердюк, +37126353082; Dmitrijs.Serdjuks@rtu.lv*

*Карина Бука-Вайваде, +37126353082; karina.buka.vaivade@gmail.com*

*Андрей Подкорытов, +37167089145; andrew-next@inbox.lv*

*Николай Иванович Ватин, +79219643762; vatin@mail.ru*

© Васильев Р., Сердюк Д.О., Бука-Вайваде К., Подкорытов А., Ватин Н.И. 2020



DOI: 10.18720/MCE.93.7

## Influence of silica fume on the pervious concrete with different levels of recycled aggregates

V.V. Galishnikova<sup>a</sup>, Sh. Abdo<sup>a\*</sup>, A.M. Fawzy<sup>b</sup>

<sup>a</sup> Peoples' Friendship University of Russia (RUDN University), Moscow, Russia

<sup>b</sup> Alexandria University, Alexandria, Egypt

\* E-mail: [eng.shamseldin13@hotmail.com](mailto:eng.shamseldin13@hotmail.com)

**Keywords:** pervious concrete, recycled aggregates, silica fume, voids content, permeability, compressive strength, tensile strength, degradation

**Abstract.** The world nowadays is trying to find alternative approaches to be used in manufacturing instead of consuming raw materials. Using recycled aggregates in new concrete is one of these effective approaches, which in turn reduces the quantity of waste and reduces the required landfills. In this present work, an attempt was made to study the effect of using recycled aggregates as an alternative to raw aggregates in pervious concrete with different levels (0 %, 25 %, 50 %, 75 % and 100 %), in addition to the impact of adding 5 % and 10 % of silica fume as a replacement of cement weight on the pervious recycled aggregate concrete properties. The concerned properties are as follows: fresh and hardened density, fresh and hardened voids content, water permeability, compressive strength, splitting tensile strength, flexural tensile strength, and potential resistance to degradation of the pervious concrete. Additionally, relations between water permeability and other parameters of the pervious concrete were deduced. Experimental results generally showed that by increasing the recycled aggregates' percentages, there was a consequent deterioration in concrete properties. Whereas, the addition of silica fume enhanced the mechanical properties. It was observed that the addition of 5 % silica fume to concrete with 50 % recycled aggregate was subsequently accompanied by 4.2 % and 5.5 % increase in the fresh and hardened pervious concrete density, respectively, while a 17.5 %, 11.7 % and 17.2 % decrease in the hardened concrete voids content, concrete permeability and concrete degradation, respectively. Regarding the strength parameters, the pervious concrete's 28 days compressive strength, 28 days splitting tensile strength and flexural tensile strength increased by 100 %, 20 % and 20.3 %, respectively. As follows, the addition of silica fume significantly improves the mechanical properties of the pervious concrete, with a slight decrease in the permeability parameters.

### 1. Introduction

Pervious concrete, also called porous concrete and permeable concrete, is a special type of concrete with high permeability that is used for concrete flatwork applications, which allows rainwater and other sources to penetrate through [1] (ACI 522.1-13). Presently, pervious concrete is mainly used in pavement, this attributes to its environmental advantages, such as reducing the rainwater runoff, maintaining the groundwater level, water pollution removal, reducing the need for retention ponds and other costly rainwater controlling, increases air and water ability to reach roots of trees, as well as it increases skid resistance and reduces friction noise [2–4]. Hence, due to all these benefits, many countries, especially in the United States, Japan and European countries, have been utilizing pervious concrete for over 30 years [5].

In order to obtain concrete with high permeability and high porosity, the fine aggregates should be excluded or minimized as possible, so that these distinctive properties could be achieved. Therefore, it is a mixture of Portland cement, water and one or two graded coarse aggregates with/out a small amount of fine aggregates. To maintain a low skeleton packing, one graded coarse aggregates are preferred, so that sufficient open pores could be formed in the matrix [6]. Convenient amounts of water and cementitious

---

Galishnikova, V.V., Abdo, Sh., Fawzy, A.M. Influence of silica fume on the pervious concrete with different levels of recycled aggregates. Magazine of Civil Engineering. 2020. 93(1). Pp. 71–82. DOI: 10.18720/MCE.93.7

Галишникова В.В., Абдо Ш., Фавзи А.М. Влияние микрокремнезёма на проницаемый бетон с различными переработанными заполнителями // Инженерно-строительный журнал. 2020. № 1(93). С. 71–82. DOI: 10.18720/MCE.93.7



materials are used to create a paste, that covers the aggregates particles but leaves free spaces between them, hence pores are formed [6, 7], where it is recommended in ACI 522R to use a water/cement ratio varied from (0.26 to 0.4). However, in case of using low water/cement ratio, sometimes it is necessary to use chemical admixtures, such as water-reducing admixture, to reach the required concrete consistency and workability. Moreover, to ensure achieving the required workability, the hand ball rolling test should be conducted [8, 9].

As the world at the present tends to minimize the consumption of raw materials and energy, therefore, rather than making new products with virgin materials, they instead try to find alternative substances to produce the same products with reasonable quality. Thus, we can reduce the quantity of waste and save more landfills. As for concrete, extracting the coarse aggregates from the demolished concrete building wreckage, and reusing it in a new concrete is the new favorable trend, where it was found that in Europe more than 850 million tons per year of demolished construction wastes are generated, which accounts for 31 % of the total waste in Europe [10]. Hence, we could preserve the raw natural aggregates from consumption, where it is expected, in the USA, by 2020 that the need for producing aggregates would be more than 2.5 billion tons per year [11].

However, using the recycled aggregates in concrete causes adverse effects, where it is observed that by increasing the percentage of the recycled aggregates' proportion, there is a consequent reduction in the concrete mechanical properties. The occurred deterioration in the mechanical properties attributes to the higher water absorption, higher content of organic and harmful substances, lower density and the higher level of crushability compared with the properties of the raw aggregates. Additionally, the existence of old cement mortars on the recycled aggregates particles weakens the concrete and affects its mechanical properties, where it was found that in case of using recycled aggregates, there are two interfacial transition zones between the recycled aggregate and the concrete matrix: The first one is between the aggregate and the old cement paste, and the second one is between the recycled aggregate and the new cement paste [12, 13]. As a result, it was noticed that replacing the raw aggregates with recycled aggregates in the pervious concrete increases the voids ratio as well as decreases the compressive and tensile strength by more than 40 % [14, 15]. Hence, in some aspects using additives, such as silica fume, ground-granulated blast furnace slag, fly ash or chemical admixtures, is mandatory to partially compensate the consequent defects of the addition of the recycled aggregates [3, 16–22]. Additionally, a water compensation due to the high water absorption of the used recycled aggregates is required, where it is recommended to recognize the (10 min.) water absorption rate of recycled aggregates, since the concrete mixing procedures could be finished in 10 min and it accounts for 90 % of the absorbed water in the saturated state of the aggregates [15]. Additionally, some researchers suggested that the best replacement percentage of the raw coarse aggregate by the recycled ones is up to 30 % [23–26], even in some researches, the best replacement percentage is up to 60 % [12, 16], where there is no significant deterioration in the pervious concrete mechanical properties, meanwhile, some researchers found out that the mechanical properties of the pervious concrete are so sensitive, that the compressive strength is reduced even by about 10 % for every 10 % recycled aggregates replacement [19].

As foregoing, to overcome the deterioration occurred in the concrete properties due to the partial replacement of the raw aggregates with the recycled ones, there are several ways to enhance the concrete properties. One of those solutions is the use of pozzolanic material called silica fume. Silica fume is a by-product material which in turn leads to a reduction in waste materials. It is generated by the smelting process in the silicon and ferrosilicon industry as non-crystalline silica [27, 28]. It can be utilized in the form of densified powders or a slurry, as a combination at the concrete mixer, or even as a part of a factory-blended cement [29].

The partial replacement of cement with silica fume is chemically and physically beneficial. Physically beneficial due to the particle average diameter which is about 0.5  $\mu\text{m}$ , thus the unreacted silica fume fills the micrometer-sized voids. Besides, its bulk density is about 600  $\text{kg}/\text{m}^3$ , which is less than the bulk density of the cement which is 1440  $\text{kg}/\text{m}^3$ , and hence the addition of silica fume will subsequently produce more gel than that produced by the cement, which means it densifies the concrete matrix. Additionally, using silica fume will reduce the consumption of cement, which in turn will reduce the emission of  $\text{CO}_2$ . For instance, it was found in Croatia that the Croatian cement industry causes around 8–9 % of total  $\text{CO}_2$  emissions [30].

In terms of chemical reaction, since it is an amorphous material, it dissolves in the concrete before the reaction [31] and reacts with calcium hydroxide (C-H) in the hydrated cement, producing more gel, calcium-silicate-hydrate (C-S-H) [32]. Hence, silica fume decreases the concrete bleeding and produces a denser interfacial transition zone around the aggregates and the concrete paste, as well as a denser matrix, which in turn increases the strength parameters [33]. Besides, the size of the capillary pores and the crystalline hydration products are gradually decreased in the interfacial transition zone, as long as the pozzolanic reactions are ongoing. Thus, the transition zone thickness is reduced and the weak link in the concrete microstructure is minimized [34].

It is observed that the silica fume is a good replacement for cement. The optimum silica fume replacement percentage is about 10 % as a replacement for cement weight [21, 35, 36]. Therefore, in this research, a percentage of 10 % of silica fume was used as a maximum replacement percentage by cement

weight. In return, there is an increase in the final cost of the concrete mixture, since the silica fume is more expensive than cement.

In this research work, the utilized recycled aggregates were extracted from concrete debris, which was collected from a demolished building with an age ranging from 40 to 50 years. The construction was in a dry environment during its lifetime. The debris was broken into pieces of about 9.5 mm size using a drilling machine and the Los Angeles machine. It was expected that no mineral or chemical admixtures were used in casting the old concrete, since in that time the concrete was just cast from conventional components.

Herein, the present research work was conducted to find out the impact of replacing 5 % and 10 % of cement weight by silica fume, on the one graded coarse aggregate pervious concrete with recycled aggregates. The replacement of recycled aggregates was at the levels of 0 %, 25 %, 50 %, 75 % and 100 % by the weight of the raw coarse aggregates. The properties of pervious concrete were concluded through permeability indices (water permeability, density and voids ratio) and strength indices (compressive, flexural tensile, splitting tensile strengths, in addition to the concrete potential to degradation). Additionally, relations between water permeability and other parameters of the pervious concrete were deduced.

## 2. Materials and Methods

### 2.1. Experimental program

**Table 1. Concrete mixes' components.**

Mix number	1	2	3	4	5	6	7	8	9	10	11	12	13	14	15
Silica fume (cement replacement ratio by weight)	0%					5%					10%				
Coarse aggregate replacement %	0%	25%	50%	75%	100%	0%	25%	50%	75%	100%	0%	25%	50%	75%	100%
Water content (L/m <sup>3</sup> )	105	108	109	111	113	105	108	109	111	113	105	108	109	111	113
Water/binder ratio	0.3														
Coarse aggregate content (kg/m <sup>3</sup> )	1430														
Coarse aggregate nominal size (mm)	9.5														
Fine aggregate content (kg/m <sup>3</sup> )	72														
Binder content (kg/m <sup>3</sup> )	350														
High range water reducer (L/m <sup>3</sup> )	2														

Table 1 shows 15 different mixtures' components for a 1 m<sup>3</sup> of concrete that have been used in this work. The mixes were designed according to (ACI-522R-10) with a 20 % designed porosity. Table 2 shows the quantity and dimensions of the specimens for each experiment of each mixture. In the results section, the plotted values were the average of the specimens' results for each experiment. In order to compensate the absorbed water by the recycled aggregate, an amount of water is added equal to the 10 min water absorption of the recycled aggregate.

### 2.2. Concrete components

In this research, all the components of the pervious recycled aggregate concrete -cement, water, aggregates and silica fume- passed the acceptance criteria experiments.

Portland cement Type I 42.5 N was used according to ASTM C150 [37], where its properties are presented in Table 3.

The coarse aggregates type, for both raw and recycled aggregate, was crushed pink limestone with single sizes of 9.5 mm. Its bulk density was 1760 kg/m<sup>3</sup> and the water absorption was 1.5 %. As for recycled coarse aggregate, the bulk density was 1630 kg/m<sup>3</sup>, while the water absorption of recycled aggregate was 7.2 %.

Natural siliceous sand, with a bulk density of 1800 kg/m<sup>3</sup> and a fineness modulus of 2.67, was used as fine aggregate.

Micro silica (silica fume), with 92 % (SiO<sub>2</sub>) content, 25000 m<sup>2</sup>/kg surface area and 600 kg/m<sup>3</sup> bulk density, was used in this study to enhance the pervious concrete properties.

A poly-carboxylate based high range water reducer (HRWR) type *F* is utilized in this work with 1040 kg/m<sup>3</sup> bulk density.

**Table 2. Quantity and dimensions of the specimens for each mixture.**

Experiment type	Number of specimens	Shape and Dimensions
-----------------	---------------------	----------------------

Fresh pervious concrete density and voids content	3	Cylinder $D = 20$ cm, $H = 20$ cm
Hardened pervious concrete density and voids content	3	Cylinder $D = 7.5$ cm, $H = 15$ cm
Water permeability test (falling head method)	3	50×50 cm <sup>2</sup> slab with a 10 cm thickness
Compressive strength	3	Cylinder $D = 15$ cm, $H = 30$ cm
Splitting Tensile strength	3	Cylinder $D = 7.5$ cm, $H = 15$ cm
Flexural tensile strength	3	15×15 cm <sup>2</sup> beam with a 45 cm span
Degradation and potential resistance	9	Cylinder $D = 10$ cm, $H = 10$ cm

**Table 3. Properties of the used Portland cement.**

Item	Percentage
Calcium oxide (CaO)	63%
Silicon dioxide (SiO <sub>2</sub> )	21.3%
Aluminum Oxide (Al <sub>2</sub> O <sub>3</sub> )	6.2%
Iron Oxide (Fe <sub>2</sub> O <sub>3</sub> )	3.9%
Magnesium oxide (MgO)	2.5%
Sulfur trioxide (SO <sub>3</sub> )	1.7%
Potassium oxide (K <sub>2</sub> O)	0.7%
Sodium oxide (Na <sub>2</sub> O)	0.5%
Loss on ignition (LOI)	2.5%

## 2.3. Methods of testing

### 2.3.1. Fresh pervious concrete density and voids content

According to ASTM c 1688 [38], to obtain those properties, a sample of fresh pervious concrete is placed and well consolidated using the standard proctor hammer in a standard measure, then the density and the voids content can be calculated.

### 2.3.2. Hardened pervious concrete density and voids content

According to ASTM C1754 [39], hardened density and voids content are determined. Samples were dried at elevated temperature (105 °C), then the dried mass was recorded, then the specimens were submerged for 30 minutes to release the bubbles from the voids. Subsequently, the submerged mass for each specimen was recorded to determine the hardened density and the voids content. According to ACI 522R, the upper limit is 2000 kg/m<sup>3</sup> and the lower limit is 1600 kg/m<sup>3</sup> with voids ratio ranges from 15 % to 35 %.

### 2.3.3. Water permeability test (falling head method)

According to ASTM C1781 [40], the water permeability is expressed as infiltration rate, where a watertight infiltration ring with a 30 cm diameter is fixed on the surface of the concrete. The time that takes for the known mass of water to infiltrate through the ring is measured, the infiltration rate is calculated then. According to ACI 522R, the upper limit is 1.2 cm/s and the lower limit is 0.2 cm/s.

### 2.3.4. Compressive strength

According to ASTM C 39 [41], the ultimate compressive strength of a material is the value of the uniaxial compressive stress, when the material fails. According to ACI 522R, the compressive strength shouldn't be less than 3 MPa.

### 2.3.5. Splitting Tensile strength

According to ASTM C496 [42], splitting tensile tests involve compressing a concrete cylinder on its side until a crack forms down the middle, causing the failure of the specimen. According to ACI 522R, the splitting tensile strength shouldn't be less than 1 MPa.

### 2.3.6. Flexural tensile strength

According to ASTM C78 [43], the flexural strength test for concrete involves loading a 15x15 cm concrete beam with 45 cm span, the load is applied at one-third and two-thirds of the span length. According to ACI 522R, the flexural tensile strength shouldn't be less than 1 MPa.

### 2.3.7. Degradation and potential resistance

According to ASTM C1747 [44] this experiment is conducted to figure out the ability of the concrete to resist degradation from impact and abrasion. Cylindrical specimens of a known mass with a 10 cm diameter and a 10 cm height were inserted in the Los Angeles machine, three at a time, for 500 cycles without the steel balls. Thereafter, the crushed specimen is placed on a 2.54 cm sieve, the retained concrete on the sieve was weighed. The amount of material left behind was subtracted from the initial mass and the difference was taken as the mass loss percentage. According to ACI 522R, the upper limit is 95 %, while the lower limit is 19 %.

### 3. Results and Discussion

#### 3.1. Density

The results of the density have standards deviation with a range of (10–25) kg/m<sup>3</sup>. The following Figures 3.1.1 and 3.1.2 show the relation between concrete density (kg/m<sup>3</sup>), recycled aggregate replacement percentage and the silica fume for the fresh and hardened pervious concrete, respectively. It's generally noticed that as a consequence of increasing the percentage of the recycled aggregates, there is an accompanying decrease in the fresh and hardened density. This decrease attributes to the lower density and higher voids ratio of the recycled aggregate itself, due to the aggregates' recycling process.

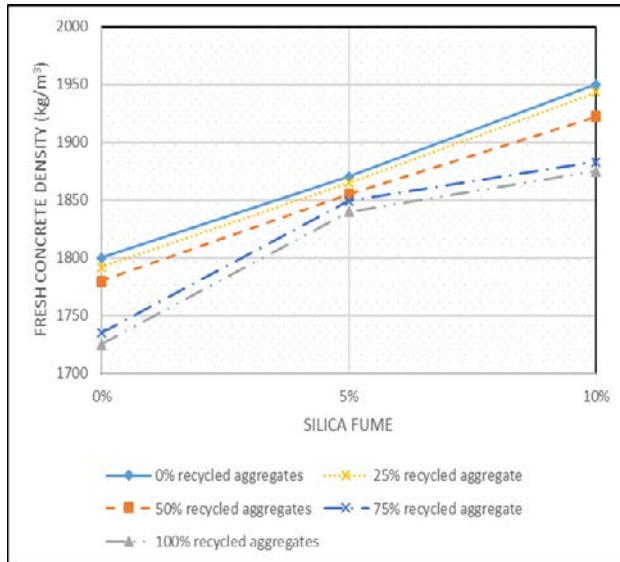


**Figure 3.1.1. Density of the fresh pervious concrete.**

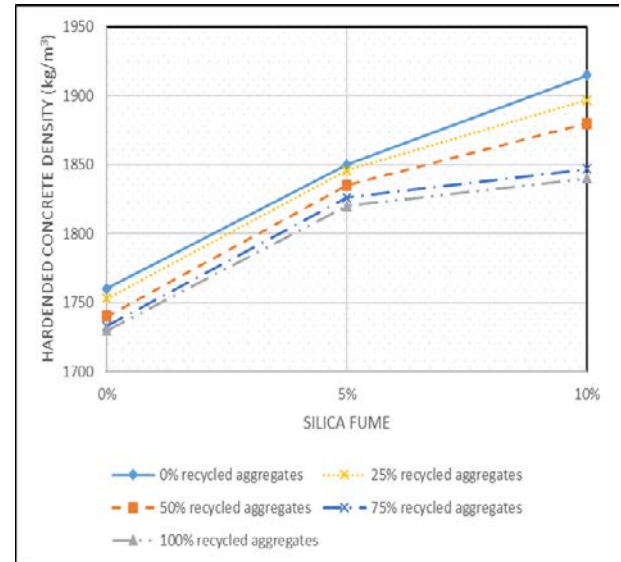


**Figure 3.1.2. Density of the hardened pervious concrete.**

#### 3.2. Voids content

The results of the voids content have standards deviation with a range of (0.5–1.5) %. Figures 3.2.1 and 3.2.2 present the relation between the voids content and recycled aggregate replacement percentage along with the silica fume for the fresh and hardened pervious concrete, respectively. Generally, it is observed that by increasing the recycled aggregate percentage in the pervious concrete, there is a subsequent increase in the voids ratio for both the fresh and hardened concrete, which agrees with a previous scientific research [16], meanwhile contradicts with other [12]. As for voids content of the fresh pervious concrete, it's noticed that adding silica fume for the mixes with/out recycled aggregate greatly decreases the voids content, but since that the fresh state of the pervious concrete is in a short limited time, it could be overlooked. As for the voids content of the hardened pervious concrete, in case of 5 % silica fume, all the mixes with/out recycled aggregate are within the limits, whereas in case of 10 % silica fume, only the mixtures with 75 % and 100 % recycled aggregate meets the specifications, since the minimum voids ratio should be not less than 15 %, according to (ACI 522R-10).

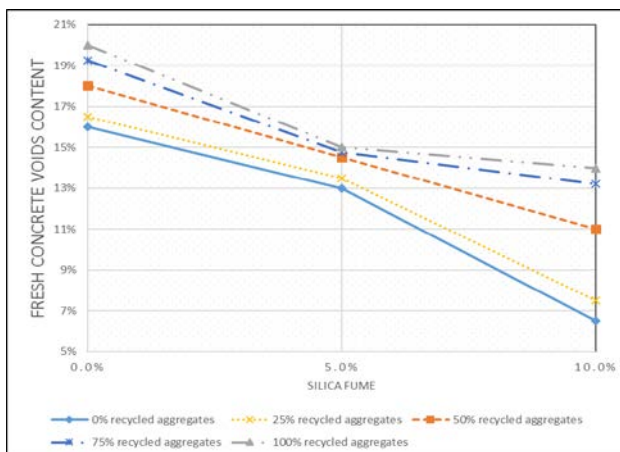


**Figure 3.2.1. Voids content in the fresh pervious concrete.**

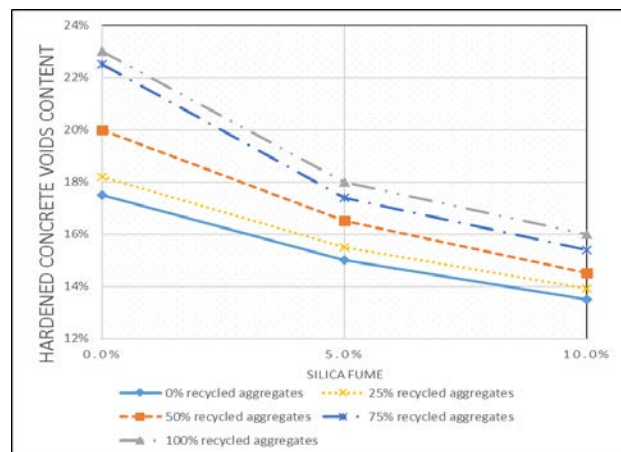


**Figure 3.2.2. Voids content in the hardened pervious concrete.**

### 3.3. Water permeability test (falling head method)

The results of the water permeability have standards deviation with a range of (0.02–0.04) cm/s. Figure 3.3 presents the relation between the water permeability and the recycled aggregate replacement percentage along with the silica fume for the hardened pervious concrete. It's clearly noticed that silica fume decreases the water permeability. Whereas, increasing the recycled aggregate percentage increases the water permeability, where its is noticed that the addition of 5 % silica fume decreased the water permeability of the concrete by (13.5 %, 12.1 %, 11.7 %, 9.2 % and 7.8 %) for the concrete with (0 %, 25 %, 50 %, 75 % and 100 %), respectively, compared with concrete mixes without silica fume as shown in Figure 3.4.

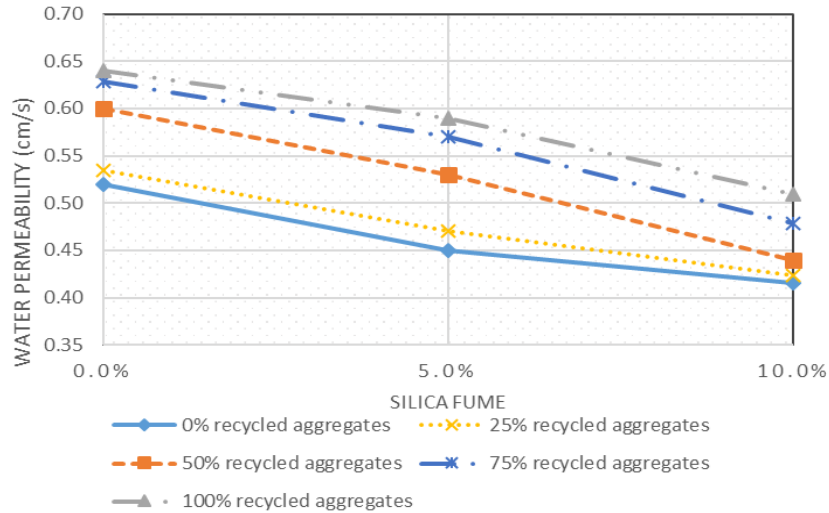


Figure 3.3. Water permeability of the hardened pervious concrete.

### 3.4. Summary of the effect of silica fume on the permeability parameters

The following Figure 3.4 shows the effect of silica fume on the permeability parameters of the recycled aggregate concrete permeability parameters. Mixes without silica fume are considered to be the control mix that all results are related to, for instance, mixes num. (6 and 11), (7 and 12), (8 and 13), (9 and 14) and (10 and 15) are compared with mix num. (1), (2), (3), (4) and (5), respectively. The Figure shows that adding silica fume subsequently increases the density of the fresh and hardened concrete, while decreases the voids content and the water permeability for both the fresh and hardened pervious concrete.

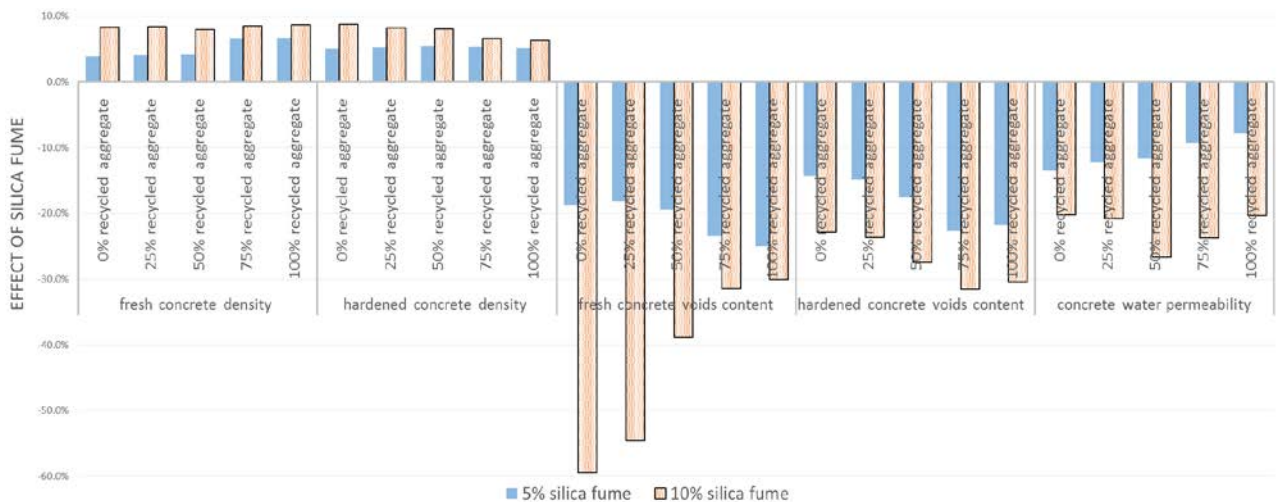
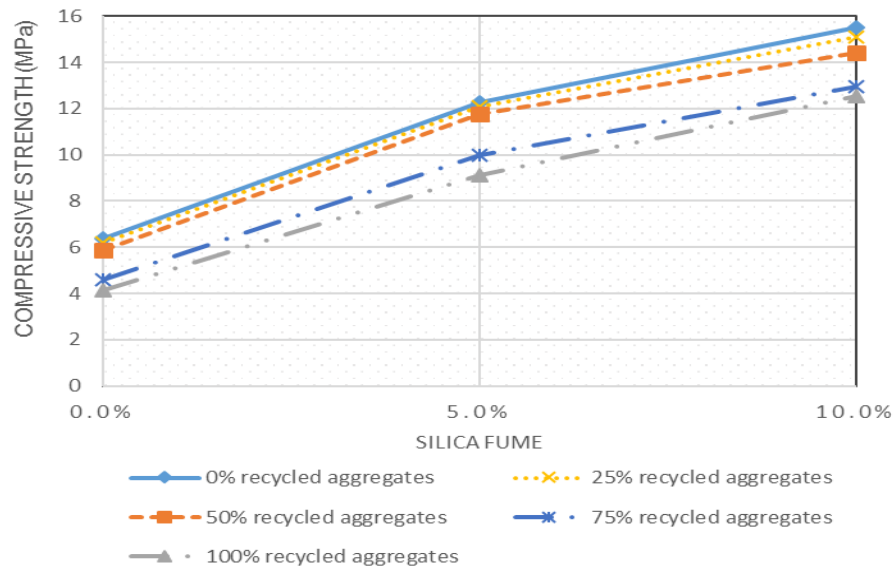


Figure 3.4. Effect of silica fume on the permeability parameters of the recycled aggregate pervious concrete.

### 3.5. Compressive strength

The results of the compressive strength have standards deviation with a range of (0.2–0.9) MPa. Figure 3.5 demonstrates the relation between 28 days concrete compressive strength (MPa), recycled aggregate replacement percentage and silica fume. It's noticed that generally by increasing the percentage of the recycled aggregates, a consequent decrease in the compressive strength was accompanied as a result. However, the reduction due to the addition of up to 50 % of recycled aggregate could be neglected. As shown in the Figure 3.9. As a result of replacing 50 % of the raw aggregates with recycled ones, there is an accompanied reduction in the compressive strength by (8 %, 4 % and 7 %) for concrete with (0 %, 5 % and 10 %) of silica fume, respectively. This may be attributed to the weakness of the concrete in general, where there is plenty of voids in this type of

concrete. Thus, the effect of the interfacial transition zone could be overlooked. Meanwhile, this contradicts with some researches [14, 26, 45], where they concluded that the best percentage for a replacing the raw coarse aggregate with recycled ones is up to 20 %. As for 100 % recycled aggregate, the amount and thickness of the interfacial transition zone between the aggregate particles and cement paste were considerably increased that the cracks propagate through it rather than through the cement mortar.



**Figure 3.5. 28-day compressive strength of the pervious concrete.**

Figure 3.9 emphasizes the explanation in the previous paragraph, where it is observed that the effect of silica fume is significantly increased for the 100 % recycled aggregate. It is noticed that adding 10 % of silica fume to the 100 % recycled aggregates, increased the compressive strength by 210 %. This is because silica fume enhances the concrete's matrix and the thickness of the interfacial transition zone in the concrete, as well as the degree of the orientation of the CH crystals in it [46].

### 3.6. Splitting tensile strength

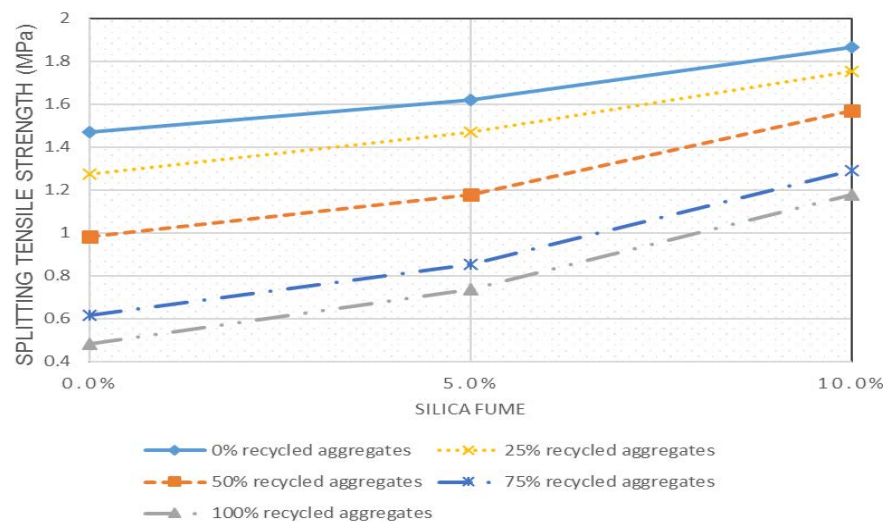


**Figure 3.6. 28 days splitting tensile Strength of the pervious concrete.**

The results of the splitting tensile strength have standards deviation with a range of (0.03–0.15) MPa. Figure 3.6 shows the relation between the 28 days pervious concrete splitting tensile strength (MPa) and the recycled aggregates replacement percentage in addition to silica fume. It is pronounced that the pervious concrete with 100 % recycled aggregate didn't meet the requirements and limits, that's in case of adding (0 % or 5 %) of silica fume.

It's also observed from the figure, that silica fume has a subsequent impact on the splitting tensile strength, especially when the percentage of the recycled aggregate increases. As shown in the Figure 3.9, the addition of 10 % silica fume for 100 % recycled aggregate pervious concrete, increases the splitting tensile strength by 148 %. This enhancement in the mechanical properties attributes to the improvements in the concrete matrix and the transition zone as a result of adding silica fume.

### 3.7. Flexural tensile strength

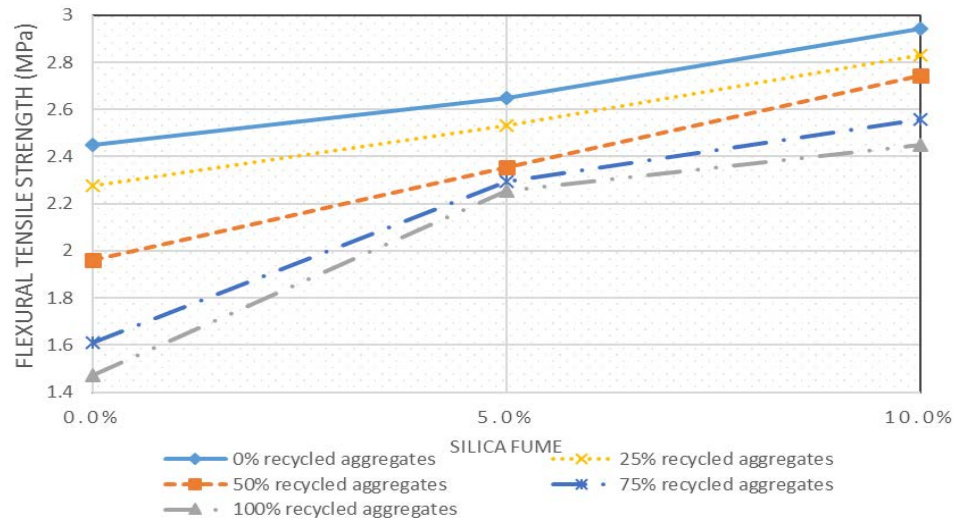


**Figure 3.7. 28 days flexural tensile strength of the 28 days pervious concrete.**

The results of the flexural tensile strength have standards deviation with a range of (0.08–0.27) MPa. Figure 3.7 shows the relation between the 28 days flexural tensile strength (MPa), the recycled aggregates replacement percentage and silica fume. It can be noticed that the flexural tensile strength is greater than the splitting tensile strength, since under bending stresses, just the member's extreme fibers are at the highest stress level, and if those fibers are defects free, the flexural strength will be controlled by the strength of those intact fibers. While if tensile stress is imposed on the concrete with the same properties, then all the fibers in the cross-section of the concrete are imposed on the same stress level and failure will initiate when the weakest fiber reaches its tensile strength.

### 3.8. Degradation and potential resistance

The results of the degradation and potential resistance have standards deviation with a range of (4–6.5) %. Figure 3.8 presents the influence of silica fume on the degradation of the pervious concrete with different percentage of recycled coarse aggregates. It is noticed from the figure that silica fume has a notable influence on the resistance to degradation of the concrete, where the degradation decreased by about 30 % when 10 % of the cement was replaced by silica fume as shown in Figure 3.9.

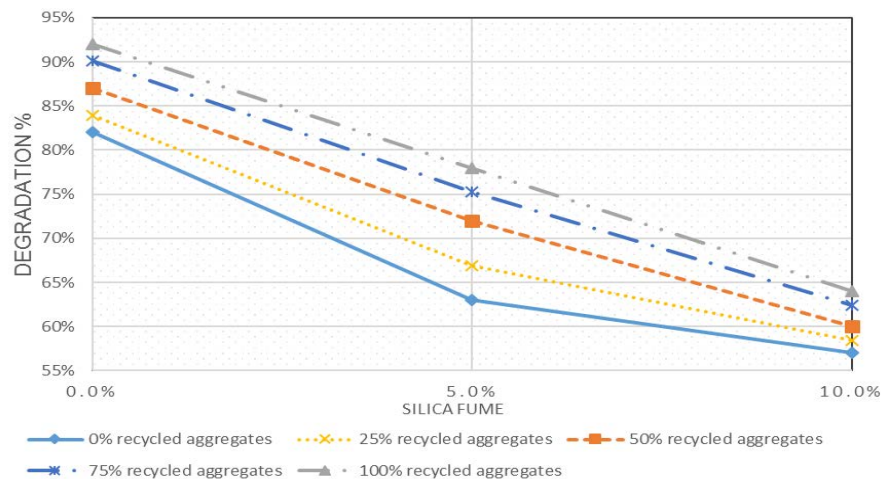


**Figure 3.8. Degradation of the pervious recycled aggregate concrete.**

### 3.9. Summary of the effect of silica fume on the strength parameters

Figure 3.9 shows the effect of silica fume on the strength parameters of the recycled aggregate concrete properties. Mixes without silica fume are considered to be the control mix that all results are related to, for instance, mixes num. (6 and 11), (7 and 12), (8 and 13), (9 and 14) and (10 and 15) are compared with mix num. (1), (2), (3), (4) and (5), respectively. From Figure 3.4 and 3.9, it is observed that replacing 10 % of cement with silica fume significantly enhance the properties, that in some cases it doesn't meet the ACI 522R limitations. Thus, replacing 5 % of cement weight by silica fume is an optimum replacement percentage. This agrees with some research works [47, 48]. From the Figure 3.9, it is observed that silica fume significantly enhanced the mechanical properties, for instance, it is shown that replacing 5 % of the cement by silica fume, doubled the compressive strength of the 50 % recycled aggregate pervious concrete. This enhancement

attributes to the low density of silica fume compared with cement. Thus, replacing the cement with silica fume, results in larger paste volume, which in turn increases the strength of the bond between the matrix and the aggregate, which is the weakest phase in the pervious concrete.

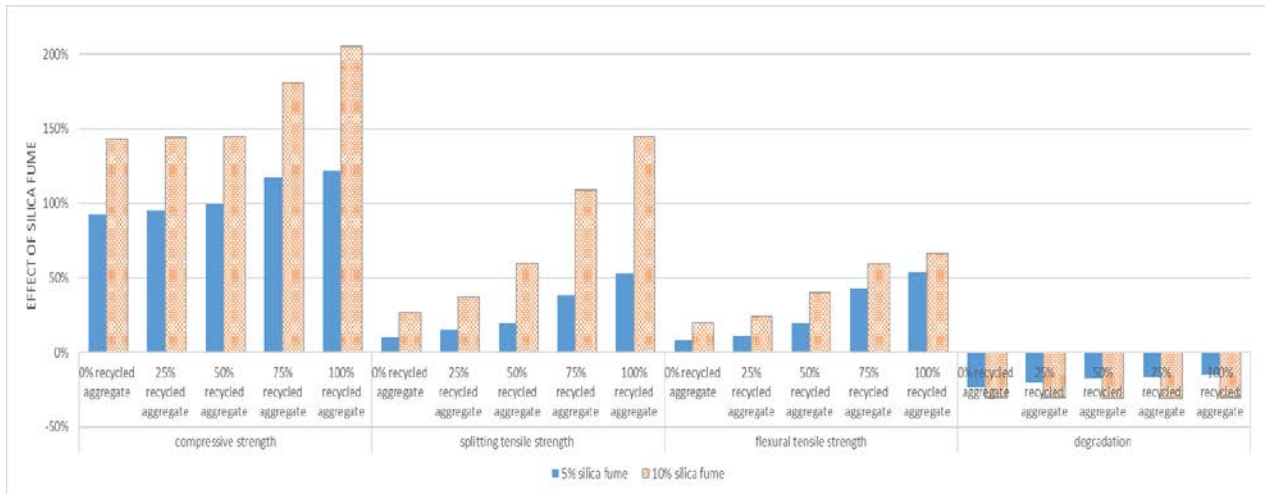


**Figure 3.9. Effect of silica fume on the strength parameters of the recycled aggregate pervious concrete.**

### 3.10. General relations between water permeability and other parameters

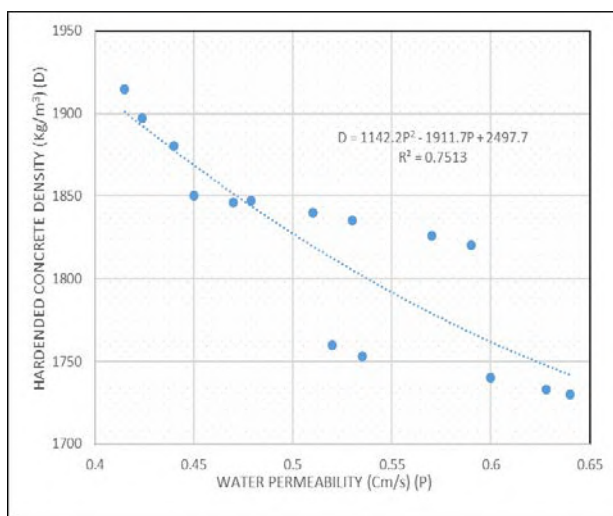
Since the water permeability is the ruling and critical parameter in pervious concrete, here in this part, an attempt was made to deduce correlations between the pervious concrete water permeability and other parameters.

Figure 3.10.1 presents the relationship between the water permeability in (cm/s) and the hardened concrete density in (kg/m<sup>3</sup>). It can be noticed that by the increase of the concrete density (*D*), there is a consequent decrease in the water permeability (*P*). The deduced formula is with a good degree of fit ( $R^2 = 0.7513$ ) and is as follows:

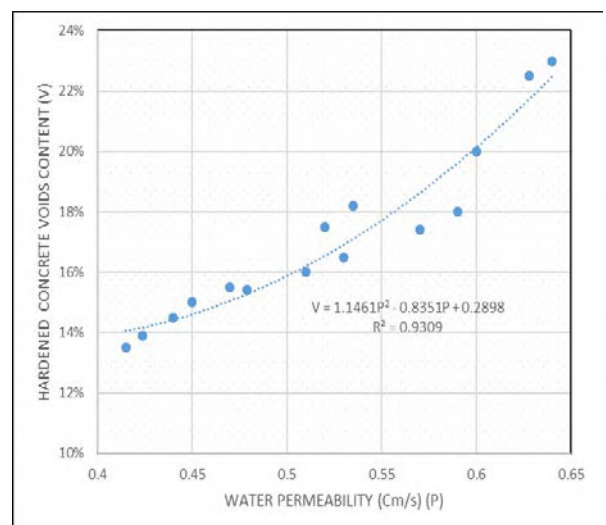
$$D = 1142.2P^2 - 1911.7P + 2497.7. \tag{1}$$

Figure 3.10.2 shows the relationship between the water permeability (*P*) in (cm/s) and the voids content percentage (*V*) of the hardened concrete. It is observed from the figure that there is a direct relationship between the voids content and the water permeability. The deduced formula is with a very good degree of fit ( $R^2 = 0.9309$ ) and is as follows:

$$V = 1.1461P^2 - 0.8351P + 0.2898. \tag{2}$$



**Figure 3.10.1. Correlation between water permeability and hardened concrete density.**



**Figure 3.10.2. Correlation between water permeability and hardened concrete voids content.**

Figure 3.10.3 shows the relationship between the water permeability in (cm/s) and the compressive strength in (MPa). It can be concluded that the relationship between the compressive strength ( $F_c$ ) and the water permeability ( $P$ ) is indirect. The deduced formula is with a good degree of fit ( $R^2 = 0.7805$ ) and is as follows:

$$F_c = -46.651P + 34.454. \tag{3}$$

Figure 3.10.4 shows the relationship between the water permeability in (cm/s) and the tensile strength in (MPa), whether it is the splitting tensile strength ( $F_t$ ) or the flexural tensile strength ( $F_b$ ). Generally, it can be concluded that the relationship between the tensile strength and the water permeability ( $P$ ) is indirect. The deduced formula between the water permeability and the splitting tensile strength is with a very good degree of fit ( $R^2 = 0.9208$ ) and it is as presented in equation (4). Additionally, the formula between the water permeability and the flexural tensile strength is also with a very good degree of fit ( $R^2 = 0.9304$ ) and it is as presented in equation (5).

$$F_t = -5.4468P + 4.0546; \tag{4}$$

$$F_b = -15.442P^2 + 10.89P + 0.9498. \tag{5}$$

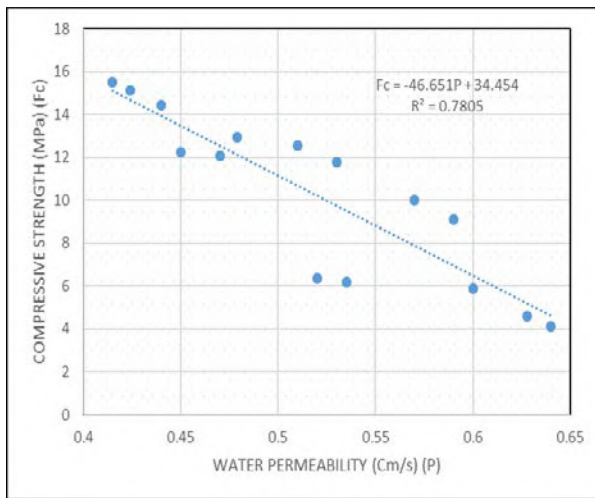


**Figure 3.10.3. Correlation between water permeability and pervious concrete compressive strength.**

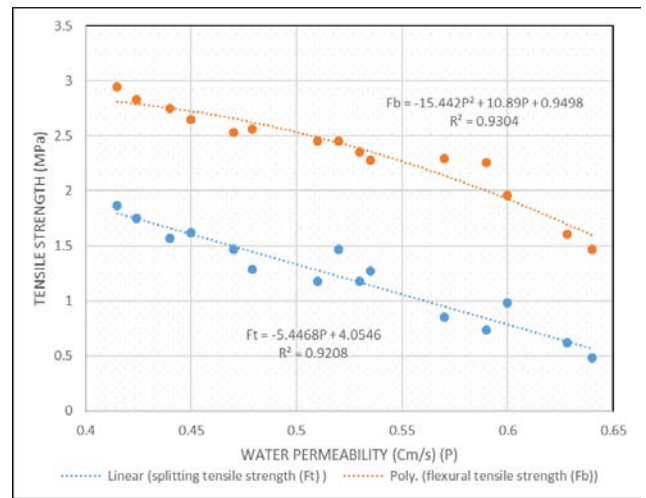


**Figure 3.10.4. Correlation between water permeability and pervious concrete tensile strength.**

Figure 3.10.5 shows the relationship between the water permeability in (cm/s) and the pervious concrete potential to degradation. It can be noticed that by the increase of the concrete water permeability ( $P$ ), there is a consequent increase in concrete degradation (Deg). The formula which estimates this correlation is with a good degree of fit ( $R^2 = 0.8599$ ) and it is as follows:

$$Deg = 1.4728P^{1.0818}. \tag{6}$$

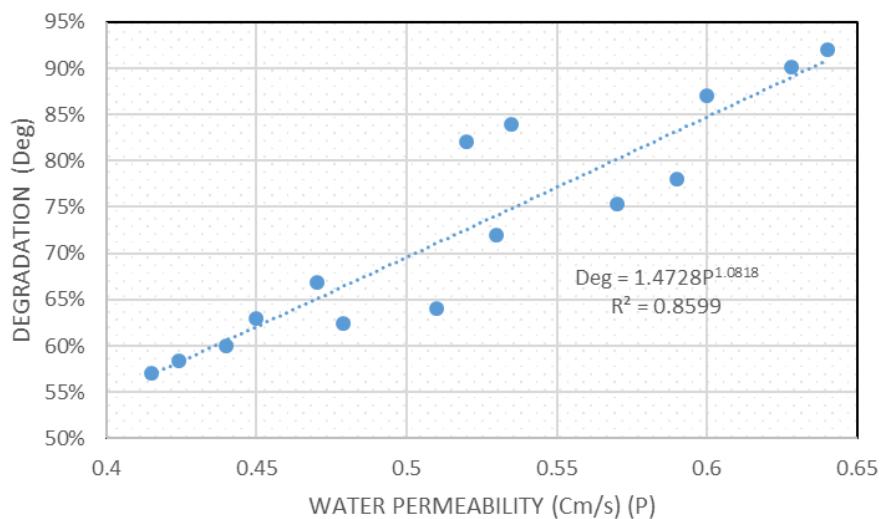


**Figure 3.10.5. Correlation between water permeability and the pervious concrete degradation.**

## 4. Conclusion

The study, in this research work, focused on the effect of replacing 5 % and 10 % of cement weight by silica fume on pervious concrete with recycled aggregates at the level of (0 %, 25 %, 50 %, 75 % and 100 %).

According to the previous findings, it is concluded that:

1. The replacement of raw aggregates with the recycled ones in the previous concrete adversely affects its mechanical properties. Meanwhile, this deterioration in the concrete properties could be neglected when up to 50 % of the raw aggregates are replaced, where the reduction in the mechanical properties is less than 10 %.

2. Generally, the addition of 10 % silica fume is not necessary, where it was found that adding 5 % silica fume is good enough to enhance the mechanical properties without affecting the permeability parameters. It was found that replacing 5 % of cement weight by silica fume in the pervious concrete with 50 % recycled aggregate, significantly increased the strength parameters and slightly decreased the permeability parameters, where the 28 days compressive strength, splitting tensile strength and the flexural tensile strength increased by 100 %, 20 % and 20.3 %, respectively. While the concrete potential to degradation, hardened density, hardened voids and water permeability decreased by 17.2 %, 5.5 % 17.5 % and 11.7 %, respectively.

3. In case of replacing 100 % of raw aggregates by recycled ones, the addition of 10 % silica fume is necessary in order to meet the specifications.

4. As a consequence of increasing the recycled aggregate replacement percentage, an increase in the used water is required, to compensate the water absorbed by the recycled aggregate.

5. By increasing the water permeability, there is a consequent increase in the voids content and the concrete potential to degradation, whereas a decrease in the concrete density, compressive and tensile strength.

## References

- Nassiri, S., Rangelov, M., Chen, Z. Preliminary Study to Develop Standard Acceptance Tests for Pervious Concrete. 2017. (May). Pp. 1–67.
- Ulloa-mayorga, V.A., Uribe-garcés, M.A., Paz-gómez, D.P., Alvarado, Y.A. Performance of pervious concrete containing combined recycled aggregates Desempeño del concreto permeable con agregados reciclados. 2018. 2018. Pp. 34–41. DOI: 10.15446/ing.investig.v38n2.67491.
- El-hassan, H., Kianmehr, P. Pervious concrete pavement incorporating GGBS to alleviate pavement runoff and improve urban sustainability. Road Materials and Pavement Design. 2016. 0(0). Pp. 1–15. DOI: 10.1080/14680629.2016.1251957. URL: <http://dx.doi.org/14680629.2016.1251957>.
- Schaefer, V., Suleiman, M. An Overview of Pervious Concrete Applications in Stormwater Management and Pavement Systems [Online]. ... Iowa State University .... 2006. (April 2014). Pp. 1–10. URL: [http://www.rmc-foundation.org/images/PCRC Files/Hydrological %26 Environmental Design/An Overview of Pervious Concrete Applications in Stormwater Management and Pavement Systems.pdf](http://www.rmc-foundation.org/images/PCRC%20Files/Hydrological%20Environmental%20Design/An%20Overview%20of%20Pervious%20Concrete%20Applications%20in%20Stormwater%20Management%20and%20Pavement%20Systems.pdf).
- Aoki, Y. Development of pervious concrete. 2009. Pp. 1–138.
- Sonebi, M., Bassuoni, M., Yahia, A. Pervious Concrete: Mix Design, Properties and Applications. RILEM Technical Letters. 2016. 1(December). Pp. 109. DOI: 10.21809/rilemtechlett.2016.24.
- Keven, J.T. Design of pervious concrete mixtures. 2017. (Version 3.0) [Online]. Pp. 30. URL: <http://scholar.google.com/scholar?hl=en&btnG=Search&q=intitle:Design+of+Pervious+Concrete+Mixtures#5>.
- Sriravindrarajah, R., Wang, N.D.H., Ervin, L.J.W. Mix Design for Pervious Recycled Aggregate Concrete. International Journal of Concrete Structures and Materials. 2012. 6(4). Pp. 239–246. DOI: 10.1007/s40069-012-0024-x.
- Rasiah, S. Environmentally Friendly Pervious Concrete for Sustainable Construction Environmentally Friendly Pervious Concrete for Our World in Concrete & Structures Environmentally Friendly Pervious Concrete for Sustainable Construction. 2010. (September).
- Malešev, M., Radonjanin, V., Marinković, S. Recycled concrete as aggregate for structural concrete production. Sustainability. 2010. 2(5). Pp. 1204–1225. DOI: 10.3390/su2051204.
- US Department of Transportation. Transportation Applications Of Recycled Concrete Aggregate. FHWA State of the Practice National Review. 2004. 39(5). Pp. 27–29.
- Zaetang, Y., Sata, V., Wongsas, A., Chindaprasirt, P. Properties of pervious concrete containing recycled concrete block aggregate and recycled concrete aggregate [Online]. Construction and Building Materials. 2016. 111. Pp. 15–21. DOI: 10.1016/j.conbuildmat.2016.02.060. URL: <http://dx.doi.org/10.1016/j.conbuildmat.2016.02.060>.
- Xiao, J., Li, W., Sun, Z., Lange, D.A., Shah, S.P. Cement & Concrete Composites Properties of interfacial transition zones in recycled aggregate concrete tested by nanoindentation [Online]. Cement and Concrete Composites. 2013. 37. Pp. 276–292. DOI: 10.1016/j.cemconcomp.2013.01.006. URL: <http://dx.doi.org/10.1016/j.cemconcomp.2013.01.006>.
- Rizvi, R., Candidate, B., Author, P. Incorporating Recycled Concrete Aggregate in Pervious Concrete Pavements. Annual Conference of the Transportation Association of Canada. 2009. Pp. 1–18.
- Yanya, Y. Blending ratio of recycled aggregate on the performance of pervious concrete. Frattura ed Integrità Strutturale. 2018. 12(46). Pp. 343–351. DOI: 10.3221/IGF-ESIS.46.31.
- Aliabdo, A.A., Elmoaty, A., Elmoaty, M.A., Fawzy, A.M. Experimental investigation on permeability indices and strength of modified pervious concrete with recycled concrete aggregate [Online]. Construction and Building Materials. 2018. 193. Pp. 105–127. DOI: 10.1016/j.conbuildmat.2018.10.182. URL: <https://doi.org/10.1016/j.conbuildmat.2018.10.182>.
- Lu, J., Yan, X., He, P., Sun, C. Sustainable design of pervious concrete using waste glass and recycled concrete aggregate [Online]. Journal of Cleaner Production. 2019. 234. Pp. 1102–1112. DOI: 10.1016/j.jclepro.2019.06.260. URL: <https://doi.org/10.1016/j.jclepro.2019.06.260>.
- Taylor, P., Aoki, Y., Ravindrarajah, R.S., Khabbaz, H. Road Materials and Pavement Design Properties of pervious concrete containing fly ash. 2012. (January 2015). Pp. 37–41. DOI: 10.1080/14680629.2011.651834.

19. El-hassan, H., Kianmehr, P., Zouaoui, S. Properties of pervious concrete incorporating recycled concrete aggregates and slag [Online]. *Construction and Building Materials*. 2019. 212. Pp. 164–175. DOI: 10.1016/j.conbuildmat.2019.03.325. URL: <https://doi.org/10.1016/j.conbuildmat.2019.03.325>.
20. Szumiec, M. *Proceedings of the International Workshop on Global Optimization 2004*.
21. Wang, F., Zheng, S.S., Wang, X.F. Influence of Silica Fume on High-Performance Concrete. *Applied Mechanics and Materials*. 2014. 670–671. Pp. 437–440. DOI: 10.4028/www.scientific.net/amm.670-671.437.
22. Rashwan, M.S., AbouRisk, S. The Properties of Recycled Concrete. *Concrete International*. 1997. 19(7). Pp. 56–60. DOI: 10.7251/COMEN1402239M.
23. Sonawane, T.R., Pimplikar, P.S.S. Use of Recycled Aggregate Concrete. *Journal of Mechanical and Civil Engineering (IOSR-JMCE)*. 2012. 1(2). Pp. 52–59.
24. Oikonomou, N.D. Recycled concrete aggregates. *Cement and Concrete Composites*. 2005. 27(2). Pp. 315–318. DOI: 10.1016/j.cemconcomp.2004.02.020.
25. Etxeberria, M., Marí, A.R., Vázquez, E. Recycled aggregate concrete as structural material. *Materials and Structures/Materiaux et Constructions*. 2007. 40(5). Pp. 529–541. DOI: 10.1617/s11527-006-9161-5.
26. Poh, S., Zhao, P., Chen, C., Goh, Y., Adebayo, H., Hung, K., Wah, C. Characterization of pervious concrete with blended natural aggregate and recycled concrete aggregates [Online]. *Journal of Cleaner Production*. 2018. 181. Pp. 155–165. DOI: 10.1016/j.jclepro.2018.01.205. URL: <https://doi.org/10.1016/j.jclepro.2018.01.205>.
27. Plassard, C., Lesniewska, E., Pochard, I., Nonat, A. Investigation of the surface structure and elastic properties of calcium silicate hydrates at the nanoscale. *Ultramicroscopy*. 2004. 100(3–4). Pp. 331–338. DOI: 10.1016/j.ultramic.2003.11.012.
28. Sadrumontazi, A., Tahmouresi, B., Saradar, A. Effects of silica fume on mechanical strength and microstructure of basalt fiber reinforced cementitious composites (BFRCC) [Online]. *Construction and Building Materials*. 2018. 162. Pp. 321–333. DOI: 10.1016/j.conbuildmat.2017.11.159. URL: <https://doi.org/10.1016/j.conbuildmat.2017.11.159>.
29. King, D. The effect of silica fume on the properties of concrete as defined in concrete society report 74, cementitious materials. 37th Conference on our world in concrete and structures, Singapore. 2012. Pp. 29–31.
30. Mikulčić, H., Vujanović, M., Duić, N. Reducing the CO<sub>2</sub> emissions in Croatian cement industry. *Applied Energy*. 2013. 101. Pp. 41–48. DOI: 10.1016/j.apenergy.2012.02.083.
31. Holland, T.C. *Silica fume user's manual*. Federal Highway Administration. 2005. Pp. 194.
32. Wang, Q.L., Bao, J.C. Effect of Silica Fume on Mechanical Properties and Carbonation Resistance of Concrete. *Applied Mechanics and Materials*. 2012. 238(November). Pp. 161–164. DOI: 10.4028/www.scientific.net/amm.238.161.
33. Fu, T.C., Yeh, W., Chang, J.J., Huang, R. The Influence of Aggregate Size and Binder Material on the Properties of Pervious Concrete. 2014. 2014.
34. P. Kumar Mehta. High-Performance, High-Volume Fly Ash Concrete for Sustainable Development [Online]. *International Workshop on Sustainable Development and Concrete Technology*. 2008. 31(4). Pp. 3–14. URL: <http://search.ebscohost.com/login.aspx?direct=true&db=psyh&AN=2009-09898-004&lang=fr&site=ehost-live&scope=site>.
35. Mazloom, M., Soltani, A., Karamloo, M., Hassanloo, A. Effects of silica fume, superplasticizer dosage and type of superplasticizer on the properties of normal and selfcompacting concrete. *Advances in Materials Research*. 2018. 7(1). Pp. 407–434. DOI: 10.12989/amr.2018.7.1.407.
36. Imam, A., Srivastava, V. Review study towards effect of Silica Fume on the fresh and hardened properties of concrete. 2018. (April). DOI: 10.12989/acc.2018.6.2.145.
37. ASTM C 150. Standard Specification for Portland Cement. ASTM International. 2015. (June 1999). Pp. 1–6. DOI: 10.1520/C0010.
38. ASTM C1688/C1688M. Standard Test Method for Density and Void Content of Freshly Mixed Pervious Concrete. ASTM International. 2014. i. Pp. 1–4. DOI: 10.1520/C1688.
39. ASTM C1754/C1754M-12. Standard Test Method for Density and Void Content of Hardened Pervious Concrete. ASTM International. 2012. Pp. 3. DOI: 10.1520/C1754.
40. ASTM C1781/C1781M. Standard Test Method for Surface Infiltration Rate of Permeable Unit Pavement [Online]. ASTM International. 2015. i. Pp. 1–6. DOI: 10.1520/C1781. URL: <http://compass.astm.org/download/C1781C1781M.8914.pdf>.
41. ASTM C39/C39M-14. Standard Test Method for Compressive Strength of Cylindrical Concrete Specimens [Online]. ASTM International. 2014. Pp. 1–8. DOI: 10.1520/C0039. URL: <http://www.astm.org/cgi-bin/resolver.cgi?C39C39M-17b>.
42. ASTM C496/C496M-11. Standard Test Method for Splitting Tensile Strength of Cylindrical Concrete Specimens [Online]. *Annual Book of ASTM Standards Vol. 04.02*. 2011. Pp. 1–5. DOI: 10.1520/C0496. URL: <http://www.c-s-h.ir/wp-content/uploads/2015/01/C-496.pdf> %0Aftp://ftp.astmtmc.cmu.edu/docs/diesel/cummins/procedure\_and\_ils/ism/Archive/ISM Procedure (Draft 10).doc.
43. ASTM Standard C78/C78M. Standard Test Method for Flexural Strength of Concrete (Using Simple Beam with Third-Point Loading). ASTM International. 2010. C78-02(C). Pp. 1–4. DOI: 10.1520/C0078.
44. ASTM C1747. Standard Test Method for Determining Potential Resistance to Degradation of Pervious Concrete by Impact and Abrasion 1. ASTM International. 2015. (c). Pp. 5–7. DOI: 10.1520/C1747.
45. Rizvi, R., Tighe, S., Henderson, V., Norris, J. Evaluating the Use of Recycled Concrete Aggregate in Pervious Concrete Pavement [Online]. *Transportation Research Record*. 2010. 2164(1). Pp. 132–140. DOI: 10.3141/2164-17. URL: <https://doi.org/10.3141/2164-17>.
46. Siddique, R., Khan, M.I. *Supplementary Cementing Materials 2008*.
47. Haji, A.A., Parikh, K.B., Shaikh, M.A., Jamnu, M.A. Experimental Investigation of Pervious Concrete With Use of Fly Ash and Silica Fume As Admixture. 2018. (March). Pp. 11–18.
48. Lund, M.S.M., Kevern, J.T., Schaefer, V.R., Hansen, K.K. Mix design for improved strength and freeze-thaw durability of pervious concrete fill in Pearl-Chain Bridges. *Materials and Structures/Materiaux et Constructions*. 2017. 50(1). DOI: 10.1617/s11527-016-0907-4.

### Contacts:

Vera Galishnikova, +7(915)379-24-68; [galishnikova-vv@rudn.ru](mailto:galishnikova-vv@rudn.ru)

Shamseldin Abdo, +7(999)519-37-18; [eng.shamseldin13@hotmail.com](mailto:eng.shamseldin13@hotmail.com)

Ahmed Fawzy, +20(111)160-96-14; [engahmedfawzy90@yahoo.com](mailto:engahmedfawzy90@yahoo.com)



DOI: 10.18720/MCE.93.8

## Lightweight cement mortar with inorganic perlite microspheres for equipping oil and gas production wells

**O.V. Kazmina, N.A. Mitina, K.M. Minaev**

*National Research Tomsk Polytechnic University, Tomsk, Russia*

\* E-mail: [mitinana@tpu.ru](mailto:mitinana@tpu.ru)

**Keywords:** cement slurry, well cementing, hollow perlite microspheres, cement stone strength

**Abstract.** In this study lightweight cement mortar was researched. Low-density mortar is used for cementing high temperature, heavily watered oil and gas wells. ISO standard methods, X-ray diffraction analysis and electron microscopy confirm that hollow microspheres of perlite are an effective lightening component for cementing slurry. The results show that admixing microspheres reduces slurry density to 1400 kg/m<sup>3</sup>. Cement stone with the 3% perlite microspheres has an increased strength of 1.9 MPa due to actual interaction of the cement matrix with the aluminosilicate substance of microspheres, the self-reinforcement of the cement matrix by use of ettringite crystals. Cellular multi-chamber structure of perlite microspheres with the reactive surface enhances water-retention of cementing slurry. Use of the perlite microspheres as a facilitating additive for grouting slurry is preferable in comparison with glass microspheres. Low-density cement mortar with perlite microspheres is recommended a lightweight solution for cementing oil and gas wells.

### 1. Introduction

In the oil and gas industry in the extraction of minerals, one uses well cementing [1–4]. The process consists in cement slurry injection in annular space on design height and displacement of drilling mud in a casing column (Figure 1). Well cementing aims to isolate productive objects, to reinforce wells, and to separate beds. Poor quality process leads to wrong assessment of oil and gas reserves, their flows to other beds with less pressure, and flooding of productive horizons. Reliable isolation of beds opened during drilling wells simultaneously ensures the protection of mineral resources that is important from environmental point of view and relevant at present.

Up to now, the world practice of well cementing uses the method of two separate plugs proposed by A. A. Perkins, “Perkins Oil Well Cementing Co.,” Calif [5]. As result of the ongoing development of drilling, as well as taking into account well construction in new complicated conditions, it is required both to improve cementing process and the technical means for its implementation and to develop compositions of cement slurries with adjustable setting times [6–10]. For instance, to cement highly watered areas in the wells with high-temperature, it is required a low-density cement system that can reduce hydrostatic pressure in the column with fluid when injecting cement slurry. In this case, standard cement cannot be used because the pressure at the bottom of the well will exceed the gradient pressure.

The increase of well depth leads to the fact that the necessary interval for the separation of beds increases, and cross-section contains a large number of horizons that must be separated. In particular, when drilling out gas and gas condensate fields to reduce the possibility of gas movement, it is required to raise grouting slurry on significant height. This can be done using the following methods:

- use of two-stage cementing with some breakage of the cement ring continuity at a height;
- reverse circulation and its combination;
- use of grouting slurry of reduced density, i.e., reducing the difference between the density of cement and one of drilling mud with simultaneous regulation other properties of grouting slurry.

---

Kazmina, O.V., Mitina, N.A., Minaev, K.M. Lightweight cement mortar with inorganic perlite microspheres for equipping oil and gas production wells. Magazine of Civil Engineering. 2020. 93(1). Pp. 83–96. DOI: 10.18720/MCE.93.8

Казьмина О.В., Митина Н.А., Минаев К.М. Облегченный цементный раствор с неорганическими перлитовыми микросферами для обустройства нефтегазодобывающих скважин // Инженерно-строительный журнал. 2020. № 1(93). С. 83–96. DOI: 10.18720/MCE.93.8



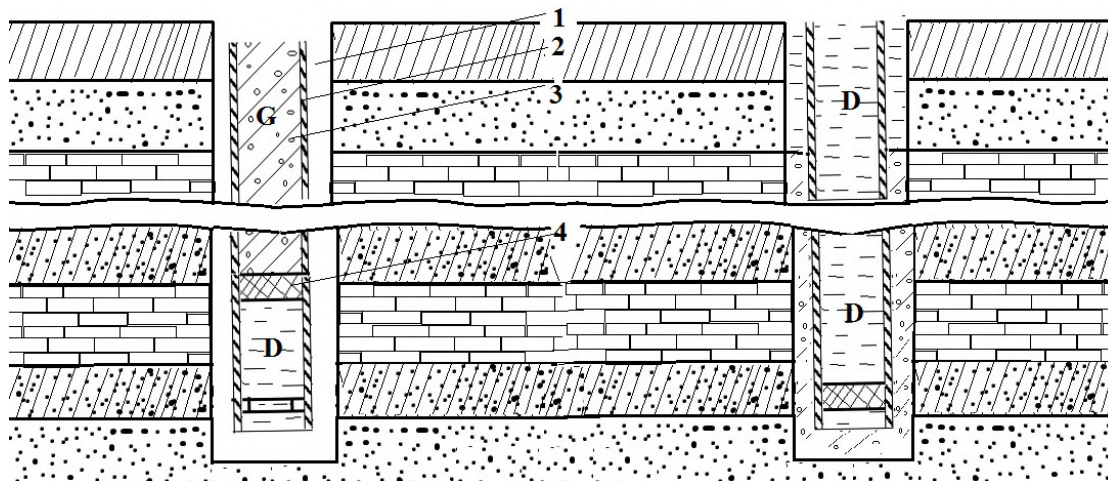


**Figure 1. Flow sheet of the process of injection of cement slurry into hole-casing clearance:**  
**1 – hole-casing clearance; 2 – casing column; 3 – cementing slurry; 4 – cement plug;**  
**D – drilling fluid; G – cementing slurry.**

Lightweight grouting slurries are widely used in oil production practice. The most well-known additions to reduce cement slurry density are bentonite, perlite, pozzolan materials, diatomite earth, and gilsonite [10, 11]. When using the majority of fillers, reduction of cement slurry density consists in retaining excess water amount with additions, i.e. in an increase of water-cement ratio or introduce of air with filler. In all cases, the introduction of fillers promotes the reduction of mechanical strength of hardened cement paste. At the same time, grouting slurries must have low and stable (regardless of the pressure in the well) apparent density, high uniformity, certain consistency (cement spreadability of 20–25 cm), tensile strength at the bend of at least 1 MPa, and heat-shielding properties in solidified state. Such properties of cement slurries can be obtained by introducing the microspheres that are characterized not only by low density and size but also by high specific strength in bulk compression into their composition [12–24]. As a result, slurries have become practically incompressible in spite of low density, which allows them to be pumped on any depth for one operation with a reverse rise to ground surface. Increased strength and crack resistance of a stone allow excluding repeated insulation work during perforation of a column, and sufficiently strong grip ensures the tightness of annular space [25].

The glass microspheres have several advantages for lightweight grouting compositions. For example, the microspheres 3M™ have ideal spherical shape, apparent density from 0.125 to 0.6 g/cm<sup>3</sup>, a thermal conductivity of 0.05–0.26 W/(m K) at 0 °C, particle size from 30 to 120 μm, 90 % of undisturbed microspheres with isostatic crushing resistance according to ISO 9001:2000. Due to possessing the complex of properties, the glass microspheres are widely used in different branches. Traditional production of the glass microspheres is based on high-temperature processing of frit. Frit powder is obtained by melting glass of certain chemical composition at temperatures about 1400 °C with following size reduction down to set value. The chemical composition is mainly borosilicate glass [16–18]. The technology relates to processes with high-energy consumption and significant material consumption.

Production of the perlite microspheres from natural raw materials excludes the stage of glass melting, is less energy- and material-consuming and hence cost-effective. Technology is based on thermal swelling of a certain fraction of perlite rock [25]. The microspheres of expanded perlite are successfully used in the composition of lightweight heat-insulating concrete and construction ceramics [26, 27]. There are also known some studies on use of the perlite microspheres as facilitating additions in the composition of grouting slurries for well cementing [12]. However, these studies do not reflect the influence of the perlite microspheres on the formation of structure and basic properties of grouting materials.

Consequently, the aim of the work is to establish the influence of the microspheres of expanded inorganic perlite on the processes of the formation of structure and the basic properties of lightweight grouting slurry.

## 2. Materials and Experimental method

### 2.1. Materials

*The microspheres.* Perlite is a widespread volcanic rock with a high content of glassy phase. The largest reserves of perlite are located in Greece and the United States, the major producers of perlite grit, microspheres and sand currently are Turkey, Hungary, Italy, and Mexico. The main factors affecting the process of swelling perlite rocks are temperature and swelling interval, the content of hard-to-remove moisture in volcanic glass, the chemical composition of the rock and the content of alkalis, and the method and mode of firing.

The perlite hollow microspheres used in this study are obtained in the industrial vertical furnace at a temperature of 1500 °C from the perlite rock of the Khasyn deposit (Russia). The chemical composition in oxides form of initial perlite rock and the microspheres is presented in Table 1. According to the chemical composition, perlite belongs to the group of aluminosilicate glasses, has a high content of SiO<sub>2</sub> – about 75 %, Al<sub>2</sub>O<sub>3</sub> – 13 %, and a significant amount of alkaline oxides. The phase composition of perlite microspheres consists of orthoclase. The radiograph of the microspheres contains the amorphous halo of the glass phase (Figure 2).

**Table 1 The oxide composition of perlite, microspheres.**

Material	Content of oxides (wt. %)							Loss on ignition, (wt. %)
	SiO <sub>2</sub>	Na <sub>2</sub> O	CaO	Fe <sub>2</sub> O <sub>3</sub>	K <sub>2</sub> O	Al <sub>2</sub> O <sub>3</sub>	MgO	
Initial perlite rock	65.0–75.0	5.0–6.0	0.5–2.0	1.0–3.0	5.0–6.0	10.0–16.0	0.2–3.0	1.0 – 4.5
Microspheres of perlite	74.7	5.3	0.6	1.2	5.1	12.8	0.3	–

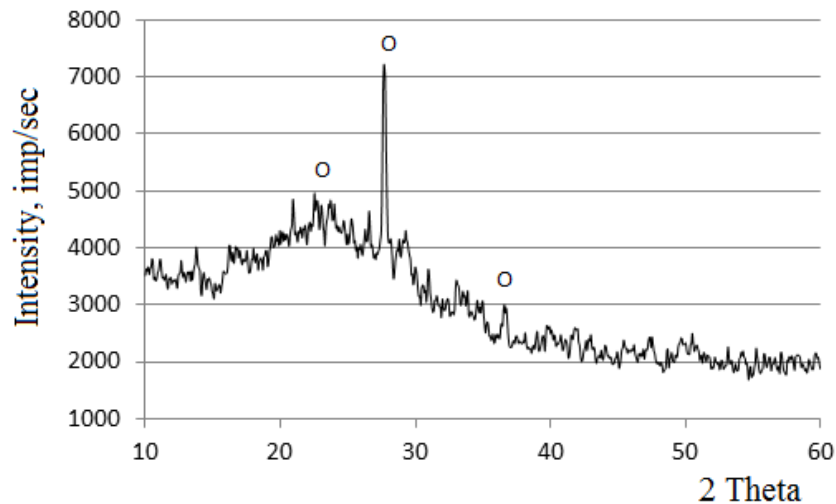


**Figure 2. XRD patterns of perlite microspheres: O – orthoclase.**

According to electron microscopy, the average size of the perlite microspheres is up to 150 μm with wall thickness of about 2 μm (Figure 3), and the shape is uneven, elongated and asymmetric, unlike the spherical shape of the borosilicate glass microspheres. The photomicrographs show that the perlite microspheres have a multi-chamber cellular structure that must help to increase the strength characteristics of the compositions.

The technical characteristics of the perlite microspheres are given in Table 2. The values of the properties indicate the principal possibility to use the perlite microspheres as facilitating addition in grouting slurries. According to the main indicators, the perlite microspheres correspond to the glass microspheres 3M™ obtained from sodium borosilicate glass.

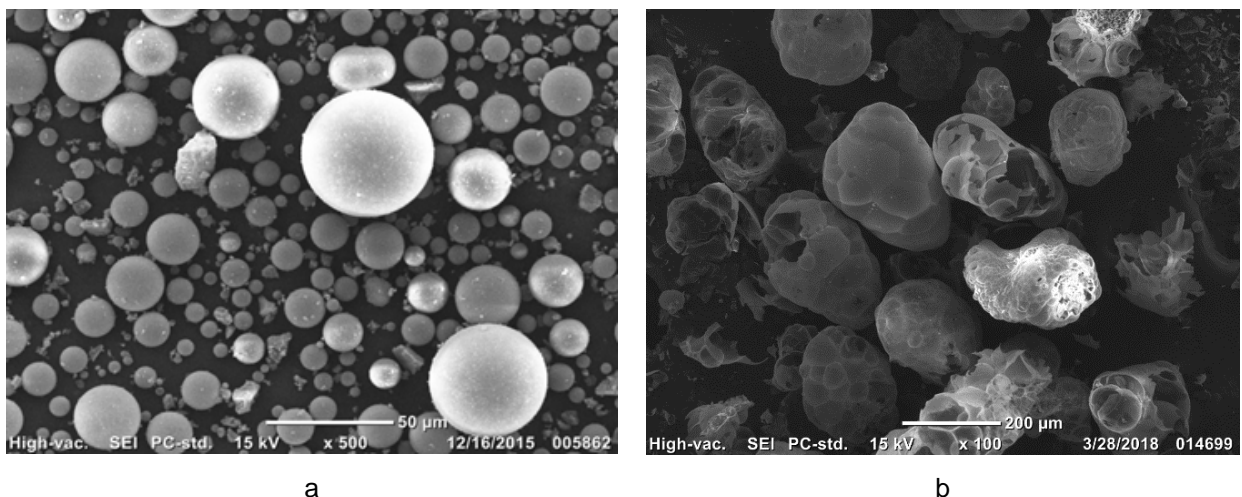


**Figure 3. Electronic microscopy of the glass microspheres (a) and the perlite microspheres (b).**

**Table 2. Physical properties of the perlite microspheres.**

Parameters	Indicator values	
	Perlite microspheres	Glass microspheres 3M™ Glass Bubbles HGS
Bulk density, kg/m <sup>3</sup>	150	50–280
True density, kg/m <sup>3</sup>	2414	150–410
Median particle size, μm	125	30–120
Microsphere wall thickness, μm	2 ± 0.5	0.52–1.29

*Grouting cement.* As the basis of the grouting composition, we have used grouting addition free cement of the class I-G oil well cement brand, intended for fastening oil and gas wells at moderate temperatures during exploration and production drilling (API Spec 10A/ISO 10426-1 2009). Chemical composition of grouting cement and its technical characteristics are presented in Tables 3 and 4.

**Table 3. The main chemical and phase composition class I-G oil well cement.**

Content (wt. %)									
SiO <sub>2</sub>	CaO	Fe <sub>2</sub> O <sub>3</sub>	Al <sub>2</sub> O <sub>3</sub>	CaO <sub>free</sub>	MgO	C <sub>3</sub> S	C <sub>2</sub> S	C <sub>3</sub> A	C <sub>4</sub> AF
20.2–20.7	66.2– 67.0	3.5–4.0	6.0–6.7	1.2	1.4–2.0	58.0–67.0	8.0–15.0	10.0–12.0	10.5–12.5

**Table 4. Technical characteristics class I-G oil well cement.**

Measured parameters	Values of parameters
Compressive strength test (8 h curing time), MPa	4.5–6.1
Free-fluid content, ml	6.4–8.5
Specific surface, m <sup>2</sup> /kg	350–370
Spreadability, mm	200–215
Thickening time, min	180–192
Sulfur trioxide (SO <sub>3</sub> ), wt.%	2.8–3.0

## 2.2. Experimental method

Lightweight grouting mixtures were prepared by mixing components following the regulatory requirements (API Spec 10A/ISO 10426-2 2003). The Amount of the perlite microspheres have been varied from 1 to 3 % by weight.

*Properties of grouting slurry.* Spreadability, the property of liquid to spread over a solid surface, is an indicator of pumpability of grouting slurry. During injection into the annular space of a well, it is necessary to preserve the mobility of the slurry for a certain time. Spreadability has been determined using the spreadability cone KR-1 (Figure 4). The truncated cone – ring of the device has dimensions: inner diameter of the upper basis is 36 mm, one of the lower bases is 64 mm, height is 60 mm, and volume is 120 cm<sup>3</sup>.

*The density of grouting cement slurry* has been determined with lever balances. The measuring range of slurry density are: on the upper scale from 0.8 to 1.5 g/cm<sup>3</sup>, on the lower scale from 1.6 to 2.6 g/cm<sup>3</sup>; measurement error ± 0.01 g/cm.

*Water segregation of grouting slurry* has been determined according to API Spec 10A/ISO 10426-2 2003 «Petroleum and natural gas industries—Cements and materials for well cementing—Part 1: Specification». The cement slurry is poured into two cylinders with a volume of 250 cm<sup>3</sup> up to mark of 250 cm<sup>3</sup>. Settling time is 2 h ± 5 min. The liquid that has been separated from a cement slurry under static conditions on the surface of cement paste is taken with a pipette, and its volume has been measured with the help of a cylinder 20 cm<sup>3</sup>.

*The thickening time of grouting cement slurry* has been determined with the atmospheric consistometer OFITE 80 in accordance with API Spec 10A (Figure 5). This property characterizes possibility to pump grouting slurry during a given time interval when well casing. The principle of operation of the consistometer is based on the determination of torque at thickening cement slurry in the body rotating at a given speed. Determination has been performed at atmospheric pressure and speed of rotation of chamber with cement slurry of 150 rpm. The working temperature of the device is up to 93 °C.

Strength tests of the samples of grouting stone at bending have been performed on the samples of 40×40×160 mm using the MATEST machine of model E160 (Figure 6). The maximum load of the device is 500 kN for the compression test and 15 kN for the bending test. The accuracy class is 1. Tests of molded samples have been performed after 2 days of storage in the thermostat at 75 °C.



Figure 4. Grout flow cone KR-1.



Figure 5. The atmospheric pressure consistometer, OFITE 80.



Figure 6. Machine for strength tests, MATEST E160.

### 3. Results and Discussion

The use of high-quality lightweight grouting materials must solve the problem of one-stage grouting the well. Therefore, such properties as the density of slurry and cement paste and its strength are of particular importance. Hardened cement paste takes a part of loads falling on the column. The increased values of mechanical strength of the stone increase bearing capacity of a casing pipe. In addition to strength characteristics, grouting slurries must have certain values of technological parameters such as spreadability, water segregation, and thickening time.

The basic characteristics of grouting slurries from Portland cement of I-G brand without additions obtained at water-cement ratio ( $W/C$ ) of 0.5 and 0.8 have been preliminary determined. Results (Table 5) have shown that slurry correspond to normative requirements on all indicators, except one of density and water segregation. At  $W/C = 0.5$  slurry density exceeds permissible values, such slurry will have low pumpability. If  $W/C$  increases up to 0.8, the density decreases, however, that is connected with violation of sedimentation stability of cement paste and increase of water segregation. As one can see from Table 5 at  $W/C = 0.8$ , the water segregation is 9.5 that exceeds the permissible values.

The introduction of the perlite microspheres into the composition of grouting slurry allows reducing the slurry density while maintaining the sedimentation stability of cement paste. To this end, the perlite microspheres which its amount varied from 0.5 to 3.0 % by weight have been added to the slurry. The slurries differing in water-cement ratio and amount of the introduced microspheres have been investigated.

**Table 5. Values of parameters of grouting slurries without microspheres.**

Measured parameters	Values of I-G parameters at $W/C$ ratio		Requirements for lightweight grouting cement at operating temperatures	
	0.5	0.8	low and normal	moderate and higher
Paste density, $\text{kg/m}^3$	1800	1600	1400–1600	1400 – 1600
Spreadability, mm	245	250	not less than 200	not less than 200
Free-fluid content, ml	0.1	9.5	not more than 7.5	not more than 7.5
Thickening time, min	95	180	not less than 90	not less than 90
Strength at the age of 2 days, MPa	4.3	3.7	not less than 0.7	not less than 1.0

It has been found that regardless of the water-cement ratio, the density of grouting slurry decreases with an increase in the amount of the microspheres being introduced into composition due to low density and high porosity of addition itself (bulk density  $150 \text{ kg/m}^3$ ) (Figure 7).

Water segregation of cement slurries is an indicator of filtration properties characterizing their water-holding capacity. In stationary state, grouting slurry is divided into phases of water and cement. Water, rising up, can wash in hardening slurry channels that will not be overgrown in the process of further hardening and are able to pass through hardened cement paste formation fluids. Therefore, to improve properties of cement paste, additional additions that increase the sedimentation stability of grouting mixture are introduced into the composition of grouting slurry. It has been established that at the  $W/C$  ratio of 0.5, the water segregation is at zero level and does not change with the introduction of the microspheres into the slurry (Figure 7). At the  $W/C$  ratio of 0.8, the water segregation at the content of the microspheres from 0.5 to 1.5 % exceeds permissible values (more than 5.9 ml), while at the content of the microspheres of 2 and 3 % it meets the requirements (API Spec 10A/ ISO 10426-1 2009) (Figure 8).

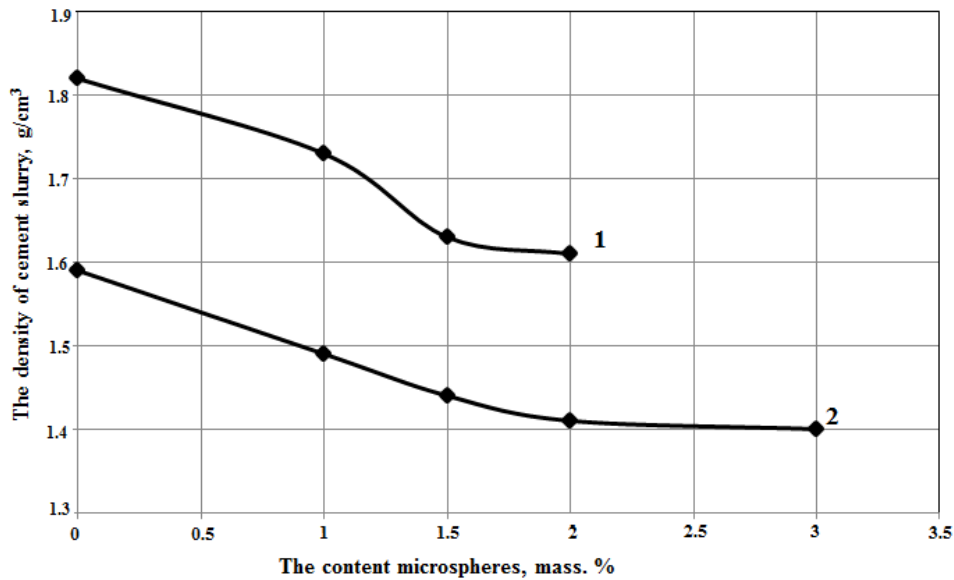


**Figure 7. The density of cement slurry with different proportions of content microspheres at a water-cement ratio: 1 – 0.5; 2 – 0.8.**

The thickening time of the paste without microspheres is more than 90 minutes. When adding microspheres, the paste obtained with the  $W/C$  ratio of 0.5, does not meet these requirements, unlike the  $W/C$  ratio = 0.8. Similar dependence is observed for spreadability index (Figure 9), which the value for the paste with the  $W/C$  ratio of 0.8 does not change and is at standard level for the cement slurries (250 mm), for the paste with the  $W/C = 0.5$  spreadability value decreases sharply with an increase of amount of the microspheres being introduced. As a result, the grouting slurry obtained at the  $W/C$  ratio of 0.8 has optimal values of indicators for density, water segregation, and thickening time.

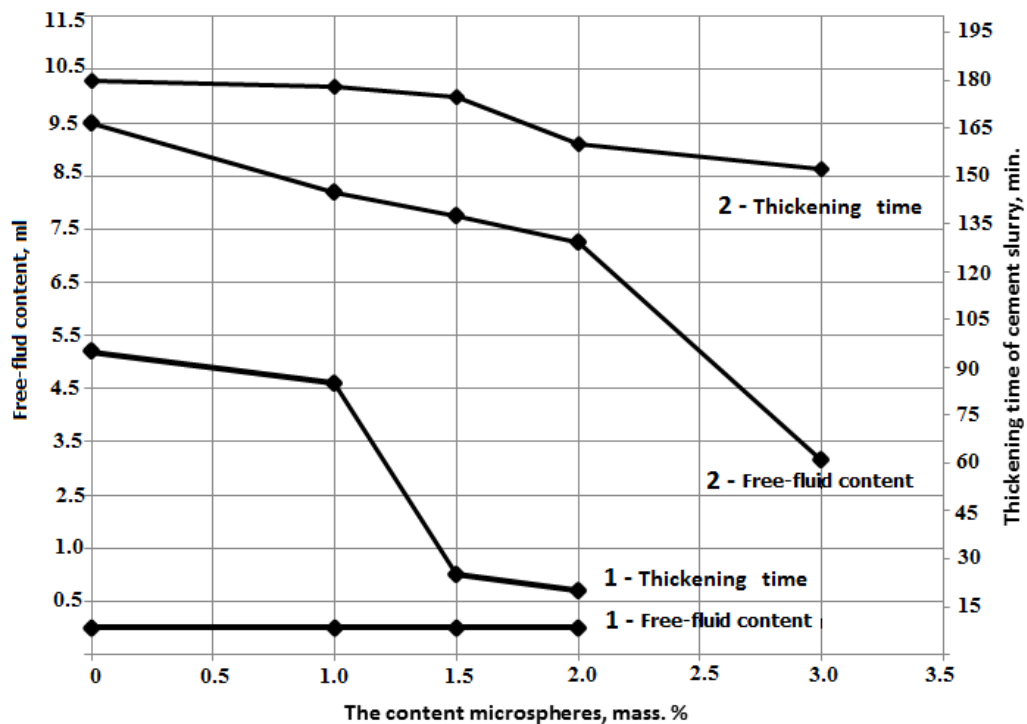


**Figure 8. Free-fluid content and thickening time of cement slurry with different content of perlite microspheres at a water-cement ratio: 1 – 0.5; 2 – 0.8.**

Regardless of water-cement ratio, the presence of the microspheres in the grouting material reduces its strength parameters however at the lower water-cement ratio of 0.5, the strength of the samples at the age of 2 days is slightly higher in comparison with the strength of the stone obtained at the  $W/C$  of 0.8 (Figure 10). This is connected with the following processes:

- Diffusion of  $CO_2$  in pores and capillaries of stone filled with air;

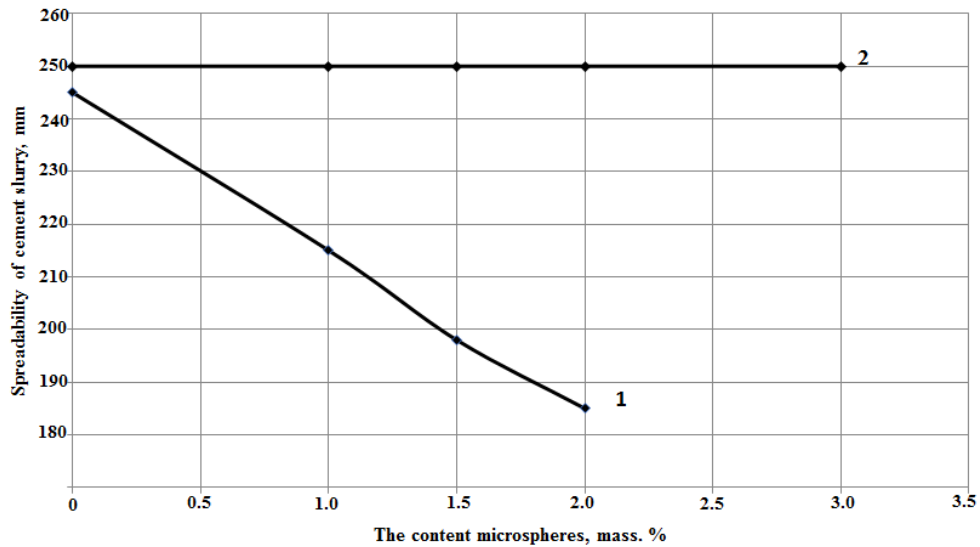


**Figure 9. Spreadability of cement slurry with different content of perlite microspheres at a water-cement ratio: 1 – 0.5; 2 – 0.8.**

- Dissolution of carbon dioxide in the liquid phase of cement slurry to form carbonic acid and its dissociation into hydrogen ions, bicarbonate and carbonate ions;
- Diffusion of the formed ions in liquid phase;
- Dissolution of calcium oxide hydrate, its dissociation and diffusion of  $\text{Ca}^{2+}$  and  $\text{OH}^-$  ions;
- Chemical interaction of carbon dioxide with dissolved calcium oxide hydrate with the formation of bicarbonate and calcium carbonate;
- Crystallization of calcium carbonate.

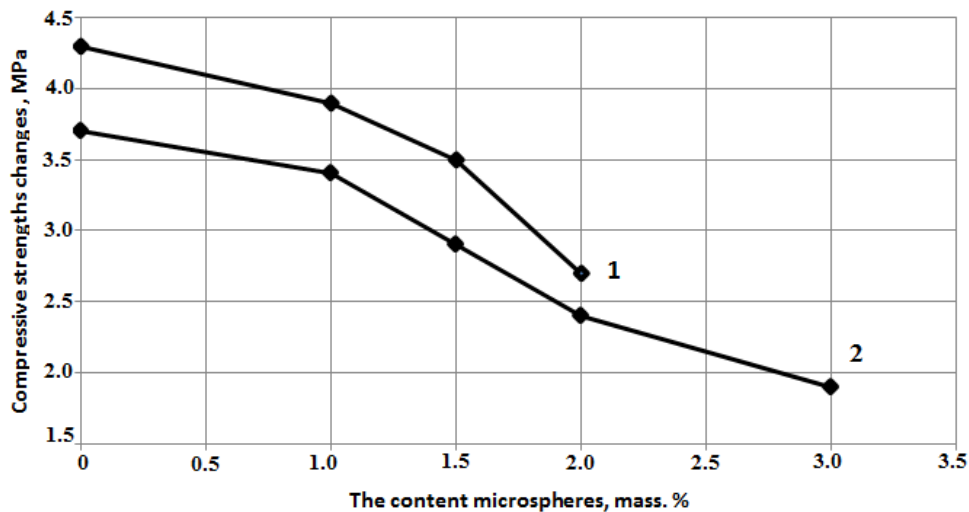
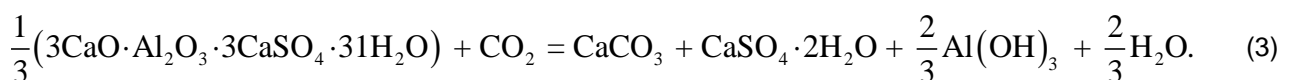
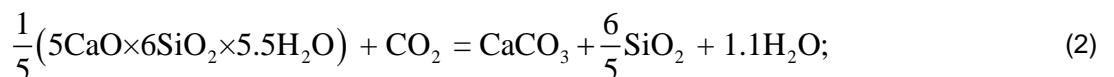


**Figure 10. Compressive strengths changes after 2 days hardened cement paste with different content of perlite microspheres at a water-cement ratio: 1 – 0.5; 2 – 0.8.**

Interaction of hydrate phases of hardening cement with  $\text{CO}_2$  occurs in accordance with the equations 1 to 3:



The x-ray diffraction data have shown the presence of the following crystalline phases on the radiograph: portlandite  $\text{Ca}(\text{OH})_2$ , calcite  $\text{CaCO}_3$ , and ettringite  $\text{Ca}_6\text{Al}_2(\text{SO}_4)_3(\text{OH})_{12} \cdot 25\text{H}_2\text{O}$  (Figure 11). The radiograph does not contain distinct reflexes of calcium hydrosilicates because of their weak crystallization that is connected with the condition of hardening of stone (low-temperature hydrothermal processing at  $75^\circ\text{C}$ ).

The intensity of portlandite reflexes in the hardened cement paste obtained at the  $W/C = 0.8$  is higher than that of the stone at the  $W/C = 0.5$  which is explained by the introduction of a large amount of water into the system. The increased intensity of calcite reflex in the sample obtained at the  $W/C = 0.5$  is probably caused by the fact that the sizes of calcium hydroxide crystals have greater dispersion and, therefore, are more active and better react with  $CO_2$  from the air, forming calcite in large quantities.

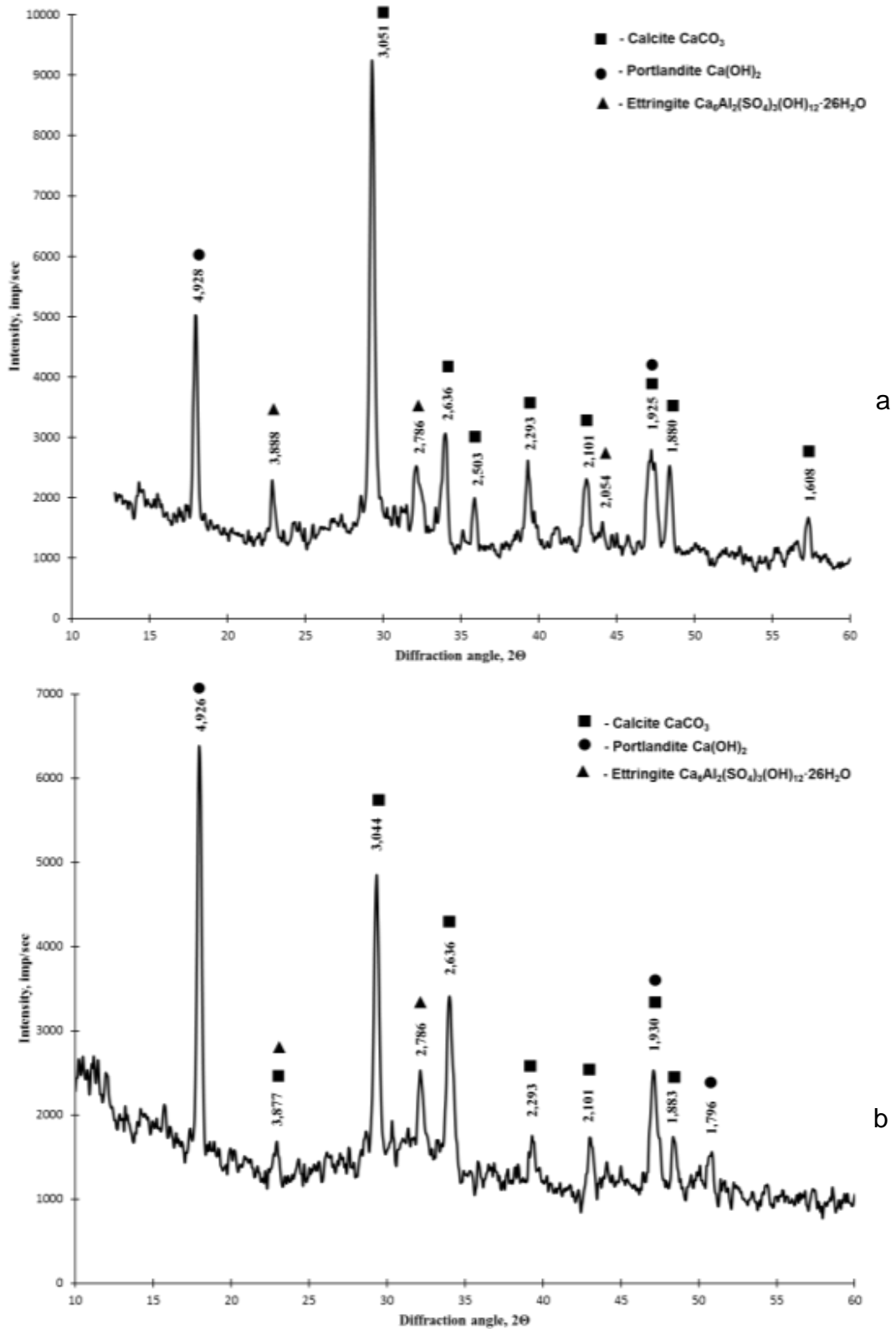


**Figure 11. XRD patterns hardened cement paste one microspheres at  $W/C$  0.5 (a), 0.8 (b).**

Thus, it has been established that at the  $W/C$  ratio = 0.8, the strength decreases with an increase in the amount the microsphere, but corresponds to the requirements, more than 0.7 MPa). The density and water segregation of the slurry at this ratio do not corresponds to the requirements for compositions containing the

microspheres in an amount from 0.5 to 2.0 %. Therefore, the composition with the amount of the microspheres equal to 3.0 %, obtained at the  $W/C$  ratio = 0.8, is optimal.

The physical and technical properties of hardened cement paste are determined by the type and amounts of crystalline hydrates being its constituents, size, and shape of crystals, size and amount of pores, degree of cement hydration, and other factors. Comparative analysis of cement paste samples obtained at  $W/C$  ratio = 0.8 with the addition of the perlite microspheres in the amount of 1.0 and 3.0 wt. %, in conditions of low-temperature (75 °C) hydrothermal treatment has shown the following. According to the x-ray phase analysis (Figure 12), the radiographs show reflexes corresponding to portlandite  $\text{Ca}(\text{OH})_2$  (PDF Number 000-44-1481 d-spacing 4.922; 2.627; 1.795 Å), ettringite  $3\text{CaO}\cdot\text{Al}_2\text{O}_3\cdot3\text{CaSO}_4\cdot32\text{H}_2\text{O}$  (PDF Number 000-41-1451 d-spacing 9.720; 5.610; 3.873; 2.772 Å), calcite  $\text{CaCO}_3$  (PDF Number 000-05-0586 d-spacing 3.035; 2.495; 2.095; 1.973; 1.875 Å). Moreover, the intensity of the basic calcite reflex is higher for the samples with 3.0 % of microspheres that indicates improvement of conditions for carbonization process.

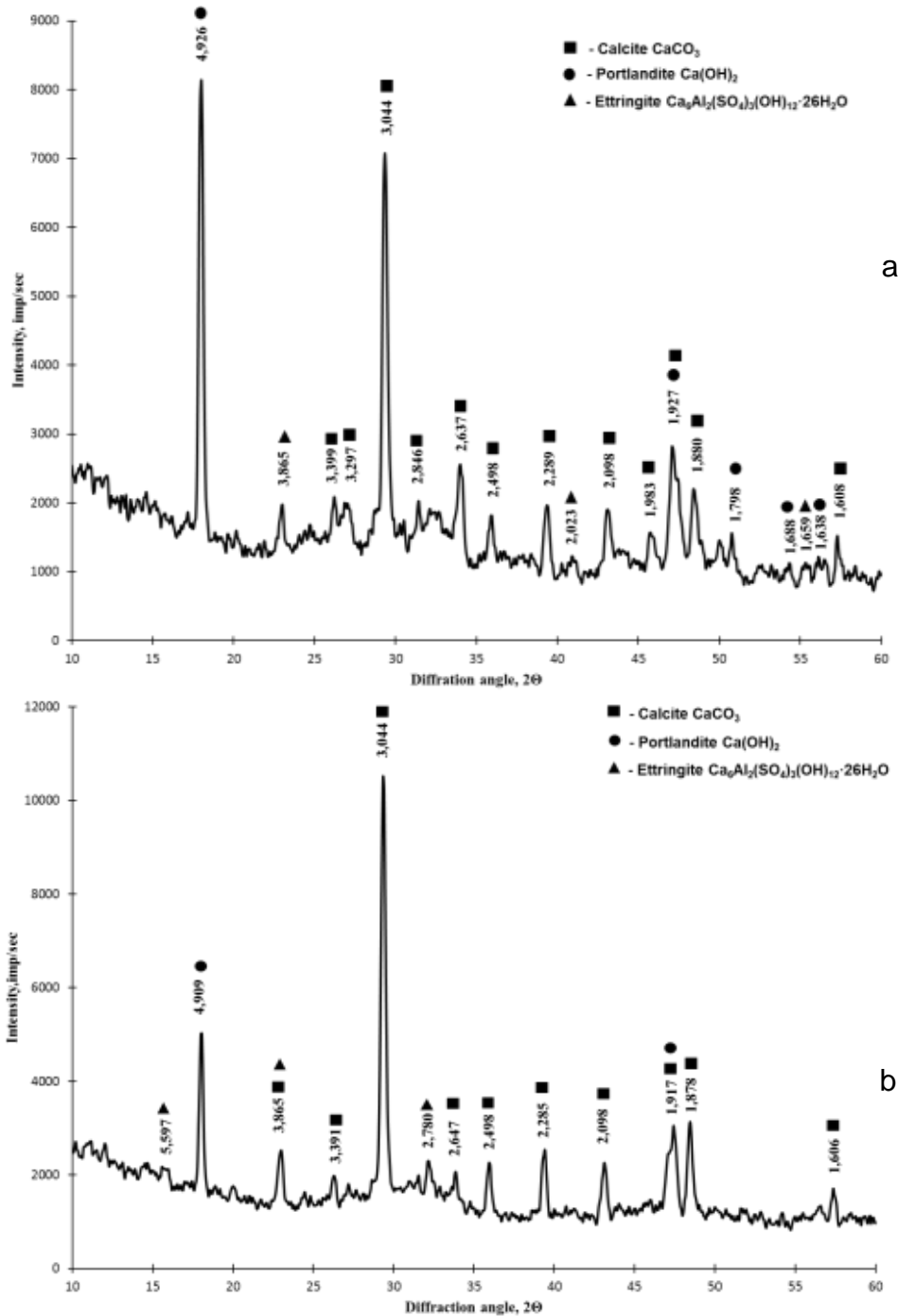
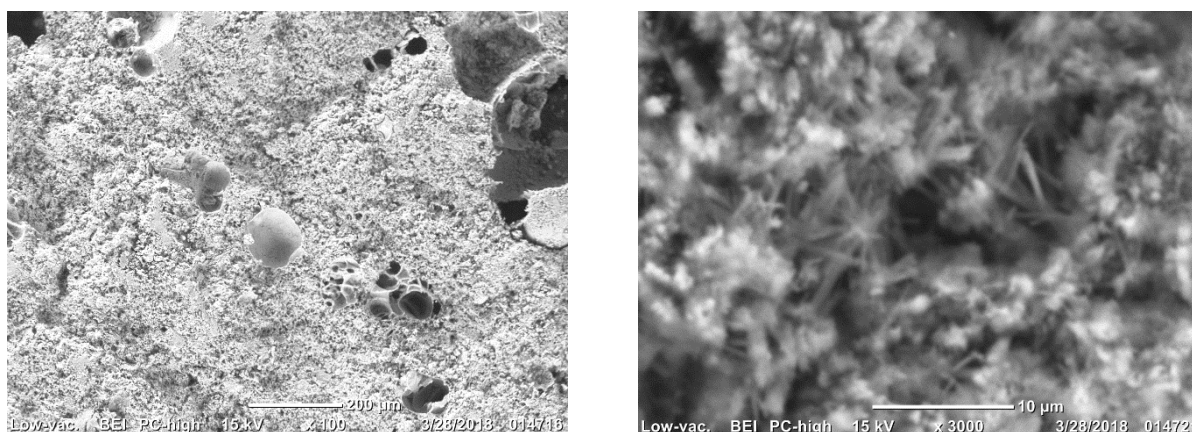


Figure 12. XRD patterns hardened cement paste at  $W/C$  0.8 with perlite microspheres 1.0 % (a) and 3.0 % (b).

According to scanning electron microscopy (Figure 13), the grouting stone obtained with the amount of the microspheres equal to 1.0 % has a dense interfacial transition zone with a surface of the microspheres that indicates strong adhesion interaction of aluminosilicate substance of the microspheres with the products of hydration of cement paste. Cement matrix has a fairly loose porous structure composed mostly by a gel-like poor crystallized formation of calcium hydrosilicates, and hydroaluminates and carbonate formations. The presence of needle crystals of ettringite with a length from 2 to 5  $\mu\text{m}$  is noted that consists with XRF data.

The microphotography of the sample obtained with 3.0 % of microspheres (Figure 14) show that cement slurry moistens well the microsphere at cement – microsphere boundary and interacts with substance of the granules to form products that harden the system as a whole. It can be noted that the surface of the microspheres is covered with highly dispersed fibrous hydrate new formations – the products of interaction of the substance of the microspheres with cement phases. Thus, the microspheres and the smallest fragments of the perlite microspheres can be centers of formation of hardened cement paste structure. The cement matrix itself has a loose structure, porosity and elongated crystals of ettringite with a length of 5–10  $\mu\text{m}$ . Increased porosity is a consequence of air entrainment in the time of the introduction of granular filler. With long-term hardening, more than 2 days, porosity is compensated by the increase in the amount of crystalline phase due to the increase in the number of crystallization centers.



**Figure 13. SEM cement slurry with perlite microspheres 1.0 % at  $W/C$  0.8.**

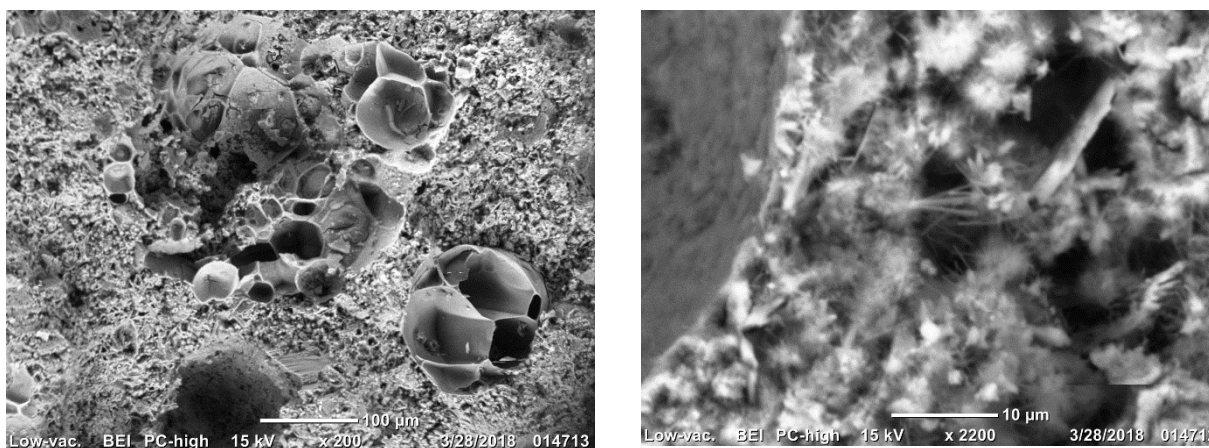


**Figure 14. SEM cement slurry with perlite microspheres 3.0 % at  $W/C$  0.8.**

The hollow perlite microspheres are effective facilitating addition for grouting slurry which introduction in amount of 3.0 % reduces slurry density from 1600 to 1400  $\text{kg/m}^3$ , at the strength of hardened cement paste of 1.9 MPa, which is by 2.7 times higher than the requirements (not less than 0.7 MPa). The hardened cement paste with the perlite microspheres has increased strength due to both the multi-chamber structure of the microspheres and the formation of hydrated phases of cement paste with the crystallization of needle-shaped ettringite as a self-reinforcing component that is justified by data of electron microscopy and x-ray phase analysis.

#### 4. Conclusions

The perlite microspheres can be used to reduce the density of grouting slurry that has a promising performance on basic properties. Analysis of obtained results has shown the effectiveness of use of the perlite microspheres as a facilitating addition and allowed to draw the following conclusions:

1. Use of the perlite microspheres as a facilitating addition for grouting slurry is preferable in comparison with glass microspheres, since the synthesis of the perlite microspheres excludes additional high-temperature

technological stage of glass melting and use abundant, relatively inexpensive rock for their production in contrast to specially melted borosilicate glass.

2. Developed composition of lightweight grouting slurry consisting of cement of grade I-G (97 %) and the perlite microspheres (3.0 %) at water-cement ratio equal 0.8, provides slurry density equal 1400 kg/m<sup>3</sup>, water segregation equal 3.5 ml, and thickening time equal 150 min that corresponds to the requirements of API Spec 10A/ ISO 10426-1 2009.

3. Low water segregation, i.e. good water holding capacity at the introduction of the perlite microspheres (3.0 %) in grouting cement mixture is explained by their cellular multi-chamber structure and reactive surface.

4. It is established that cement paste with the perlite microspheres in amount of 3.0 % at the age of 2 days has increased strength of 1.9 MPa in comparison with specified value up to 0.7 MPa that is caused by intensive formation of cement matrix crystals at direct participation of aluminosilicate substance of the microspheres, self-reinforcement of cement matrix with ettringite crystals and formation of durable structural frame from perlite microspheres with multi-chamber structure.

## 5. Acknowledgments

This research was supported by Tomsk Polytechnic University CEP grant Number DR1aP\_75/2019

## References

- Pang, X., Cuello Jimenez, W., Iverson, B.J. Hydration kinetics modeling of the effect of curing temperature and pressure on the heat evolution of oil well cement. *Cement and Concrete Research*. 2013. 54. Pp. 69–76 DOI: 10.1016/j.cemconres.2013.08.014.
- Vidal, A.V., Araujo, R.G.S., Freitas, J.C.O. Sustainable cement slurry using rice husk ash for high temperature oil well. *Journal of Cleaner Production*. 2018. 204. Pp. 292–297. DOI: 10.1016/j.jclepro.2018.09.058.
- Labus, M., Such, P. Microstructural characteristics of wellbore cement and formation rocks under sequestration conditions. *Journal of Petroleum Science and Engineering*. 2016. 138. Pp. 77–87. DOI: 10.1016/j.petrol.2015.12.010.
- Balthar, V.K. C.B.L.M., Filho, R.D.T., De Moraes Rego Fairbairn, E., De Miranda C.R. Durability of Lightweight Slurries for Oilwell Cementing. *Key Engineering Materials*. 2016. 711. Pp. 203–210. DOI: 10.4028/www.scientific.net/KEM.711.203.
- Dwight, K. *Smith Cementing*. – New York: Henry L. Doherty Memorial Fund of AIME, 1976, – r.174
- Kmieć, M., Karpiński, B., Antoszkiewicz, M., Szkodo, M. Laboratory research on the influence of swelling clay on the quality of borehole cementing and evaluation of clay-cutting wellbore tool prototype. *Applied Clay Science*. 2018. 164. Pp. 13–25. DOI: 10.1016/j.clay.2018.04.028.
- Bu, Y., Hou, X., Wang, C., Du, J. Effect of colloidal nanosilica on early-age compressive strength of oil well cement stone at low temperature. *Construction and Building Materials*. 2018. 171. Pp. 690–696. DOI: 10.1016/j.conbuildmat.2018.03.220.
- Moradi, S.S.T., Nikolaev, N.I., Leusheva, E.L. Improvement of cement properties using a single multi-functional polymer. *International Transaction Journal of Engineering. A: Basics*. 2018. 31(1). Pp. 181–187. DOI: 10.5829/ije.2018.31.01a.24.
- Ghabezloo S. Effect of the variations of clinker composition on the poroelastic properties of hardened class G cement paste. *Cement and Concrete Research*. 2011. 41(8). Pp. 920–922. DOI: 10.1016/j.cemconres.2011.03.022.
- Choolaei, M., Rashidi, A.M., Ardjmand, M., Yadegari, A., Soltanian, H. The effect of nanosilica on the physical properties of oil well cement. *Materials Science and Engineering. A*. 2012. 538. Pp. 288–294. DOI: 10.1016/j.msea.2012.01.045.
- Da Silva Araujo Filho, R.G., De Oliveira Freitas, J.C., De Freitas Melo, M.A., Braga, R.M. Lightweight oil well cement slurry modified with vermiculite and colloidal silicon. *Construction and Building Materials*. 2018. 166. Pp. 908–915. DOI: 10.1016/j.conbuildmat.2017.12.243.
- Bubnov, A.S., Boyko, I.A., Khorev, V.S. Strength properties of cement slurries with lightweights applied in oil and gas wells. *IOP Conference Series: Earth and Environmental Science*. 2015. 24(012010). DOI: 10.1088/1755-1315/24/1/012010.
- Inozemtcev, A.S. Average density and porosity of high-strength lightweight concrete. *Magazine of Civil Engineering*. 2014. 51(7). Pp. 31–37. DOI: 10.5862/MCE.51.4.
- Steshenko, A.B., Kudyakov, A.I. Cement based foam concrete with aluminosilicate microspheres for monolithic construction. *Magazine of Civil Engineering*. 2018. 84(8). Pp. 86–96. DOI: 10.18720/MCE.84.9.
- Mastalygina, E.E., Ovchinnikov, V.A., Chukhlanov, V.Yu. Light heat-resistant polymer concretes based on oligoxyhydridesiloxysilane and hollow spherical fillers. *Magazine of Civil Engineering*. 2019. 90(6). Pp. 37–46. DOI: 10.18720/MCE.90.4
- Ren, S., Liu, J.C., Guo, A.R., Zang, W.J., Geng, H.T., Tao, X., Du, H.Y. Mechanical properties and thermal conductivity of a temperature resistance hollow glass microspheres/borosilicate glass buoyance material. *Materials Science and Engineering. A*. 2016. 674. Pp. 604–614. DOI: 10.1016/j.msea.2016.08.014.
- Osamu Saito, Norihiko Yagi. Yoshinori Ito Glass frit useful for the preparation of glass bubbles, and glass bubbles prepared by using it. Patent US 5064784A, 1991.
- Howell, P.A., St. Paul. Glass bubbles of increased collapse strength. Patent US 4391646A, 1983.
- Wang, X., Zhang, Y., Lv, F., Shen, B., et al. Cross-linked polystyrene microspheres as density-reducing agent in the drilling fluid. *Journal of Petroleum Science and Engineering*. 2011. 78(2). Pp. 529–533. DOI: 10.1016/j.petrol.2011.06.016.
- Hua, Z., Lin, M., Guo, J., Xu, F., Li, Z., Li, M. Study on plugging performance of cross-linked polymer microspheres with reservoir pores. *Journal of Petroleum Science and Engineering*. 2013. 105. Pp. 70–75. DOI: 10.1016/j.petrol.2013.03.008.
- Liu, H., Bu, Y., Sanjayan, J.G., Nazari, A., Shen Z. The application of coated superabsorbent polymer in well cement or plugging the microcrack. *Construction and Building Materials*. 2016. 104. Pp. 72–84. DOI: 10.1016/j.conbuildmat.2015.12.058.
- Liu, H., Bu, Y., Nazari, A., Sanjayan, J.G., Shen Z. Low elastic modulus and expansive well cement system: The application of gypsum microsphere. *Construction and Building Materials*. 2016. 106. Pp. 27–34. DOI: 10.1016/j.conbuildmat.2015.12.105.

23. Choolaeia, M., Rashidi, A.M/, Ardjmanda, M., Yadegari, A., Soltanian, H. The effect of nanosilica on the physical properties of oil well cement. *Materials Science and Engineering. A.* 2012. 538. Pp. 288– 294. DOI: 10.1016/j.msea.2012.01.045.
24. Mata, C., Calubayan, A. Use of hollow glass spheres in lightweight cements – Selection Criteria, Society of Petroleum Engineers. SPE Asia Pacific Oil and Gas Conference and Exhibition 2016; Perth; Australia. 2016. code 132952.
25. Angelopoulos, P.M., Taxiarchou, M., Paspaliaris, I. Production of durable expanded perlite microspheres in a Vertical Electrical Furnace. *IOP Conference Series: Materials Science and Engineering.* 2016. 123(012061). DOI: 10.1088/1757-899X/123/1/012061.
26. Tajra, F., Elrahman, M.A., Chung, S.-Y., Stephan, D. Performance assessment of core-shell structured lightweight aggregate produced by cold bonding pelletization process. *Construction and Building Materials.* 2018. 179. Pp. 220–231. DOI: 10.1016/j.conbuildmat.2018.05.237
27. Farnood Ahmadi, P., Ardeshir, A., Ramezaniapour, A.M., Bayat, H. Characteristics of heat insulating clay bricks made from zeolite, waste steel slag and expanded perlite. *Ceramics International.* 2018. 44(7). Pp. 7588–7598. DOI: 10.1016/j.ceramint.2018.01.175.

**Contacts:**

*Olga Kazmina, +7(909)544-60-38; kazmina@tpu.ru*

*Natalia Mitina, +7(3822)563-169; mitinana@tpu.ru*

*Konstantin Minaev, +7(3822)563-169; minaevkm@tpu.ru*

© Kazmina, O.V., Mitina, N.A., Minaev, K.M., 2020



DOI: 10.18720/MCE.93.8

## Облегченный цементный раствор с неорганическими перлитовыми микросферами для обустройства нефтегазодобывающих скважин

**О.В. Казьмина, Н.А. Митина, К.М. Минаев**

*Национальный исследовательский Томский политехнический университет, г. Томск, Россия*

\* E-mail: [mitinana@tpu.ru](mailto:mitinana@tpu.ru)

**Ключевые слова:** цементный раствор, цементирование скважин, полые перлитовые микросферы, прочность цементного камня

**Аннотация.** Объектом данного исследования является облегченный тампонажный раствор. Данный раствор имеет пониженную плотность и используется для цементирования высокотемпературных, сильно обводненных нефтяных и газовых скважин. С использованием стандартных методов ISO, рентгенофазового анализа и электронной микроскопии доказано, что полые микросферы из перлита являются эффективной облегчающей добавкой для тампонажного раствора. Результаты показывают, что введение микросфер уменьшает плотность раствора до 1400 кг/м<sup>3</sup>. Цементный камень с перлитовыми микросферами в количестве 3 %, имеет повышенную прочность 1,9 МПа. Это обусловлено активным взаимодействием цементной матрицы с алюмосиликатным веществом микросфер, самоармированием цементной матрицы с помощью кристаллами этtringита. Сотовая поликамерная структура перлитовых микросфер с реакционноспособной поверхностью обеспечивает высокую водоудерживающую способность тампонажного раствора. Применение перлитовых микросфер в качестве облегчающей добавки для тампонажного раствора является предпочтительнее по сравнению со стеклянными микросферами. Облегченный раствор с перлитовыми микросферами рекомендуется в качестве легкого раствора для цементирования нефтяных и газовых скважин.

### Литература

- Pang X., W. Cuello Jimenez, Iverson B.J. Hydration kinetics modeling of the effect of curing temperature and pressure on the heat evolution of oil well cement // *Cement and Concrete Research*. 2013. 54. Pp. 69–76. DOI: 10.1016/j.cemconres.2013.08.014.
- Vidal A.V., Araujo R.G.S., Freitas J.C.O. Sustainable cement slurry using rice husk ash for high temperature oil well // *Journal of Cleaner Production*. 2018. 204. Pp. 292–297. DOI: 10.1016/j.jclepro.2018.09.058.
- Labus M., Such P. Microstructural characteristics of wellbore cement and formation rocks under sequestration conditions // *Journal of Petroleum Science and Engineering*. 2016. 138. Pp. 77–87. DOI: 10.1016/j.petrol.2015.12.010.
- Balthar V.K. C.B.L.M., Filho R.D.T., De Moraes Rego Fairbairn E., De Miranda C.R. Durability of Lightweight Slurries for Oilwell Cementing // *Key Engineering Materials*. 2016. 711. Pp. 203–210. DOI: 10.4028/www.scientific.net/KEM.711.203.
- Dwight K. Smith Cementing. New York: Henry L. Doherty Memorial Fund of AIME, 1976. 174 p.
- Kmieć M., Karpiński B., Antoszkiewicz M., Szkodo M. Laboratory research on the influence of swelling clay on the quality of borehole cementing and evaluation of clay-cutting wellbore tool prototype // *Applied Clay Science*. 2018. 164. Pp. 13–25. DOI: 10.1016/j.clay.2018.04.028.
- Bu Y., Hou X., Wang C., Du J. Effect of colloidal nanosilica on early-age compressive strength of oil well cement stone at low temperature // *Construction and Building Materials*. 2018. 171. Pp. 690–696. DOI: 10.1016/j.conbuildmat.2018.03.220.
- Moradi S.S.T., Nikolaev N.I., Leusheva E.L. Improvement of cement properties using a single multi-functional polymer // *International Transaction Journal of Engineering. A: Basics*. 2018. 31(1). Pp. 181–187. DOI: 10.5829/ije.2018.31.01a.24.
- Ghabezloo S. Effect of the variations of clinker composition on the poroelastic properties of hardened class G cement paste // *Cement and Concrete Research*. 2011. 41(8). Pp. 920–922. DOI: 10.1016/j.cemconres.2011.03.022.
- Choolaei M., Rashidi A.M., Ardjmand M., Yadegari A., Soltanian H. The effect of nanosilica on the physical properties of oil well cement // *Materials Science and Engineering. A*. 2012. 538. Pp. 288–294. DOI: 10.1016/j.msea.2012.01.045.
- Da Silva Araujo Filho R.G., De Oliveira Freitas J.C., De Freitas Melo M.A., Braga R.M. Lightweight oil well cement slurry modified with vermiculite and colloidal silicon // *Construction and Building Materials*. 2018. 166. Pp. 908–915. DOI: 10.1016/j.conbuildmat.2017.12.243.
- Bubnov A.S., Boyko I.A., Khorev V.S. Strength properties of cement slurries with lightweights applied in oil and gas wells // *IOP Conference Series: Earth and Environmental Science*. 2015. 24(012010). DOI: 10.1088/1755-1315/24/1/012010.
- Иноземцев А.С. Средняя плотность и пористость высокопрочных легких бетонов // *Инженерно-строительный журнал*. 2014. № 7(51). С. 31–37. DOI: 10.5862/MCE.51.4

14. Стешенко А.Б., Кудряков А.И. Цементный пенобетон с алюмосиликатной микросферой для монолитного домостроения // Инженерно-строительный журнал. 2018. № 8(84). С. 86–96. doi: 10.18720/MCE.84.9
15. Масталыгина Е.Е., Овчинников В.А., Чухланов В.Ю. Легкие жаростойкие полимербетоны на основе олигооксигидридсилметиленилсилоксилана и полых сферических наполнителей // Инженерно-строительный журнал. 2019. № 6(90). С. 37–46. DOI: 10.18720/MCE.90.4
16. Ren S., Liu J.C., Guo A.R., Zang W.J., Geng H.T., Tao X., Du H.Y. Mechanical properties and thermal conductivity of a temperature resistance hollow glass microspheres/borosilicate glass buoyance material // Materials Science and Engineering. A. 2016. 674. Pp. 604–614. DOI: 10.1016/j.msea.2016.08.014.
17. Osamu Saito, Norihiko Yagi/ Yoshinori Ito Glass frit useful for the preparation of glass bubbles, and glass bubbles prepared by using it. Patent US 5064784A, 1991.
18. Howell P.A., St. Paul. Glass bubbles of increased collapse strength. Patent US 4391646A, 1983.
19. Wang X., Zhang Y., Lv F., Shen B., et al. Cross-linked polystyrene microspheres as density-reducing agent in the drilling fluid // Journal of Petroleum Science and Engineering. 2011. 78(2). Pp. 529–533. DOI: 10.1016/j.petrol.2011.06.016.
20. Hua Z., Lin M., Guo J., Xu F., Li Z., Li M. Study on plugging performance of cross-linked polymer microspheres with reservoir pores // Journal of Petroleum Science and Engineering. 2013. 105. Pp. 70–75. DOI: 10.1016/j.petrol.2013.03.008.
21. Liu H., Bu Y., Sanjayan J.G., Nazari A., Shen Z. The application of coated superabsorbent polymer in well cement or plugging the microcrack // Construction and Building Materials. 2016. 104. Pp. 72–84. DOI: 10.1016/j.conbuildmat.2015.12.058.
22. Liu H., Bu Y., Nazari A., Sanjayan J.G., Shen Z. Low elastic modulus and expansive well cement system: The application of gypsum microsphere // Construction and Building Materials. 2016. 106. Pp. 27–34. DOI: 10.1016/j.conbuildmat.2015.12.105.
23. Choolaeia M., Rashidi A.M., Ardjmanda M., Yadegari A., Soltanian H. The effect of nanosilica on the physical properties of oil well cement // Materials Science and Engineering. A. 2012. 538. Pp. 288–294. DOI: 10.1016/j.msea.2012.01.045.
24. Mata C., Calubayan A. Use of hollow glass spheres in lightweight cements – Selection Criteria, Society of Petroleum Engineers // SPE Asia Pacific Oil and Gas Conference and Exhibition 2016; Perth; Australia. 2016. code 132952.
25. Angelopoulos P.M., Taxiarchou M., Paspaliaris I. Production of durable expanded perlite microspheres in a Vertical Electrical Furnace // IOP Conference Series: Materials Science and Engineering. 2016. 123(012061). DOI: 10.1088/1757-899X/123/1/012061.
26. Tajra F., Elrahman M.A., Chung S.-Y., Stephan D. Performance assessment of core-shell structured lightweight aggregate produced by cold bonding pelletization process // Construction and Building Materials. 2018. 179. Pp. 220–231. DOI: 10.1016/j.conbuildmat.2018.05.237
27. Farnood Ahmadi P., Ardeshir A., Ramezaniapour A.M., Bayat H. Characteristics of heat insulating clay bricks made from zeolite, waste steel slag and expanded perlite // Ceramics International. 2018. 44(7). Pp. 7588–7598. DOI: 10.1016/j.ceramint.2018.01.175.

#### **Контактные данные:**

*Ольга Викторовна Казьмина, +7(909)544-60-38; эл. почта: kazmina@tpu.ru*

*Наталья Александровна Митина, +7(382-2)563-169; эл. почта: mitinana@tpu.ru*

*Константин Мадестович Минаев, +7(3822)563-169; эл. почта: minaevkm@tpu.ru*



DOI: 10.18720/MCE.93.9

## Strength of underground pipelines under seismic effects

**K.S. Sultanov<sup>a</sup>, J.X. Kumakov<sup>b</sup>, P.V. Loginov<sup>a</sup>, B.B. Rikhsieva<sup>a</sup>**

<sup>a</sup> Institute of Mechanics and Seismic Stability of Structures of the Academy of Sciences of the Republic of Uzbekistan, Tashkent, Republic of Uzbekistan

<sup>b</sup> Tashkent Institute of Architecture and Construction, Tashkent, Republic of Uzbekistan

\* E-mail: [sultanov.karim@mail.ru](mailto:sultanov.karim@mail.ru)

**Keywords:** strength, earthquake-resistance, pipeline, soil, interaction, mechanical properties, numerical methods, strain rate, stress

**Abstract.** A brief analysis of calculation methods to assess underground pipeline earthquake resistance, their advantages and disadvantages are given in the paper. The analysis of the models of underground pipeline-soil interaction under seismic (dynamic) effect is given. The coupled problems of underground pipeline-soil interaction at seismic wave propagation in a soil medium with embedded pipeline are set. One-dimensional non-stationary wave problems for the soil medium and the pipeline are solved numerically using the method of characteristics and the finite difference method. Numerical solutions are obtained in the form of a change in longitudinal stresses over time in various sections of the pipeline. An analysis of the obtained numerical solutions shows a significant dependence of longitudinal stresses on wave processes in the soil medium, dynamic stress state of soil and mechanical properties of soil and the pipeline material. A factor of a multiple increase in longitudinal stresses in the underground pipeline under its dynamic interaction with soil is revealed. It is shown that the main reason for this increase in stresses is the dynamic stress state of soil around the pipeline under its interaction with soil. The results obtained are the grounds for the development of a new regulatory calculation of underground trunk pipeline strength under seismic effect.

### 1. Introduction

Usage of underground pipelines, which make up some of the most important backbone systems for any population, including water, gas, and oil pipelines, has been on a rise all over the world [1–5]. Their stability under various conditions (seismic ones, landslides, mudflows, transport and sea accidents, etc.) becomes a particularly urgent problem [1–7], since a rise in accident rate of underground pipelines leads to large economic and environmental losses [1]. To prevent this damage, it is necessary to determine the causes of underground pipeline damage under dynamic loads of different nature.

Studies of underground pipeline strength and stability under static and dynamic loads have a long history and have been carried out by many researchers all over the world. The most significant results of the studies are given in [1–9].

Based on the results given in [1–12], the process of the stress state formation, which affects the strength of underground pipelines under dynamic (especially, seismic) loads, is a very complicated one as there are a lot of factors which define the basic determinant indices of this process. Among them are the factors of dynamic (wave) processes in the pipeline itself and dynamic behavior of an underground pipeline depending on its design features [1–4]; the underground pipe-soil interaction factor [1, 13–16]; the factor of surrounding soil with complex mechanical properties [8, 10, 17–31]; the factor of pipelines conveying fluid or gas (thermal and mechanical characteristics) [32, 33]; the factor of dynamic (seismic) load characteristics [32–34], etc. The consideration of all these factors in mathematical statement of the problem leads to complex equations, the solution of which is possible under significant simplifications [32–38]. The attempts to construct generalized models of underground pipeline strain considering complex ground and geological conditions, various models

---

Sultanov, K.S., Kumakov, J.X., Loginov, P.V., Rikhsieva, B.B. Strength of underground pipelines under seismic effects. Magazine of Civil Engineering. 2020. 93(1). Pp. 97–120. DOI: 10.18720/MCE.93.9

Султанов К.С., Кумаков Ж.Х., Логинов П.В., Рихсиева Б.Б. Прочность подземных трубопроводов при сейсмических воздействиях // Инженерно-строительный журнал. 2020. № 1(93). С. 97–120. DOI: 10.18720/MCE.93.9



of pipe-soil interaction and the effect of corrosive wear on the inside and the outside of the pipe were carried out in [8, 11, 12].

However, determining the qualitative and quantitative impact of each of the above factors is a separate, independent problem in evaluating the underground pipeline strength.

The aim of this study, based on the above factors, is to determine the longitudinal stresses in underground trunk pipelines under longitudinal seismic effects, taking into account the pipeline-soil interaction forces.

The objectives of the paper are:

1. An analysis of existing methods for determining longitudinal stresses under seismic effects.
2. A development of the models of underground pipeline-soil interaction.
3. The statement of the problem of longitudinal underground pipeline-soil interaction under plane seismic waves.
4. The method of solution of wave problem and its substantiation.
5. Comparative analysis of longitudinal stresses in an underground pipeline at various models of pipeline-soil interaction under seismic loads.

## 2. Methods

### 2.1. Methods to determine longitudinal seismic stresses in underground pipelines

Currently, there are three basic methods to determine longitudinal seismic stresses in underground pipelines. As described in [9] the first method is based on the hypothesis of the equality of longitudinal strains in the pipeline and soil under seismic loading. Here, the seismic load is taken in the form of plane elastic wave propagating in soil, changing according to a sinusoidal law. Such a statement allows analytical determining the maximum elastic strain in soil [9]. It is assumed that an underground long pipeline receives the strain equal to the maximum elastic strain of soil. Longitudinal stress is determined from Hooke's Law at a known longitudinal pipeline strain. This simple method is laid as the basis for determining longitudinal seismic stresses in the regulatory documents (Building Code) in the Commonwealth of Independent States countries (SNiP 2.05.06-85\* (RF) and in Uzbekistan (KMK 2.01.03-96).

It is obvious that under seismic waves propagation in soil medium with embedded pipeline, the longitudinal strain of the pipeline cannot be equal to the soil strain, as it is assumed in [9].

As noted in [12–16], this method can estimate the upper limit of seismic stress in an underground pipeline. Calculations by this method [38] show that longitudinal stresses in underground steel pipelines, depending on ground conditions, reach values from 20 to 100 MPa. These values of longitudinal stresses do not exceed the tensile strength of steel pipe. This circumstance is corrected in [38] by introducing coefficient  $m_3$ , which is determined by formula

$$m_3 = \tau_{np} / \tau_3, \quad (1)$$

where  $\tau_{np} = f\sigma_N + c$ ,

$f$  is the coefficient of internal friction in soil,

$\sigma_N$  is normal stress, determined by the pipeline laying depth in soil,

$c$  is cohesion force in soil,

$\tau_3$  is shear stress at the pipe-soil contact.

The definition of  $\tau_3$  in [38] is proposed experimentally, which is associated with many difficulties.

In [38], a final value of longitudinal stress in the underground pipeline is estimated multiplying coefficient  $m_3$ , determined by this method, by the value of longitudinal stress. Due to the complexity of determining shear stress  $\tau_3$ , this method of estimating longitudinal seismic stress in an underground pipeline has not found its wide application in practice. However, due to its simplicity, this method is still included into the regulatory documents of the CIS countries, without taking into account coefficient  $m_3$ .

The fact that the first method is based on an incorrect hypothesis on longitudinal strains equality of the pipeline and soil makes us look for other methods to determine longitudinal seismic stresses in an underground pipeline. As a result, the second method was proposed.

The second method for determining longitudinal seismic stresses in an underground pipeline was developed in [38]. This method is based on the hypothesis that a longitudinal seismic stress in an underground pipeline is generated by the interaction force at the pipe-soil contact, determined in the simplest case as

$$\tau = K_x u, \quad (2)$$

where  $\tau$  is the force (shear stress) of interaction,

$K_x$  is coefficient of longitudinal interaction,

$u$  is relative displacement equal to  $u = u_2 - u_1$ ;

$u_1$  is absolute displacement of soil particles,

$u_2$  is absolute displacement of pipeline particles (section).

In the general case, the values of  $u_1$  and  $u_2$ , and, accordingly,  $u$  should be determined for each section of the pipeline, i.e. they are the variable values along the pipeline length. They also vary in time as seismic wave parameters and are the functions of time parameters  $t$  and coordinate  $x$  directed along the pipeline axis

$$u_1 = u_1(t, x), \quad u_2 = u_2(t, x), \quad u = u(t, x). \quad (3)$$

Relationship (2) in [13–16] is attributed to V.A. Florin (1938), and the ones in [10–12] to other researchers. Using the external surface force (2), solutions to a number of one-dimensional problems on the underground pipeline vibrations were obtained in [13–16], and longitudinal stresses in the pipeline were determined.

The second method was further developed in [38]. Here, when solving one-dimensional problems of underground pipeline longitudinal vibrations, seismic load is considered to be known and taken in the form of function  $u_1 = u_1(t)$ , i.e. the absolute soil displacement depends on time only. Such a simplification is equivalent to the fact that soil medium is a non-deformable body and moves as a rigid body. Obviously, this simplification is opposite to the hypothesis of the first method, where soil is considered a deformable medium.

In [1–4, 13–16], many complex problems on underground pipeline longitudinal vibrations were considered and solved, the statements of which were similar or close to the ones of the second method.

In [38], longitudinal stresses in the pipeline were determined from the solution of one-dimensional stationary problem of longitudinal plane seismic wave propagation in an elastic underground pipeline, using relationships (2), (3). In [38], the results of the first method are taken as the first approximation by solving the equations of pipeline longitudinal vibrations. In [38], the first method is referred to as a «static» method and criticized as an inaccurate one.

Further, the solution of the first method is taken as the basis for determining longitudinal stresses in soil. Then in [38], a dynamic coefficient is introduced, which specifies the value of longitudinal stress in underground pipeline. The value of dynamic coefficient  $n_D$  varies within  $n_D = 0.2–3$ . As a result, the range of longitudinal stresses obtained in [38] varies from 4 to 300 MPa, which is an inaccurate value.

Besides, the essence of dynamic coefficient  $n_D$  and the problem statement on seismic vibrations of underground pipelines were not revealed in [38]. A number of significant drawbacks of the second method were noted in [13–16]. The second method, as well as the first one, does not lead to a more accurate and reliable determination of longitudinal stresses in the underground pipeline. This circumstance led to the formulation of the third method.

The basics of the third method are given in [11]. In [11], longitudinal stress in an underground pipeline is determined from solving coupled wave problems. The third method includes the advantages of the first two methods. Since it is practically very difficult to determine experimentally the change in soil displacements  $u_1 = u_1(t, x)$  on soil-pipeline contact surface, it is proposed to determine function  $u_1 = u_1(t, x)$  based on the solution of the problem of seismic wave propagation in soil with embedded pipeline.

In this case, firstly, it becomes possible to take into account not only the elastic properties, but dissipative (viscous, plastic) properties of soil as well. Secondly, in this case, dynamic stress normal to the outer surface of the pipeline  $\sigma_{ND}(t, x)$  becomes known along the pipeline length.

Obviously, the shear stress (friction)  $\tau$  tends to Coulomb friction  $\tau_{np}$  at increasing relative displacement  $u$ . It follows that coefficient  $K_x$  in (2) should depend on  $\sigma_N$ ; the latter, in turn, consists of two components

$$\sigma_N = \sigma_{NS} + \sigma_{ND}, \quad (4)$$

where  $\sigma_{NS}$  is the static normal stress, determined by the pipeline laying depth in soil.

The fact that the value of  $\sigma_{ND}$  may be greater than  $\sigma_{NS}$ , significantly affects the stress state of underground pipeline. Essentially, the value of  $\sigma_{ND}$  varies in the range  $-\sigma_{ND\max} \leq \sigma_{ND} \leq \sigma_{ND\max}$ . This means that on the pipe-soil contact surface, the soil separation from the pipeline may occur.

In addition, in the second method, the direction of the interaction force is not explicitly taken into account (2). The sign  $\tau$  can be precisely determined only from relation

$$\tau = \text{sgn}(v)K_x(\sigma_N)u, \quad (5)$$

where  $v = v_2 - v_1$ ,  $v_2$  is the velocity of soil particles,  $v_1$  – velocity of pipeline particles on the contact surface. Obviously, at  $v < 0$ ,  $\text{sgn}(v) = -1$ , and at  $v > 0$ ,  $\text{sgn}(v) = +1$ . The case at  $v = 0$  is considered as a special case [11].

As is shown in [10], at critical value of  $u = u_*$ , soil separation from the pipeline occurs and the shear stress on the surface of their contact is determined from the Coulomb-Amontons law, i.e. in this case  $\tau = \tau_{np}$ . Experimental studies of the underground pipelines-soil interaction under static and dynamic loads in [11] show that in fact there is no clear boundary in the pipe-soil contact.

A certain contact layer of soil is involved in the interaction, the thickness of which depends on the outer diameter and the roughness of pipeline outer surface and on strain properties of the pipeline and soil, on disturbed or undisturbed soil structure.

As shown in [11], this contact layer of the pipeline-soil interaction is strained strongly – till the destruction. The soil beyond the contact layer may be strained elastically or non-elastically without destruction.

Further, taking into account all the above factors and equations (3)–(5), the problem of seismic wave propagation in a pipeline is solved and the longitudinal (seismic) stress is determined.

The third method, as you can see, is quite complicated. However, it is more accurate and reliable in contrast to the former ones [11, 12].

Thus, the development of the methods to determine longitudinal stresses led to the formulation of the third method. In this paper, longitudinal seismic stresses in an underground pipeline are determined by the third method. According to [11, 12], in the simplest case, when considering one-dimensional coupled problems on seismic waves propagation in soil and along the underground pipeline, the pipeline-soil interaction forces play a significant role. Therefore, we will consider this issue separately.

## 2.2. Models of underground pipeline-soil interaction

In essence, an interaction model is a pipeline response to seismic effects. Seismic load is transferred to the pipeline through soil. The soil is strained under seismic impact. Soil strains near the boundary of contact with the pipeline differ from the ones that occur far from this boundary [11, 12]. As a result, a contact soil layer is formed at this boundary. The existence of the contact soil layer is experimentally and theoretically shown in [11, 12]. In [11], various laws of strain of the contact layer are considered. In [12], the cases and limits of applicability of these interaction laws are discussed, which are, in essence, the laws of special strain of the contact layer.

Based on the results of experimental and theoretical studies [11, 12], the process of underground pipeline-soil interaction is most reliably described by equations

$$\text{at } \sigma_N > \sigma_N^*, 0 \leq u \leq u_*$$

$$\frac{d\tau}{K_{xD}(\sigma_N, I_S)dt} + \mu_S(\sigma_N, I_S, \dot{u}) \frac{\tau}{K_{xS}(\sigma_N, I_S)} = \frac{du}{dt} + \mu_S(\sigma_N, I_S, \dot{u})u \quad (6)$$

$$\frac{du}{dt} \geq 0$$

$$\frac{d\tau}{K_{xR}(\sigma_N, I_S)dt} = \frac{du}{dt}, \quad \frac{du}{dt} < 0 \quad (7)$$

$$\text{at } \sigma_N > \sigma_N^*, u > u_*$$

$$\tau = f\sigma_N, \quad \frac{du}{d\tau} \geq 0 \quad (8)$$

$$\tau=0, \quad \frac{du}{dt} < 0 \quad (9)$$

$$\text{at } \sigma_N \leq \sigma_N^*, \quad \tau=0, \quad (10)$$

where  $K_{xD}$  is the variable coefficient of dynamic interaction (at  $\dot{u} \rightarrow \infty$ );

$K_{xS}$  is variable coefficient of quasistatic interaction (at  $\dot{u} \rightarrow 0$ );

$K_{xR}$  is variable coefficient of interaction during reverse pipeline motion relative to soil;

$\mu_S$  is variable shear viscosity of soil;

$\dot{u} = du/dt$  is pipeline displacement rate relative to soil;

$I_S = u/u_*$  is a parameter characterizing the structural destruction of the soil contact layer,

$0 \leq I_S \leq 1$ , at  $I_S = 0$  the soil contact layer or contact bonds between the outer surface of the pipeline and soil are not destroyed, and at  $I_S = 1$  these bonds are completely destroyed;

$f$  is coefficient of internal friction of soil;

$\sigma_N^*$  is tensile strength of soil (hereinafter, the compressive stresses are assumed to be positive).

Parameter  $\mu_S$  is related to shear viscosity coefficient  $\eta_S$  by relationship

$$\mu_S = K_{xD} K_{xS} [(K_{xD} - K_{xS}) \eta_S]. \quad (11)$$

Interaction functions  $K_{xD}$ ,  $K_{xS}$ ,  $K_{xR}$  determined from the results of experimental studies in [11] have the following form

$$K_{xD}(\sigma_N, I_S) = K_{xD}^*(\sigma_N) \exp[\alpha(1 - I_S)], \quad (12)$$

$$K_{xS}(\sigma_N, I_S) = K_{xS}^*(\sigma_N) \exp[\beta(1 - I_S)], \quad (13)$$

$$K_{xR}(\sigma_N, I_S) = K_{xDN}^*(\sigma_N) / (1 - I_S), \quad (14)$$

where  $K_{xD}^*$  and  $K_{xS}^*$  are the secant coefficients of dynamic and quasistatic interaction of disturbed soil with the pipeline at  $u = u_*$ ;

$K_{xDN}$  and  $K_{xSN}$  are initial values of the interaction coefficients;

$\alpha$  and  $\beta$  are dimensionless coefficients characterizing the degree of change in  $K_{xDN}$  and  $K_{xSN}$ .

For the disturbed ( $I_S = 1$ ) contact soil layer from (12) and (13) we obtain

$$K_{xDN} = K_{xD}^* \exp(\alpha), \quad K_{xSN} = K_{xS}^* \exp(\beta). \quad (15)$$

It follows from (15) that

$$\beta = \alpha + \ln(\gamma_* / \gamma_N), \quad (16)$$

where  $\gamma_* = K_{xD}^* / K_{xS}^*$ ;  $\gamma_N = K_{xDN} / K_{xSN}$ .

Based on experimental results [11] we get

$$K_{xS}^*(\sigma_N) = K_{NS} \sigma_N, \quad K_{xD}^*(\sigma_N) = K_{ND} \sigma_N. \quad (17)$$

In [11] it is stated that  $\gamma_* \geq \gamma_N$ , so

$$\begin{aligned} \beta &\geq \alpha; \quad \mu_S^* = B\dot{u}/(\gamma_* u_*), \\ \gamma_* &= \gamma_N + (\gamma_*^m - \gamma_N)(\dot{u}/C_S)^\kappa \\ \mu_S(\sigma_N, I_S, \dot{u}) &= \mu_S^* \exp[\varphi(1 - I_S)], \end{aligned} \quad (18)$$

where  $\gamma_*^m$  is the limit value of  $\gamma_*$ ,

$\kappa$  and  $\varphi$  are the dimensionless coefficients.

In [11], at  $\sigma_N > 1$  MPa, it is recommended to replace formula (8) with the following formula

$$\tau = \tau_0 + f \sigma_N / \left(1 + f \sigma_N / (\tau_* - \tau_0)\right), \quad (19)$$

where  $\tau_0$  is the cohesion force of the soil contact layer;

$\tau_*$  is the limiting value of the friction force,  $\tau_* = 0.7\text{--}0.9$  MPa.

The parameters of the interaction model  $B, K_{NS}, fu, \gamma_*^m, \alpha, u_*, \kappa, \varphi$  considered in [11] are determined from experimental results and have the following values for loess soils of disturbed structure and for steel pipeline:  $\gamma_N = 1.1$ ;  $f = 0.5$ ;  $K_{NS} = 100 \text{ m}^{-1}$ ;  $u_* = 3 \cdot 10^{-3} \text{ m}$ ;  $\sigma_N^* = 0.15 \text{ MPa}$ ;  $\varphi = 0$ ;  $\alpha = 3$ ;  $\kappa = 0.1$ ;  $\gamma_*^m = 10$ ;  $B = 200$ ;  $C_S = 100 \text{ m/s}$ ;  $\tau_0 = 0$ .

As can be seen, the interaction model described by equations (6)–(19) is more complicated than the one described by (2). However, an account for such determining factors, as the interaction rate, disturbance of the soil contact layer, cohesion forces and internal friction of soil leads to such cumbersome equations. In the simplest cases, not considering these factors, one can use equations (2) and (8) with the corresponding conditions as a model of interaction.

The law of interaction (2) is often used [1–4, 12–16, 28] in longitudinal stress calculations of underground pipelines. It is considered that the coefficient of longitudinal interaction  $K_x$ , determined from the results of static experiments, takes into account the pipeline laying depth. However, in [12–16, 38], the fact that a further increase in relative displacement value in (2) leads to soil separation from the pipeline and the value of  $\tau$  after separation does not depend on  $u$ , is not taken into account. The Coulomb Law (8) is satisfied at this stage of interaction.

In [11] it was shown that the second stage of interaction for loess soils of disturbed structure occurs at  $u_* = 3 \cdot 10^{-3} \text{ m}$ . Such relative displacements between the underground pipeline and soil during strong earthquakes are possible [38, 69]. So in calculations it is necessary to take into account the entire interaction process for  $\tau(u)$ . In this case, to avoid the break between dependences (2) and (8) at point  $u = u_*$ , it is necessary to express the interaction coefficient  $K_x$  depending on  $\sigma_N$  taking into account (4).

In this case, the law of interaction (2) takes the form [11]

$$\tau = K_{xS}(\sigma_N) u e^{[\beta(1-I_S)]} \text{ at } \sigma_N > \sigma_N^*, \quad 0 \leq u \leq u_*, \quad \frac{du}{dt} \geq 0, \quad (20)$$

where function  $K_{xS}(\sigma_N)$  is determined from relationship (17).

In this case, the entire interaction process is described by equations (20), (8)–(10), and the value of  $u_*$  can be determined from the relationship

$$u_* = f / K_{NS}. \quad (21)$$

In [38], the interaction law of a model analogous to Kelvin – Voigt one is used, which does not describe soil relaxation. However, due to its simplicity, a Kelvin – Voigt-type interaction model is often used in calculations. Given the above factors, the Kelvin-Voigt type interaction model has the form [11]

$$\tau = K_{xS}(\sigma_N, I_S) u + \eta_S(\sigma_N, I_S) \frac{du}{dt} \text{ at } \sigma_N > \sigma_N^*, \quad 0 \leq u \leq u_*, \quad \frac{du}{dt} > 0, \quad (22)$$

where  $\eta_S(\sigma_N, I_S)$  is the soil shear viscosity coefficient, determined from relationships

$$\begin{aligned} \eta_S(\sigma_N, I_S) &= \eta_S^*(\sigma_N) \exp(\alpha_S(1 - I_S)) \\ \eta_S^*(\sigma_N) &= f \sigma_N / C_S, \quad u_* = f \left(1 - \frac{du}{C_S dt}\right) / K_{ND}, \end{aligned} \quad (23)$$

where  $C_S$  is the shear wave propagation in soil. In this case the interaction process is described by equations (22), (8)–(10).  $K_{xS}(\sigma_N, I_S)$  is determined from (13).

From relationships (23) it is seen that at  $\frac{du}{dt} \rightarrow C_S$ ,  $u_* \rightarrow 0$ ; which does not correspond to reality.

Nevertheless, interaction models (20) and (22) in simplified versions are widely used in calculating the underground pipelines strength under seismic loads.

The above analysis of the process and the laws of interaction show that they are quite complex. As will be shown below, longitudinal stress in an underground pipeline substantially depends on the correct choice of the interaction model.

### 2.3. The statement of the problem of longitudinal interaction of an underground pipeline with soil when exposed to plane seismic waves and the method to solve them

The problem of soil interaction with an underground pipeline laying on a certain depth from the surface is a three-dimensional one. With some simplifications it can be reduced to a two-dimensional problem. In these two cases, mathematical statement of the problem leads to complex partial differential equations describing the process of pipeline-soil interaction with many unknowns. Obtaining a solution to these equations is a rather laborious and complex mathematical problem.

With some more powerful simplifications, the problem can be reduced to one-dimensional problem. Consider an underground pipeline as an extended rod with an  $x$  axis, on the outer surface of which an interaction (friction) force  $\tau$  acts, defined by equations (2) or (6)–(10) or (20). When using these equations to determine interaction force  $\tau$ , it is necessary to know the absolute value of soil displacement  $u_1$  as a function  $u_1(t, x)$  and the dynamic pressure  $\sigma_{ND}$  normal to the outer surface of the pipeline as a function  $\sigma_{ND}(t, x)$ .

The value of  $\sigma_{NS}$  is determined by the pipeline laying depth in soil and is assumed constant over time and along the pipeline length. To determine the functions  $u_1(t, x)$  and  $\sigma_{ND}(t, x) = K_\sigma \sigma_2(t, x)$  ( $K_\sigma$  is the soil lateral pressure coefficient,  $\sigma_2$  – longitudinal stress in soil), consider the soil medium around an underground pipeline as a cylindrical rod with a radius  $R = H$ , where  $H$  is the pipeline laying depth in soil, determined by the distance from the outer (day) soil surface to the pipeline axis  $x$ , which is also the axis of soil cylinder.

Initial sections  $x = 0$  of the pipeline and soil coincide. Outer surface of the pipeline in contact with soil, in this case, is the surface of a cylindrical cavity with a diameter  $D_B = D_H$ , where  $D_H$  is the outer diameter of the pipeline inside soil cylinder. Soil medium can also be considered as a half-space with an  $x$  axis coinciding with the pipeline axis with a cylindrical cavity of diameter  $D_B$  along the  $x$  axis. In both cases, the one-dimensional motion of soil is described by the same equations.

At the section  $x = 0$  (the initial section of the pipeline and soil), a load that generates a plane wave in soil half-space and the pipeline is defined by equations

$$\begin{aligned} \sigma &= \sigma_{\max} \sin(\pi t/T), \quad 0 \leq t \leq \theta, \\ \sigma &= 0, \quad t > \theta, \end{aligned} \quad (24)$$

where  $T$  is the half-time of load,

$\theta$  is load action time,

$\sigma_{\max}$  is load amplitude,

$\sigma$  is longitudinal stress acting along the  $x$  axis.

Considered simplifications of the «soil medium-pipeline» system lead to a description of their motion under dynamic load (24) by equations

$$\begin{aligned} \rho_{0i} \frac{\partial v_i}{\partial t} - \frac{\partial \sigma_i}{\partial x} + \kappa_i \sigma_{\tau i} &= 0 \\ \frac{\partial v_i}{\partial x} - \frac{\partial \varepsilon_i}{\partial t} &= 0, \end{aligned} \quad (25)$$

where  $v_i$  is the particle velocity (mass velocity) of the pipeline and soil on the same section  $x = x_i$ ;

$\rho_{0i}$  is the initial density of the pipe and soil material;

$\kappa_1 = \text{sgn}(v)$  for pipeline,

$\kappa_2 = -\text{sgn}(v)$  for soil;

$v = v_2 - v_1$  is relative velocity;

$\sigma_{\tau i}$  is reduced friction force acting per unit length of the pipeline and soil; at  $i = 1$  all parameters and variables of equation (25) refer to the pipeline, and at  $i = 2$  – to soil.

Values of  $\sigma_{\tau i}$  for the pipeline and soil are determined from relationship

$$\sigma_{\tau i} = 4D_{H1}\tau / (D_{Hi}^2 - D_{Bi}^2), \quad (26)$$

where  $\tau$  is the interaction force (friction force) acting between the pipeline and soil;

$D_{Hi}$  is outer diameters of the pipeline and cylindrical soil rod;

$D_{Bi}$  is inner diameters of the pipeline and cylindrical soil rod;  $D_{B2} = D_{H1}$ .

In fact, the surface interaction force (friction) is reduced by equation (26) to volume force, which is a consequence of reducing the problem to a one-dimensional statement [10–16]. Equations (25) contains three unknown variables  $\sigma_i$ ,  $\varepsilon_i$  and  $v_i$ , for the determination of which (25) it is closed by the laws of strain of the pipeline and soil in the form

$$\frac{\partial \varepsilon_i}{\partial t} + \mu_i \varepsilon_i = \frac{\partial \sigma_i}{E_{Di} \partial t} + \mu_i \frac{\sigma_i}{E_{Si}}, \quad (27)$$

where  $E_{Di}$  is the dynamic compression modulus;

$E_{Si}$  is static compression modulus;

$\mu_i$  is volume viscosity parameter related to the volume viscosity coefficient  $\eta_i$  by the ratio

$$\mu_i = \frac{E_{Di} E_{Si}}{(E_{Di} - E_{Si}) \eta_i}. \quad (28)$$

Equation of state (27) is a model of a standard linear viscoelastic body that takes into account the creep and relaxation of deformable bodies. Note that the basis of the interaction law (6) is equation (27). To close the equation in the case of ground condition ( $i = 2$ ), the elastic-viscoplastic law of soft soils strain proposed by G.M. Lyakhov, cited in [10], can be used.

Thus, the solution to the problem of underground pipeline-soil interaction under plane seismic waves generated by a load (24) is reduced to solving two systems of differential equations of a hyperbolic type for the pipeline ( $i = 1$ ) and soil ( $i = 2$ ) [10]. These systems of equations are connected through the law of interaction (6)–(10), by means of relation (26). As a result, we have coupled boundary value problems with boundary conditions at  $x = 0$ , relation (24) and  $x = C_{0i}t$  at the wave front

$$\sigma_i = C_{0i} \rho_{0i} v_i, \quad v_i = C_{0i} \varepsilon_i, \quad C_{0i} = (E_{Di} / \rho_{0i})^{1/2}, \quad (29)$$

where  $C_{0i}$  is the velocity of longitudinal wave propagation in the pipeline ( $i = 1$ ) and soil ( $i = 2$ ).

In the case of a load generating a wave (24), the jumps in stresses  $\langle \sigma_i \rangle$ , strains  $\langle \varepsilon_i \rangle$ , and particle velocities  $\langle v_i \rangle$  are equal to zero and the boundary conditions (29) take the form

$$\langle \sigma \rangle = 0, \quad \langle \varepsilon \rangle = 0, \quad \langle v \rangle = 0 \quad \text{at} \quad x = C_{0i}t. \quad (30)$$

Note that the front end of the pipeline can be load-free (24), later the pipeline receives motion only through the effect of the interaction force, determined by relations (6)–(10), (26).

The system of partial differential equations (25), (27) with boundary conditions (24), (30) is numerically solved. Equations (24), (27) are of hyperbolic type and have real characteristic relations, which have the form

$$\left. \begin{aligned}
 d\sigma_i - C_{0i}\rho_{0i}dv_i &= -C_{0i}^2\rho_{0i}g_i(\sigma_i, \varepsilon_i)dt + \kappa_i C_{0i}\sigma_{\tau i}dt \text{ at } dx/dt = +C_{0i} \\
 d\sigma_i + C_{0i}\rho_{0i}dv_i &= -C_{0i}^2\rho_{0i}g_i(\sigma_i, \varepsilon_i)dt - \kappa_i C_{0i}\sigma_{\tau i}dt \text{ at } dx/dt = -C_{0i} \\
 d\sigma_i - C_{0i}^2\rho_{0i}d\varepsilon_i &= C_{0i}^2\rho_{0i}g_i(\sigma_i, \varepsilon_i)dt \text{ at } dx/dt = 0 \\
 g_i(\sigma_i, \varepsilon_i) &= \sigma_i/\eta_i - E_{Di}E_{Si}(\varepsilon_i - \sigma_i/E_{Di})/[(E_{Di} - E_{Si})\eta_i]
 \end{aligned} \right\} \quad (31)$$

In contrast to [10], in equations (25) and (31) there is an additional term related to  $\kappa_i$  and so, these equations are nonlinear. The wave fronts in the pipeline and soil are the lines of weak discontinuity, hence at the front  $\tau = 0$ . This leads to linear equations of the wave fronts and characteristics in both media. The application of the method of characteristics to equations (25), (27) leads to ordinary differential equations (31). The application of numerical methods to the solution of ordinary differential equations increases the accuracy of solution when compared to their application in partial differential equations [10].

To increase the accuracy of solution [10], equations (31) are reduced to a dimensionless form through the relations

$$\left. \begin{aligned}
 x^\circ &= \mu_1 x/C_{01}, \quad t^\circ = \mu_1 t, \quad \sigma_i^\circ = \sigma_i/\sigma_{\max}, \quad v_i^\circ = v_i/v_{\max} \\
 \varepsilon_i^\circ &= \varepsilon_i/\varepsilon_{\max}, \quad v_{\max} = -\sigma_{\max}/C_{01}\rho_{01}, \quad \varepsilon_{\max} = \sigma_{\max}/E_{D1}
 \end{aligned} \right\} \quad (32)$$

In these dimensionless variables, basic equations take the form

$$\left. \begin{aligned}
 K_{\rho i} \frac{\partial v_i^\circ}{\partial t^\circ} + \frac{\partial \sigma_i^\circ}{\partial x^\circ} - \kappa_i \sigma_{\tau i}^\circ &= 0 \\
 \frac{\partial v_i^\circ}{\partial x^\circ} + \frac{\partial \varepsilon_i^\circ}{\partial t^\circ} &= 0 \\
 K_{\varepsilon i} \frac{\partial \varepsilon_i^\circ}{\partial t^\circ} + \kappa_{\varepsilon i} K_{\mu i} \varepsilon_i^\circ &= \frac{\partial \sigma_i^\circ}{\partial t^\circ} + \kappa_{\mu i} \gamma_i \sigma_i^\circ \\
 K_{\rho i} = \frac{\rho_{0i}}{\rho_{01}}, \quad K_{C i} = \frac{C_{0i}}{C_{01}}, \quad K_{\varepsilon i} = \frac{E_{Di}}{E_{D1}}, \quad K_{\mu i} = \frac{\mu_i}{\mu_1} \\
 K_{v i} = \frac{\rho_{0i} C_{0i}}{\rho_{01} C_{01}}, \quad \gamma_i = \frac{E_{Di}}{E_{Si}}, \quad \sigma_{\tau i}^\circ = \sigma_{\tau i} \frac{C_{01}}{\sigma_{\max} \mu_1}
 \end{aligned} \right\} \quad (33)$$

boundary conditions in dimensionless variables take the form

$$\left. \begin{aligned}
 \sigma^\circ &= \sin(\pi t^\circ/\mu_1 T), \quad 0 \leq t^\circ \leq \mu_1 \theta \\
 \sigma^\circ &= 0, \quad t^\circ > \mu_1 \theta \\
 \sigma_1^\circ = 0, \quad \varepsilon_1^\circ = 0, \quad v_1^\circ = 0 &\text{ at } x^\circ = t^\circ \\
 \sigma_2^\circ = 0, \quad \varepsilon_2^\circ = 0, \quad v_2^\circ = 0 &\text{ at } x^\circ = K_{C i} t^\circ
 \end{aligned} \right\} \quad (34)$$

Characteristic relations take the form

$$\left. \begin{aligned}
 d\sigma_i^\circ + K_{v i} dv_i^\circ &= K_{\mu i} (K_{\varepsilon i} \varepsilon_i^\circ - \gamma_i \sigma_i^\circ) dt^\circ + \kappa_i K_{C i} \sigma_{\tau i}^\circ dt^\circ \text{ at } dx^\circ/dt^\circ = +K_{C i} \\
 d\sigma_i^\circ - K_{v i} dv_i^\circ &= K_{\mu i} (K_{\varepsilon i} \varepsilon_i^\circ - \gamma_i \sigma_i^\circ) dt^\circ - \kappa_i K_{C i} \sigma_{\tau i}^\circ dt^\circ \text{ at } dx^\circ/dt^\circ = -K_{C i} \\
 d\sigma_i^\circ - K_{\varepsilon i} d\varepsilon_i^\circ &= K_{\mu i} (K_{\varepsilon i} \varepsilon_i^\circ - \gamma_i \sigma_i^\circ) dt^\circ \text{ at } dx^\circ/dt^\circ = 0
 \end{aligned} \right\} \quad (35)$$

In equations (33)–(35) at  $i = 1$ ,  $K_\rho = K_C = K_\varepsilon = K_\mu = K_v = 1$ .

Equations (35) at boundary conditions (34) (at zero initial conditions) are solved numerically by the finite difference method in an implicit scheme. The difference equations for system (35) are similar to the equations

given in [10]. The difference is the presence in (35) of nonlinear terms related to the interaction force  $\sigma_{ti}^\circ$ . In contrast to [1], computer calculations are performed on two parallel characteristic planes  $t^\circ x^\circ$  (Figure 1) (for the pipeline ( $i = 1$ ) and for soil ( $i = 2$ )). The axes  $t^\circ$ ,  $x^\circ$  and grids of discrete points are similar.

The initial sections  $x^\circ = 0$  for both planes coincide. Boundaries confined by wave fronts are different. In the pipeline, the wave propagates along the line  $x^\circ = t^\circ$  ( $K_{C1} = 1$ ), and in soil – along the line  $x^\circ = K_{C2}t^\circ$  ( $K_{C2} = C_{02}/C_{01} < 1$ ,  $C_{02} < C_{01}$ ) (Figure 1).

The time  $\Delta t^\circ$  and space  $\Delta x^\circ$  steps are chosen from the Courant stability condition for this case.

$$\Delta x^\circ \geq K_{C1} \Delta t^\circ > K_{C2} \Delta t^\circ. \tag{36}$$

Condition (36) ensures that the characteristic lines on the calculated layer  $j$  do not go beyond the lines  $i-1$  and  $i+1$  (Figure 1) on which all wave parameters are considered known. On the line  $j + 1$ , the wave parameters are first determined in soil, then knowing the interaction force  $\sigma_{ti}$ , the wave parameters in the pipeline are calculated. There are three types of calculation points in each time layer  $j + 1$ , point 1 at the initial section, point 2 inside the area, point 3 at the wave front. The wave parameters at these points are calculated according to their calculation algorithms. At points 1 and 3, they are calculated with account for the boundary conditions (34).

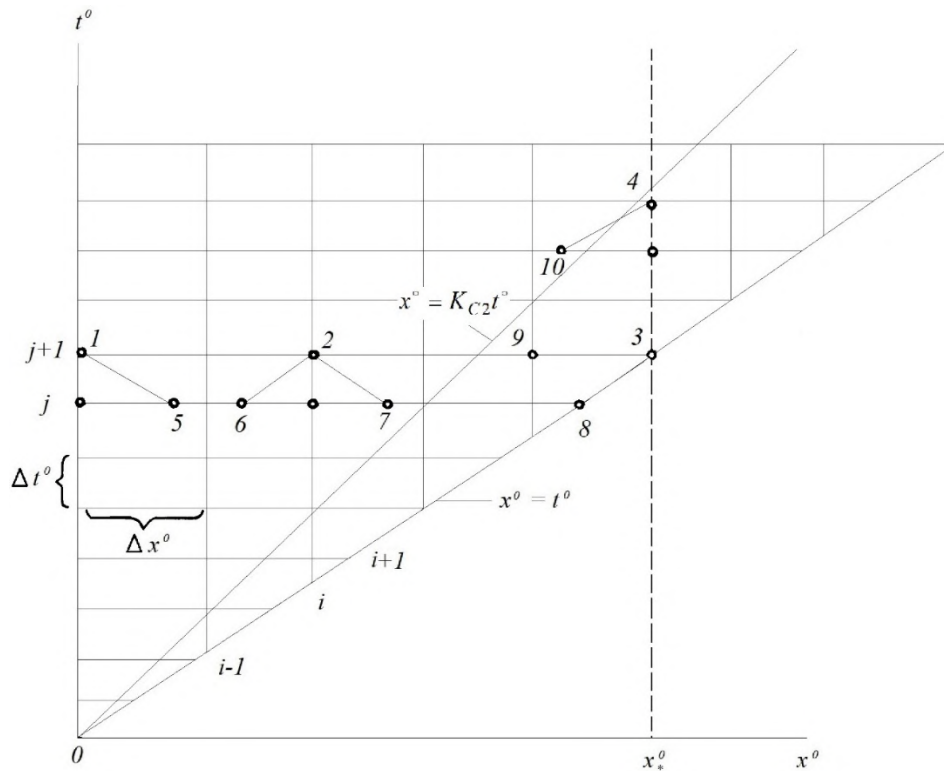


**Figure 1. Sampling scheme on the characteristic planes of numerical solution.**

At the intermediate points of type 9, the wave parameters are determined by interpolation method. The values of the known wave parameters in the time layer  $j$  at non-nodal points of 5, 6, 7 types are determined by interpolation too. In calculations, soil medium has an unlimited boundary. The wave front  $x^\circ = K_{C2}t^\circ$  can extend to infinity. The pipeline may have a finite length  $x^\circ = x_*^\circ$  or may have an infinite length (in calculations  $x_*^\circ = 1\ 000\ 000.0$ ). In the case of a finite length of the pipeline after the front has traveled the distance  $x^\circ = x_*^\circ$ , the boundary conditions at the final section of the pipeline are set in the form:

in case of a free end

$$\sigma^\circ = 0 \text{ at } x^\circ = x_*^\circ \tag{37}$$

in case of a fixed end

$$v^{\circ} = 0 \text{ at } x^{\circ} = x_{*}^{\circ}. \quad (38)$$

Based on the compiled algorithm, a program has been developed in Pascal algorithmic language and implemented in Delphi programming for calculating the wave parameters in the pipeline and soil, taking into account the interaction forces.

The reliability of the algorithm and computer program is proved by comparing the results of numerical solutions with the available experimental results on the underground pipeline-soil interaction under dynamic loading [11].

#### 2.4. Reliability substantiation of the algorithm, program and numerical solutions

In the statement considered here, even for the simplest cases (elastic soil, elastic pipeline, with the law of interaction (2)), the problem has no analytical solution. Experimental studies of the underground pipeline-soil interaction in [4, 12–15, 38] were carried out under the impact of a static load on the pipeline. The soil in these cases remained undisturbed. In [11], field experiments were carried out, the statement of which coincides with the one considered in the paper. The difference lies in the fact that there the dynamic load was created by the explosion. The set-up and the diagram of the experiment are given in detail in [11].

The main objective of the experiment [11] was to determine the law of interaction of an underground pipeline with soil. In experiments, an asbestos-cement pipe of a length  $L = 3.9$  m;  $D_{H1} = 0.32$  m;  $D_{B1} = 0.28$  m;  $C_{01} = 5000$  m/s;  $\gamma_1 = 1.1$ ;  $\mu_1 = 10\,000$  s<sup>-1</sup>; laying depth  $H = 1.7$  m was used. Characteristics of loess soil were: volume density  $\rho_{02} = 1620\text{--}1760$  kg/m<sup>3</sup> (in calculations  $\rho_{02} = 1700$  kg/m<sup>3</sup>); moisture content  $W = 18\text{--}21$  %;  $C_{02} = 1000$  m/s;  $K_{\sigma} = 0.3$ ;  $\gamma_2 = 4$ ;  $\mu_2 = 100$  s<sup>-1</sup>.

Load characteristics (24), according to experimental data [11] were:  $\sigma_{\max} = 0.7$  MPa,  $T = \theta = 0.03$  s.

The laws of interaction (6)–(10) and its characteristics are given in paragraph 2.2. In the experiment, the end of the pipeline was rigidly fixed. Therefore, condition (38) is satisfied at the end of the pipe as a boundary condition.

In the experiment in [11], the stresses generated by a plane blast wave were measured at the front and rear ends of the pipe, as well as the acceleration of the pipe and its displacement relative to soil and the stress normal to the outer surface of the pipe. The changes in shear stresses, relative displacements in time on the pipe contact surface with loess soil of a disturbed structure were determined according to the sensors records [11]; dependencies  $\tau(u)$  were constructed.

A numerical solution program allows us to consider a problem in the statement similar to that of an experiment in [11]. Using the above initial experimental data [11], the changes of  $u(t)$ ,  $\tau(t)$  and  $\tau(u)$  were obtained by numerical solution of a theoretical problem similar to the experiment based on the developed algorithm and software.

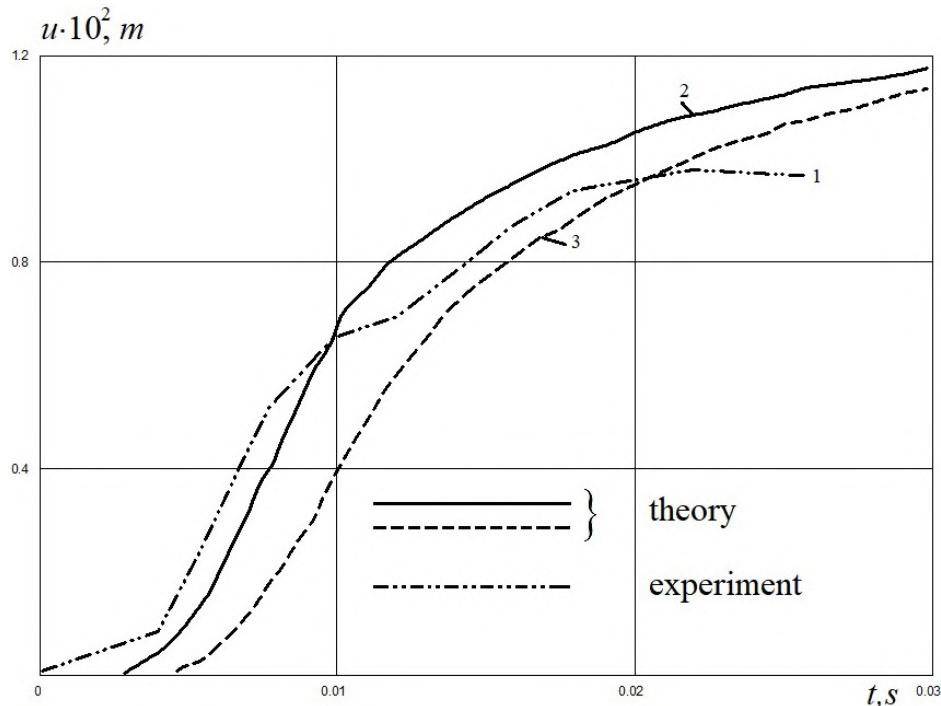


Figure 2. Change of relative displacement in time on the pipe-soil contact surface.

Comparison results of the numerical solution with the experiment are shown in Figures 2–4.

Figure 2 shows the changes in relative displacements in time. Curve 1 was obtained using the relative displacement sensor in the experiment [11] on a pipe section; the sensor was located at a distance of  $x = 3.625$  m from the front end. Curves 2 and 3 were obtained by numerical solution and refer to the distances  $x = 1.95$  m and  $3.625$  m, respectively, from the front end (initial section) of the pipe.

As seen from Figure 2, the results of calculations on a computer well agree with the experimental results (the scatter is 5–10 %).

Figure 3 shows similar comparisons of dependency  $\tau(t)$ . Here, curve 1 was obtained from the results of experimental measurements, and curves 2 and 3 – by numerical solution of a theoretical problem, the statement of which corresponds to the experimental statement. As seen from Figure 3, the experimental and theoretical curves coincide satisfactorily. Here, curves 2 and 3 relate to pipe sections at the distances of  $x = 1.95$  m and  $3.625$  m from the initial section.

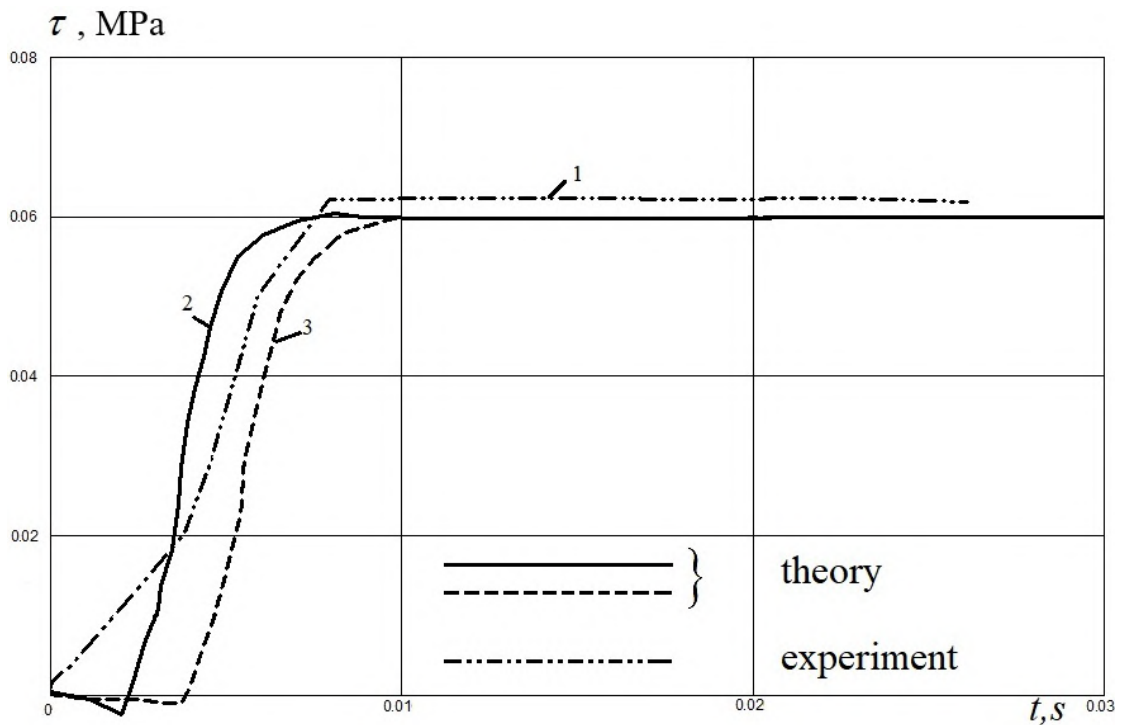


Figure 3. Change of shear stress in time on the pipe-soil contact surface.

Figure 4 shows a comparison of experimental and theoretical diagrams  $\tau(u)$  plotted from dependences  $\tau(t)$  and  $u(t)$  in Figures 2 and 3. Due to the short length of the pipe ( $L = 3.9$  m) theoretical dependences  $\tau(u)$  are identical (curves 2,3) in its sections  $x = 1.95$  m and  $3.625$  m. The coincidence of theoretical curves 2 and 3 at the initial stage of interaction, where the value of  $\tau$  varies depending on  $u$ , with experimental one  $\tau(u)$  is qualitatively satisfactory. Quantitatively, the scatter is 30–40 %. In the second section  $\tau(u)$ , where the pipe-soil slippage occurs, the agreement between experimental and theoretical results is good. Here the scatter is about 3 %.

In general, the agreement between experimental and theoretical diagrams  $\tau(u)$  can be considered satisfactory (Figure 4). In the considered theoretical problem, one of the main components is the interaction law (6)–(10). A comparison of numerical solutions with the experiment, given in Figures 2–4, shows the reliability of the developed algorithms, computer programs and numerical solutions of the problem.

### 3. Results and Discussion

#### 3.1. Longitudinal stresses in an underground pipeline in the case of an interaction model of the Hooke's law type

The interaction models considered above (6), (20), (22), are derived from the Hooke, Kelvin–Voigt laws, a law of a standard linear body for shear stresses and strains, respectively, [11]. So, they can be called the interaction models of the Hooke's, Kelvin-Voigt laws and the law of a standard body.

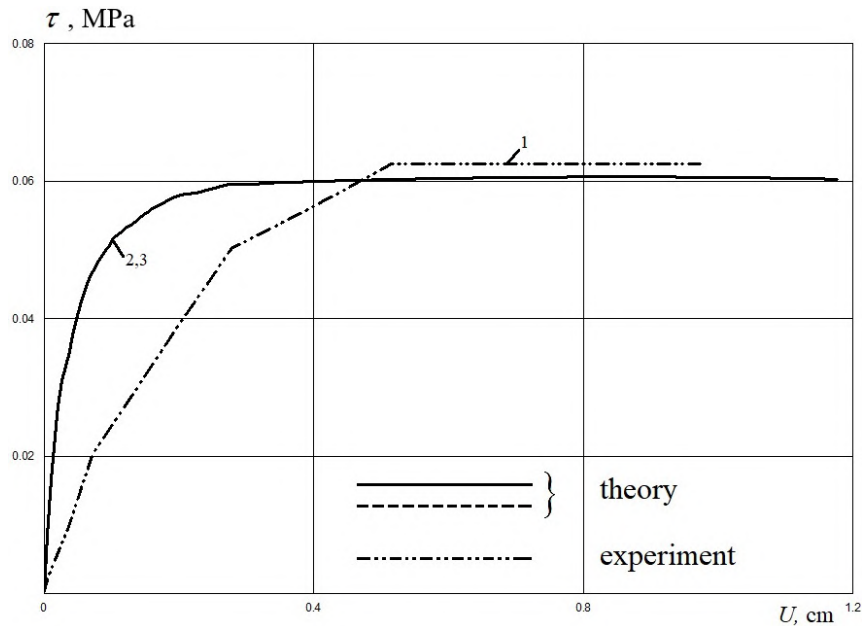


**Figure 4. Theoretical and experimental diagrams of changes of shear stress on the pipe-soil contact surface.**

In computer calculations, interaction models (6), (20) and (22) can be used separately or in combination with equations (7)–(10). In the case when interaction models (6), (20) and (22) between the pipeline and soil are used, excluding equations (7)–(10) and setting  $\kappa_1 = \kappa_2 = 1$  in equation (25), an elastic or viscoelastic interaction force is obtained on the pipeline-soil contact surface.

At  $\kappa_i = 1$ , the force of interaction does not serve as the friction force. After the relative displacement reaches  $u = u_{\max}$  or at  $du/dt < 0$ , the shear stress  $\tau$  does not change the sign, but gradually decreases to zero and only at  $u < 0$ ,  $\tau < 0$ . The case  $\kappa_i = 1$  is applicable when the value of the relative displacement is small, i.e.  $u \ll u_*$  and the structural bonds between the particles of the pipeline and soil are not broken; here the elastic forces act between them.

The developed algorithm and a program for numerical solution to the problem under consideration allow us to obtain results both for the case when an elastic (viscoelastic) bond is held between the pipeline and soil in the interaction process, and when this bond is not held on their contact surface. In the latter case, the force of interaction serves as the friction force.

The first case occurs when the structural bonds have been formed between the outer surface of the pipeline and soil; the bonds have a sufficient rigidity after the pipe has lain in soil for a long time. However, even in this case, at  $u > u_*$ , the contact layer of soil is destroyed and the pipeline separation from soil occurs; under longitudinal interaction, the interaction force serves as the friction force.

The second case occurs when the contact bonds are not formed between the pipe outer surface and soil (pipelines laid in soil of a disturbed structure) if the pipe-soil contact layer is disturbed (destroyed).

Consider the results of computer calculations obtained for the above cases when only condition (20) is satisfied between the pipeline and soil on their contact surface.

Let us start with the simplest case when the wave processes in soil surrounding the pipeline are not taken into account. In this case, in (4),  $\sigma_{ND} = 0$ , and  $\sigma_{NS}$  is approximately determined by the pipe laying depth

$$\sigma_{NS} = \gamma_{g2}H + \gamma_{g1}\pi(D_{H1}^2 - D_{B1}^2)/4D_{H1}, \quad (39)$$

where  $\gamma_{g2}$  is the specific volume weight of soil,

$\gamma_{g1}$  is specific volume weight of the pipeline material,

$H$  is the pipeline laying depth.

The law of interaction (20) takes the form

$$\tau = K_{NS}\sigma_{NS}ue^{[\beta(1-I_s)]} \quad (40)$$

and is fulfilled at all values of  $u$ .

The initial data are:  $D_{H1} = 0.2$  m;  $D_{B1} = 0.18$  m;  $\gamma_{g1} = 780$  kN/m<sup>3</sup>;  $\mu_1 = 10^4$  s<sup>-1</sup>;  $C_{01} = 5000$  m/s;  $H = 1$  m;  $L = 1000$  m;  $\gamma_{g2} = 200$  kN/m<sup>3</sup>;  $K_{NS} = 100$  m<sup>-1</sup>;  $\sigma_{\max} = 0.5$  MPa;  $T = 0.01$  s.

Consider two calculation options at the above initial data:  $\beta = 2$ ;  $\kappa = +1$  and  $\beta = 0$ ;  $\kappa = \text{sgn}(v)$ . In the first option, the shear stress on the outer surface of the pipeline depends only on value of  $u$ . The structural bonds between the pipeline and soil are elastic ones and not broken at all values of relative displacement  $u$ . In the second option, the structural bonds between the soil particles and the outer surface of the pipeline are broken and the interaction force serves as the friction force. In this case,  $\tau$  is determined from equations (40), (8)–(10). In these options, the relative displacement value is  $u = u_1$ , and  $u_2 = 0$ . The problems with similar statements are considered in [38].

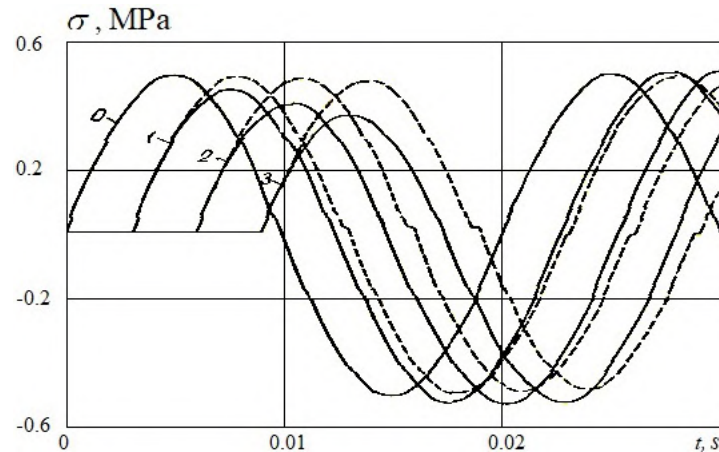


**Figure 5. Changes of longitudinal stresses in the pipeline at  $x = 0; 15; 30; 45$  m, not considering the wave processes in soil at  $\sigma_N = \sigma_{NS} = \text{const}$  in the case of interaction model of Hooke's type.**

Figure 5 shows the changes of longitudinal stresses related to these options. Here the solid curves are the calculations results of the first option, and the dashed curves – of the second option. Curves 0–3 refer to the distances  $x = 0; 15; 30; 45$  m, respectively. Curves 0 ( $x = 0$ ) present the load given by the formula (24). In both options, the value of normal static soil pressure on the pipeline by formula (39) is equal to  $\sigma_{NS} = 0.023$  MPa and is constant along the pipeline length.

As seen from Figure 5, the amplitudes of the load, set at the front end of the pipeline, remain constant over time (curves 0). The stress amplitudes in the next sections of the pipeline in both options vary differently (curves 1–3). In the first option ( $\beta = 2$ ;  $\kappa = +1$ ), the oscillations amplitudes of the first stresses decrease more noticeably in comparison with the second option ( $\beta = 0$ ;  $\kappa = \text{sgn}(v)$ ). With an increase in time, this unloading decreases already in the next oscillations.

In both options, the relative displacement, i.e. the displacement of the pipeline relative to soil occurs only as a result of a steel pipe strain under longitudinal seismic stress of the amplitude of  $\sigma_{\max} = 0.5$  MPa. According to the data in [38], during 9 point magnitude earthquakes, longitudinal stresses in loess soils reach an amplitude of up to 0.5 MPa. Here, it is conditionally assumed that this load in the pipeline section  $x = 0$  acts on the end of the pipeline. The change limits in shear stress and relative displacement are insignificant in the considered sections of the pipeline: in the first option:  $-100 \leq \tau \leq 100$  Pa;  $-6 \cdot 10^{-5} \leq u \leq 5 \cdot 10^{-5}$  m; in the second option:  $-20 \leq \tau \leq 20$  Pa;  $-8 \cdot 10^{-5} \leq u \leq 0$  m. Due to insignificant values of the relative displacement, and hence the shear stress, the amplitudes of longitudinal stresses along the pipeline practically do not change. A seismic stress wave of the amplitude of  $\sigma_{\max} = 0.5$  MPa does not affect significantly the pipeline in the considered options.

An increase in  $\sigma_{\max}$  at  $x = 0$  leads to similar results in Figure 5, with an increase in the stress amplitude in the pipeline cross sections.

Calculation results of considered options (Figure 5) show that it is impossible to determine and evaluate seismic stresses in the pipeline without account for the wave processes in soil. It follows that in the statement of the problem considered here and in similar problems [38], it is not possible to determine the longitudinal stresses in the pipeline not considering the wave processes in soil surrounding the pipeline. The results in Figure 5, of the changes in longitudinal stresses along the pipeline, correspond to the changes in wave parameters in viscoelastic rods [11]. This once again indirectly confirms the reliability of the obtained numerical solutions.

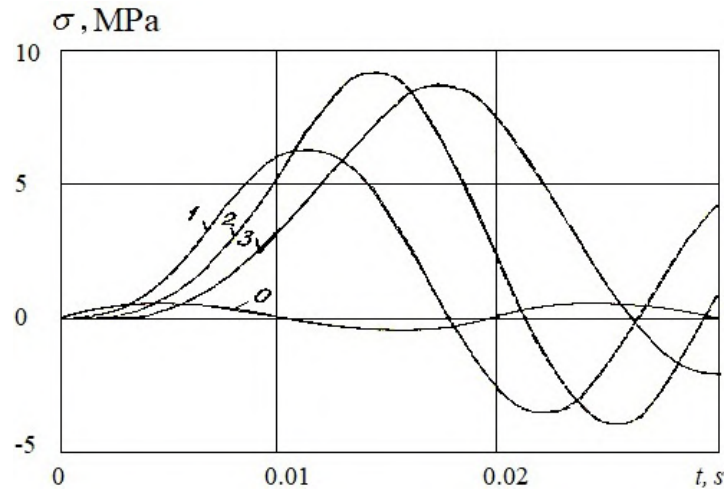


**Figure 6. Change of longitudinal stresses in the pipeline at  $x = 0; 5; 10; 15$  m, considering the soil movement at  $\sigma_N = \sigma_{NS} = const$  in the case of interaction model of Hooke's type.**

Now consider the change in longitudinal stresses in the pipeline taking into account wave processes in soil. Figure 6 shows the change of longitudinal stresses in the pipeline when a plane wave generated by the load (24) on section  $x = 0$  of the pipeline and soil propagates through the soil surrounding the pipeline.

The characteristics of the pipeline, soil and load remained unchanged as in the case shown in Figure 5 ( $\beta = 2$ ). Curves 0–3 in this case refer to distances  $x = 0; 5; 10; 15$  m, respectively. In calculations, the soil pressure normal to the pipeline, determined by the pipe laying depth  $H = 1$  m, remains along the entire length of the pipeline as in [38].

The dynamic component of normal pressure,  $\sigma_{ND}$ , i.e.  $\sigma_N = \sigma_{NS} = const$  is not taken into account. When determining the longitudinal stress in the pipeline, only the soil displacement is taken into account, determined from the solution of equations (25), (27) at  $i = 2$ . Soil displacement values further enter equation (40) when determining the shear stress (interaction force) on the pipeline-soil contact surface.

Curve 0 in Figure 6 is the set load generating the wave. The amplitude of this load,  $\sigma_{max} = 0.5$  MPa, remains constant over time. In the following sections  $x = 5; 10; 15$  m (curves 1–3), the amplitudes of longitudinal stress increase significantly, from about 12 to 18 times, compared with the amplitude of  $\sigma_{max} = 0.5$  MPa. This is due to soil displacement under wave propagation through it. Since the soil stiffness is approximately five times less ( $C_{01} = 5000$  m/s;  $C_{02} = 1000$  m/s) than the pipeline material, the soil displacement is significantly greater than the pipeline displacement as a result of their strain under the load (24).

As a result, the pipeline stress state actually determines the soil motion. Even in the case when the front end of the pipeline is load-free (24), the pattern in Figure 6 practically does not change, which confirms the significant and determinant role of soil medium in longitudinal stress formation in the pipeline. The value of relative displacement in the case shown in Figure 6 varies within  $-0.5 \cdot 10^{-3} \leq u \leq 1 \cdot 10^{-3}$  m, and the value of shear stress varies within  $-2 \cdot 10^{-2} < \tau < 2 \cdot 10^{-2}$  MPa. As seen, in this case, the values of relative displacement are an order of magnitude greater, and the values of shear stress are three orders of magnitude greater than in the previous case. In addition, in the case shown in Figure 5, the interaction force on the outer surface of the pipeline is always a passive resistance force, which leads to the wave amplitude attenuation over time.

In Figure 6, this interaction force due to the large strain in soil, hence, a greater displacement of soil relative to the pipeline, turns from a passive force into an active one. Under this active force, longitudinal stress in the pipeline increases too. The action of an active force occurs along the entire outer surface of the pipeline along its length. Therefore, the value of the interaction force dominates when comparing with the load at the front end of the pipeline. Due to this circumstance, the load (24) at the front end of the pipeline does not play a significant role at  $\sigma_{max} = 0.5$  MPa. The results in Figure 6 are obtained at  $u_* \rightarrow \infty$ , i.e. in this case, equation (20) is used and not equations (7)–(10). Note that with the above values of the initial data, an account of equations (7)–(10) does not practically affect the change in longitudinal stresses (Figure 6).

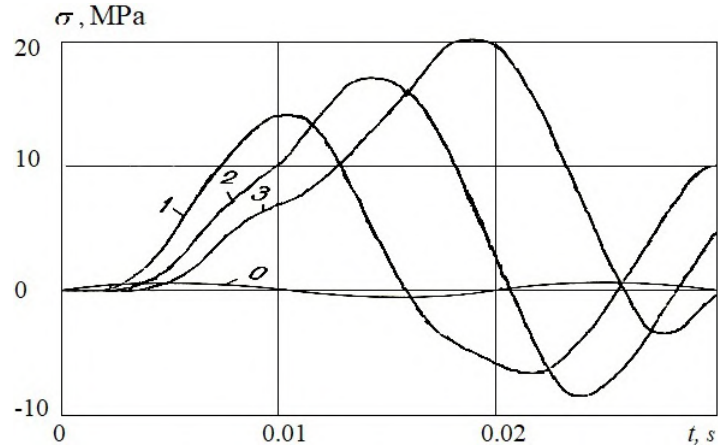


**Figure 7. Change of longitudinal stresses in the pipeline at  $x = 0; 5; 10; 15$  m, considering the soil movement at  $\sigma_N = \sigma_{NS} + \sigma_{ND}$  in the case of interaction model of Hooke's type.**

Consider the case of changes of longitudinal stresses in the pipeline with dynamic changes in the stress state of soil (Figure 7). In this case, the stress normal to the outer surface is  $\sigma_N = \sigma_{NS} + \sigma_{ND} \neq const$  according to (4). The value of  $\sigma_{ND} = K_\sigma \sigma_2(t, x)$  is determined by longitudinal stress in soil  $\sigma_2(t, x)$ . Lateral pressure coefficient is  $K_\sigma = 0.3$ . The values of all other initial data of the problem remain unchanged. As seen from Figure 7, the amplitude of longitudinal stresses in comparison with the case at  $\sigma_N = \sigma_{NS} = const$  (Figure 6), increases by two or more times. In Figure 7, just as in Figure 6, curves 0–3 relate to the distances from the initial section  $x = 0$  (curve 0),  $x = 5; 10; 15$  m (curves 1–3), respectively.

Calculations of longitudinal stresses for pipeline sections  $x = 30; 60; 90$  m show that the amplitude  $\sigma_{1max}$  increases asymptotically. At  $x = 90$  m,  $\sigma_{1max} = 27$  MPa and in the next sections of the pipeline this value of longitudinal stress remains unchanged. An account of dynamic component of the normal stress leads to a three-time increase in longitudinal stresses in the pipeline, compared with the case when it is not taken into account. At the maximum stress in soil surrounding the pipeline,  $\sigma_{2max} = 0.5$  MPa, longitudinal stress in the pipeline increases ( $\sigma_{1max} = 27$  MPa) by 54 times.

In this case, the relative displacement and shear stress on the pipeline profile vary within  $-1.5 \cdot 10^{-3} < u < 0$  m and  $-2 \cdot 10^{-2} < \tau < 4 \cdot 10^{-2}$  MPa. Compared to Figure 6, the value of relative displacement is of the same order ( $abs(u) = 1.5 \cdot 10^{-3}$  m), and the value of shear stress, on account of the addition of  $\sigma_{ND}$ , increases by about 2 times. As a result, an increase in the pipeline longitudinal stress is three times greater in Figure 7 than in the case shown in Figure 6.

In the above options, the frequency of longitudinal waves in soil is taken as  $f = 0.5T^{-1} = 50$  s<sup>-1</sup>. Under low-frequency seismic loads, at  $f = 1-10$  s<sup>-1</sup>, the value of longitudinal stresses in the pipeline increases to 100 MPa or more. The determination of longitudinal stresses in the pipeline under low-frequency seismic wave propagation in soil is beyond the limits of this investigation.

### 3.2. Longitudinal stresses in an underground pipeline in the case of an interaction model of the Kelvin-Voigt law type

Consider the effect of laws (22) and (6) on the values of longitudinal stresses in the pipeline.

The interaction model (22) is constructed by analogy with the Kelvin – Voigt law [11]. In this case, the shear viscosity function  $\eta_S(\sigma_N, I_S)$  is determined from relations (23). According to (23), the shear viscosity coefficient of disturbed soil on the underground pipeline-soil contact surface is determined by formula

$$\eta_S^*(\sigma_N) = f \sigma_N / C_S. \quad (41)$$

At the pipe laying depth  $H = 1$  m, according to (39),  $\sigma_{NS} = 0.23 \cdot 10^5$  Pa. Taking the values of the coefficient of internal friction as equal to  $f = 0.5$  and  $C_S = 500$  m/s, we get  $\tau_{np} = 0.115 \cdot 10^5$  Pa,  $\eta_S^* = 23$  Pa·s/m.

The initial data for calculations in this case are  $K_{NS} = 100 \text{ m}^{-1}$ ;  $\alpha_S = 1.2$ ;  $\beta = 2$ ;  $C_{01} = 5000 \text{ m/s}$ ;  $H = 1 \text{ m}$ ;  $T = 0.01 \text{ s}$ ;  $L = 1000 \text{ m}$ ;  $\gamma_{g1} = 780 \text{ kN/m}^3$ ;  $\gamma_{g2} = 200 \text{ kN/m}^3$ ;  $\mu_1 = 10^4 \text{ c}^{-1}$ ;  $D_H = 0.2 \text{ m}$ ;  $D_B = 0.18 \text{ m}$ ;  $C_S = 500 \text{ m/s}$ ;  $\sigma_{\max} = 0.5 \text{ MPa}$ .

The values of initial data for equation (40), in this case, are supplemented by the values of the parameters of equations (22), (23).

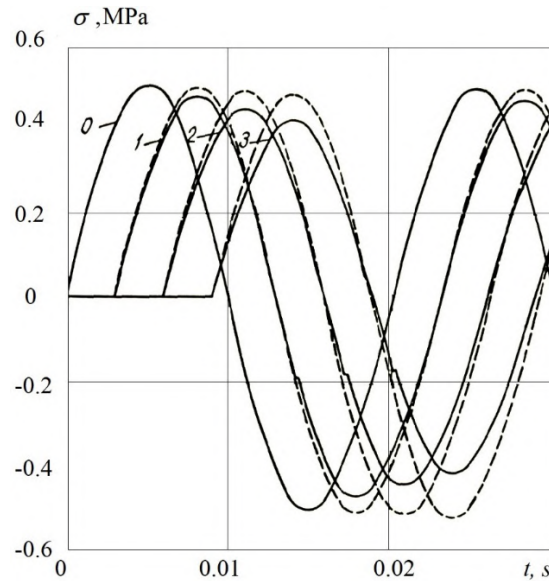


**Figure 8. Change of longitudinal stresses in the pipeline at  $x = 0; 15; 30; 45 \text{ m}$ , not considering the wave processes in soil at  $\sigma_N = \sigma_{NS} = \text{const}$  in the case of interaction model of Kelvin-Voigt type.**

First consider the case when the wave processes in the soil surrounding the underground pipeline are not taken into account  $\beta = 0$ ;  $\alpha_S = 0$ . This case corresponds to the linear law of interaction of the Kelvin-Voigt type. Calculation results are given in Figure 8 (dashed curves 0–3). Here, curve 0 is the set load at  $x = 0$  changing according to equation (24). As seen from Figure 8, the wave amplitude at distances  $x = 15; 30; 45 \text{ m}$  (dashed curves 1–3, respectively) attenuates slightly. In this case, the viscosity coefficient is  $\eta_S^* = 23 \text{ Pa}\cdot\text{s/m}$ .

Shear stress of the interaction  $\tau$  determined by equation (22) varies within  $-20 < \tau < 10 \text{ Pa}$ ; relative displacement varies within  $-8 \cdot 10^{-5} < u < 2 \cdot 10^{-5} \text{ m}$ , i.e. these parameters are the same as in the case shown in Figure 5, at elastic interaction. Therefore, the change of stress over time at fixed sections of the underground pipeline is identical when using interaction models (20) and (22).

To identify the effect of shear viscosity of soil  $\eta_S^*$  on the stress state of an underground pipeline, the value of  $C_S$  in calculations was assumed to be artificially undervalued and equal to  $0.5 \text{ m/s}$ . The values of the remaining parameters did not change. Solid curves 1–3 in Figure 8 belong to this case. Here  $\eta_S^* = 23 \cdot 10^3 \text{ Pa}\cdot\text{s/m}$ , i.e. 1000 times more than in the former option. In this option, the amplitude of the first entry of longitudinal stress into the pipeline decreases by 10–15 % compared to the case when  $C_S = 500 \text{ m/s}$  (dashed curves in Figure 8).

Weak effect of the viscous component of equation (22) is explained by small values of the relative displacement velocity  $du/dt$  ( $-3 \cdot 10^{-2} < du/dt < 2 \cdot 10^{-2} \text{ m/s}$ ).

It follows that at an underground pipeline-soil interaction under seismic load, it is impossible to ignore the wave processes occurring in soil.

Consider the case of an underground pipeline-soil interaction according to model (22), taking into account the wave processes in soil medium. The initial data for the calculations are the same as in the former case (Figure 8, dashed curves).

First assume that  $\sigma_N = \sigma_{NS} = \text{const}$ , i.e. the pressure normal to the outer surface of the pipe along the entire length of the pipeline is considered as constant. The calculation results of this case are shown in Figure 9 in the form of graphs of change in longitudinal stress over time for sections  $x = 0; 15; 30; 45 \text{ m}$

(curves 0–3, respectively). In contrast to Figure 8, there is 1.2–2 times increase in stress amplitude in the pipeline sections. This is due to an increase in soil displacement relative to the pipeline caused by soil strain.

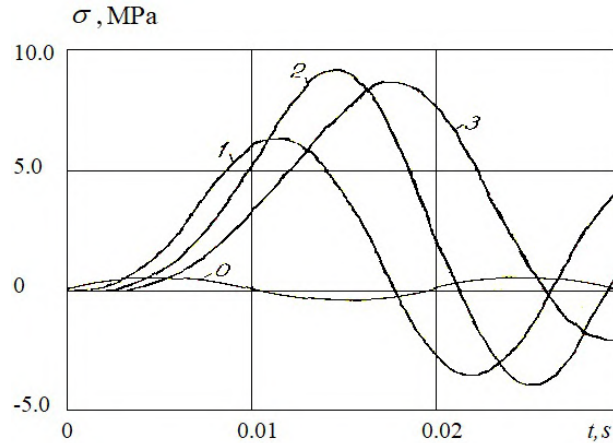


**Figure 9. Change of longitudinal stresses in the pipeline at  $x = 0; 5; 10; 15$  m, considering the wave processes in soil at  $\sigma_N = \sigma_{NS} = const$  in the case of interaction model of Kelvin-Voigt type.**

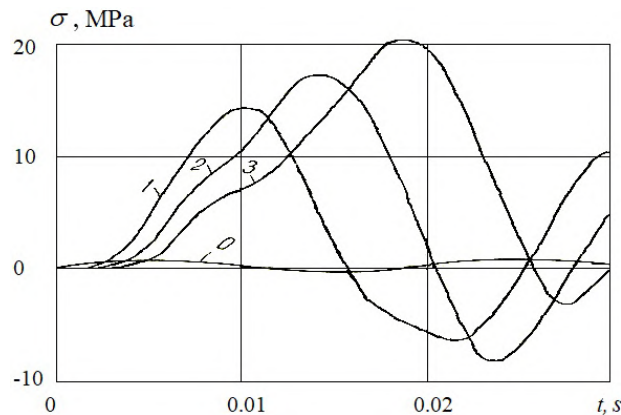


**Figure 10. Change of longitudinal stresses in the pipeline at  $x = 0; 15; 30; 45$  m, considering the wave processes in soil at  $\sigma_N = \sigma_{NS} + \sigma_{ND}$  in the case of interaction model of Kelvin-Voigt type.**

The values of relative displacement in this option of calculation vary within  $-10^{-4} < u < 10^{-4}$  m, and the shear stresses vary within  $-200 < \tau < 200$  Pa. As noted above, here a stress increase in the pipeline occurs due to the transformation of interaction force from a passive force into an active one.

An account for dynamic component of normal stress on the pipeline  $\sigma_{ND}$  leads to an even greater increase in longitudinal stress in the pipeline (Figure 10). In Figure 10, where  $\sigma_N = \sigma_{NS} + \sigma_{ND} \neq const$  is taken in calculations, the longitudinal stress is doubled compared with the case shown in Figure 9, where  $\sigma_N = \sigma_{NS} = const$ .

However, the results obtained in calculations using the Hooke's type (Figures 5–7) and the Kelvin-Voigt type interaction models (Figures 8–10) are quantitatively identical. An account for shear viscosity of soil according to the Kelvin-Voigt model does not noticeably affect the maximum stress values. The results of calculations of longitudinal stresses in an underground pipeline in the case of the Hooke's type interaction model and in the case of the Kelvin-Voigt model are quantitatively and qualitatively identical (Figures 5–10).

### **3.3. Longitudinal stresses in an underground pipeline interacting with soil according to the model of a standard viscoelastic body**

Consider the results of calculations of longitudinal stresses in an underground pipeline interacting with soil, taking into account the volume viscosity of soil. In this case, equation (6) is used as a model of interaction.

The initial data for the reference dependencies (8)–(18) and calculations are given above. For clarity, we will give them again:  $C_{01} = 5000$  m/s;  $\gamma_{g1} = 780$  kN/m<sup>3</sup>;  $\gamma_N = 1.5$ ;  $\gamma_*^m = 4$ ;  $\beta = 2.5$ ;  $\varphi = 1.2$ ;  $K_{NS} = 100$  m<sup>-1</sup>;  $C_S = 500$  m/s;  $T = 0.01$  s;  $H = 1$  m;  $D_H = 0.2$  m;  $D_B = 0.18$  m;  $L = 1000$  m;  $\sigma_{max} = 0.5$  MPa.

The results of computer calculations of longitudinal stresses in the pipeline, obtained only with equation (6) taken as the law of interaction, are shown in Figure 11. Curves 0–3 here relate to distances  $x = 0; 5; 10; 15$  m, respectively. In this option of calculations, similar to the cases of the Hooke and Kelvin-Voigt types of interaction model the wave processes in soil are not taken into account at first. Curve 0 in Figure 11 refers to the change in stress at cross section  $x = 0$  (initial section), i.e. this is a load generating a wave. As seen from Figure 11 at a distance of  $x = 5$  m from the initial section, the amplitude of longitudinal stress decreases by  $\approx 50\%$  (curve 1).

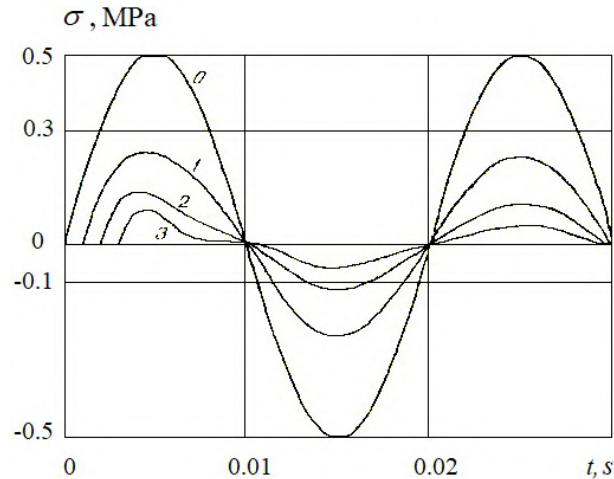


**Figure 11. Change of longitudinal stresses in the pipeline at fixed values of  $x = 0; 5; 10; 15$  m, not considering the wave processes in soil at  $\sigma_N = \sigma_{NS} = const$  in the case of interaction model of a standard body type.**

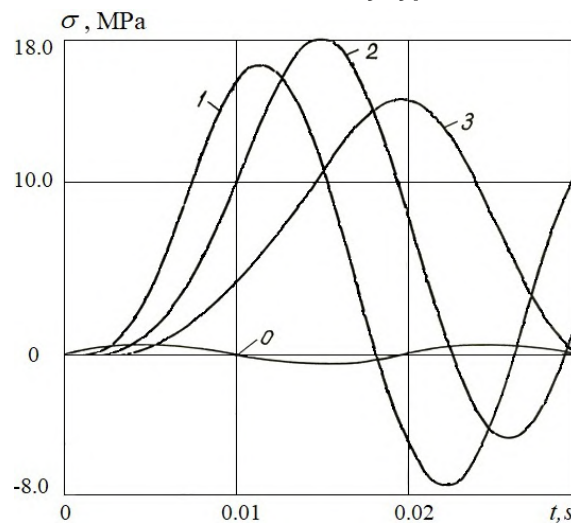


**Figure 12. Change of longitudinal stresses in the pipeline at fixed values of  $x = 0; 5; 10; 15$  m, not considering the wave processes in soil at  $\sigma_N = \sigma_{NS} = const$  in the case of interaction model of a standard body type.**

The stress in the subsequent sections of the underground pipeline at  $x = 10$  and  $15$  m substantially attenuates (curves 2 and 3). Compared to the interaction models of the Hooke's and Kelvin-Voigt types, the stress wave attenuation along the underground pipeline is significant. This shows the effect of considering the volume viscosity of soil in the pipe-soil interaction. In this case, the stress amplitudes attenuate in subsequent stress fluctuations as well, which correspond to the results of known experiments [11].

The account of wave processes in soil medium according to the law of interaction (6) at  $\sigma_N = \sigma_{NS} = const$  is shown in Figure 12. Curves 0–3 refer to the same sections of the underground pipeline  $x = 0; 5; 10; 15$  m, respectively. Compared with the case when the laws of interaction of the Hooke's (Figure 6) and Kelvin-Voigt types (Figure 9) were used, a significant increase in the amplitude of longitudinal stresses is observed here. In all sections, the amplitudes of longitudinal stresses are almost two times higher than the results in Figures 6 and 9. This effect is further enhanced at  $\sigma_N = \sigma_{NS} + \sigma_{ND} \neq const$  (Figure 13). An account for dynamic components of dynamic stress normal to the outer surface of the pipeline leads to 30–35% increase in the amplitude of longitudinal stresses in the same sections  $x = 5; 10; 15$  m from the initial section  $x = 0$ .

The results of calculations using the interaction model (6) of a standard body type show that in this case the change limits of the relative displacement  $-4 \cdot 10^{-4} < u < 9 \cdot 10^{-4}$  m and shear stress  $-65 \cdot 10^3 < \tau < 60 \cdot 10^3$  Pa are greater than for the laws of interaction of the Hooke's and Kelvin-Voigt types.

In all cases, an account for the wave processes in the soil surrounding the underground pipeline by the changes in dynamic normal stress  $\sigma_{ND}$  and soil displacement  $u_2$  leads to 40–50 times increase in the amplitude of longitudinal stress in the pipeline as compared with the amplitude of initial stress  $\alpha_{\max} = 0.5$  MPa.

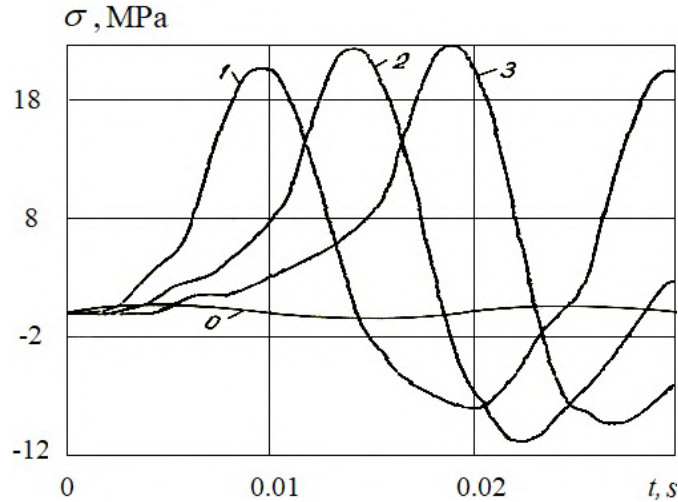


**Figure 13. Change of longitudinal stresses in the pipeline at  $x = 0; 5; 10; 15$  m, considering the wave processes in soil at  $\sigma_N = \sigma_{NS} + \sigma_{ND}$  in the case of interaction model of a standard body type.**

The greatest increase in the amplitude of longitudinal stress is observed in the case of using the law of interaction of a standard viscoelastic body type.

### 3.4. Longitudinal stresses in an underground pipeline interacting with soil according to a generalized interaction model

Changes in longitudinal stresses in the underground pipeline when using the law of generalized interaction (6)–(10) are shown in Figure 14. The values of the initial parameters remained the same as in Figure 13.

Here, curves 0–3 relate to sections  $x = 0; 5; 10; 15$  m. In this case, the amplitude of longitudinal stresses in the pipeline is approximately 20 % less than in the case when only the interaction law (6) was used. This is explained by a decrease in the value of active shear stress – the interaction force in the case of the complete law (6)–(10).

According to estimated data [38], during the Gazli earthquake (1976), longitudinal stresses in underground gas pipelines amounted to  $\sigma_1 = 83.5\text{--}167.0$  MPa. These values of longitudinal stresses are 3–7 times higher than the longitudinal stresses obtained above. However, the period of seismic wave vibrations in the Gazli earthquake was  $T = 0.5$  s [38]. As noted above, the determination of longitudinal stresses for low-frequency seismic waves is considered separately.

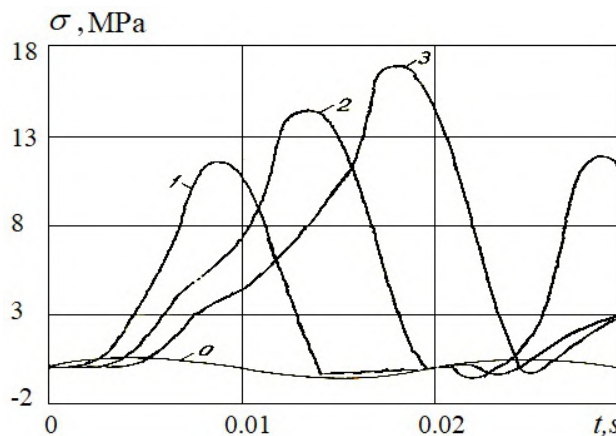


**Figure 14. Change of longitudinal stresses in the pipeline at  $x = 0; 5; 10; 15$  m, considering the wave processes in soil at  $\sigma_N = \sigma_{NS} + \sigma_{ND}$  in the case of a generalized interaction model.**

Thus, the values of longitudinal stresses in underground pipelines interacting with soil by various interaction laws and at the frequency of incident seismic wave  $f = 50 \text{ s}^{-1}$  are given in this paper, with and without an account for the wave processes in soil medium.

#### 4. Conclusions

1. The coupled wave problems of the underground pipeline-soil interaction under the influence of a seismic load were formulated taking into account the strain characteristics of the pipeline and soil and various laws of interaction.

2. For the numerical solution of the stated coupled wave problem, the method of characteristics with the subsequent application of the finite difference method in an implicit scheme was used. The chosen method of numerical solution and its advantages and disadvantages were substantiated.

3. An algorithm and program for solving numerical solution of coupled wave problems for an extended underground pipeline and for soil medium were compiled. Numerical solutions of test problems were obtained, the results of which were compared with experimental results and the reliability of the developed algorithms and a program for numerical solution of the problems under consideration were shown.

4. The analysis of the obtained numerical solutions, in the form of a change in longitudinal stresses in the underground pipeline, related to the statement of wave and dynamic theory of earthquake resistance of underground structures was carried out. The advantages and disadvantages of the considered theories were shown.

5. The results of calculations of longitudinal stresses in underground gas pipelines during the Gazli earthquake were considered and compared with the results of numerical solutions.

6. Longitudinal stresses of underground pipelines at their interaction with soil were determined according to non-linear laws of interaction of Hooke's type, Kelvin-Voigt type and a standard body. The advantages and disadvantages of the considered laws of interaction of underground pipelines with soil and their influence on the stress state of underground pipeline were shown.

7. The application of the developed method for calculating the stresses in underground pipelines improves the regulatory method by refining the KMK-2.01.03-96 (Building Code).

#### References

1. Muravyeva, L., Vatin, N. Risk Assessment for a Main Pipeline under Severe Soil Conditions on Exposure to Seismic Forces. *Applied Mechanics and Materials*. 2014. 635–637. Pp. 468–471. DOI: 10.4028/www.scientific.net/AMM.635-637.468.
2. Muravyeva, L., Vatin, N. The Safety Estimation of the Marine Pipeline. *Applied Mechanics and Materials*. 2014. 633–634. Pp. 958–964. DOI: 10.4028/www.scientific.net/AMM.633-634.958.
3. Muravyeva, L., Vatin, N. Application of the Risk Theory to Management Reliability of the Pipeline. *Applied Mechanics and Materials*. 2014. 635–637. Pp. 434–438. DOI: 10.4028/www.scientific.net/AMM.635-637.434.
4. Lalin, V.V., Kushova, D.A. New Results in Dynamics Stability Problems of Elastic Rods. *Applied Mechanics and Materials*. 2014. 617. Pp. 181–186. DOI: 10.4028/www.scientific.net/AMM.617.181.
5. Jung, J.K., O'Rourke, T.D., Argyrou, C. Multi-directional force–displacement response of underground pipe in sand. *Canadian Geotechnical Journal*. 2016. No. 11(53). Pp. 1763–1781. DOI: 10.1139/cgj-2016-0059.
6. Gao, F.-P., Wang, N., Li, J., Han, X.-T. Pipe–soil interaction model for current-induced pipeline instability on a sloping sandy seabed. *Canadian Geotechnical Journal*. 2016. No. 11(53). Pp. 1822–1830. DOI: 10.1139/cgj-2016-0071.
7. Wijewickreme, D., Monroy, M., Honegger, D.G., Nyman, D.J. Soil restraints on buried pipelines subjected to reverse-fault displacement. *Canadian Geotechnical Journal*. 2017. No. 10(54). Pp. 1472–1481. DOI: 10.1139/cgj-2016-0564.
8. Muravieva, L., Bashirzade, S. Behaviour underground pipelines laid in saturated soil. *Russian journal of transport engineering*. 2015. No. 3(2). DOI: 10.15862/01TS315.
9. Housner, G. Introduction to earthquake engineering, Second Edition, Shunzo Okamoto. ISBN 0–86008-361–6. University of Tokyo Press, 1984. 7–3-1 Hongo, Bunkyo-ku, Tokyo 113–91, Japan. 652 p. *Earthquake Engineering & Structural Dynamics*. 1985. No. 2(13). Pp. 278–278. DOI: 10.1002/eqe.4290130213
10. Sultanov, K.S., Loginov, P.V., Ismoilova, S.I., Salikhova, Z.R. Quasistaticity of the process of dynamic strain of soils. *Magazine of Civil Engineering*. 2019. 85(1). Pp. 71–91. DOI: 10.18720/MCE.85.7.
11. Sultanov, K.S., Bakhodirov, A.A. Laws of Shear Interaction at Contact Surfaces Between Solid Bodies and Soil. *Soil Mechanics and Foundation Engineering*. 2016. No. 2(53). Pp. 71–77. DOI: 10.1007/s11204-016-9367-7.
12. Bakhodirov, A.A., Ismailova, S.I., Sultanov, K.S. Dynamic deformation of the contact layer when there is shear interaction between a body and the soil. *Journal of Applied Mathematics and Mechanics*. 2015. No. 6(79). Pp. 587–595. DOI: 10.1016/j.jappmathmech.2016.04.005.
13. Israilov, M.S. Coupled seismic vibrations of a pipeline in an infinite elastic medium. *Mechanics of Solids*. 2016. No. 1(51). Pp. 46–53. DOI: 10.3103/S0025654416010052.
14. Georgievskii, D.V., Israilov, M.S. Seismodynamics of extended underground structures and soils: Statement of the problem and self-similar solutions. *Mechanics of Solids*. 2015. No. 4(50). Pp. 473–484. DOI: 10.3103/S0025654415040135.
15. Israilov, M.S. A new approach to solve the problems of seismic vibrations for periodically nonuniform buried pipelines. *Moscow University Mechanics Bulletin*. 2016. No. 1(71). Pp. 23–26. DOI: 10.3103/S0027133016010052.

16. Israilov, M.Sh. Analogiya lineynoy tsepochki i seismicheskiye kolebaniya segmentnykh i vyazkouprugikh truboprovodov. Izvestiya Rossiyskoy akademii nauk. Mekhanika tverdogo tela. 2018. № 3. Pp. 119–128. DOI: 10.7868/S0572329918030121.
17. Liyanage, K., Dhar, A.S. Stresses in cast iron water mains subjected to non-uniform bedding and localised concentrated forces. International Journal of Geotechnical Engineering. 2018. No. 4(12). Pp. 368–376. DOI: 10.1080/19386362.2017.1282338.
18. Smith, A., Dixon, N., Fowmes, G. Monitoring buried pipe deformation using acoustic emission: quantification of attenuation. International Journal of Geotechnical Engineering. 2017. No. 4(11). Pp. 418–430. DOI: 10.1080/19386362.2016.1227581.
19. Meyer, V., Langford, T., White, D.J. Physical modelling of pipe embedment and equalisation in clay. Géotechnique. 2016. No. 7(66). Pp. 602–609. DOI: 10.1680/jgeot.15.T.024.
20. Feng, W., Huang, R., Liu, J., Xu, X., Luo, M. Large-scale field trial to explore landslide and pipeline interaction. Soils and Foundations. 2015. No. 6(55). Pp. 1466–1473. DOI: 10.1016/j.sandf.2015.10.011.
21. Matsushashi, M., Tsushima, I., Fukatani, W., Yokota, T. Damage to sewage systems caused by the Great East Japan Earthquake, and governmental policy. Soils and Foundations. 2014. No. 4(54). Pp. 902–909. DOI: 10.1016/j.sandf.2014.06.019.
22. Lam, S.Y., Haigh, S.K., Bolton, M.D. Understanding ground deformation mechanisms for multi-propped excavation in soft clay. Soils and Foundations. 2014. No. 3(54). Pp. 296–312. DOI: 10.1016/j.sandf.2014.04.005.
23. Zhang, Z., Zhang, M. Mechanical effects of tunneling on adjacent pipelines based on Galerkin solution and layered transfer matrix solution. Soils and Foundations. 2013. No. 4(53). Pp. 557–568. DOI: 10.1016/j.sandf.2013.06.007.
24. Williams, E.S., Byrne, B.W., Blakeborough, A. Pipe uplift in saturated sand: rate and density effects. Géotechnique. 2013. No. 11(63). Pp. 946–956. DOI: 10.1680/geot.12.P.067.
25. Chatterjee, S., Randolph, M.F., White, D.J. The effects of penetration rate and strain softening on the vertical penetration resistance of seabed pipelines. Géotechnique. 2012. No. 7(62). Pp. 573–582. DOI: 10.1680/geot.10.P.075.
26. Sultanov, K.S. The attenuation of longitudinal waves in non-linear viscoelastic media. Journal of Applied Mathematics and Mechanics. 2002. No. 1(66). Pp. 115–122. DOI: 10.1016/S0021-8928(02)00015-1.
27. Sultanov, K.S., Khusanov, B.É. Determination of the slump-type settlement of a nonlinearly deformable soil mass during wetting. Soil Mechanics and Foundation Engineering. 2002. No. 3(39). Pp. 81–84. DOI: 10.1023/A:1020329100803.
28. Akimov, M.P., Mordovskoy, S.D., Starostin, N.P. Calculating thermal insulation thickness and embedment depth of underground heat supply pipeline for permafrost soils. Magazine of Civil Engineering. 2014. 46(2). Pp. 14–23. DOI: 10.5862/MCE.46.3.
29. Kalugina, J.A., Keck, D., Pronozin, Y.A. Determination of soil deformation moduli after National Building Codes of Russia and Germany. Magazine of Civil Engineering. 2017. 75(7). Pp. 139–149. DOI: 10.18720/MCE.75.14.
30. Mirsaidov, M.M., Sultanov, T.Z. Use of linear heredity theory of viscoelasticity for dynamic analysis of earthen structures. Soil Mechanics and Foundation Engineering. 2013. No. 6(49). Pp. 250–256. DOI: 10.1007/s11204-013-9198-8.
31. Mirsaidov, M.M., Sultanov, T.Z., Sadullaev, S.A. An assessment of stress-strain state of earth dams with account of elastic-plastic, moist properties of soil and large strains. Magazine of Civil Engineering. 2013. 40(5). Pp. 59–68. DOI: 10.5862/MCE.40.7.
32. Samarin, O.D. The temperature waves motion in hollow thick-walled cylinder. Magazine of Civil Engineering. 2018. 78(2). Pp. 161–168. DOI: 10.18720/MCE.78.13.
33. Loktionova, E.A., Miftakhova, D.R. Fluid filtration in the clogged pressure pipelines. Magazine of Civil Engineering. 2017. 76(8). Pp. 214–224. DOI: 10.18720/MCE.76.19.
34. Singh, M., Viladkar, M.N., Samadhiya, N.K. Seismic response of metro underground tunnels. International Journal of Geotechnical Engineering. 2016. No. 2(11). Pp. 1–11. DOI: 10.1080/19386362.2016.1201881.
35. Chernysheva, N.V., Kolosova, G.S., Rozin, L.A. Combined Method of 3d Analysis for Underground Structures in View of Surrounding Infinite Homogeneous and Inhomogeneous Medium. Magazine of Civil Engineering. 2016. 62(2). Pp. 83–91. DOI: 10.5862/MCE.62.8.
36. Lanzano, G., Bilotta, E., Russo, G., Silvestri, F. Experimental and numerical study on circular tunnels under seismic loading. European Journal of Environmental and Civil Engineering. 2015. No. 5(19). Pp. 539–563. DOI: 10.1080/19648189.2014.893211.
37. Chang, D.-W., Cheng, S.-H., Wang, Y.-L. One-dimensional wave equation analyses for pile responses subjected to seismic horizontal ground motions. Soils and Foundations. 2014. No. 3(54). Pp. 313–328. DOI: 10.1016/j.sandf.2014.04.018.
38. Erdik, M., Rashidov, T., Safak, E., Turdukulov, A. Assessment of seismic risk in Tashkent, Uzbekistan and Bishkek, Kyrgyz Republic. Soil Dynamics and Earthquake Engineering. 2005. No. 7–10(25). Pp. 473–486. DOI: 10.1016/j.sandf.2014.04.018.

### **Contacts:**

*Karim Sultanov, +998909702535; sultanov.karim@mail.ru*

*Jakhongir Kumakov, +998901765500; sultanov.karim@mail.ru*

*Pavel Loginov, +998909801765; lopavi88@mail.ru*

*Barno Rikhsieva, +998977750936; barno.khusanova@mail.ru*

© Sultanov, K.S., Kumakov, J.X., Loginov, P.V., Rikhsieva, B.B., 2020



DOI: 10.18720/MCE.93.9

## Прочность подземных трубопроводов при сейсмических воздействиях

**К.С. Султанов<sup>a</sup>, Ж.Х. Кумаков<sup>b</sup>, П.В. Логинов<sup>a</sup>, Б.Б. Рихсиева<sup>a</sup>**

<sup>a</sup> *Институт механики и сейсмостойкости сооружений Академии наук Республики Узбекистан, г. Ташкент, Республика Узбекистан*

<sup>b</sup> *Ташкентский архитектурно-строительный институт, г. Ташкент, Республика Узбекистан*

\* E-mail: [sultanov.karim@mail.ru](mailto:sultanov.karim@mail.ru)

**Ключевые слова:** прочность, сейсмостойкость, трубопровод, грунт, взаимодействия, механические свойства, численные методы, скорость деформации, напряжения

**Аннотация.** Приводится краткий анализ методов расчета на сейсмостойкость подземных трубопроводов, их преимущества и недостатки. Приведен анализ моделей взаимодействия подземных трубопроводов с грунтом при сейсмических (динамических) воздействиях. Поставлены связанные задачи о взаимодействии подземного трубопровода с грунтом при прохождении сейсмической волны в грунтовой среде, включающей трубопровод. Одномерные нестационарные волновые задачи для грунтовой среды и для трубопровода решены численно с применением метода характеристик и метода конечных разностей. Получены численные решения в виде изменения продольных напряжений по времени в различных сечениях трубопровода. Анализом полученных численных решений показана существенная зависимость значения продольных напряжений от волновых процессов в грунтовой среде и динамического напряженного состояния грунта, а также механических свойств грунта и материала трубопровода. Обнаружен фактор многократного возрастания продольного напряжения в подземном трубопроводе при его динамическом взаимодействии с грунтом. Показано, что главной причиной такого возрастания напряжения является динамическое напряженное состояние грунта вокруг трубопровода при его взаимодействии с грунтом. Полученные результаты являются основой для разработки нового нормативного расчета прочности подземных магистральных трубопроводов при сейсмических воздействиях.

### Литература

1. Muravyeva L., Vatin N. Risk Assessment for a Main Pipeline under Severe Soil Conditions on Exposure to Seismic Forces // *Applied Mechanics and Materials*. 2014. 635–637. Pp. 468–471. DOI: 10.4028/www.scientific.net/AMM.635-637.468.
2. Muravyeva L., Vatin N. The Safety Estimation of the Marine Pipeline // *Applied Mechanics and Materials*. 2014. 633–634. Pp. 958–964. DOI: 10.4028/www.scientific.net/AMM.633-634.958.
3. Muravyeva L., Vatin N. Application of the Risk Theory to Management Reliability of the Pipeline // *Applied Mechanics and Materials*. 2014. 635–637. Pp. 434–438. DOI: 10.4028/www.scientific.net/AMM.635-637.434.
4. Lalin V.V., Kushova D.A. New Results in Dynamics Stability Problems of Elastic Rods // *Applied Mechanics and Materials*. 2014. 617. Pp. 181–186. DOI: 10.4028/www.scientific.net/AMM.617.181.
5. Jung J.K., O'Rourke T.D., Argyrou C. Multi-directional force–displacement response of underground pipe in sand // *Canadian Geotechnical Journal*. 2016. No. 11(53). Pp. 1763–1781. DOI: 10.1139/cgj-2016-0059.
6. Gao F.-P., Wang N., Li J., Han X.-T. Pipe–soil interaction model for current-induced pipeline instability on a sloping sandy seabed // *Canadian Geotechnical Journal*. 2016. No. 11(53). Pp. 1822–1830. DOI: 10.1139/cgj-2016-0071.
7. Wijewickreme D., Monroy M., Honegger D.G., Nyman D.J. Soil restraints on buried pipelines subjected to reverse-fault displacement // *Canadian Geotechnical Journal*. 2017. No. 10(54). Pp. 1472–1481. DOI: 10.1139/cgj-2016-0564.
8. Muravieva L., Bashirzade S. Behaviour underground pipelines laid in saturated soil // *Russian journal of transport engineering*. 2015. No. 3(2). DOI: 10.15862/01TS315.
9. Housner G. Introduction to earthquake engineering, Second Edition, Shunzo Okamoto. ISBN 0–86008-361–6. University of Tokyo Press, 1984. 7–3-1 Hongo, Bunkyo-ku, Tokyo 113–91, Japan. 652 p. // *Earthquake Engineering & Structural Dynamics*. 1985. No. 2(13). Pp. 278–278. DOI: 10.1002/eqe.4290130213
10. Султанов К.С., Логинов П.В., Исмоилова С.И., Салихова З.П. Квазистатичность процесса динамического деформирования грунтов // *Инженерно-строительный журнал*. 2019. № 1(85). С. 71–91. DOI: 10.18720/MCE.85.7
11. Sultanov K.S., Bakhodirov A.A. Laws of Shear Interaction at Contact Surfaces Between Solid Bodies and Soil // *Soil Mechanics and Foundation Engineering*. 2016. No. 2(53). Pp. 71–77. DOI: 10.1007/s11204-016-9367-7.
12. Bakhodirov A.A., Ismailova S.I., Sultanov K.S. Dynamic deformation of the contact layer when there is shear interaction between a body and the soil // *Journal of Applied Mathematics and Mechanics*. 2015. No. 6(79). Pp. 587–595. DOI: 10.1016/j.jappmathmech.2016.04.005.

13. Israilov M.S. Coupled seismic vibrations of a pipeline in an infinite elastic medium // *Mechanics of Solids*. 2016. No. 1(51). Pp. 46–53. DOI: 10.3103/S0025654416010052.
14. Georgievskii D.V., Israilov M.S. Seismodynamics of extended underground structures and soils: Statement of the problem and self-similar solutions // *Mechanics of Solids*. 2015. No. 4(50). Pp. 473–484. DOI: 10.3103/S0025654415040135.
15. Israilov M.S. A new approach to solve the problems of seismic vibrations for periodically nonuniform buried pipelines // *Moscow University Mechanics Bulletin*. 2016. No. 1(71). Pp. 23–26. DOI: 10.3103/S0027133016010052.
16. Исраилов М.Ш. Аналогия линейной цепочки и сейсмические колебания сегментных и вязкоупругих трубопроводов // *Известия Российской академии наук. Механика твердого тела*. 2018. № 3. Pp. 119–128. DOI: 10.7868/S0572329918030121.
17. Liyanage K., Dhar A.S. Stresses in cast iron water mains subjected to non-uniform bedding and localised concentrated forces // *International Journal of Geotechnical Engineering*. 2018. No. 4(12). Pp. 368–376. DOI: 10.1080/19386362.2017.1282338.
18. Smith A., Dixon N., Fowmes G. Monitoring buried pipe deformation using acoustic emission: quantification of attenuation // *International Journal of Geotechnical Engineering*. 2017. No. 4(11). Pp. 418–430. DOI: 10.1080/19386362.2016.1227581.
19. Meyer V., Langford T., White D.J. Physical modelling of pipe embedment and equalisation in clay // *Géotechnique*. 2016. No. 7(66). Pp. 602–609. DOI: 10.1680/jgeot.15.T.024.
20. Feng W., Huang R., Liu J., Xu X., Luo M. Large-scale field trial to explore landslide and pipeline interaction // *Soils and Foundations*. 2015. No. 6(55). Pp. 1466–1473. DOI: 10.1016/j.sandf.2015.10.011.
21. Matsuhashi M., Tsushima I., Fukatani W., Yokota T. Damage to sewage systems caused by the Great East Japan Earthquake, and governmental policy // *Soils and Foundations*. 2014. No. 4(54). Pp. 902–909. DOI: 10.1016/j.sandf.2014.06.019.
22. Lam S.Y., Haigh S.K., Bolton M.D. Understanding ground deformation mechanisms for multi-propped excavation in soft clay // *Soils and Foundations*. 2014. No. 3(54). Pp. 296–312. DOI: 10.1016/j.sandf.2014.04.005.
23. Zhang Z., Zhang M. Mechanical effects of tunneling on adjacent pipelines based on Galerkin solution and layered transfer matrix solution // *Soils and Foundations*. 2013. No. 4(53). Pp. 557–568. DOI: 10.1016/j.sandf.2013.06.007.
24. Williams E.S., Byrne B.W., Blakeborough A. Pipe uplift in saturated sand: rate and density effects // *Géotechnique*. 2013. No. 11(63). Pp. 946–956. DOI: 10.1680/geot.12.P.067.
25. Chatterjee S., Randolph M.F., White D.J. The effects of penetration rate and strain softening on the vertical penetration resistance of seabed pipelines // *Géotechnique*. 2012. No. 7(62). Pp. 573–582. DOI: 10.1680/geot.10.P.075.
26. Sultanov K.S. The attenuation of longitudinal waves in non-linear viscoelastic media // *Journal of Applied Mathematics and Mechanics*. 2002. No. 1(66). Pp. 115–122. DOI: 10.1016/S0021-8928(02)00015-1.
27. Sultanov K.S., Khusanov B.É. Determination of the slump-type settlement of a nonlinearly deformable soil mass during wetting // *Soil Mechanics and Foundation Engineering*. 2002. No. 3(39). Pp. 81–84. DOI: 10.1023/A:1020329100803.
28. Акимов М.П., Мордовской С.Д., Старостин Н.П. Определение толщины теплоизоляции и заглубления подземного трубопровода теплоснабжения в многолетнемерзлых грунтах // *Инженерно-строительный журнал*. 2014. № 2(46). С. 14-23. DOI: 10.5862/MCE.46.3
29. Калугина Ю.А., Кек Д., Пронозин Я.А. Расчетные модули деформации грунта согласно национальным стандартам России и Германии // *Инженерно-строительный журнал*. 2017. № 7(75). С. 139–149. doi: 10.18720/MCE.75.14
30. Mirsaidov M.M., Sultanov T.Z. Use of linear heredity theory of viscoelasticity for dynamic analysis of earthen structures // *Soil Mechanics and Foundation Engineering*. 2013. No. 6(49). Pp. 250–256. DOI: 10.1007/s11204-013-9198-8.
31. Мирсаидов М.М., Султанов Т.З., Садуллаев Ш.А. Оценка напряженно-деформированного состояния грунтовых плотин с учетом упругопластических, влажностных свойств грунта и больших деформаций // *Инженерно-строительный журнал*. 2013. № 5(40). С. 59–68. DOI: 10.5862/MCE.40.7
32. Самарин О.Д. Распространение температурных волн в пустотелом толстостенном цилиндре // *Инженерностроительный журнал*. 2018. № 2(78). С. 161–168. doi: 10.18720/MCE.78.13
33. Локтионова Е.А., Мифтахова Д.Р. Фильтрация жидкости в засоренных напорных трубопроводах // *Инженерно-строительный журнал*. 2017. № 8(76). С. 214–224. doi: 10.18720/MCE.76.19
34. Singh M., Viladkar M.N., Samadhiya N.K. Seismic response of metro underground tunnels // *International Journal of Geotechnical Engineering*. 2016. No. 2(11). Pp. 1–11. DOI: 10.1080/19386362.2016.1201881.
35. Чернышева Н.В., Колосова Г.С., Розин Л.А. Пространственные расчеты подземных сооружений с учетом работы окружающего бесконечного массива в однородных и неоднородных областях комбинированным способом // *Инженерно-строительный журнал*. 2016. №2(62). С. 83-91. DOI: 10.5862/MCE.62.8
36. Lanzano G., Bilotta E., Russo G., Silvestri F. Experimental and numerical study on circular tunnels under seismic loading // *European Journal of Environmental and Civil Engineering*. 2015. No. 5(19). Pp. 539–563. DOI: 10.1080/19648189.2014.893211.
37. Chang D.-W., Cheng S.-H., Wang Y.-L. One-dimensional wave equation analyses for pile responses subjected to seismic horizontal ground motions // *Soils and Foundations*. 2014. No. 3(54). Pp. 313–328. DOI: 10.1016/j.sandf.2014.04.018.
38. Erdik M., Rashidov T., Safak E., Turdukulov A. Assessment of seismic risk in Tashkent, Uzbekistan and Bishkek, Kyrgyz Republic // *Soil Dynamics and Earthquake Engineering*. 2005. No. 7–10(25). Pp. 473–486. DOI: 10.1016/j.sandf.2014.04.018.

### **Контактные данные:**

*Карим Султанович Султанов, +998909702535; эл. почта: sultanov.karim@mail.ru*

*Жахонгир Хамзаевич Кумаков, +998901765500; эл. почта: sultanov.karim@mail.ru*

*Павел Викторович Логинов, +998909801765; эл. почта: lopavi88@mail.ru*

*Барно Бахтияровна Рихсиева, +998977750936; эл. почта: barno.khusanova@mail.ru*



DOI: 10.18720/MCE.93.10

## The influence of polyfunctional modifier additives on properties of cement-ash fine-grained concrete

**L.I. Dvorkin**

*National University of Water Environmental Engineering, Rivne, Ukraine*

\* E-mail: [dvorkin.leonid@gmail.com](mailto:dvorkin.leonid@gmail.com)

**Keywords:** ash, strength, shrinkage, abrasion, additives, superplasticizer, structure

**Abstract.** The object of the study is the properties of cement-ash concrete with the addition of a polyfunctional modifier (PFM) intended for floors of industrial enterprises. The PFM composition includes a naphthalene-formaldehyde type superplasticizer and a vinyl acetate-vinylversatate copolymer. A prerequisite for the use of PFM additives in cement-ash concrete is the ability to actively influence the structure formation processes and, as a consequence, the properties of concrete with it. Using well-known chemical and physical methods, experimental data have been obtained on the effect of PFM additives on the degree of cement hydration, the kinetics of changes in the plastic strength of cement-ash stone during hardening. It was found that the introduction of the PFM additive allows one to reduce the open porosity and average pore sizes of cement-ash stone and also increase the pore size uniformity index. To study the properties of cement-ash concrete with PFM additive, the method of mathematical planning of experiments was applied, as a result of which a complex of mathematical models of water demand, water separation, volume of air involved, concrete strength under compression and bending was obtained. The models make it possible to quantitatively evaluate the effect on the indicated properties of concrete of water and ash-cement ratios, the content and ratio of PFM components, as well as design the compositions of cement-ash concrete with desired properties. The studies, the results of which are presented in the article, showed the possibility, with the help of PFM additives, to significantly improve the properties of cement-ash concrete, which are important when using them for floors of industrial enterprises and, in particular, reduce ultimate shrinkage deformations by 30–50 %, reduce by 1.5–3 times their abrasion and up to 20 % increase resistance to shock.

### 1. Introduction

To date, thanks to the studies of many authors [1–9], the foundations of the theory of cement concrete with active mineral fillers have been developed. In accordance with this theory, the properties of filled cement systems are the result of the chemical, physico-chemical and physico-mechanical effects of the fillers at various levels of their structure. Due to the vitreous aluminosilicate phase, fly ash has pozzolanic activity and chemically interacts with  $\text{Ca}(\text{OH})_2$  released during the hydrolysis of clinker minerals. The introduction of fly ash into cement-water systems not only increases the volume of hydrated compounds, but also accelerates the hydrolysis process of clinker minerals [10–13].

Having a high specific surface, in addition to direct chemical interaction with cement, ash actively affects the physicochemical processes when cement is hardened. As the condensation-crystallization structure of the cement stone is formed, epitaxial contacts are formed between the cement paste and the grains of ash [3]. In accordance with the Gibbs – Folmer theory, the energy of formation of crystal nuclei also significantly decreases in the presence of crystallization centers, which serve filler particles [14].

Ash not only increases the cohesive and adhesive strength of the cement matrix in the concrete mixture, but also reduces the voidness of the aggregate [15–17]. For fine-grained concrete (FGC), this consequence of the introduction of ash filler seems to be especially important.

---

Dvorkin, L.I. The influence of polyfunctional modifier additives on properties of cement-ash fine-grained concrete. Magazine of Civil Engineering. 2020. 93(1). Pp. 121–133. DOI: 10.18720/MCE.93.10

Дворкин Л.И. Влияние добавок полифункционального модификатора на свойства цементно-зольного мелкозернистого бетона // Инженерно-строительный журнал. 2020. № 1(93). С. 121–133. DOI: 10.18720/MCE.93.10



This work is licensed under a [CC BY-NC 4.0](https://creativecommons.org/licenses/by-nc/4.0/)

Noting the general technical and economic feasibility of introducing fly ash into FGC intended for floor coverings, problematic issues should also be pointed out.

For the floor covering material, increased tensile strength is especially important. There are indications [3] that in the period 28...180 days, the growth rate of tensile strength of ash-containing concrete is approximately the same as that of non-ash concrete. In other works, however, it is noted that for concrete with ash, as well as with other active mineral additives, a higher ratio of tensile strength to compressive strength observed [18].

Many studies contain conflicting data on the modulus of elasticity, creep, and shrinkage of ash-containing concrete [19–22].

The most negative consequence of introducing ash into a concrete mixture intended for flooring is a decrease in abrasion resistance [5].

To date, there are a number of experimental data showing the effectiveness of the joint introduction of fly ash and surfactant additives into concrete mixtures [13, 24]. In addition to reducing interfacial surface energy when creating an adsorption-active medium, which has a positive effect on the size of adhesive contacts, surfactants also have a deflocculation effect on highly dispersed ashes, prone to aggregation [20].

Superplasticizers (SP) made it possible to obtain essentially a new type of cast concrete and provide a reduction in the water demand of the concrete mix by 20...30 % and more, which is approximately two times higher than when using traditional plasticizers [25]. However, the introduction of superplasticizers additives into cement-ash concrete does not allow to significantly increase the ratio of tensile strength to compressive strength and to achieve high deformability, adhesive ability and wear resistance desired for concrete intended for flooring [26, 27]. In this direction, an additional introduction of polymer additives into concrete and, in particular, additives based on polyvinyl acetate polymers is promising [28, 29]. For superplasticizers and polyvinyl acetate polymers characteristic a different mechanism of action, which suggests that the integral modifying effect of complex additives will be stronger than the individual components.

The purpose of the work was to conduct the necessary set of studies to reveal the peculiarities of the combined effect of additives of superplasticizer and polyvinyl acetate polymer on cement-ash concrete intended for flooring industrial enterprises.

The main objectives of the research:

1. To determine the joint effect of additives of naphthalene formaldehyde superplasticizer (SP) and vinyl acetate polymer with versatate (PVAV) on the features of hydration and structure formation of cement-ash systems.

2. To obtain a set of experimental-statistical models describing the combined effect of complex additives SP + PVAV as a polifunctional modifier PFM on the properties of concrete mixtures and the strength properties of concrete, taking into account their water-cement ( $W/C$ ) and ash-cement ( $A/C$ ) ratios.

3. To determine the effect of PFM additives on the deformation properties and resistance of cement-ash concrete to abrasion and impact.

## 2. Materials and Research Methods

The starting materials for the studies were Portland cement CEM II 42.5 N containing 20 % blast furnace granulated slag, silica sand with a fineness modulus of  $M_f = 2.4$ , and fly ash. Cement was made on the basis of clinker containing  $C_3S - 61.5\%$ ,  $C_2S - 17.5\%$ ,  $C_3A - 6.8\%$ ,  $C_4AF - 14.2\%$ . The specific surface of the cement was  $330 \text{ m}^2/\text{kg}$ , normal consistency  $27.1\%$ , initial setting time 1 hour 30 minutes, final – 3.5 hours, compressive strength after 28 days normal hardening –  $53.4 \text{ MPa}$ , bending strength –  $6.1 \text{ MPa}$ .

The chemical composition of the fly ash:  $\text{SiO}_2 + \text{Al}_2\text{O}_3 + \text{Fe}_2\text{O}_3 - 84.5\%$ ,  $\text{SO}_3 - 2.8\%$ ,  $\text{CaO} - 2.4\%$ ,  $\text{MgO} - 1.8\%$ ,  $\text{Na}_2 + \text{K}_2\text{O} - 2.5\%$ ; loss on ignition –  $3.9\%$ , specific surface –  $325 \text{ m}^2/\text{kg}$ , CaO absorption activity –  $43.9 \text{ mg/g}$ .

The polyfunctional modifier included a powdery S-3 superplasticizer – a condensation product of naphthalenesulfonic acid and formaldehyde containing a mixture of oligomers and polymers (the so-called «active substance») and unreacted salt –  $\beta$  naphthalenesulfonic acid and sodium sulfate [29]. The content of the «active substance» in the superplasticizer was not less than  $69\%$  and the pH of the  $2.5\%$  aqueous solution was  $7...9$ . The second component of the PFM was a polymer of vinyl acetate with vinyl versatate (PVAV) – a powder with a particle size of  $10...40 \mu\text{m}$  and a density of  $0.45 \text{ g/cm}^3$ . Compared to polyvinyl acetate PVAV is more resistant to the action of an alkaline medium of cement.

For the implementation of algorithmic experiments, three-level, four-factor  $B_4$  plan was selected in the work, which is close in properties to  $D$  – optimal ones [31]. A distinctive feature of this plan is the almost identical accuracy of forecasting the output parameters in the field of variation of factors.

As the criteria for the cast consistency of the FGC, the cone spread on the shaking table was selected, which, by standard determination, was 220...240 mm, and the cone immersion was 12–14 cm, respectively.

### 3. Results and Discussion

At the first stage of the study, we studied the effect of PFM additives on the hydration and structure formation of cement-ash stone.

The degree of cement hydration ( $\alpha$ ) was determined by a chemical method [14, 32]:

$$\alpha = h/W, \quad (1)$$

where  $h$  is the amount of hydrated i.e non-evaporating water at 105 °C, attached to 1 g of cement after a certain time from the moment of mixing;

$W$  is the amount of non-evaporating water attached to 1 g of cement after its complete hydration.

For this purpose, samples with sizes 2×2×2 cm were made from cement and ash-cement paste with  $W/C = 0.5$ , which were crushed after the set period under normal conditions of hardening, treated with acetone to remove free water, and calcined to determine the amount of chemically bound water. The amount of non-evaporating water corresponding to the complete hydration of the cement was determined by multi-stage mixing and calcination until the termination of growth in hydrated moisture content.

The mean values of the degree of hydration of samples with PFM additives are given in Table 1. It follows from them that PFM and their components have a certain stabilizing effect on the process of hydration of cements, while the influence of SP S-3 is much weaker than PVAV. By the age of seven days of hardening, the stabilizing effect of PFM on cement hydration is significantly reduced and does not exceed 5 % by 28 days.

**Table 1. The degree of cement hydration in cement and cement-ash pastes with additives PFM.**

No.	PFM additive content, % by weight of cement	Fractional content of PFM components, %		Ash-cement ratio ( $A/C$ )	The degree of hydration at days		
		S-3	PVAV		1	7	28
Portland cement CEM-II (C)							
1	–	–	–	–	0.23	0.39	0.66
2	1	100	–	–	0.18	0.35	0.65
3	1	–	100	–	0.17	0.31	0.65
4	1	50	50	–	0.17	0.33	0.70
5	3	100	–	–	0.16	0.33	0.67
6	3	–	100	–	0.16	0.30	0.67
7	3	50	50	–	0.16	0.32	0.67
Portland cement CEM-II; fly ash (A)							
8	–	–	–	0.4	0.29	0.40	0.71
9	1	100	–	0.4	0.16	0.39	0.69
10	1	–	100	0.4	0.15	0.33	0.66
11	1	50	50	0.4	0.16	0.38	0.69
12	3	100	–	0.4	0.14	0.33	0.65
13	3	–	100	0.4	0.11	0.36	0.64
14	3	50	50	0.4	0.14	0.37	0.68

The structural and mechanical characteristic of the hardening dispersed systems is plastic strength [14]. The value of plastic strength in the initial period of hardening of cement and cement-ash pastes was determined using a conical plastomer. The immersion depth of the cone was fixed by an indicator with a division price of 0.01 mm. The calculations of plastic strength ( $P_m$ ) were carried out according to the formula:

$$P_m = 0.096F / h^2, \quad (2)$$

where  $F$  is the load acting on the cone, N;

$h$  is the immersion depth of the cone, mm.

The obtained plastograms (Figure 1) have characteristic two sections. The first section of the plastogram corresponds approximately to the initial of setting time, and the inflection point to the final of ash-cement pastes setting.

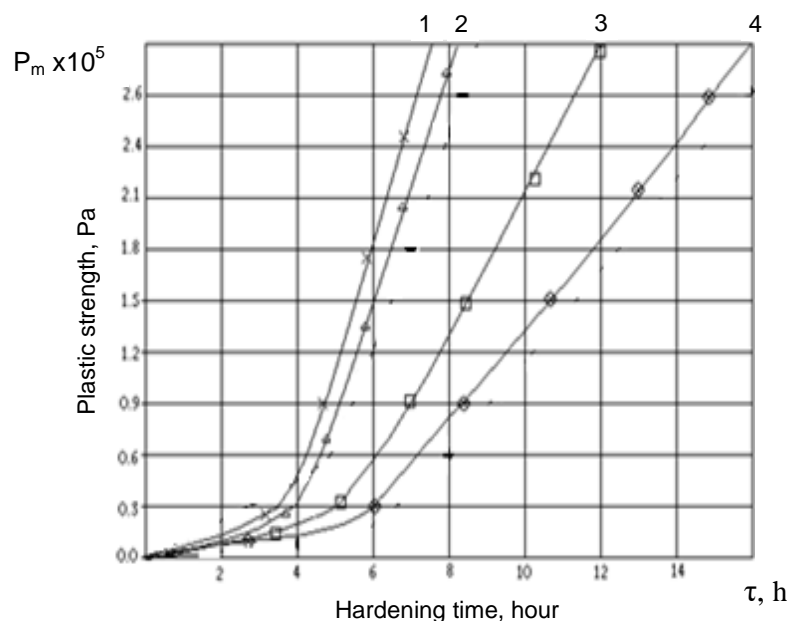


**Figure 1. Kinetics of changes in the plastic strength of cement-ash pastes ( $A/C = 0.4$ ):**  
 1 – 1 % S-3; 2 – 3 % S-3; 3 – 1.5 % S-3 + 1.5 % PVAV; 4 – 3 % PVAV.

Moreover, if the first section of plastograms mainly characterizes the formation of a thixotropic coagulation structure, the second – the period of the coagulation structure strengthening and the beginning of the formation of a crystallization structure. An analysis of plastograms shows that ash and PVAV additives slightly lengthen the period of coagulation structure formation. The addition of superplasticizer, especially in ash-cement pastes, causes a more intensive increase in plastic strength in the second section of plastograms.

The nature of the modification of cement stone with PFM additives is largely determined by improvement of its pore structure. The parameters of the pore structure of cement stone were calculated according to GOST 12730.4–78 (Russian standard) by approximating the water absorption curves by an exponential function of the type [14, 32]:

$$W_{\tau} = W_{\max} \left[ 1 - e^{-(\bar{\lambda}\tau)^{\infty}} \right], \quad (3)$$

where  $W_{\max}$  is the conditional value of maximum water absorption, %;

$\bar{\lambda}$  is coefficient characterizing the average size of the capillaries;

$\infty$  is coefficient characterizing the uniformity of capillary sizes;

$\tau$  is the duration of water saturation, h.

The kinetics of water absorption was determined on samples cubes with dimensions of 7x7x7 cm with continuous hydrostatic weighing according to GOST 12730.3. Three samples were made for each concrete composition.

The main results of the calculation of the parameters of the pore structure are given in Table 2. Analysis data of Table 2 shows that both with constant  $W/C$  and especially with  $W/C$  equal of cement normal consistency ( $K_{n.c}$ ) the introduction of surfactant additives changes the parameters of the pore structure of cement and cement-ash stone. The most significant decrease in open porosity is observed when using the water reducing effect of additives, which affects the decrease in  $K_{n.c}$ . The value of the integral porosity for a number of compositions increases somewhat, especially with the introduction of polyvinyl acetate type additives, which can be explained by the air-entraining effect of the latters. In all cases, with the introduction of PVAV and PFM additives, including them, there is a pore redistribution towards an increase in the volume of closed pores and a decrease in open pores available for saturation with water. At the same time, there is a clear tendency towards a decrease in the average pore size and an increase in their uniformity.

The experimental planning conditions for the study properties of ash-cement concrete are given in Table 3. As can be seen from Table 3, when planning the experiment, it was supposed to study a fairly wide range of compositions of ash-cement concrete, which include both compositions without PFM and compositions that contain up to 3 % PFM.

**Table 2. The main parameters of the pore structure of cement and cement-ash stone.**

No.	Additive	Porosity, %		The average pore size indicator $\bar{\lambda}$	Uniformity indicator pore size $\alpha$
		Integral, $P_i$	Open, $P_o$		
Cement stone with $W/C = 0.3$					
1	–	23.5	19.8	1.54	0.79
2	3 % PVAV	25.1	18.7	1.25	0.82
3	15 % S-3+1.5 % PVAV	25.4	17.8	1.31	0.81
4	3 % S-3	23.9	16.9	1.30	0.83
Cement stone with $W/C = K_{n.c}^*$					
6	–	21.6	18.5	1.49	0.78
7	3 % PVAV	22.8	16.5	1.31	0.80
9	1.5 % S-3+1.5 % PVAV	20.1	15.5	1.28	0.81
10	3 % S-3	18.8	15.1	1.25	0.85
Cement-ash stone with $W/C = 0.3$ and $A/C = 0.4$					
11	–	22.9	21.5	1.41	0.79
12	3 % PVAV	23.4	20.3	1.31	0.82
14	1.5 % S-3+1.5 % PVAV	24.1	20.8	1.32	0.85
15	3 % S-3	21.5	19.5	1.28	0.87
Cement-ash stone with $W/C = K_{n.c}$ and $A/C = 0.4$					
16	–	22.5	20.1	1.40	0.80
17	3 % PVAV	22.1	18.3	1.29	0.85
19	1.5 % C-3+1.5 % PVAV	21.4	16.1	1.29	0.86
20	3 % C-3	19.5	16.0	1.25	0.88

\*  $K_{n.c}$  – normal consistency of cement paste.

**Table 3. Experimental Planning Conditions.**

No.	Factors	Coded designation	Levels of variation		
			–1	0	+1
1	PFM content, % cement mass	$X_1$	0	1.5	3
2	The part of S-3 in the composition of the PFM, %	$X_2$	0	0.5	1.0
3	Water-cement ratio ( $W/C$ )	$X_3$	0.4	0.5	0.6
4	Ash-cement ratio ( $A/C$ )	$X_4$	0.1	0.4	0.7

Tested cubes with a rib size of 70 mm hardened under normal conditions.

To calculate the basic compositions of concrete, the absolute volume condition was used:

$$C / \rho_c + A / \rho_a + W / \rho_w + S / \rho_s = 1000, \quad (4)$$

where  $C$ ,  $A$ ,  $W$ ,  $S$  are the consumptions of cement, ash, water and sand;

$\rho_c$ ,  $\rho_a$ ,  $\rho_w$ ,  $\rho_s$  are the densities of these materials.

From the formula (4) it is possible to find the consumption of cement, then the remaining components at the given values of  $A/C$ ,  $W/C$  and  $n = S/C$ :

$$C = \left( \frac{1000}{1 / \rho_c + (A/C) / \rho_a + W/C + n / \rho_s} \right) \rho_c, \quad (5)$$

$$A = C \cdot (A/C); \quad S = C \cdot (S/C); \quad W = C \cdot (W/C)..$$

The calculated water consumption for a given  $W/C$  was corrected taking into account the achievement of the necessary spreading or immersion of the cone to achieve a cast consistency of the mixture, and also the influence of additives included in the PMF. With the corrected consumption of water, the consumptions of cement and ash were adjusted at the given values of  $W/C$  and  $A/C$ . Sand consumption was specified from condition (4).

The main concrete compositions used when obtaining of models (6)–(9) are given in Table 4.

**Table 4. Examples of concrete compositions used in the models (6)–(9).**

PFM content, % cement weight	The share of S-3 in the PFM	Water- cement ratio	Ash-cement ratio	The composition of the concrete mixture, kg/m <sup>3</sup>			
				W	C	A	S
1	0.75	0.5	0.4	238	477	191	1416
1.5	0.5	0.5	0.4	235	471	188	1432
2.6	0.75	0.45	0.4	212	472	189	1491
1.5	0.5	0.6	0.7	245	409	286	1358
3	0.5	0.5	0.4	208	415	166	1575
3	0.5	0.6	0.4	204	340	136	1680
3	1	0.45	0.4	204	454	181	1536

The planning matrix and the results of the experiments are given in Table 5. In each row of the matrix, the samples were duplicated and the average values of the output parameters were found. The regression equations adequate for the experimental data obtained for the water demand, volume of the entrained air compressive and bending strength are shown in Table 6.

**Table 5. Planning matrix and the results of experiments to determine the properties of ash-cement concrete.**

No.	Coded Factor Values				Water demand, l/m <sup>3</sup>	Volume of air entrained, %	28-days strength, MPa	
	X <sub>1</sub>	X <sub>2</sub>	X <sub>3</sub>	X <sub>4</sub>			compressive	bending
1	+1	+1	+1	+1	255	1.1	25.8	4.3
2	+1	+1	+1	-1	220	1.5	24.2	3.8
3	+1	+1	-1	+1	250	0.6	45.3	5.7
4	+1	+1	-1	-1	195	0.7	43.5	5.1
5	+1	-1	+1	+1	335	1.5	22.2	4.8
6	+1	-1	+1	-1	310	2.9	27.4	4.1
7	+1	-1	-1	+1	283	1.7	42.1	6.1
8	+1	-1	-1	-1	225	2.1	44.2	5.9
9	-1	+1	+1	+1	275	1.1	24.3	3.8
10	-1	+1	+1	-1	240	1.5	25.7	3.2
11	-1	+1	-1	+1	390	1.1	44.1	5.8
12	-1	+1	-1	-1	351	1.6	46.2	5.3
13	-1	-1	+1	+1	375	1.9	24.9	3.7
14	-1	-1	+1	-1	343	2.1	21.5	3.4
15	-1	-1	-1	+1	385	1.1	40.5	5.7
16	-1	-1	-1	-1	347	1.3	43.1	5.4
17	+1	0	0	0	230	1.5	33.6	4.7
18	-1	0	0	0	260	1.7	37.5	5.0
19	0	+1	0	0	228	0.9	38.5	5.1
20	0	-1	0	0	265	1.4	36.6	5.6
21	0	0	+1	0	220	1.7	29.5	4.0
22	0	0	-1	0	295	1.3	48.9	6.5
23	0	0	0	+1	275	1.1	31.1	4.7
24	0	0	0	-1	235	1.5	32.0	4.1

**Table 6. Regression equations for properties of cast ash-cement FGC with PFM additives.**

No.	Property	Regression equation
1	Water demand, l/m <sup>3</sup>	$y_1 = 235.3 - 37.13X_1 - 25.98X_2 - 29X_3 + 19.99X_4 + 9.48X_1^2 + 10.69X_2^2 + 19.19X_4^2 + 25.44X_1X_3 - 19.94X_2X_3$ (6)
2	Volume of air entrained, %	$y_2 = 1.355 - 0.33X_1 + 0.213X_2 - 44X_3 + 0.242X_4 + 0.242X_1^2 - 0.208X_2^2 + 0.142X_3^2 - 0.058X_4^2 - 0.2X_1X_2$ (7)
3	Compressive strength, MPa ( $R_c$ )	$y_4 = 36.7 - 1.07X_2 - 9.88X_3 - 1.21X_1^2 + 0.79X_2^2 + 2.44X_3^2 - 5.21X_4^2 - 0.21X_1X_2 + 0.46X_3X_4$ (8)
4	Bending strength, MPa ( $R_{t,b}$ )	$y_5 = 5.03 + 0.18X_1 - 0.15X_2 + 0.92X_3 + 0.24X_4 + 0.19X_1^2 + 0.31X_2^2 + 0.21X_3^2 - 0.64X_4^2 - 0.12X_1X_2 + 14X_1X_3$ (9)

In accordance with the well-known recommendations [34], when using ash, a possible (up to 20...30 %) reduction in compressive strength at the age of 28 days should be taken into account. As follows from the data obtained (Table 5), the decrease in the strength of cement-ash concrete is completely leveled with the introduction of the proposed additives.

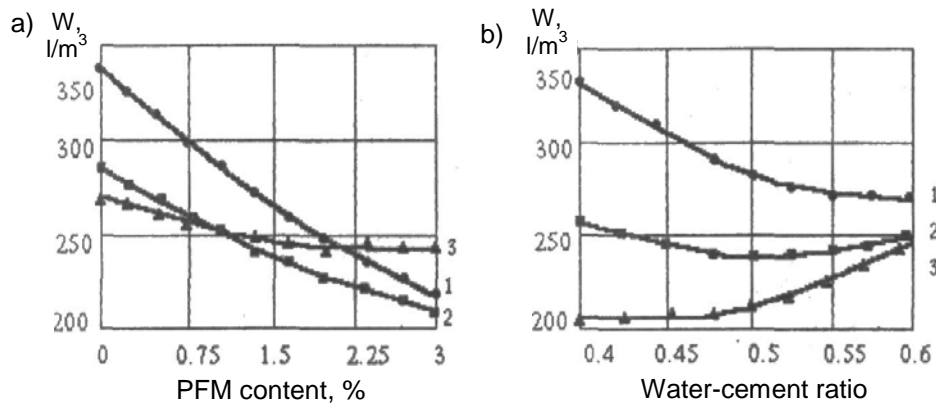


**Figure 2. Estimated dependencies of water demand of ash-cement concrete mixes with additives (PFM): a)  $W/C$ : 1 – 0.4; 2 – 0.5; 3 – 0.6; ( $X_2 = 0$ ;  $X_4 = 0$ ); b) the content of the PFM: 1 – 0; 2 – 1.5; 3 – 0.3 %; ( $X_2 = 0$ ;  $X_4 = 0$ ).**

When analyzing the mathematical model of the water demand of the mixture, attracts attention that the influence of factors which characterize the amount ( $X_1$ ) and composition ( $X_2$ ) of PFM in ash-cement cast mixtures and mixtures without the addition of ash is quite close. The significant effect of the interaction between  $X_1$  and  $X_2$  shows that the greatest plasticizing effect, both at large and low doses of PFM, occurs when the S-3 superplasticizer prevails in the latter. Opposite but close in magnitude linear and quadratic effects at  $X_3$  show that, its increased values, leads to an insignificant increase in water demand, while at the same time at low  $W/C$  ( $X_3 < 0$ ), water demand significantly increases. This pattern is well known in concrete technology as a rule of constancy of water demand [14].

Graphical dependences of water demand, volume of air entrained, compressive and bending strength, depending on water-cement ratio, PFM content and composition obtained by analyzing the regression equations are shown in Figures 2, 3, 4. It follows from them that for certain values of ash-cement and water-cement ratios, it is possible to change the main properties of concrete mixtures and concrete in a significant range, choosing of the PFM consumption and the ratio of its constituent components.

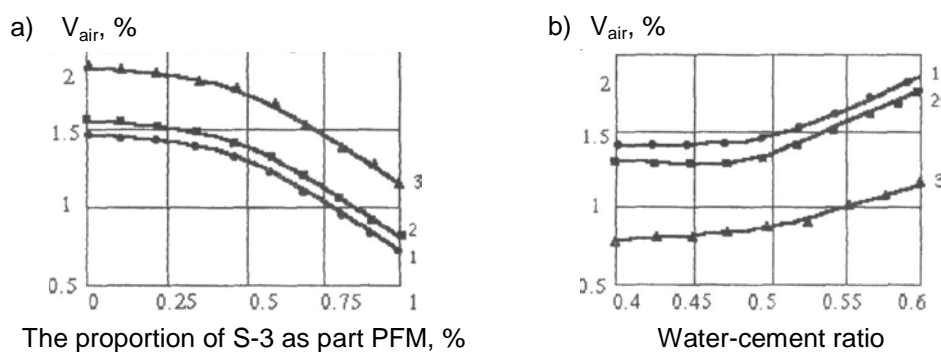


**Figure 3. Air entrainment of ash-cement concrete mixtures with PFM additives: a)  $W/C$ : 1 – 0.4; 2 – 0.5; 3 – 0.6; ( $X_1 = 0$ ;  $X_4 = 0$ ); b) the part of S-3 in the PFM: 1 – 0.4; 2 – 0.5; 3 – 0.6; ( $X_1 = 0$ ;  $X_4 = 0$ ).**

The criteria of the deformability of concrete and its crack resistance are the ratios of the splitting tensile strength or bending strength to a static or dynamic elastic modulus [14]. These parameters are quite close. As shown in [11], for fine-grained concrete, the formulas for calculating the tensile strength at splitting ( $R_{t.sp}$ ) and tensile strength at bending ( $R_{t.b}$ ) differ only in the coefficients:

$$R_{t.sp} = 0.57R_c^{2/3}, \quad R_{t.b} = 0.99R_c^{2/3}, \quad (10)$$

where  $R_c$  is compressive strength at 28 days.

Comparison of the experimental values of the static ( $E_c$ ) and dynamic elastic moduli ( $E_{dyn}$ ) shows that the ratio  $E_c/E_{dyn}$  for concrete is in the range 0.87...0.95. The lower values are typical for concrete with a

compressive strength of less than 25 MPa. The ratio  $R_{t.sp}/E_{dyn}$  is close to the value of ultimate extensibility and is called the conditional extensibility ( $\varepsilon_c$ ) [11]. It is easy to show that:

$$\varepsilon_c = \frac{R_{t.sp}}{E_{dyn}} \approx \frac{0.57 \times R_{t.b}}{0.99 \times 1.1 E_c} \approx 0.52 \frac{R_{t.b}}{E_c}. \quad (11)$$

Table 7 shows the calculated values of the studied parameters depending on various parameters of concrete compositions. Values  $R_{t.b}$  are calculated using model (8). Values  $E_c$  are calculated using the formula [14]:

$$E_c = \frac{5.2 \times 10^4 R_c}{23 + R_c}, \quad (12)$$

where  $R_c$  is concrete compressive strength calculated according to model (8).

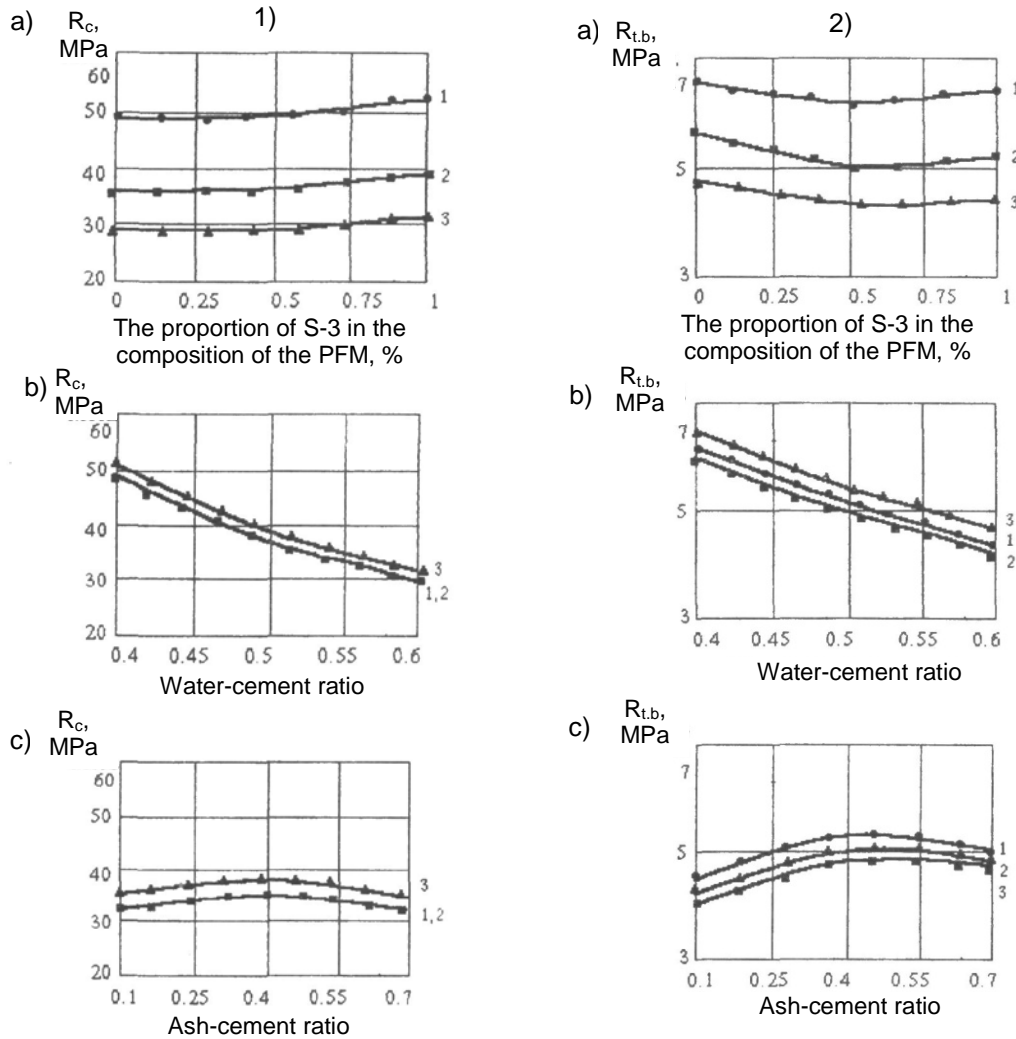


**Figure 4. The effect of the composition of ash-cement FGC with PFM additives on the compressive strength (1) and bending (2) ( $X_1 = 0$ ): a)  $W/C$ : 1 – 0.4; 2 – 0.5; 3 – 0.6; ( $X_1 = 0$ ;  $X_4 = 0$ ); b) the proportion of S-3 in the PFM: 1 – 0.4; 2 – 0.5; 3 – 0.6; ( $X_1 = 0$ ;  $X_4 = 0$ ); c) the proportion of S-3 in the composition of the PFM: 1 – 0.4; 2 – 0.5; 3 – 0.6; ( $X_1 = 0$ ;  $X_3 = 0$ ).**

Shrinkage curves of investigated concrete determination in accordance with Russian State Standard GOST 24544–81 on prisms with dimensions 70×70×280 mm are shown in Figure 5. Their analysis shows that for all the studied compositions, shrinkage deformations stabilize by 100 days. Concretes without PFM additives have the highest shrinkage values. Their ultimate shrinkage, depending on the  $W/C$ , fluctuates in the range 0.2...0.7 mm/m typical for fine-grained concrete. In the first stages of hardening, the addition of fly ash increases shrinkage deformations, which are then aligned with deformations of concrete without ash. PFM additives consisting of S-3 and PVAV reduce ultimate shrinkage deformations by 30...50 %. Moreover, the degree of reduction of shrinkage deformations increases with the increase in the plasticizing effect of PFM.

**Table 7. Estimated values of the deformability of cast FGC with additives PFM.**

No.	PFM additive, % cement mass	Mass fraction of S-3 in the PFM	Water cement ratio	$R_{c1}$ , MPa	$R_{t,b}$ , MPa	$E_c$ , $\times 10^{-5}$ MPa	$\varepsilon_c$ , $\times 10^{-5}$ mm
1	0	–	0.5	35.49	4.66	25.24	9.6
2	1	0	0.4	48.57	6.51	28.23	12.0
3	1	0.5	0.4	48.91	6.09	28.29	11.2
4	1	1	0.4	50.83	6.28	28.64	11.4
5	3	0	0.4	47.74	6.59	28.07	12.2
6	3	0.5	0.4	47.81	6.31	28.09	11.7
7	3	1	0.4	49.46	6.35	28.39	11.6
8	1	0	0.6	28.80	4.63	23.13	10.4
9	1	0.5	0.6	29.15	4.43	23.25	9.9
10	1	1	0.6	31.07	4.63	23.90	10.1
11	3	0	0.6	27.98	5.03	22.83	11.5
12	3	0.5	0.6	28.05	4.61	22.86	10.5
13	3	1	0.6	29.70	4.65	23.44	10.3

**Note:** In the calculations, the ash-cement ratio of 0.4 is adopted.

To determine the abrasion of the investigated concrete, we used cubic samples with an edge size of 7 cm in an air-dry state, hardening for 28 days. The tests were carried out on a device whose working body is a rotating disk using an abrasive material obtained by mixing corundum up to quartz (GOST 13087–81). The test results are shown in Figure 6.

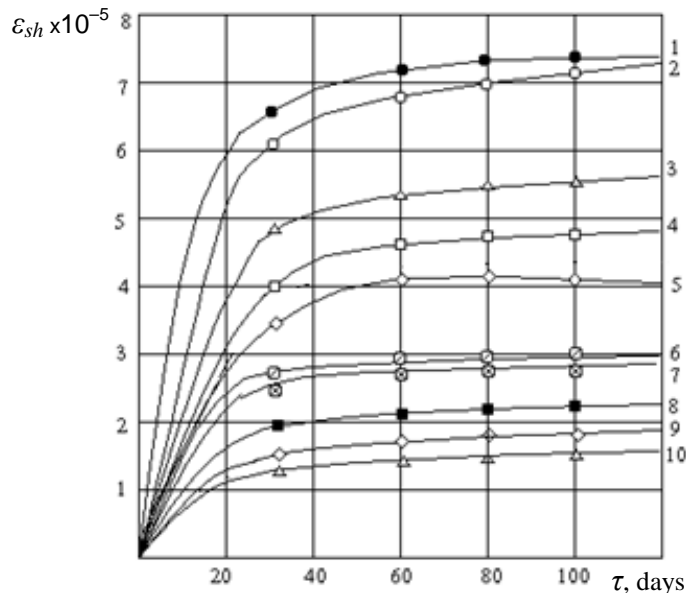


**Figure 5. Shrinkage deformation ( $\varepsilon_{sh}$ ) of ash-cement concrete with additives PFM: 1–5 –  $W/C = 0.6$ : 1 – concrete without additives  $A/C = 0.4$ ; 2 – concrete without additives  $A/C = 0$ ; 3 – concrete with the addition of 3 % PVAV;  $A/C = 0.4$ ;  $W/C = 0.6$ ; 4 – concrete with the addition of 3 % PFM (50 % S-3; 50 % PVAV);  $A/C = 0.4$ ; 5 – concrete with the addition of 3 % S-3;  $A/C = 0.4$ ; 6–10 –  $W/C = 0.4$ ; 6 – concrete without additives  $A/C = 0.4$ ; 7 – concrete without additives  $A/C = 0$ ; 8 – concrete with PVAV additive 3 %; 9 – concrete with the addition of 3 % PFM, (50 % S-3; 50 % PVAV); 10 – concrete with the addition of 3 % S-3.**

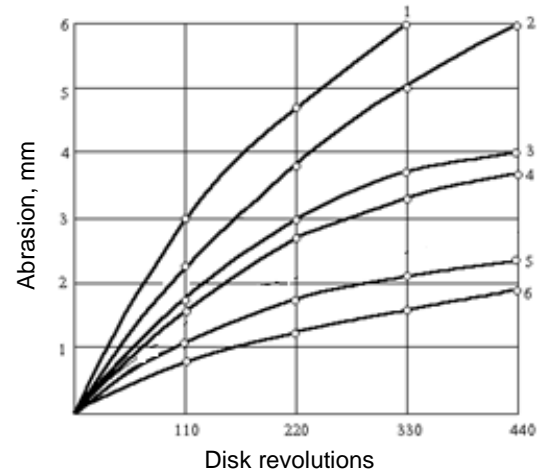


**Figure 6. Abrasion of ash-cement concrete with PFM additives ( $W/C = 0.5$ ;  $A/C = 0.4$ ): 1 – without PFM; 2 –  $A/C = 0$  without PFM; 3 – 1 % PFM (0.5 % S-3 + 0.5 % PVAV); 4 – 1 % PVAV; 5 – 3 % PFM (1.5 % S-3 + 1.5 % PVAV); 6 – 3 % PVAV.**

The nature of the curves in Figure 6 confirms the well-known conclusion [33] on the power dependence of concrete abrasion depth on the number of disk revolutions ( $N$ ).

$$U = KN^m. \quad (13)$$

The coefficients  $K$  and  $m$  depend on the composition of concrete and the type of additives. Already 1 % of PFM reduced abrasion by more than 1.5, and 3 % by more than 3 times. At the same time, an increase in the proportion of PVAV in the composition of PFM increases the abrasion resistance.

Comparative impact tests of concrete were carried out using a pendulum driver on samples 4x4x16 cm in size [32]. When determining the impact work, for convenience of comparison, the found values of the fracture load of the samples were recalculated to the specific work of the impact per 1 cm<sup>2</sup> of their cross section. The results of determining the impact resistance of concrete are shown in Table 8.

**Table 8. Concrete impact test results (W/C = 0.5) for impact.**

No.	Ash-cement ratio	Additive PFM, % mass of cement	The composition of the PFM in parts by weight		Work Impact, J	Specific work impact, J/cm <sup>2</sup>
			C-3	PVAV		
1	–	–	–	–	154	9.6
2	–	1	1	–	161	10.1
3	–	1	0.5	0.5	160	10.0
4	–	1	–	1	165	10.3
5	–	3	1	–	165	10.3
6	–	3	0.5	0.5	163	10.2
7	–	3	–	1	170	10.6
8	0.4	–	–	–	165	10.3
9	0.4	1	1	–	170	10.6
10	0.4	1	0.5	0.5	172	10.7
11	0.4	1	–	1	175	10.9
12	0.4	3	1	–	175	10.9
13	0.4	3	0.5	0.5	180	11.2
14	0.4	3	–	1	182	11.4

Ash-cement concrete with PFM additives showed a higher impact resistance, which is consistent with known data [14]. The increase in impact work in ash-cement concrete with PFM additives compared to non-additive amounted to 20 %. The increase in impact strength with S-3 and PVAV additives can be explained by the adsorption modification of the structure of cement stone which becomes more dispersed as a result of an increase in the supersaturation due to surface-active substances during the hardening of cement paste [14]. The change in the mass ratio of S-3 and PVAV in the composition of PFM did not lead to a significant change in their effect on impact strength. An analysis of the results suggests that the introduction of the proposed PFM additive into the composition of cement-ash concrete makes it possible to remove the known limitations on their use in the conditions of abrasion and impact [3, 34].

The practical technology of cast FGC with PFM additives can be based on the direct introduction of additives in the manufacture of finished mixtures or on the preliminary receipt of dry mixtures that are mixed with water per object. It is possible to use the combined method, when only one component of PFM is introduced into the dry mixture, the second one is used in the form of an aqueous solution or emulsion in preparing the concrete mixture ready for use.

#### 4. Conclusions

1. Additives of polyfunctional modifiers, including the superplasticizer of the naphthalene-formaldehyde type (S-3) and the polymer of vinyl acetate and vinyl versatate (PVAV) actively influence the hydration process of cement and cement-ash pastes, having a certain stabilizing effect in the first stages of hardening. It affects a decrease in the degree of hydration and a slowdown in the growth of plastic strength, especially at the stage of coagulation structure formation. By the age of 28 days, the stabilizing effect of PFM additives on the degree of hydration of cement and cement-ash pastes becomes almost imperceptible.

2. The introduction of PFM additives significantly affects the parameters of the pore structure of cement-ash stone, reducing open porosity, average pore size and increasing the uniformity of their distribution.

3. The analysis of experimental data and mathematical models obtained by their statistical processing shows that the properties of ash-cement concrete mixtures and the properties of concrete significantly depend on the composition of the PFM and their dosage. The introduction of PFM additives allows to adjust the water demand and air content of concrete mixtures, as well as to increase the ultimate extensibility of concrete.

4. The introduction of PFM additive including naphthalene formaldehyde superplasticizer S-3 and a polymer of vinyl acetate with vinyl versatate PVAV in an amount of 1.5...3 % with a 1:1 ratio of water-cement and ash-cement ratio in the range of 0.4–0.5 allows to obtain fine-grained concrete of classes B25...B35. The introduction of the PFM additive allows, when optimal values of its consumption and composition, by 30–50 % to reduce shrinkage deformations, increase the abrasion resistance by 1.5–3 times and increase the resistance of cement-ash concrete to impact by up to 20 %.

## References

- Kalra, T., Rana, R. A review on Fly Ash Concrete. International Journal of Latest Research in Engineering and Computing (ULREC). 2015. Vol. 3. Iss. 2. Pp. 7–10.
- Dvorkin, L., Nwaubani, S., Dvorkin, O. Construction materials. Nova Science Publishers, New York. 2001. 409 p.
- Dvorkin, L., Solomatov, V., Vyrovoy, V., Chudnovskiy, S. Tsementnyye betony s mineralnymi napolnitelyami [Cement Concrete with Mineral Fillers]. Kiev: Budivelnik, 1991. 136 p.
- Ramachandran, V., Feldman, R., Boduen, Dzh. Nauka o betone [Concrete Science]. M.: Stroyizdat. 1986. 278 p.
- Nagrockienc, D., Griskas, G., Skripiunas. Properties of concrete modified with mineral additives. Construction and Building Materials. 2017. Vol. 135. No. 15. Pp. 37–42.
- Vatin, N.I., Petrosov, D.V., Kalachev, A.I., Lahtinen, P. Use of ashes and ash-and-slag wastes in construction. Magazine of Civil Engineering. 2011. 22(4). Pp. 16-21. (rus). DOI: 10.5862/MCE.22.2
- Klyuyev, S.V., Klyuyev, A.V., Sopin, D.M., Netebenko, A.V., Kazlitin, S.A. Heavy loaded floors based on fine-grained fiber concrete. Magazine of Civil Engineering. 2013. 38(3). Pp. 7–14. (rus). DOI: 10.5862/MCE.38.1.
- Celik, K., Meral, C., Mancio, M., Mehta, P., Monteiro, P. A comparative study of self consolidating concretes incorporating high-volume natural pozzolan or high-volume fly ash. Construction and Building Materials. 2014. Vol. 67. Pp. 14–19.
- Weshe, K. Fly Ash in Concrete: Properties and Performance. CRC Press [Online]. 1991. 365 p. URL: [https://www.academia.edu/6064988/Fly\\_Ash\\_in\\_Concrete\\_Properties\\_and\\_Performance](https://www.academia.edu/6064988/Fly_Ash_in_Concrete_Properties_and_Performance)
- Madurwar, K., Burile, A., Sorte, A. Compressive Strength of Cement and Fly Ash Mortar. Proceeding of Sustainable Infrastructure Development and Management (SID14) [Online]. 2019. URL: <http://dx.doi.org/10.2139/ssrn.3376014>
- Stechyshon, M., Sanitskiy, M., Poznyak, O. Durability properties of high volume fly ash self compacting fiber reinforced concretes [Online]. Vostochno-Yevropeyskiy zhurnal peredovoykh tekhnologiy. 2015. No. 3 (11). Pp. 49–53. URL: [http://nbuv.gov.ua/UJRN/Vejpte20153\(11\)\\_II](http://nbuv.gov.ua/UJRN/Vejpte20153(11)_II)
- Verma, A., Srivastava, D., Sing, N. A review on Partial Replacement of Cement by Fly Ash and Effect of Steel Fibers. Journal of Mechanical and Civil Engineering. 2017. Vol. 14, Iss. 3. Pp. 104–107.
- Coud, V., Soni, N. Partial Replacement of cement with fly ash in concrete and its effect. JOSP Journal of Engineering. 2016. Vol. 6. Iss. 10. Pp. 69–75.
- Dvorkin, L., Dvorkin, O. Basics of Concrete Science: Optimum Design of Concrete Mixtures. Kindle Edition. Amazon. 2012. 237 p.
- Rasamane, N.P., Ambily, P.S. Fly Ash as a sand replacement material in concrete. The Indian concrete Journal. 2013. 87(7).
- Kumar, R., Kumar, A., Khan, M. A review on effect of Partial Replacement of Cement by Fly Ash in Concrete. International Research Journal of Engineering and Technology (IRSET). 2016. Vol. 3. Iss. 4. Pp. 1039–1041.
- Kalra, T., Rana, R. A review on Fly Ash Concrete. International Journal of Latest Research and Computing. Vol. 3. Issue 2. 2015. Pp. 7–10.
- Kokubu, I., Yamada, D. Tsementy s dobavkoy zoly [Ash cement] / Shestoy mezhdunarodnyy kongress po khimii tsementa. Moscow: Stroyizdat. 1976. Vol. Z. Pp. 83–94.
- Barabanshchikov, Yu.G., Arkharova, A.A., Ternovskii, M.V. On the influence on the efficiency of anti-shrinkage additives superplasticizer. Magazine of Civil Engineering. 2014. 51(7). Pp. 23–30. (rus). DOI: 10.5862/MCE.51.3
- Singh, V., Srivastava, V., Agarwal, V., Harison, A. Effect of Fly Ash as Partial Replacement of Cement in PPC Concrete. International Journal of Innovative Research in Science Engineering and Technology. 2015. Vol. 4. Iss. 7.
- Malhotra, V., Mehta, P. High-Performance, High-Volume Fly Ash Concrete. Supplementary Cementing Materials for Sustainable Development Inc. Ottawa. 2005. 124 p.
- Naik, T., Ramme, B., Kraus, R., Siddique, R. Long-Term Performance of High-Volume Fly Ash Concrete Pavements. ACI Materials Journal. 2003. Vol. 100. No. 2. Pp. 150–155.
- Telford, T. The Properties and Use of Coal Fly Ash. London. 2001. 261 p.
- Fediuk, R.S., Lesovik, V.S., Liseitsev, Yu.L., Timokhin, R.A., Bituyev, A.V., Zaiakhanov, M.Ye., Mochalov, A.V. Composite binders for concretes with improved shock resistance. Magazine of Civil Engineering. 2019. 85(1). Pp. 28–38. DOI: 10.18720/MCE.85.3
- Dvorkin, L., Dvorkin, O., Ribakow, V. Construction Materials Based on Industrial Waste Products. Nova Science Publishers. New York, 2016. 231 p.
- Choure, A., Chandak, R. Experimental Study on concrete Containing Fly Ash. International Research Journal of engineering and Technology. 2017. Vol. 4. Iss. 2. Pp. 202–205.
- Oderji, S., Chen, B., Snakya, C., Ahmad, M., Ali Shan, S. Influence of superplasticizers and retarders on the workability of one-part alkali-activated fly ash / slag binders cured at room temperature [Online]. Construction and Building Materials. 2019. Vol. 229. 116891. URL: <https://doi.org/10.1016/j.conbuildmat.2019.116891>
- Demura, K., Oochama, Y. Polymer-Modified Concrete / Polymer Concrete. CMC Publishing. 2002.
- Solomatov, V. Polimertsementnyye betony i plastbetony [Polymer-cement concrete and plastic concrete]. M.: Stroyizdat, 1967. 184 p.
- Ivanov, F., Batrakov, V., Moskvina, V. Klassifikatsiya plastifikatsionnykh dobavok po efektu ikh deystviya [Classification of plasticizing additives by the effect of their action]. Beton i zhelezobeton. 1981. No. 4. Pp. 33–34.
- Dvorkin, L., Dvorkin, O., Ribakow, V. Mathematical Experiments Planning in Concrete Technology. Nova Science Publishers. New York, 2012. 173 p.
- Bolshakov, V., Dvorkin, L. Structure and Properties of Building Materials. Trans Tech Publication. 2016. 211 p.
- Denisov, A., Domokeyev, A., Ivanov, O., Kulkova, V. Betonnyye pokrytiya polov promyshlennykh zdaniy [Concrete flooring for industrial buildings]. Moscow: Stroyizdat. 1971. 128 p.
- Rekomendatsii po primeneniyu zoly, shlaka i zoloshlakovoy smesi teplovykh elektrostantsiy v tyazhelykh betonakh i stroitelnykh rastvorakh [Recommendations on the use of ash, slag and ash-slag mixture of thermal power plants in heavy concrete and mortar]. Moscow: Stroyizdat. 1977. 25 p.

## Contacts:

Leonid Dvorkin, +38(068)3533338; [dvorkin.leonid@gmail.com](mailto:dvorkin.leonid@gmail.com)



DOI: 10.18720/MCE.93.10

## Влияние добавок полифункционального модификатора на свойства цементно-зольного мелкозернистого бетона

**Л.И. Дворкин**

*Национальный университет водного хозяйства и природопользования, Ровно, Украина*

\* E-mail: [dvorkin.leonid@gmail.com](mailto:dvorkin.leonid@gmail.com)

**Ключевые слова:** Зола-унос, прочность, усадка, истираемость, добавки, суперпластификатор, структура

**Аннотация.** Объектом исследования являются свойства цементно-зольных бетонов с добавкой полифункционального модификатора (ПФМ), предназначенных для полов промышленных предприятий. В состав ПФМ входит суперпластификатор нафталин-формальдегидного типа и сополимер винилацетата с винилверсататом. Предпосылкой к использованию добавки ПФМ в составе цементно-зольных бетонов является возможность с его помощью активно влиять на процессы структурообразования и, как следствие, на свойства бетона. С применением известных химических и физических методов получены экспериментальные данные о влиянии добавки ПФМ на степень гидратации цемента, кинетику изменения пластической прочности цементно-зольного камня в процессе твердения. Установлено, что введение добавки ПФМ позволяет уменьшить открытую пористость и средние размеры пор цементно-зольного камня а также увеличить показатель однородности пор по размерам. Для изучения свойств цементно-зольных бетонов с добавкой ПФМ применен метод математического планирования экспериментов, в результате реализации которых получен комплекс математических моделей водопотребности, водоотделения, объема вовлеченного воздуха, прочности бетона при сжатии и изгибе. Модели позволяют количественно оценить влияние на указанные свойства бетона водо- и золоцементного соотношений, содержания и соотношения компонентов ПФМ, а также проектировать составы цементно-зольных бетонов с заданными свойствами. Исследования, результаты которых приведены в статье, показали возможность с помощью добавки ПФМ существенно улучшить свойства цементно-зольных бетонов, важные при использовании их для полов промышленных предприятий и, в частности, на 30–50 % уменьшить предельные усадочные деформации, снизить в 1.5–3 раза их истираемость и до 20 % повысить сопротивление ударным воздействиям.

### Литература

1. Kalra T., Rana R. A review on Fly Ash Concrete // International Journal of Latest Research in Engineering and Computing (ULREC). 2015. Vol. 3. Iss. 2. Pp. 7–10.
2. Dvorkin L., Nwaubani S., Dvorkin O. Construction materials. Nova Science Publishers, New York, 2001. 409 p.
3. Дворкин Л., Соломатов В., Выровой В., Чудновский С. Цементные бетоны с минеральными наполнителями. Киев: Будивельник, 1991. 136 с.
4. Рамачандран В., Фельдман Р., Бодуэн Дж. Наука о бетоне. М.: Стройиздат, 1986. 278 с.
5. Nagrockienc D., Griskas G., Skripiunas. Properties of concrete modified with mineral additives [Электронный ресурс] // Construction and Building Materials. 2017. Vol. 135. No. 15. Pp. 37–42. URL: <https://doi.org/10.1016/j.conbuildmat.2016.12.215>
6. Ватин Н., Петросов Д., Калачев А., Лахтинен П. Применение зол и золошлаковых отходов в строительстве // Инженерно-строительный журнал. 2011. № 4(22). С. 16–21.
7. Клюев С., Клюев А., Сопин Д., Нетребенко А., Казлитин С. Тяжелонагруженные полы на основе мелкозернистых бетонов // Инженерно-строительный журнал. 2013. № 3. С. 7–15.
8. Celik K., Meral C., Mancio M., Mehta P., Monteiro P. A comparative study of self consolidating concretes incorporating high-volume natural pozzolan or high-volume fly ash // Construction and Building Materials. 2014. Vol. 67. Pp. 14–19.
9. Weshe K. Fly Ash in Concrete: Properties and Performance [Электронный ресурс]. CRC Press, 1991. 365 p. URL: [https://www.academia.edu/6064988/Fly\\_Ash\\_in\\_Concrete\\_Properties\\_and\\_Performance](https://www.academia.edu/6064988/Fly_Ash_in_Concrete_Properties_and_Performance)
10. Madurwar K., Burile A., Sorte A. Compressive Strength of Cement and Fly Ash Mortar [Электронный ресурс] // Proceeding of Sustainable Infrastructure Development and Management (SID14). 2019. URL: <http://dx.doi.org/10.2139/ssrn.3376014>
11. Stechyshon M., Sanitsky M., Poznyak O. Durability properties of high volume fly ash self compacting fiber reinforced concretes [Электронный ресурс] // Восточно-Европейский журнал передовых технологий. 2015. № 3 (11). С. 49–53. URL: [http://nbuv.gov.ua/UJRN/Vejpte20153\(II\)\\_II](http://nbuv.gov.ua/UJRN/Vejpte20153(II)_II)

12. Verma A., Srivastova D., Sing N. A review on Partial Replacement of Cement by Fly Ash and Effect of Steel Fibers // Journal of Mechanical and Civil Engineering. 2017. Vol. 14. Iss. 3. Pp. 104–107.
13. Coud V., Soni N. Partial Replacement of cement with fly ash in concrete and its effect // JOSP Journal of Engineering. 2016. Vol. 6. Iss. 10. Pp. 69–75.
14. Dvorkin L., Dvorkin O. Basics of Concrete Science: Optimum Design of Concrete Mixtures. Kindle Edition. Amazon. 2012. 237 p.
15. Rasamane N.P., Ambily P.S. Fly Ash as a sand replacement material in concrete [Электронный ресурс] // The Indian concrete Journal. 2013. 87(7). URL: [https://www.researchgate.net/profile/Rajamane\\_Parshwanath/publication/255787523\\_Fly\\_ash\\_as\\_a\\_sand\\_replacement\\_material\\_in\\_concrete\\_-\\_A\\_study/links/5747379c08ae707fe21e3ad5/Fly-ash-as-a-sand-replacement-material-in-concrete-A-study.pdf](https://www.researchgate.net/profile/Rajamane_Parshwanath/publication/255787523_Fly_ash_as_a_sand_replacement_material_in_concrete_-_A_study/links/5747379c08ae707fe21e3ad5/Fly-ash-as-a-sand-replacement-material-in-concrete-A-study.pdf)
16. Kumar R., Kumar A., Khan M. A review on effect of Partial Replacement of Cement by Fly Ash in Concrete // International Research Journal of Engineering and Technology (IRSET). 2016. Vol. 3. Iss. 4. Pp. 1039–1041.
17. Kalra T., Rana R. A review on Fly Ash Concrete // International Journal of Latest Research and Computing. 2015. Vol. 3. Iss. 2. Pp. 7–10.
18. Кокубу И., Ямада Д. Цементы с добавкой золы // Шестой международный конгресс по химии цемента. М.: Стройиздат. 1976. Т. 3. С. 83–94.
19. Барабанщиков Ю., Архарова А., Терновский М. О влиянии суперпластификатора на эффективность противосадочной добавки // Инженерно-строительный журнал. 2014. № 7(51). С. 123–135. DOI: 10.5862/MCE.51.3.
20. Singh V., Srivastava V., Agarwal V., Harison A. Effect of Fly Ash as Partial Replacement of Cement in PPC Concrete // International Journal of Innovative Research in Science Engineering and Technology. 2015. Vol. 4. Iss. 7.
21. Malhotra V., Mehta P. High-Performance, High-Volume Fly Ash Concrete. Supplementary Cementing Materials for Sustainable Development Inc. Ottawa, 2005. 124 p.
22. Naik T., Ramme B., Kraus R., Siddique R. Long-Term Performance of High-Volume Fly Ash Concrete Pavements // ACI Materials Journal. 2003. Vol. 100. No. 2. Pp. 150–155.
23. Telford T. The Properties and Use of Coal Fly Ash. London, 2001. 261 p.
24. Федюк Р., Лесовик В., Лисейцев Ю., Тимохин Р., Битуев А., Заяханов М., Мочалов А. Композиционные вяжущие для бетонов повышенной ударной стойкости // Инженерно-строительный журнал. 2019. №1(85). С. 28–38. DOI: 10.18720/MCE.85.3.
25. Dvorkin L., Dvorkin O., Ribakow V. Construction Materials Based on Industrial Waste Products. Nova Science Publishers. New York, 2016. 231 p.
26. Choure A., Chandak R. Experimental Study on concrete Containing Fly Ash // International Research Journal of engineering and Technology. 2017. Vol. 4. Iss. 2. Pp. 202–205.
27. Oderji S., Chen B., Snakya C., Ahmad M., Ali Shan S. Influence of superplasticizers and retarders on the workability of one-part alkali-activated fly ash / slag binders cured at room temperature [Электронный ресурс] // Construction and Building Materials. 2019. Vol. 229. 116891. URL: <https://doi.org/10.1016/j.conbuildmat.2019.116891>
28. Demura K., Oochama Y. Polymer-Modified Concrete / Polymer Concrete. CMC Publishing. 2002.
29. Соломатов В. Полимерцементные бетоны и пластбетоны. М.: Стройиздат, 1967. 184 с.
30. Иванов Ф., Батраков В., Москвин В. Классификация пластифицирующих добавок по эффекту их действия // Бетон и железобетон. 1981. № 4. С. 33–34.
31. Dvorkin L., Dvorkin O., Ribakow V. Mathematical Experiments Planning in Concrete Technology. Nova Science Publishers. New York, 2012. 173 p.
32. Bolshakov V., Dvorkin L. Structure and Properties of Building Materials. Trans Tech Publication. 2016. 211 p.
33. Денисов А., Домокеев А., Иванов О., Кулькова В. Бетонные покрытия полов промышленных зданий. М.: Стройиздат. 1971. 128 с.
34. Рекомендации по применению золы, шлака и золошлаковой смеси тепловых электростанций в тяжелых бетонах и строительных растворах. М.: Стройиздат, 1977. 25 с.

**Контактные данные:**

*Леонид Иосифович Дворкин, +38(068)3533338; эл. почта: [dvorkin.leonid@gmail.com](mailto:dvorkin.leonid@gmail.com)*

© Дворкин Л.И., 2020



DOI: 10.18720/MCE.93.11

## Impact behavior of rehabilitated post-tensioned slabs previously damaged by impact loading

A. Jahami<sup>a\*</sup>, Y. Tamsah<sup>a</sup>, J. Khatib<sup>b</sup>, O. Baalbaki<sup>a</sup>, M. Darwiche<sup>a</sup>, S. Chaaban<sup>a</sup>

<sup>a</sup> Beirut Arab University, Beirut, Lebanon

<sup>b</sup> University of Wolverhampton, Wolverhampton, UK

\* E-mail: [ahjahamy@hotmail.com](mailto:ahjahamy@hotmail.com)

**Keywords:** rockfall, impact load, post-tension, shear reinforcement, energy, repair

**Abstract.** Accidental rockfalls are common hazards in many countries, where many structures and infrastructure are damaged by the impact of falling rocks. This research aims to study the efficiency of shear reinforcement as rehabilitation techniques for PT “post-tensioned” slabs damaged by falling rocks. Two simply supported PT slabs were considered in this study. Each has a dimension of (6.6 m×3 m×0.25 m) and was subjected to an impact from a 605 Kg reinforced concrete falling block at a height of 20 m. The first slab (PT-1) was hit at its center of gravity, while the second one (PT-2) was hit at the mid-span of its free edge. After impact, both slabs were repaired by replacing the damaged parts and adding shear ties in order to prevent any future collapse when new impact occurred. The impact test was repeated again after repairing, and both punching shear capacity and normal stresses were recorded. Results showed that the repaired slabs were able to resist the repeated impact successfully. Both punching shear and normal stress capacities were higher than the applied stresses. Moreover, using shear reinforcement helped in changing the crack pattern from shear to flexure. At the end of this study, some recommendations were suggested for further studies.

### 1. Introduction

Lebanon is characterized by its varied terrain (coast, mountains, and valleys). With the increase in population, people moved to live in the mountain region increasing the percentage of inhabitants there. Lebanon is also characterized by the heavy rain falling in the winter, causing incidents of landslides particularly in mountain areas resulting in rock falls onto the surfaces of residential buildings, leaving severe damage to the structure and threatening lives. This phenomenon is not limited in Lebanon but is a phenomenon that is spread throughout the world especially the mountain regions, which drew the attention of many researchers. The main issue related to this phenomenon is the impact caused by the rapid and sudden load application. Generally, most of the design codes do not include the impact load analysis -due to both falling objects and explosions- in analyses procedures; therefore, in the past ten years, numerous researches were conducted in this domain [1–6].

Iqbal [7] examined the behavior of post-tensioned slabs subjected to impact loading. Eight 800 mm×800 mm×100 mm (l×w×t) samples were considered in this study four of which were non-prestressed concrete samples and the others were prestressed at different stress levels. The impactor consisted of a 243 Kg steel mass dropped from two different heights 0.5 m and 1 m respectively. Results showed that post-tension slabs had a higher load capacity and a lower mid-span deflection compared to the non-prestressed concrete slabs. Yet, both types of slabs failed due to punching shear.

Al Rawi [8] studied numerically the effect of impact loads on prestressed concrete slabs compared to non-prestressed concrete slabs of equivalent moment capacity. Non-prestressed slabs gave better load capacity and deflection. In addition, Kumar [9] studied the efficiency of reinforced concrete slabs compared to

Jahami, A., Tamsah, Y., Khatib, J., Baalbaki, O., Darwiche, M., Chaaban, S. Impact behavior of rehabilitated post-tensioned slabs previously damaged by impact loading. Magazine of Civil Engineering. 2020. 93(1). Pp. 134–146. DOI: 10.18720/MCE.93.11

Джахми А., Темсах Е., Хатиб Дж., Баалбаки О., Дарвич М., Чаабан С. Свойства восстановленных предварительно напряжённых плит, ранее повреждённых ударной нагрузкой // Инженерно-строительный журнал. 2020. № 1(93). С. 134–146. DOI: 10.18720/MCE.93.11



prestressed concrete slabs of the same thicknesses in absorbing impact energy. The study concluded that prestressed concrete slabs absorb more impact energy than reinforced concrete slabs causing less damage.

To strengthen RC elements to resist impact loads, there are many techniques that are used nowadays. A commonly used technique is fiber-reinforced polymers (FRP), and several researchers based their studies on it [10–12]. One of the important researches done in this field was conducted by Radnic [13]. It studied the behavior of two way reinforced concrete slabs strengthened with “carbon fiber reinforced polymer” (CFRP) sheets when subjected to impact loads. Eight samples of 100 cm×100 cm×5.5 cm dimensions were cast for experimental testing divided into two sets as follows: the first set consisted of four of normal samples and the second set was of four samples strengthened with CFRP sheets at the bottom surface. Three of each set of samples were subjected to an impact from different heights, and the fourth was subjected to a normal static test for comparison. When subjected to impact load, samples strengthened with CFRP gave a 10 % larger load capacity than the normal samples. This percentage increased to 25 % for the sample subjected to a static load. The low performance for CFRP in strengthening is due to the punching shear failure that occurred to all tested samples; which cannot be resisted by the CFRP sheets. This conclusion was confirmed by another study done by Jahami [14], where the behavior of post-tensioned slabs strengthened with CFRP sheets was compared numerically to post-tensioned slabs. A similar percentage difference in load capacity was reached. This proves how critical is the punching shear failure in impact loading and that CFRP is not ideal to resist impact loads.

Hao [15] investigated the effect of using steel fibers in concrete on the impact behavior of reinforced concrete beams. Three cases were considered in the study: the first was the control sample without fibers, the second one contained spiral steel fibers, and the third one contained hooked-end steel fibers. Each sample was subjected to a repeated impact from a 15.2 Kg mass dropped from a height of 5 meters. Results showed that spiral steel fibers are better in absorbing the impact energy and enhancing the structural performance for RC beams under impact loading. Some researchers studied the efficiency of different types of fibers in punching shear resistance. Harajli [16] did a comparative study between steel fibers and polypropylene fibers to determine which of them serves better in punching shear resistance. The results showed that both types increased the punching shear capacity in a significant way and in a similar ratio. In addition, the failure observed for both fibers was a ductile failure and more energy was dissipated compared to normal concrete. Furthermore, Mostafaei [17] studied the effect of external prestressing on punching shear behavior of SFRC “steel fiber reinforced concrete” slabs. Results showed that using external prestressing helped in increasing punching shear capacity significantly. Also, the combination of steel fiber and prestressing helped in improving the ductility and energy dissipation of slabs.

In conclusion, the effect of impact loads on reinforced concrete slabs has been extensively investigated. However, very few researchers have studied the behavior of post-tensioned slabs under impact load and the optimum repair techniques. This research aimed to study the rehabilitation of post-tensioned slabs previously damaged by the impact falling objects; which simulated the case of falling rocks in mountainous areas. As for non-mountainous areas, other types of impact may occur such as blast impact. These impacts may be considered in future research. In this study, two drop cases were considered; a drop at the center of gravity of the slab and a drop at the mid-span of the slab free edge. The following parameters were considered in this study; punching shear capacity, flexural normal stresses, slab vibration, slab damping ratio, damage mode, and the extent of damage.

## 2. Methods

### 2.1. Slabs preparation

Two PT “post-tensioned” slabs are considered in this study each having a 660 cm×300 cm×25 cm dimensions. The slabs are prestressed with six equally distributed mono strands and reinforced with-10mm diameter bottom and top mesh at 250 mm spacing (Figures 1 and 2). The prestressing mono-strands have a draped profile and are grouted after casting the concrete to form a bonded system. Slabs’ dimensions and reinforcements considered the different gravity loads that act on a residential floor. The supporting system consisted of 10 cm diameter steel cylinders of 12 cm height resting on steel I-shaped beams, and the whole system is supported on two (60 cm×60 cm) concrete strip footings (Figure 3). As for the falling mass used to hit the slabs, a 605 Kg reinforced concrete block (60 cm×60 cm×60 cm) is cast inside an 8mm thickness steel mold to protect the concrete core from severe damage after impact; to be used for multiple drops (Figure 4).

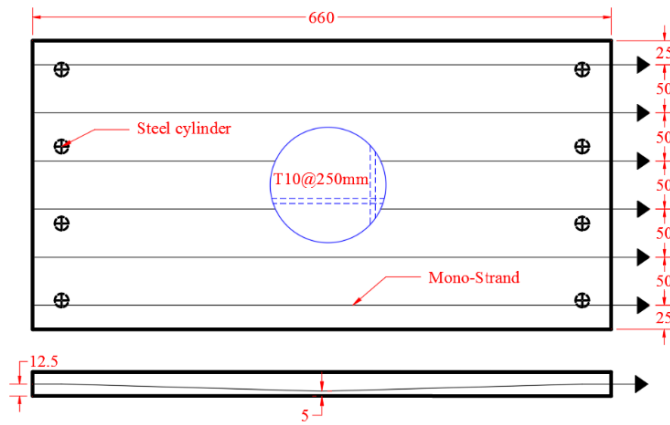


Figure 1. PT slab reinforcement (cm).



Figure 2. PT slab execution.

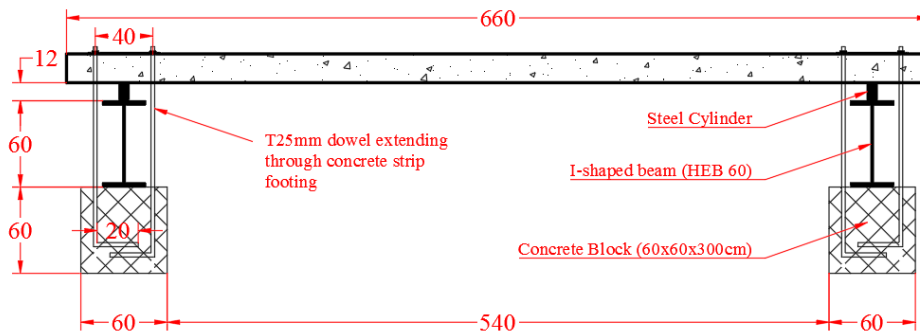


Figure 3. Slab supporting system (cm).



Figure 4. RC block reinforcement (cm).

The compressive strength test was conducted on three 15 cm diameter and 30 cm height cylinders specimens taken from the concrete batch after 28 days. The actual compressive strength of concrete is 32 MPa. The reinforcing steel rebars have yield and ultimate strengths of 585 MPa and 662 MPa respectively, and prestressed cables have yield and ultimate strengths of 1680 MPa and 1860 MPa respectively.

The experimental setup was prepared on different stages. During the First stage, all the timber formwork for the strip footings was set at a depth of 40 cm underground and the steel supporting system was prepared. Couples of 25 mm diameter steel dowels were added between the supports and extended to the concrete strip footings (Figure 3); in order to prevent the uplifting of slabs during impact. The footings then were cast and cured by water for about 7 days. After that, the I-shaped beams were placed over the strip footings and the steel cylinders were attached to them by bolts. Each cylinder had two 8 mm diameter and 15 cm length rebar welded to it and embedded inside the PT slab to form a pin support condition (Figure 5).

In the second stage, the slab formworks were prepared and the non-prestressed reinforcement was placed taking into consideration a clear cover of 2 cm. Then mono strands were placed as detailed in Figure 1, and special bursting steel was placed at the boundaries. After that concrete was cast and cured for two weeks with water, and mono-strands were stressed at 1400 MPa and grouted. Finally, a (150 cm×150 cm) neoprene pad was placed at the impact zone to redistribute pressure after hitting the slab with the falling block. One slab was hit at the center and named "PT-1", and the other was hit at the free edge of the mid-span and named "PT-2" as shown in Figure 6.

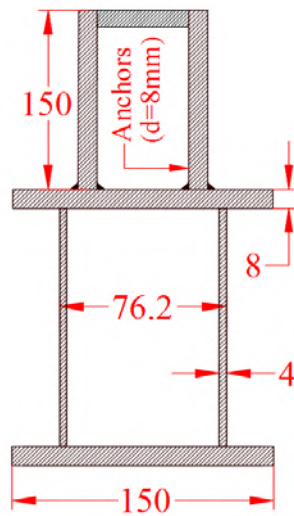


Figure 5. Steel cylinders (mm).

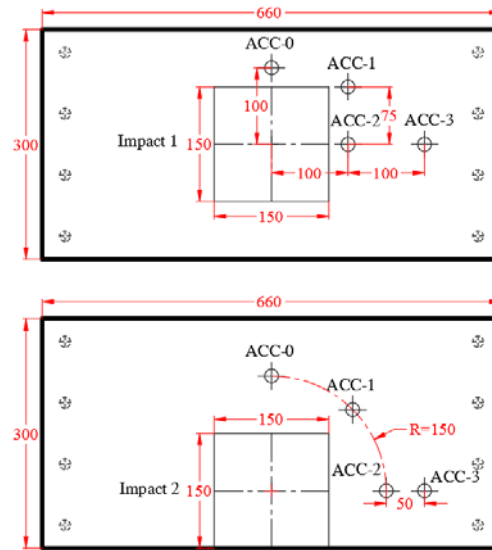


Figure 6. Impact position (cm).

In order to record the impact force and the slab displacement, the piezoelectric accelerometer sensors were used in this study. This type of sensors is adequate in the case of impact load; since it can record a large number of readings in a very short time. These sensors were used by much previous research [18, 19]. Four accelerometers were placed in each slab (PT-1 and PT-2) as illustrated in Figure 6. The position of each accelerometer was chosen such that it covers the critical slab zones. The data acquisition system used in this experiment consisted of: a (cDAQ-9178) with eight channels and a measurement card (NI 9234) which were provided by National Instrument [20]

On the testing day, a crane used to hold the 605 Kg RC block at a height of 20 m, where the total provided energy for the slabs was estimated based on the following equation:

$$E = mgh \quad (1)$$

Where  $E$  is the total provided energy for the system in (J),  $m$  is the mass of the falling object in (Kg),  $g$  is the gravitational acceleration and equal to (9.81 m/s<sup>2</sup>), and  $h$  is the height of the falling object (m). In this case, the total provided energy was 118.7 KJ. The block height and position were specified exactly using a theodolite device. Each slab was hit once and different data were recorded including Impact load, mid-span displacement, type of damages and their extent in the different slabs. Results showed that the impact load was 1217 KN for slab PT-1 and 965 KN for slab PT-2. These values will be used to repair the slabs in the rehabilitation process.

## 2.2. Rehabilitation process

After the impact test, slabs were repaired so it can withstand another future impact. The proposed method was using shear reinforcement as a strengthening technique; since the mode of failure for slabs subjected to impact loading is punching shear. First, the damaged parts were removed. Removal area was determined based on punching shear analysis; where shear reinforcement distributed area must continue to reach a limit where concrete can alone resist the applied shear stress. Equation 2 shows the concrete two-way shear strength, whereas equation 4 shows the shear stresses carried by shear reinforcement [21]:

$$v_{con} = ((\beta_p \sqrt{f'_c} + 0.3 f_{pc}) + v_p) \quad (2)$$

$$\beta_p = \min(3.5, (\alpha_s d / b_0 + 1.5)) \quad (3)$$

$$v_s = \frac{A_v f_y}{b \cdot s} \quad (4)$$

Where  $v_{con}$  is the punching shear capacity of concrete,  $\beta_p$  is the factor used to compute  $v_{con}$  in pre-stressed concrete slab,  $f_y$  is the rebar yield strength,  $f'_c$  is the concrete compressive strength,  $f_{pc}$  is the average pre-compression stress in the critical section,  $v_p$  is the vertical component of all effective pre-stress stresses crossing the critical section,  $v_s$  is the shear stress carried by shear reinforcement and it is the difference between the applied shear stress  $v_a$  and  $v_{con}$ ,  $A_v$  is the total area of rebar legs at the critical section,  $b$  is the perimeter of the critical section, and  $s$  is the spacing of shear reinforcement and must be less than  $(d/2)$ , where  $d$  is the effective depth of the section.

Therefore, for the PT slab subjected to an impact at its center of gravity "PT-1", the removal area was (2 m x 3 m). Whereas for the slab subjected to an impact at the mid-span of its free edge "PT-2", the removal area was (4.8 m x 3 m). Figure 7 shows the removed area for slabs "PT-1" and "PT-2". The new slabs were named "PT-1R" for the rehabilitated "PT-1" slab and "PT-2R" for the rehabilitated "PT-2" slab. ACI code recommends reducing the concrete shear strength when using shear reinforcement to  $\frac{1}{6} \sqrt{f'_c}$ . For more details regarding punching shear analysis and design, check Table 1:

**Table 1. Punching shear calculation details for rehabilitated samples "PT-1R" and PT-2R".**

Sample	$V_a$ (N)	$d$ (mm)	$b$ (mm)	$s$ (mm)	$f'_c$ (MPa)	$f_y$ (MPa)	$v_a$ (MPa)	$v_{con}$ (MPa)	$v_s$ (MPa)
PT-1R	1216685	220	2880	100	31	585	1.92	0.93	0.99
PT-2R	964716	220	1940	100	31	585	2.26	0.93	1.33

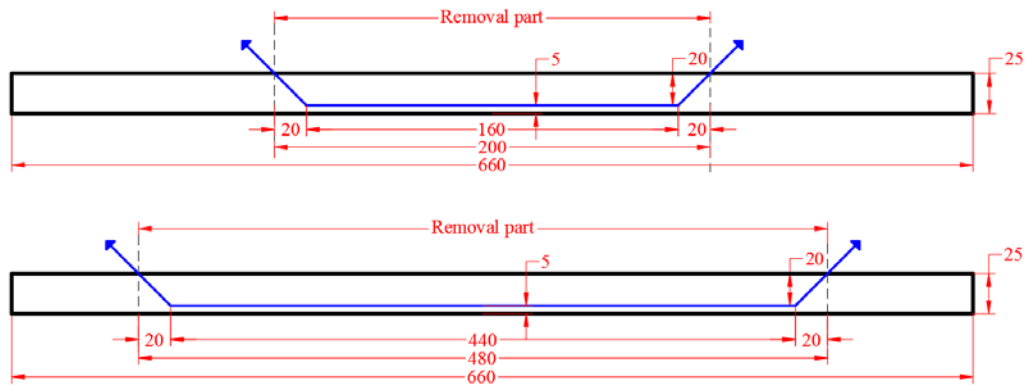


**Figure 7. Removal area for both PT-1R and PT-2R & added mono-strands (cm).**

Once the damaged zone is removed, all severely damaged non-prestressed reinforcement were replaced with new ones. A set of 10 mm diameter cross ties (punching shear reinforcement) was prepared – (Figure 8) – and attached to both top and bottom flexural reinforcement at a spacing of 10cm to cover the whole zone. As for the prestressing steel, all ducts were removed so strands are working as non-prestressed steel; since no bond remains between strands and concrete. Hence, and to regain the prestressing behavior in this zone, new mono strands were installed beside the old ones (Figure 9). The original flexural strength for both slabs before the first impact was 107.5 KN.m, whereas, after rehabilitation, the flexural strength increased to 118.6 KN.m. In order to achieve a better connection between the old and new concrete, an inclination of 45 degrees was performed in the interface. This interface was roughened to increase the friction between old and new concrete. Figure 10 shows slab PT-1R after finishing rehabilitation procedure before casting.

Finally, the new concrete was cast and cured with water for 2 weeks (Figure 11). Concrete mix strength was prepared to be the same as the old concrete cast for the first time. Three cylinders were tested at the impact test day and showed a compressive strength of 31 MPa. After casting, new sheets of neoprene pads were fixed at the impact zone as done previously, and accelerometers were placed at the same previous locations to have a valid comparison of the results with those of the original slabs before rehabilitation.

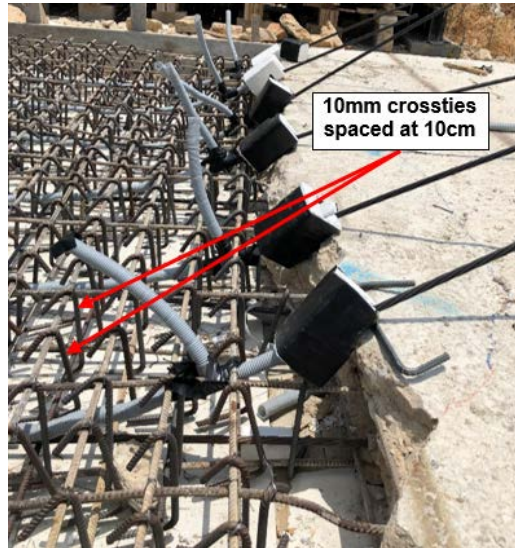


Figure 8. Crossties used in rehabilitation as punching shear reinforcement.

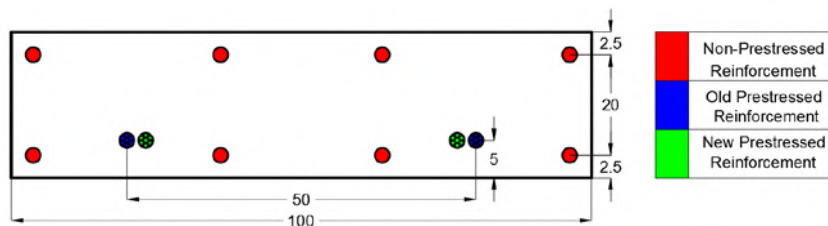


Figure 9. Flexural reinforcements detailing.



Figure 10. PT-1R slab before the concrete cast.



Figure 11. Concrete cast for PT-1R.

### 3. Results and Discussion

#### 3.1. Impact load analysis

Table 2 summarizes the results of the impact testing for PT slabs before and after repair. Although the mass and height of the drop were maintained the same, the impact load was increased after repair regardless of the location of the dropped mass. This increase is 44 % and 71 % when the mass is dropped at the center (PT-1 and PT-1R) and at the edge (PT-2 and PT-2R) respectively. This is due to the position of the block at the moment it hits the slab. The block in case (PT-1) fell approximately at its flat surface, whereas for case (PT-1R) it fell at one of its edges as illustrated in the blue hatched zone in Figure 12. In addition, the block in case (PT-1) fell approximately at the center of the slab, while in case (PT-1R) it landed slightly to the right side of the neoprene pad limit (Figure 12). Therefore, accelerometer “ACC-2” which was closer to the drop position for slab PT-1R recorded a larger acceleration value than slab PT-1. As for cases (PT-2 and PT-2R), the block fell nearly in the same position in both cases. But in case (PT-2R) the block fell at one of its edges as shown in Figure 13 (blue hatch), while it fell on its flat surface for case (PT-2). Hence, accelerometer “ACC-0” that lies behind the hitting block edge for slab PT-2R recorded a larger acceleration value than slab PT-2.

Another important finding is the dynamic increase factor (DIF) for the impact test, which is the ratio between the static load (weight of block) and the equivalent load due to impact. For the impact energy of

118.7 KJ, the static weight for the falling object was magnified by 206.3, 296.8, 163.6, and 280 times for slabs PT-1, PT-1R, PT-2, and PT-2R respectively. This difference in the DIF factor is due to the variation in impact loads described earlier. This increase factor (DIF) is very important to be determined for any future analysis and design procedure.

**Table 2. Applied load and punching shear analysis.**

Slab	Static load (KN)	Impact load (KN)	Dynamic impact factor (DIF)	Applied punching shear stress $v_a$ (MPa)	Punching shear capacity $v_c$ (MPa)	Shear demand ratio ( $v_a/v_c$ )
PT-1	5.9	1217	206.3	1.92	1.83	1.05
PT-1R	5.9	1751	296.8	2.76	4.08	0.67
PT-2	5.9	965	163.6	2.26	1.83	1.23
PT-2R	5.9	1652	280	3.87	4.44	0.87

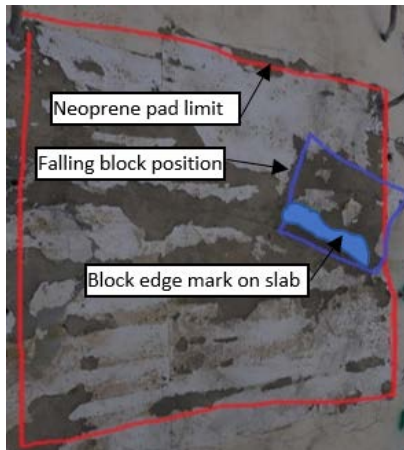


**Figure 12. Position of the falling block on collision with slab PT-1R**

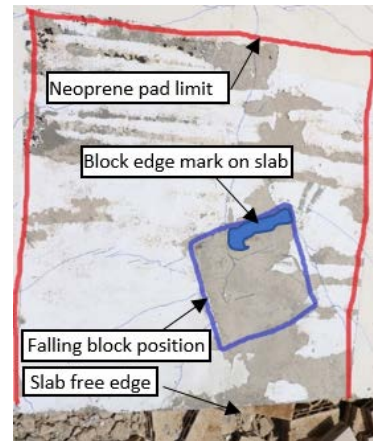


**Figure 13. Position of the falling block on collision with slab PT-2R**

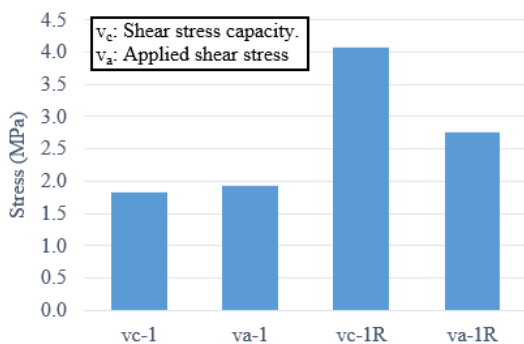


**Figure 14. Shear stress for slabs PT-1 and PT-1R**

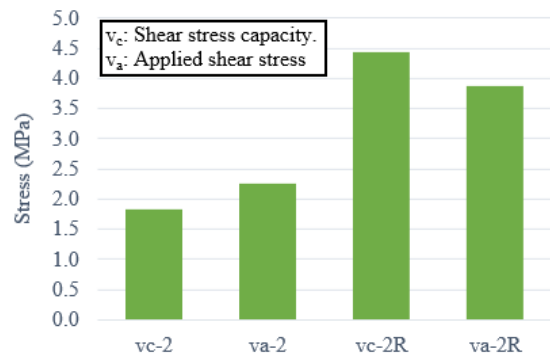


**Figure 15. Shear stress for slabs PT-2 and PT-2R**

Figure 14 shows the shear stress capacity and the applied shear stress for both slabs PT-1 and PT-1R. An increase of the punching shear capacity was observed from 1.83 MPa for slab PT-1 (before repair) to 4.08 MPa for slab PT-1R (after repair). This leads to a reduction in the shear demand ratio ( $v_n/v_{nc}$ ) from 1.05 for slab PT-1 to 0.67 for slab PT-1R. As for slabs PT-2 and PT-2R, similar improvement was recorded where the shear capacity was increased from 1.83 MPa to 4.44 MPa respectively (Figure 15). This improvement was better for slab PT-2R than slab PT-1R; since the critical perimeter  $b$  for the edge drop case (PT-2R) is less than the critical perimeter for the center drop case (PT-1R), which led to a higher shear stress carried by crossties  $v_s$  in slab (PT-2R) than slab (PT-1R).

In order to prove the efficiency of the rehabilitation technique, a comparative study is conducted in order to prove the efficiency of the repair technique of slabs PT-1R and PT-2R in terms of flexural normal stresses. To achieve this goal, the outputs of the numerical analysis obtained in a previous investigation conducted by the authors were used to assess the flexure mode of failure [8]. Two main parameters were studied: the tensile stress at the bottom non-prestressed rebars and the compressive stress at the concrete top surface. Both parameters were studied using the dynamic properties of both concrete and steel rebars and not the static properties. The dynamic properties were examined using the CEB-FIP Model Code [22] that relates the dynamic to static properties for both steel and concrete based on strain rate. The dynamic yield strength of

non-prestressed rebars was 720 MPa compared to 585 MPa for static strength, while the dynamic compressive strength of concrete was 47 compared to a static strength of 32 MPa.

Figure 16 plots the axial tensile stress at steel rebars  $f_s$  below the impact zone. It can be noted that the non-prestressed rebars at slabs PT-1 and PT-1R reached a tensile stress value of 542 MPa and 452 MPa respectively, which is around 75 % and 63 % of the dynamic yield stress (720 MPa) of reinforcing rebars. On the other hand, rebars in slab PT-2 were yielded as shown in Figure 16, whereas slab PT-2R recorded a rebar tensile stress of 653 MPa, which is around 91 % of the dynamic yield stress. This suggests that both repaired slabs (PT-1R and PT-2R) did not experience any yielding in steel rebars.

The second parameter was represented in Figure 17, where the compressive stresses in concrete  $f_c$  at the top fibre of the slabs are shown in the impact zone. As per ACI318-14 [21] requirements, the stress in compression should not exceed  $0.85f'_c$  (i.e. 40 MPa) to avoid failure of concrete in compression. Results show that top compressive stresses for slabs PT-1 and PT-2 were 36 MPa and 41 MPa respectively, which means that slab PT-2 failed in compression. However, there was no compressive failure for both slabs after repairing, where the compressive stress was 30 MPa and 34 MPa for slabs PT-1R and PT-2R respectively. It was realized that for both top and bottom stresses slab PT-2R had higher values than slab PT-1R; because for slab PT-2R, the slab is hit at the mid-span of its free edge, which will lead to a higher top and bottom strain.

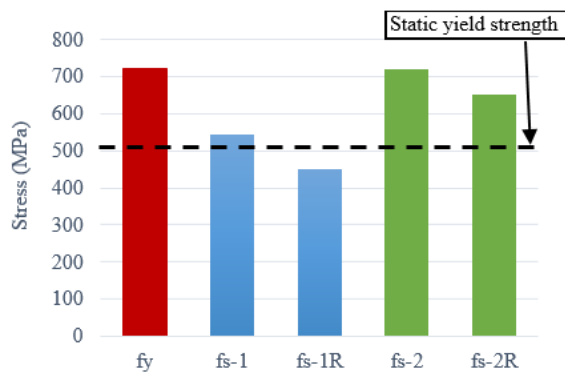


Figure 16. Rebar tensile stresses for slabs (PT-1, PT-1R, PT-2, and PT-2R)

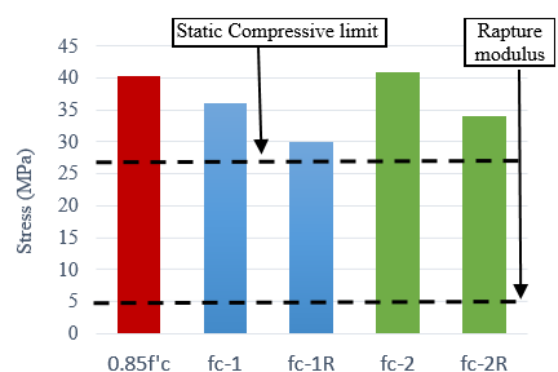


Figure 17. Top compression stresses for slabs (PT-1, PT-1R, PT-2, and PT-2R)

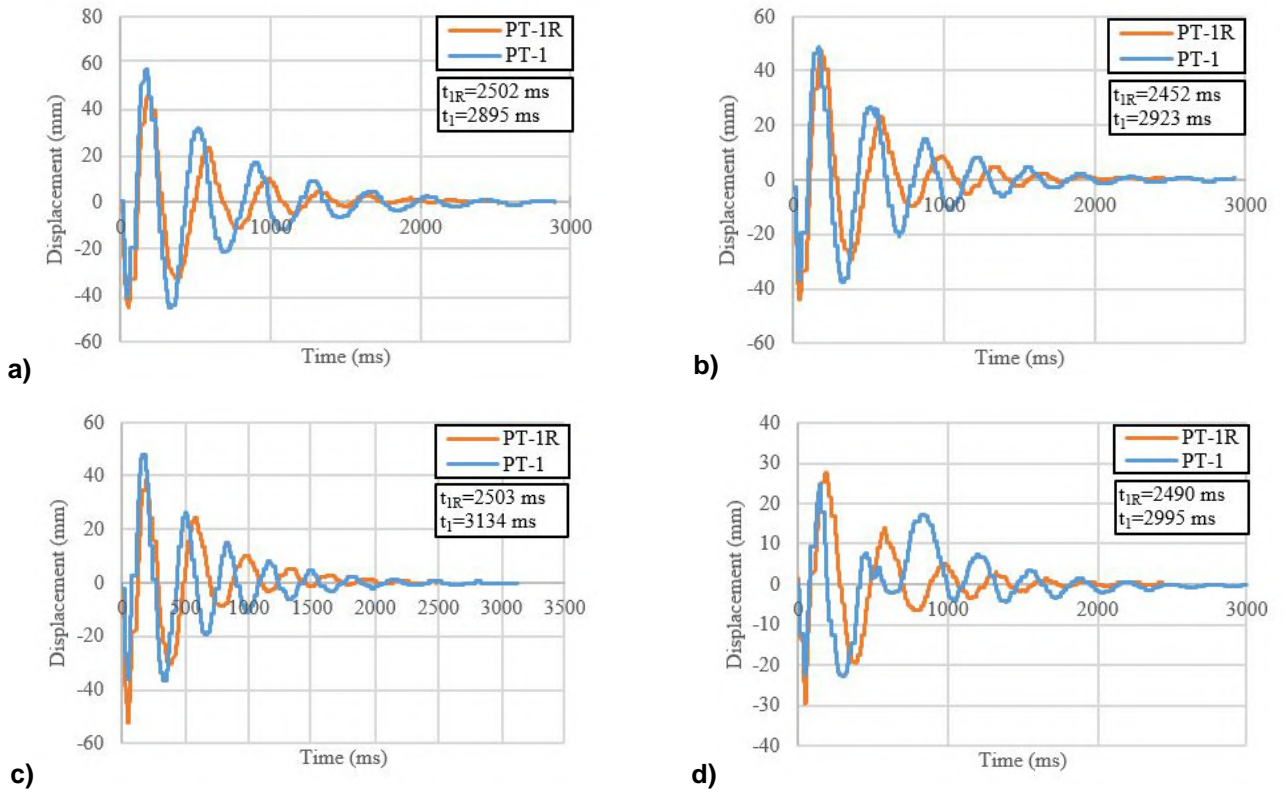
### 3.2. Vibration analysis

The displacement at each accelerometer was recorded using the double integration method for the acceleration curves. Table 3 summarizes the maximum displacement values for each accelerometer. For slab PT-1, the maximum displacement was recorded at ACC0 with a value of 40.4 mm. However, for slab PT-1R the maximum displacement was recorded at ACC2 (52.7 mm). This is due to the position of the block on collision where the edge of the block touched the slab first near ACC2. Compared to the displacement values at slab PT-1, the values recorded for slab PT-1R were higher; since the impact load was higher. A similar trend was realized for slabs PT-2 and PT-2R, where the maximum displacement was recorded at ACC2 (38.1 mm) for slab PT-2 and ACC0 (42 mm) for slab PT-2R. The higher displacement values for the repaired slab PT-2R is due to the higher impact load because of the position of the falling block. ACC1 results were not included since there were cracks across the accelerometers during impact.

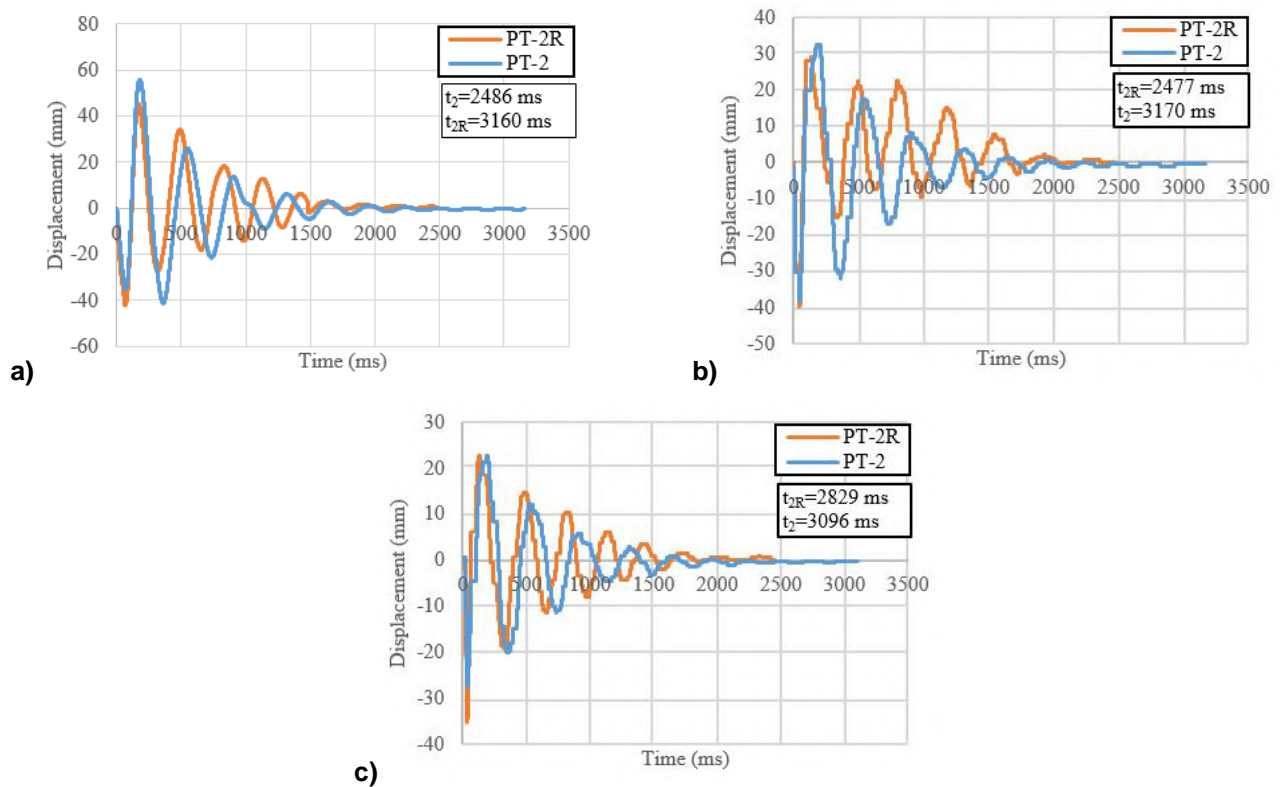
One of the indicators that shows the efficiency of the repair technique is the “impact force to maximum displacement” (F/D) ratio, which is introduced for each accelerometer in Table 3. This ratio shows the force needed for each slab to generate a unit displacement. It can be clearly noticed that slab PT-1R performed better than slab PT-1 since it has a higher (F/D) ratio at all points (except ACC2). Results also showed an increase in the (F/D) ratio for slab PT-2R compared to slab PT-2. Moreover, it can be noticed that repairing techniques has more efficiency for the edge drop (PT-2 and PT-2R) than the central drop (PT-1 and PT-1R) in terms of (F/D) ratio. For more details, Figures 18 and 19 show the full displacement – time curves for slabs (PT-1 and PT-1R) and (PT-2 and PT-2R).

Table 3. Displacement results at each accelerometer.

Slab	ACC0 (mm)	ACC1 (mm)	ACC2 (mm)	ACC3 (mm)	(F/D) <sub>0</sub> (KN/mm)	(F/D) <sub>1</sub> (KN/mm)	(F/D) <sub>2</sub> (KN/mm)	(F/D) <sub>3</sub> (KN/mm)
PT-1	40.4	37.0	35.7	22.9	30.1	32.9	34.1	53.1
PT-1R	45.0	43.5	52.7	29.3	38.9	40.3	33.2	59.8
PT-2	35.4	--	38.1	27.8	27.3	--	25.3	34.8
PT-2R	42.0	--	40.0	35.0	39.3	--	41.3	47.2



**Figure 18. Displacement – Time curves for slabs PT-1 and PT-1R at: (a): ACC0 (b): ACC1 (c): ACC2 (d): ACC3**



**Figure 19: Displacement – Time curves for slabs PT-2 and PT-2R at: (a): ACC0 (b): ACC2 (c): ACC3.**

Based on the displacement – time curves illustrated in Figures 18 and 19, vibration analysis was conducted in order to compare the slabs before and after repairing in terms of damping. It can be noted that the vibration time “t” for slab PT-1 was longer than that of slab PT-1R. For example, the vibration time at ACC0 for slabs PT-1 and PT-1R was 2895 and 2502 ms respectively. This trend was realized also for ACC2 where the vibration period was 3134 ms for slab PT-1 compared to 2503 ms for slab PT-1R, although the block falls on its edge and near ACC2 in the case of slab PT-1R. As for the slabs with the edge drop (PT-2 and PT-2R),

ACC0 recorded a vibration time of 3160 ms for slab PT-2 while for slab PT-2R the time was 2486 ms. The trend was the same for the remaining accelerometers (ACC2 and ACC3). This may be due to better damping for the repaired slabs compared to the original ones.

In order to find the damping ratio for each slab, the maximum displacement for each cycle from the displacement – time curves shown in Figures 18 and 19 was plotted and the exponential trend curve passing through these points were presented. This trend curve is called the decaying curve and has the formula  $y = Ae^{-w_n \zeta t}$ , where  $y$  is the displacement,  $A$  is a constant,  $w_n$  is the natural frequency and is presented by  $2\pi/T_n$ , where  $T_n$  is the period of vibration,  $\zeta$  is the damping ratio, and  $t$  is the time [23]. Two displacement – time curves (ACC0 and ACC2) were considered for both slabs PT-1 and PT-1R in order to find the damping ratio (Figure 20). Based on the derived exponential functions, the damping coefficient for slab PT-1 at ACC0 is 0.093, whereas for slab PT-1R it is 0.131. The same trend was realized at ACC2, where the value of damping ratio coefficient for slab PT-1 was 0.08 and for PT-1R was 0.11 (Figure 22). Regarding the edge drop case, the time – displacement curves (ACC0 and ACC3) for slabs PT-2 and PT-2R were analyzed (Figure 21). The damping ratio for slab PT-2 at ACC0 was 0.097 whereas for slab PT-2R it was 0.11. As for ACC3, damping ratio values were 0.082 for slab PT-2 and 0.093 for slab PT-2R (Figure 23). This difference in both cases (central and free-edge drop) may be due to varying boundary conditions; since the supports may have been damaged after the first impact. In addition, the original concrete slab parts near the supports were not repaired or replaced causing a difference in the mechanical properties in these zones.

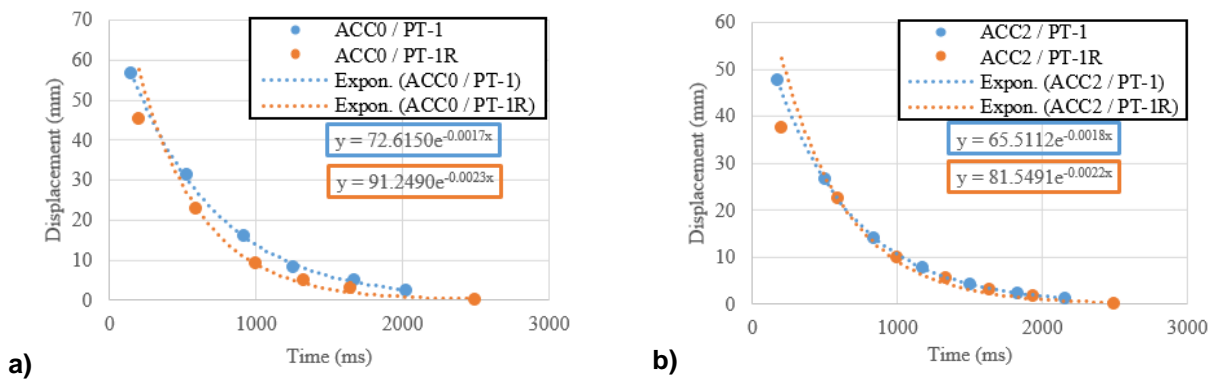


Figure 20. Decaying functions for PT-1 and PT-1R at the following accelerometers: (a): ACC0 (b): ACC2

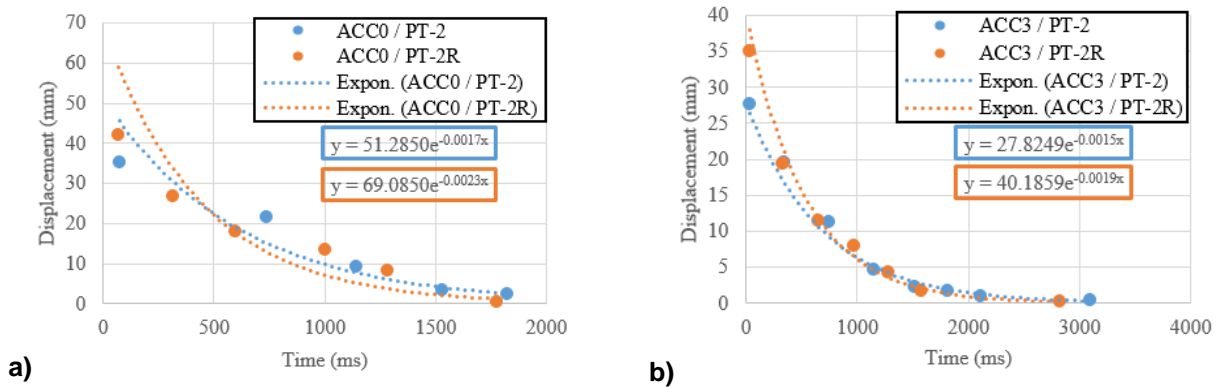


Figure 21. Decaying functions for PT-2 and PT-2R at the following accelerometers: (a): ACC0 (b): ACC3

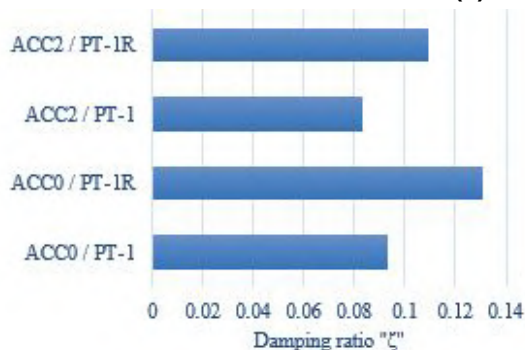


Figure 22. Damping ratio for slabs PT-1 and PT-1R

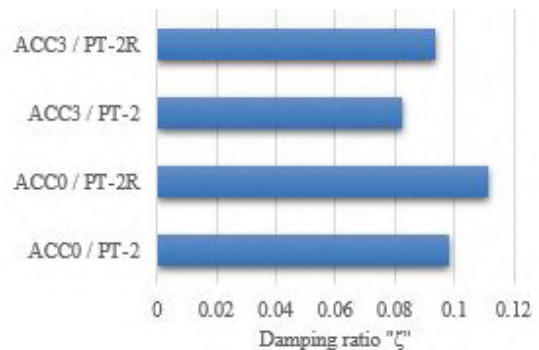


Figure 23. Damping ratio for slabs PT-2 and PT-2R

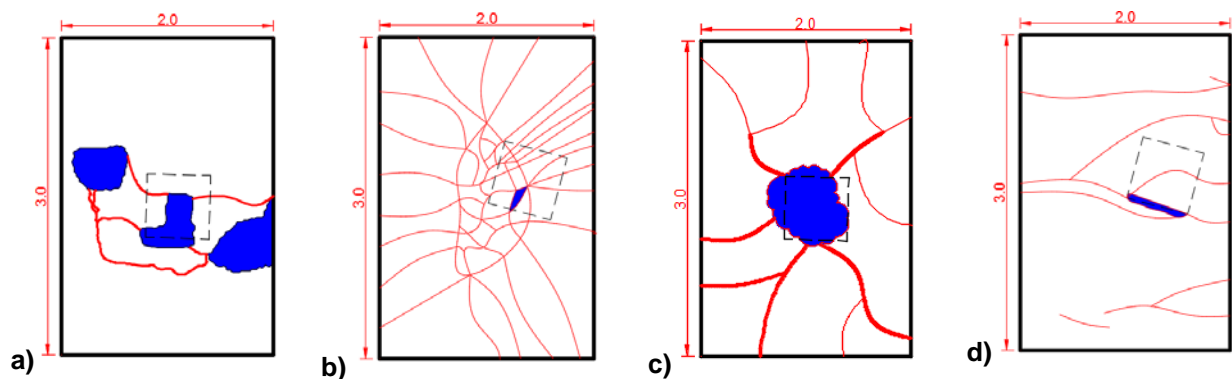
### 3.3. Damage Analysis

Table 4 summarizes the damage analysis results. Both slabs PT-1 and PT-2 failed under punching shear mode. This can be shown in Figures 24 and 25. These figures show the distribution of cracks prior to the replacement of concrete parts for both cases (2 m×3 m for central drop case and 4.8 m×3 m for edge drop case). According to these Figures, a spalling phenomenon (Hatched in blue) was observed in both cases. The total spalled zone in tension was 0.82 m<sup>2</sup> for slab PT-1, whereas this area increased to reach 1.1 m<sup>2</sup> for slab PT-2. In addition, crushing of concrete occurred at the top face due to excessive compressive stresses, where the area of crushed concrete was 0.42 m<sup>2</sup> for slab PT-1 and 0.73 m<sup>2</sup> for slab PT-2. This agrees with the previous punching shear analysis carried out (Table 2) where the impact caused the slab to fail under punching shear. Moreover, the damage that occurred for the PT slab subjected to edge impact (PT-2) was more severe than the damage that occurred for the PT slab subjected to central impact (PT-1).

Moreover, slabs PT-1R and PT-2R that were repaired using shear reinforcement had a different crack pattern. Results showed that the damage is changed from punching shear to flexural damage (Figure 25). Slab PT-1R experienced a tiny spalling zone due to the tilting of the block during impact where it fell at its edge as was illustrated in Figures 24b and 24d. As for slab PT-2R, there were no spalling zones as shown in Figure 25. Besides, a distribution for flexural (hairy cracks) was observed for both slabs. These cracks reflect the effect of the concentrated pressure on both slabs from the falling block.

**Table 4. Damaged zone areas for tested slabs.**

Slab	Crack pattern	Spalling area at tension (m <sup>2</sup> )	Spalling area at compression (m <sup>2</sup> )
PT-1	Punching shear	0.82	0.42
PT-1R	Flexural	0.01	0.04
PT-2	Punching shear	1.1	0.73
PT-2R	Flexural	0	0



**Figure 24. Structural damage (m)**

(a): Bottom damage for PT-1 (b): Bottom damage for PT-1R  
(c): Top damage for PT-1 (d): Top damage for PT-1R

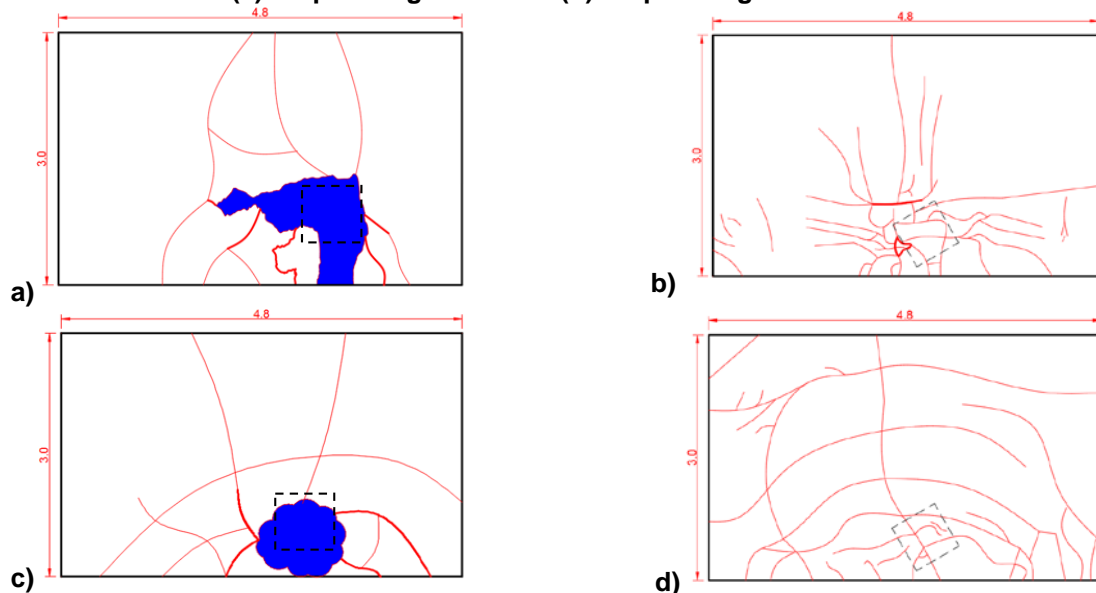


**Figure 25. Structural damage (m)**

(a): Bottom damage for PT-2 (b): Bottom damage for PT-2R  
(c): Top damage for PT-2 (d): Top damage for PT-2R

## 4. Conclusion

The following conclusions can be made:

1. The position and angle of the falling block have a great effect on the value of impact load acting on PT slabs. Slabs PT-1R and PT-2R, where the falling object landed on its edge, experienced 44 % and 71 % higher impact load than slabs PT-1 and PT-2 respectively, where the falling object landed on its flat surface.
2. Using shear reinforcement helped in enhancing the punching shear capacity for PT slabs when subjected to impact loads. The punching shear resistance was increased by 123% for slabs PT-1 and PT-1R (central drop case), and by 146 % for slabs PT-2 and PT-2R (edge drop case). This improvement was better for edge drop case than central drop case.
3. The normal stress capacity of the repaired slabs was enough to prevent flexural failure. This was proved by showing that both top fibre stresses in compression and bottom rebar stresses in tension were below the ultimate limit specified by the ACI code. The top fiber stress reached 75 % of the code limit for slab PT-1R and 85 % for slab PT-2R. As for the bottom rebar stress, rebars in slab PT-1R reached 63 % of the limit yield strength while in slab PT-2R they reached 91 % of the yield strength. It was concluded that both top and bottom stresses were higher for the edge drop case (PT-2R) than the central drop case (PT-1R) due to the higher strain resulted from the drop upon the free edge.
4. In terms of displacement, the repaired slabs showed a better performance than the original slabs for both central and edge drop case. This was shown in terms of the "Impact force to maximum displacement" ( $F/D$ ) ratio, where the repaired slabs (PT-1R and PT-2R) had a higher ratio than the original slabs (PT-1 and PT-2). This means that repaired slabs dragged higher forces to cause the same amount of displacement as the original slabs.
5. The repaired slabs (PT-1R and PT-2R) showed to have a higher damping ratio  $\zeta$  than the original slabs (PT-1 and PT-2). This may be due to the damage occurred for the non-replaced parts near supports; which cause the slabs to dampen in a higher ratio.
6. The crack pattern for PT slabs subjected to impact load is punching shear, where a spalling of concrete occurred at the impact point. Slab PT-2 had a more spalled area in tension and compression than slab PT-1. Using shear reinforcement as a repair technique helped in changing the crack pattern from punching shear to flexure (similar to the effect of concentrated load on slab) for both slabs PT-1R and PT-2R. This helps in preventing brittle failure; since the flexural failure, if happened, is usually designed to be ductile.
7. The results of this investigation suggest that further research is necessary. These include studying the effect of the falling angle and position of the block on the impact resistance of post-tensioned slabs.

## References

1. Choi, J.H., Choi, S.J., Kim, J.H.J., Hong, K.N. Evaluation of blast resistance and failure behavior of prestressed concrete under blast loading. *Construction and Building Materials*. 2018. 173. Pp. 550–572. DOI:10.1016/j.conbuildmat.2018.04.047. URL: <https://doi.org/10.1016/j.conbuildmat.2018.04.047>.
2. Temsah, Y., Jahami, A., Khatib, J., Sonebi, M. Numerical analysis of a reinforced concrete beam under blast loading. *MATEC Web of Conferences*. 2018. 149. Pp. 1–5. DOI:10.1051/mateconf/201714902063.
3. Temsah, Y., Jahami, A., Khatib, J., Sonebi, M. Numerical Derivation of Iso-Damaged Curve for a Reinforced Concrete Beam Subjected to Blast Loading. *MATEC Web of Conferences*. 2018. 149. Pp. 1–5. DOI:10.1051/mateconf/201714902016.
4. Zhang, D., Yao, S.J., Lu, F., Chen, X.G., Lin, G., Wang, W., Lin, Y. Experimental study on scaling of RC beams under close-in blast loading. *Engineering Failure Analysis*. 2013. 33. Pp. 497–504. DOI:10.1016/j.engfailanal.2013.06.020.
5. Mougín, J.P., Perrotin, P., Mommessin, M., Tonnelo, J., Agbossou, A. Rock fall impact on reinforced concrete slab: An experimental approach. *International Journal of Impact Engineering*. 2005. 31(2). Pp. 169–183. DOI:10.1016/j.ijimpeng.2003.11.005.
6. Jahami, A., Temsah, Y., Baalbaki, O., Darwiche, M., Al-Rawi, Y., Al-Ilani, M., Chaaban, S. Effect of Successive Impact Loads From a Drop Weight on a Reinforced Concrete Flat Slab. *MATEC Web of Conferences*. 2019. 281. Pp. 02003. DOI:10.1051/mateconf/201928102003.
7. Iqbal, M.A., Kumar, V., Mittal, A.K. Experimental and numerical studies on the drop impact resistance of prestressed concrete plates. *International Journal of Impact Engineering*. 2019. 123. Pp. 98–117. DOI:10.1016/j.ijimpeng.2018.09.013. URL: <https://doi.org/10.1016/j.ijimpeng.2018.09.013>.
8. Al Rawi, Y., Timsah, Y., Ghanem, H., Jahami, A., Elani, M. The effect of impact loads on prestressed concrete slabs. *The Second European and Mediterranean Structural Engineering and Construction Conference*. (July)2018.
9. Kumar, V., Iqbal, M.A., Mittal, A.K. Energy absorption capacity of prestressed and reinforced concrete slabs subjected to multiple impacts. *Procedia Structural Integrity*. 2017. 6. Pp. 11–18. DOI:10.1016/j.prostr.2017.11.003. URL: <https://doi.org/10.1016/j.prostr.2017.11.003>.
10. Almusallam, T., Al-Salloum, Y., Alsayed, S., Iqbal, R., Abbas, H. Effect of CFRP strengthening on the response of RC slabs to hard projectile impact. *Nuclear Engineering and Design*. 2015. 286. Pp. 211–226. DOI:10.1016/j.nucengdes.2015.02.017.
11. Kong, X., Qi, X., Gu, Y., Lawan, I.A., Qu, Y. Numerical evaluation of blast resistance of RC slab strengthened with AFRP. *Construction and Building Materials*. 2018. 178. Pp. 244–253. DOI:10.1016/j.conbuildmat.2018.05.081. URL: <https://doi.org/10.1016/j.conbuildmat.2018.05.081>.
12. Ali, T., Yehia, S. Study on Strengthening of RC Slabs with Different Innovative Techniques. *Open Journal of Civil Engineering*. 2016. 06(04). Pp. 516–525. DOI:10.4236/ojce.2016.64044.

13. Radnić, J., Matešan, D., Grgić, N., Baloević, G. Impact testing of RC slabs strengthened with CFRP strips. *Composite Structures*. 2015. 121. Pp. 90–103. DOI:10.1016/j.compstruct.2014.10.033.
14. Jahami, A., Temsah, Y., Khatib, J., Sonebi, M. Numerical study for the effect of carbon fiber reinforced. *Symposium on Concrete Modelling (CONMOD2018)*. (August)Delft, Netherlands, 2018. Pp. 259–267.
15. Hao, Y., Hao, H., Chen, G. Experimental tests of steel fibre reinforced concrete beams under drop-weight impacts. *Key Engineering Materials*. 2015. 626(August). Pp. 311–316. DOI:10.4028/www.scientific.net/KEM.626.311.
16. Harajli, M.H., Maalouf, D., Khatib, H. Effect of fibers on the punching shear strength of slab-column connections. *Cement and Concrete Composites*. 1995. 17(2). Pp. 161–170. DOI:10.1016/0958-9465(94)00031-S.
17. Mostafaei, H., Vecchio, F.J., Gauvreau, P., Semelawy, M. Punching shear behavior of externally prestressed concrete slabs. *Journal of Structural Engineering*. 2011. 137(1). Pp. 100–108. DOI:10.1061/(ASCE)ST.1943-541X.0000283.
18. Abir, J., Longo, S., Morantz, P., Shore, P. Optimized estimator for real-time dynamic displacement measurement using accelerometers. *Mechatronics*. 2016. 39. Pp. 1–11. DOI:10.1016/j.mechatronics.2016.07.003.
19. Yang, J., Li, J.B., Lin, G. A simple approach to integration of acceleration data for dynamic soil-structure interaction analysis. *Soil Dynamics and Earthquake Engineering*. 2006. 26(8). Pp. 725–734. DOI:10.1016/j.soildyn.2005.12.011.
20. Automated Test and Automated Measurement Systems - National Instruments, 2019. URL <https://www.ni.com/en-lb.html> [accessed 22 August 2019].
21. Building Code Requirements For Structural Concrete (ACI 318-14). Farmington Hills, Michigan: American Concrete Institute, ACI. 2014.
22. MC90, CEB-FIP Model Code 1993, Design Code, 6th edition, Thomas Telford, Lausanne, Switzerland, 1993.
23. Chopra, Anil K. *Dynamics Of Structures*. 4th edn. 2009.

### **Contacts:**

*Ali Jahami, +96171859962; ahjahamy@hotmail.com*

*Yehya Temsah, +9613723790; ytemsah@bau.edu.lb*

*Jamal Khatib, +96170382861; j.m.khatib@wlv.ac.uk*

*Ossama Baalbaki, +9613348851; obaalbaki@bau.edu.lb*

*Mohamad Darwiche, +96176602500; m.darwich@bau.edu.lb*

*Sandy Chaaban, +9613627858; s.chaaban@bau.edu.lb*

© Jahami, A.,Temsah, Y.,Khatib, J.,Baalbaki, O.,Darwiche, M.,Chaaban, S., 2020



DOI: 10.18720/MCE.93.12

## Properties of cement-bound mixes depending on technological factors

**E.A. Vdovin\***, **V.F. Stroganov**

*Kazan State University of Architecture and Engineering, Kazan, Russia*

\* E-mail: [vdovin007@mail.ru](mailto:vdovin007@mail.ru)

**Keywords:** cement-bound mixes, sodium formate, technological factors, workability, density, humidity, mixture manufacturability time

**Abstract.** The influence of technological factors on the properties of cement-bound mixes, hardening at positive and negative temperatures in the construction of pavements, is studied. The relationships between density and strength of cement-bound mixes and the content of cement and water are established. The optimal moisture contents of mixes (10.5–11.5 %) were determined, which ensure the maximum material density from 2000 to 2300 kg/m<sup>3</sup> with a cement content of 6 to 12 % by weight of the crushed stone mix. The influence of complex antifreeze additives on the mix technological properties (density, workability, constructability time) was studied. It was shown that sodium formate additives contribute to increasing the mix density and reducing the mix technological hardness (workability) under positive and negative temperatures. The influence of temperature and the amount of functional additives on the constructability time of cement-bound mixes is considered. It was established that additives contribute to preservation of the required workability of mixes at negative temperatures (down to -15 °C) for 1–2 hours and provide the necessary conditions for efficient work performance without reducing their quality and reducing the technological cycle period.

### 1. Introduction

The importance of influence of technological factors on the properties of cement-mineral materials (cement primers, cement-bound mixes (CBM), concrete, etc.) is noted in many works [1–17]. CBM preparation for road construction is associated with the need to determine the optimal moisture and maximum density. Their relationship with the properties and the forming material structure is considered in [18, 19], especially under the conditions of paving at low and subzero temperatures down to -15 °C. The relevance of this problem is shown in works [25–23]. The literature analysis showed that CBM have significant porosity and, when exposed to negative temperatures, the number of pores and capillaries in which water passes into ice increases with the occurrence of stresses that cause material destruction. Thus, work at low temperatures requires the development of technology for the construction of cement-bound layers of pavement, providing the maximum material density. To achieve the greatest degree of compaction of CBM, placed in road pavements at low and negative temperatures, antifreeze additives can be used, which reduce the CBM open porosity and preserve the liquid phase in mixes [24–31]. However, the higher efficiency of antifreeze additives is provided by the use of additives with multifunctional effect. In this regard, we have developed complex antifreeze additives based on sodium formate (FN) using a hardening accelerator - calcium chloride (CC) and C-3 superplasticizer, which is a polycondensation product of naphthalenesulfonic acid and formaldehyde (SP). It should be noted that the superplasticizer included in the complex composition is designed to reduce moisture, improve technological properties and increase the CBM density. Calcium chloride, in addition to accelerating hardening, enhances the anti-frost effect of sodium formate, and its low content in the complex additive prevents the destruction development during hardening of cement-mineral material. The development of work technology at low temperatures is based on the results of studies of the influence of technological factors on the properties of materials using new modifiers. Based on the properties of the developed functional additives and the relevance of their application, the following work aim is formulated: to study the influence of

Vdovin, E.A., Stroganov, V.F. Properties of cement-bound mixes depending on technological factors. Magazine of Civil Engineering. 2020. 93(1). Pp. 147–155. DOI: 10.18720/MCE.93.12

Вдовин Е.А., Строганов В.Ф. Влияние технологических факторов на свойства цементощебеночных смесей для дорожных одежд // Инженерно-строительный журнал. 2020. № 1(93). С. 147–155. DOI: 10.18720/MCE.93.12



This work is licensed under a [CC BY-NC 4.0](https://creativecommons.org/licenses/by-nc/4.0/)

technological factors on the properties of cement-bound mixes with functional additives based on sodium formate, hardening at low temperatures in the construction of pavements.

## 2. Methods

The studies were carried out using crushed stone mixes of limestone and dolomite rocks, including substandard crushed stone of stone quarries of (0–40) mm fractions. The grain size distribution and physico-mechanical properties of mixes are given in Tables 1 and 2.

**Table 1. The grain size distribution of the crushed stone mixture.**

Maximal grain size, mm	The total residue on the sieves with hole sizes, mm								
	40	20	10	5	2.5	1.25	0.63	0.315	0.14
40	5	37	56	70	80	85	86	88.5	91

**Table 2. Physico-mechanical properties of the crushed stone mixes.**

Fraction size, mm	Bulk density, kg/m <sup>3</sup>	Water absorption, %	Attrition grade	Strength grade	Frost-resistance indicator
0-40	1600	9.1	IV	200	10

The Portland cement of CEM I 42.5N grade of the following mineral and chemical compositions (Tables 3 and 4) was used in the studies.

**Table 3. Mineral composition of the cement.**

Name	C <sub>3</sub> S	C <sub>2</sub> S	C <sub>3</sub> A	C <sub>4</sub> AF
Content, %	58	17	8	13

**Table 4. Chemical composition of cement.**

Name	SiO <sub>2</sub>	Al <sub>2</sub> O <sub>3</sub>	Fe <sub>2</sub> O <sub>3</sub>	CaO	MgO	SO <sub>3</sub>	R <sub>2</sub> O (Na <sub>2</sub> O+0.65 K <sub>2</sub> O)	CaO <sub>sv</sub>
Content, %	21.1	5.85	4.2	65.4	1.13	1.03	1.07	0.16

The following substances were used as components of complex antifreeze additives:

- Sodium formate (FN) - sodium salt of formic acid HCOONa, a water-soluble product of the “chemically pure” grade;
- Crystalline calcium chloride CaCl<sub>2</sub> (CC), a water-soluble product of the “chemically pure” grade;
- Superplasticizer C-3 (SP) - sodium salt of the condensation product of  $\beta$ -naphthalenesulfonic acid and formaldehyde. It was used in the form of a 2.5% aqueous solution with pH in the range of 7–9.
- Batched water - water that complies with the requirements of EN 1008: 2002.

The composition of the cement-crushed stone mixes was selected according to the Russian State Standard GOST 23558. The cement content in CBM varied from 6 to 12 % by weight of the dry crushed stone mixture, and the moisture content varied from 7 to 15 % by weight of the dry CBM.

The density of the finished CBM was determined according to the Russian State Standard GOST 10181, the compressive strength of the samples was determined according to the Russian State Standard GOST 10180 after hardening them for 28 days under normal conditions (temperature (20 ± 2) °C, moisture not less than 90 %). The dimensions of the samples were adopted taking into account the maximum size of the aggregate in accordance with the Russian State Standard GOST 10180. Cement-bound mixes were compacted using the laboratory vibratory platform of the S-135-A type, providing vertical vibrations of the filled form with a frequency of 2900 ± 100 vibrations per minute and an amplitude of 0.5 ± 0.05 mm.

Technological hardness (workability) of CBM was determined in 200×200×200 mm molds for formation of concrete samples according to the method of B. Skramtaev using a metal cone according to the Russian State Standard GOST 10181.

The influence of FN and CC additives on the hardness and density of mixes with a constant SP content was studied using the experiment-planning method according to V. Kleiman's contour-graphic scheme [43]. The tests were carried out on mixes of optimal moisture with addition of 9% cement. The content of anti-frost components of additives (FN, CC) was changed in accordance with the plan of the two-factor experiment (Figure 1). The test results were used to construct dependencies with isolines of equal density and technological hardness (Figure 5).

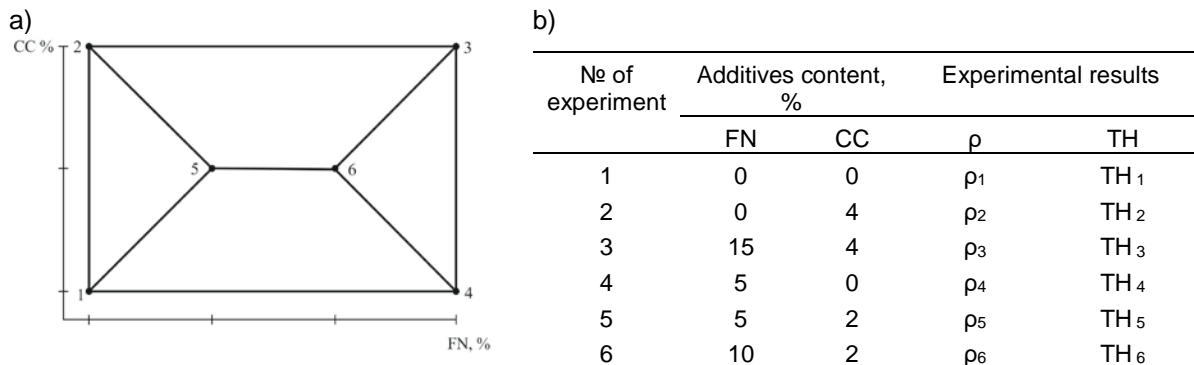


**Figure 1. Experiment planning: a) contour-graphic scheme of experiment planning; b) experiment plan.**

When studying the influence of aging time and temperature on workability of mixes in additives, the FN content was changed at a constant content of CC and SP.

In all experiments CBM after preparation was placed in chambers with the required temperature and moisture conditions (Figures 2–5, Table 5): for normal storage (temperature  $(20 \pm 2)^\circ\text{C}$ , moisture not less than 90 %) and with temperatures  $-5^\circ\text{C}$ ,  $-15^\circ\text{C}$ . After exposure in chambers, the properties of CBM were determined.

### 3. Results and Discussion

The influence of the amount of the introduced cement and water on the indicators determining the optimum moisture, maximum density, and strength of the material is preliminary examined.

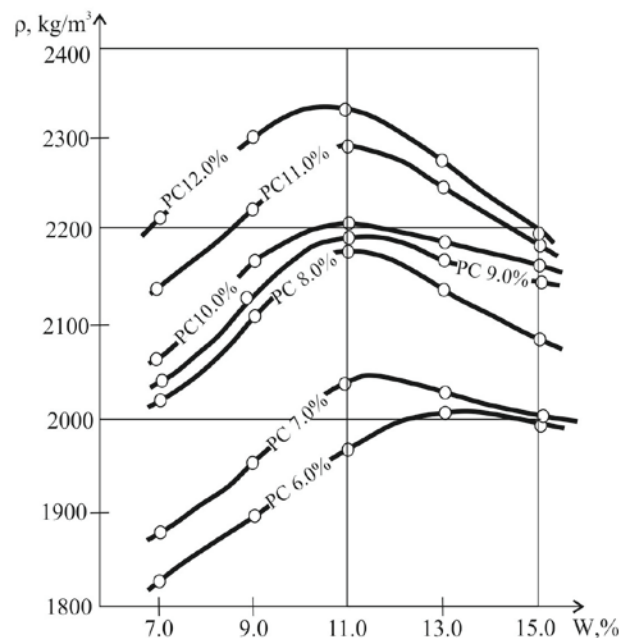


**Figure 2. Relationship between CBM density and the mix moisture.**

For all CBM studied with a cement content from 6 to 12 % by weight of the crushed stone mixture, the optimal moisture content of mixes were determined. These optimal moistures are in the range of 10.5–11.5 %, ensuring the maximum density of the material from 2000 to 2300  $\text{kg/m}^3$  (Figure 2). The compressive strength of samples obtained from optimally moistened mixes at the age of 28 days increased from 3.5 to 14.5 MPa (Figure 3). It was established that a twofold increase in the cement content in the mixture provided a more than fourfold increase in the strength of the material. The addition of one percent of cement is equivalent to a strength increment of 1.8 MPa.

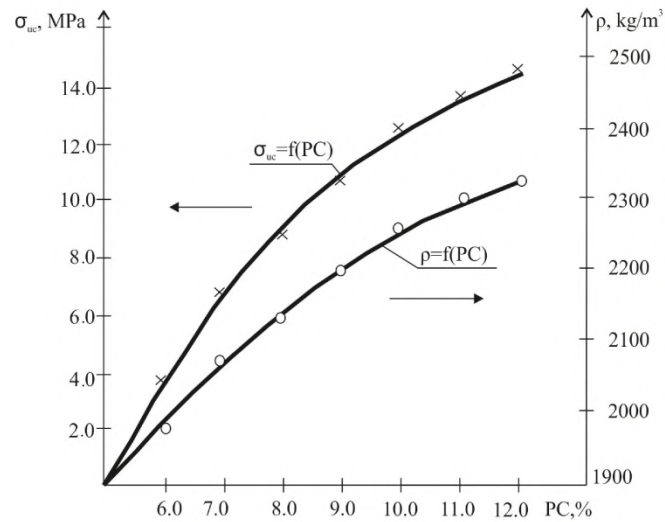


**Figure 3. Relationship between density and strength of CBM and the cement content at optimum moisture.**

It was shown that with increasing content of water and binder, the technological hardness (workability) of mixes decreases (Figure 4). This can be explained by the fact that crushed stone mixes of low-strength carbonate rocks are characterized by significant hydrophilicity and water absorption, due to the developed specific surface and high porosity. As a result of the liquid phase absorption by aggregate a sharp loss of workability of mixture occurs after preparation of CBM. The minimum mixture hardness is achieved at a level of 5–6 s with a 15 % water content and a 11–12 % cement content. The highest value of technological hardness (200–210 s) is typical for mixes with a minimum content of water of 7 % and cement of 6–7 %. Increasing the water content in CBM for achieving the required workability helps to reduce the density and strength of material, and increasing the cement content reduces the deformability and crack resistance.

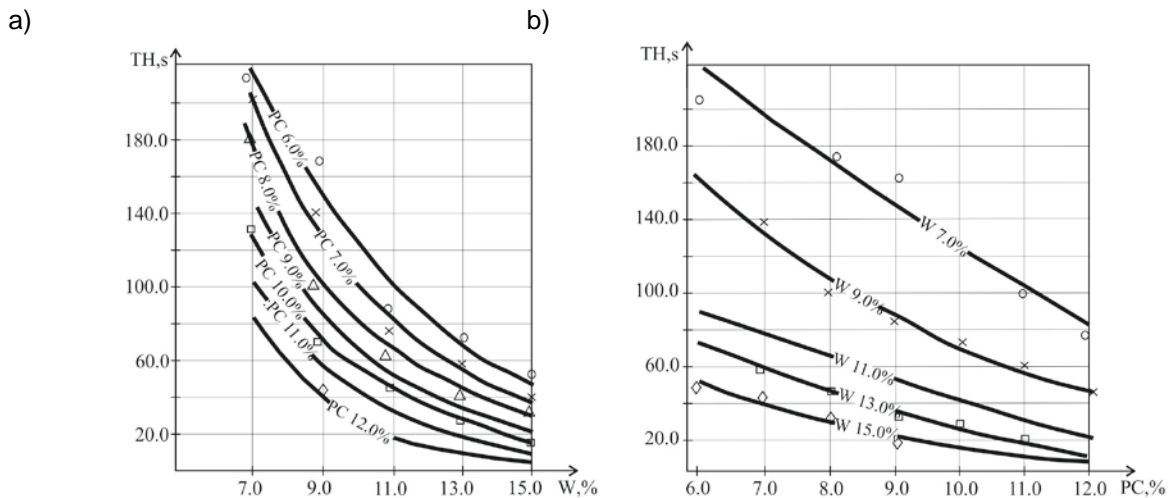


**Figure 4. Relationship between technological hardness and content of water (a) and cement (b)**

To solve these problems, especially at low and subzero temperatures, CBM was modified with complex functional additives based on sodium formate, calcium chloride and C-3 superplasticizer.

The influence of complex additives on the hardness and density of mixes was studied. It was found that for various moistures of mixes with a constant content of C-3 additive (2 %), the density significantly depends on the FN content and is practically not associated with a change in CC additives (Figure 5). The contours of technological hardness repeat the shape of the density contours. FN additives promote density increase and improve the CBM workability. In particular, with FN introduction, the hardness decreased for three times from 42 s to 14 s. The influence of calcium chloride on workability was not significant. Consequently, the presence of FN in antifreeze compositions increases the constructability of mixes, and density increase provides an improvement in the structural and mechanical characteristics of the material.

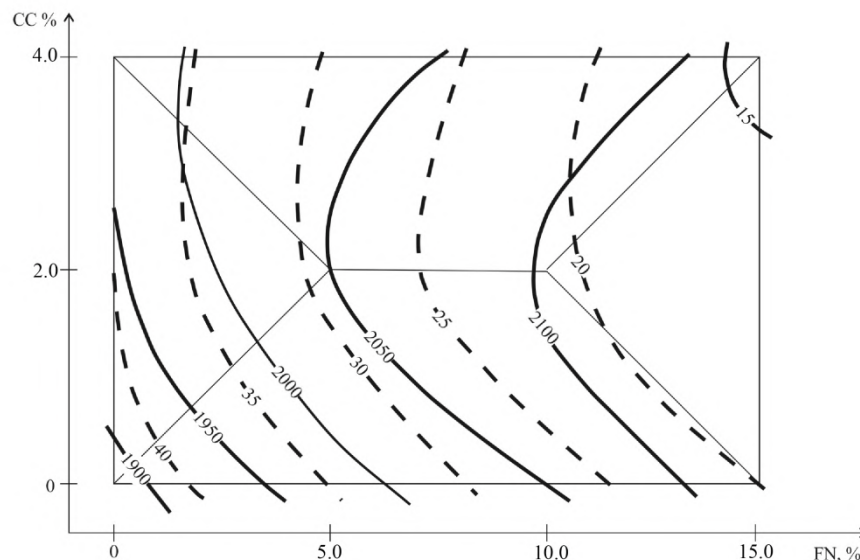


**Figure 5. Relationship between FN and CC content on the technological hardness (-----) and density ( \_\_\_\_\_ ) of CBM at SP = const.**

Workability of CBM is associated with duration and temperature aging of mixes (Table 5). When the air temperature drops to  $-15\text{ }^{\circ}\text{C}$ , a decrease in workability indicators begins earlier after preparation and occurs more intensively than at temperature of  $-5\text{ }^{\circ}\text{C}$ . Three-hour aging of mixes until the moment of compaction increases the hardness of mixes by 5–6 times, which limits the constructability time of mixes and shortens the technological cycle period. Preservation of the required indicators of mix workability in time we call the constructability.

**Table 5. Relationship between temperature and FN content and the CBM technological hardness change in time.**

Additives content, % of cement mass			Temperature, $^{\circ}\text{C}$	Technological hardness of CBM, s, after preparation of mixes, min								
FN	CC	SP		0	20	40	60	90	120	150	180	
-	-	-	+20	45	54	66	85	98	114	130	>200	
7	2	2	-5	13	20	25	31	38	46	55	64	
5	2	2	-5	15	22	29	36	45	56	68	79	
3	2	2	-5	17	24	30	38	47	58	73	86	
7	2	2	-15	13	21	30	41	50	67	80	85	
5	2	2	-15	15	24	36	52	60	70	83	90	
3	2	2	-15	17	25	40	55	66	73	84	91	
3	2	2	+20	17	24	36	44	60	70	98	136	

Exploration of the influence of complex additives on preserving the CBM constructability time showed that FN additives contribute to the stability of this process (Table 5). The hardness of mixes without additives is 1.5 times higher than that for mixes with additives, and is 2–3 times higher than that of mixes aged at subzero temperatures. Thus, antifreeze components contribute to the extension of the CBM constructability time at low and subzero temperatures. This ensures performing high-quality work on the construction of pavement layers and achieving the required construction and technical properties of road construction materials.

The positive influence of the developed functional additives on the CBM technological properties at low and subzero temperatures occurs mainly due to the preservation of the liquid phase in the optimal amount from the point of view of gaining strength and ensuring the constructability time of mixture. The batched water for CBM pavement layers is a solution of complex functional additives. As it is known, when additives are dissolved, solvates are formed, which are compounds of particles of a dissolved substance with water molecules. In case of using the developed additives, along with lowering the freezing temperature, plasticization of mixes occurs. Lowering the freezing point and workability depends on the number of bound water molecules, i.e. the composition of the solvates, and the strength of this bond depends on the electrical properties of the particles, their size and concentration of solution, which is provided by the complexity and functionality of the used additives.

The practical significance of the obtained results is the possibility to regulate the CBM properties for road pavement, taking into account technological factors under various weather and climatic conditions of work, which is achieved by using optimal mixes with complex additives.

#### 4. Conclusions

1. The optimum moistures of cement-bound mixes (10.5-11.5%) have been established, which ensure the maximum material densities from 2000 to 2300 kg/m<sup>3</sup>.
2. The recommended range of Portland cement content by weight of crushed stone mixture (6.0 %–9.0 %) was determined, which provides the necessary level of strength (from  $\sigma_{uc} = 4.0$  MPa at  $\rho = 2000$  kg/m<sup>3</sup> to  $\sigma_{uc} = 10.0$  MPa at  $\rho = 2200$  kg/m<sup>3</sup>) for structural layers of pavement.
3. It was found that the presence of sodium formate in complex functional additives improves the constructability of mixes, and an increase in density provides an improvement in the structural and mechanical characteristics of material.
4. The influence of complex additives on preserving the constructability time of cement-bound mixes was studied. It was shown that sodium formate additives contribute to the stability of this process. The influence of temperature and the amount of functional additives on the constructability time of the use of cement-bound mixes is considered. It was established that additives contribute to maintaining the required workability of mixes at negative temperatures (up to -15 °C) for 1–2 hours and provide the necessary conditions for efficient work without reducing their quality and reducing the technological cycle period.
5. The positive influence of the developed functional additives on the technological properties of CBM at low and subzero temperatures occurs mainly due to the formation in the liquid phase of solvates, i.e. the compounds of solute particles with water molecules that lower its freezing temperature and plasticize the mixture.
6. The practical significance of the obtained results is the possibility of regulating the CBM properties for road pavement, taking into account technological factors under various weather and climatic conditions of work, which is achieved by using optimal mixes with complex additives.

#### References

1. Li, K., Stroeve, M., Stroeve, P., Sluys, L.J. Effects of technological parameters on permeability estimation of partially saturated cement paste by a DEM approach. *Cement and Concrete Composites*. 2017. 84. Pp. 222–231. DOI: 10.1016/j.cemconcomp.2017.09.013.
2. McElroy, P., Emadi, H., Surowiec, K., Casadonte, D.J. Mechanical, rheological, and stability performance of simulated in-situ cured oil well cement slurries reinforced with alumina nanofibers. *Journal of Petroleum Science and Engineering*. 2019. 183. No. 106415. DOI: 10.1016/j.petrol.2019.106415.
3. Kostrzanowska-Siedlarz, A., Gołaszewski, J. Rheological properties and the air content in fresh concrete for self-compacting high performance concrete. *Construction and Building Materials*. 2015. 94. Pp. 555–564 DOI: 10.1016/j.conbuildmat.2015.07.051.
4. Asghari, A.A., Feys, D., De Schutter, G. Time evolution of rheology of cement pastes affected by mixture design and mixing procedure. *ACI Materials Journal*. 2018. 115(5). Pp. 707-716. DOI:10.14359/51702348.
5. Deng, X.J., Klein, B., Zhang, J.X., Hallbom, D., de Wit, B. Time-dependent rheological behaviour of cemented backfill mixture. *International Journal of Mining, Reclamation and Environment*. 2018. 32(3). Pp. 145–162. DOI: 10.1080/17480930.2016.1239305.
6. Saxena, S.K., Kumar, M., Singh, N.B. Effect of Alccofine powder on the properties of Pond fly ash based Geopolymer mortar under different conditions. *Environmental Technology and Innovation*. 2018. 9. Pp. 232–242. DOI: 10.1016/j.eti.2017.12.010.
7. Kavyateja, B.V., Guru Jawahar, J., Sashidhar, C. Investigation on ternary blended self-compacting concrete using fly ash and alccofine. *International Journal of Recent Technology and Engineering*. 2019. 7(5). Pp. 447–451.
8. Visser, A.T. Potential of South African road technology for application in China. *Journal of Traffic and Transportation Engineering (English Edition)*. 2017. 4(2). Pp. 113–117. DOI: 10.1016/j.jtte.2017.03.004.
9. Öz, H.Ö. Properties of pervious concretes partially incorporating acidic pumice as coarse aggregate. *Construction and Building Materials*. 2018. 166. Pp. 601–609 DOI: 10.1016/j.conbuildmat.2018.02.010.
10. Mymrin, V., Aibuldinov, E.K., Alekseev, K., Petukhov, V., Avanci, M.A., Kholodov, A., Taskin, A., Catai, R.E., Iarozinski N, A. Efficient road base material from Kazakhstan's natural loam strengthened by ground cooled ferrous slag activated by lime production waste. *Journal of Cleaner Production*. 2019. 231. Pp. 1428–1436. DOI: 10.1016/j.jclepro.2019.05.250.
11. Poulidakos, L.D., Papadaskalopoulou, C., Hofko, B., Gschösser, F., Cannone Falchetto, A., Bueno, M., Arraigada, M., Sousa, J., Ruiz, R., Petit, C., Loizidou, M., Partl, M.N. Harvesting the unexplored potential of European waste materials for road construction. *Resources, Conservation and Recycling*. 2017. 116. Pp. 32–44. DOI: 10.1016/j.resconrec.2016.09.008.
12. Vishwakarma, V., Ramachandran, D. Green Concrete mix using solid waste and nanoparticles as alternatives – A review. 2018 *Construction and Building Materials*. 162. Pp. 96–103. DOI: 10.1016/j.conbuildmat.2017.11.174.
13. Mengue, E., Mroueh, H., Lancelot, L., Medjo Eko, R. Physicochemical and consolidation properties of compacted lateritic soil treated with cement. *Soils and Foundations*. 2017. 57(1). Pp. 60–79. DOI: 10.1016/j.sandf.2017.01.005.
14. Dolżycki, B., Jaskuła, P. Review and evaluation of cold recycling with bitumen emulsion and cement for rehabilitation of old pavements *Journal of Traffic and Transportation Engineering (English Edition)*. 2019. 6(4). Pp. 311–323. DOI: 10.1016/j.jtte.2019.02.002.
15. Anggraini, V., Asadi, A., Syamsir, A., Huat, B.B.K. Three point bending flexural strength of cement treated tropical marine soil reinforced by lime treated natural fiber. *Measurement: Journal of the International Measurement Confederation*. 2017. 111. Pp. 158–166. DOI: 10.1016/j.measurement.2017.07.045.

16. Nguyen, L., Fatahi, B., Khabbaz, H. Predicting the Behaviour of Fibre Reinforced Cement Treated Clay. *Procedia Engineering* 2016. 143. Pp. 153–160. DOI: 10.1016/j.proeng.2016.06.020.
17. Rezaeian, M., Ferreira, P.M.V., Ekinci, A. Mechanical behaviour of a compacted well-graded granular material with and without cement. *Soils and Foundations*. 2019. 59(3). Pp. 687–698. DOI: 10.1016/j.sandf.2019.02.006.
18. Amini, O., Ghasemi, M. Laboratory study of the effects of using magnesium slag on the geotechnical properties of cement stabilized soil. *Construction and Building Materials*. 2019. 223. Pp. 409–420. DOI: 10.1016/j.conbuildmat.2019.07.011.
19. MolaAbasi, H., Saberian, M., Li, J. Prediction of compressive and tensile strengths of zeolite-cemented sand using porosity and composition. *Construction and Building Materials*. 2019. 202. Pp. 784–795. DOI: 10.1016/j.conbuildmat.2019.01.065.
20. Dołzycki, B., Jaczewski, M., Szydłowski, C. The Influence of Binding Agents on Stiffness of Mineral-cement-emulsion Mixtures. *Procedia Engineering*. 2017. 172. Pp. 239–246. DOI: 10.1016/j.proeng.2017.02.103.
21. Kurta, I., Zemlyansky, V. Preconditions for Technological Development of the Construction Industry of the North for the Arrangement of the Mineral Complex of the Russian Arctic. *Procedia Engineering*. 2016. 165. Pp. 1542–1546. DOI: 10.1016/j.proeng.2016.11.891.
22. Shirzadi Javid, A.A., Arjmandi Nejad, M.A. Packing density and surface finishing condition effects on the mechanical properties of various concrete pavements containing cement replacement admixtures. *Construction and Building Materials*. 2017. 141. Pp. 307–314. DOI: 10.1016/j.conbuildmat.2017.03.021.
23. Shen, A., Lin, S., Guo, Y., He, T., Lyu, Z. Relationship between flexural strength and pore structure of pavement concrete under fatigue loads and Freeze-thaw interaction in seasonal frozen regions. *Construction and Building Materials*. 2018. 174. Pp. 684–692. DOI: 10.1016/j.conbuildmat.2018.04.165.
24. Karagol, F., Demirboga, R., Khushefati, W.H. Behavior of fresh and hardened concretes with antifreeze admixtures in deep-freeze low temperatures and exterior winter conditions. *Construction and Building Materials*. 2015. 76. Pp. 388–395. DOI: 10.1016/j.conbuildmat.2014.12.011.
25. Aïtcin, P.-C. Historical background of the development of concrete admixtures. *Science and Technology of Concrete Admixtures*. 2016. Pp. 41–52. DOI: 10.1016/B978-0-08-100693-1.09003-2
26. Polat, R. The effect of antifreeze additives on fresh concrete subjected to freezing and thawing cycles. *Cold Regions Science and Technology*. 2016. 127. Pp. 10–17. DOI: 10.1016/j.coldregions.2016.04.008.
27. Çullu, M., Arslan, M. The effects of antifreeze use on physical and mechanical properties of concrete produced in cold weather. *Composites Part B: Engineering*. 2013. 50. Pp. 202–209. DOI: 10.1016/j.compositesb.2013.02.012.
28. Demirboğa, R., Karagöl, F., Polat, R., Kaygusuz, M.A. The effects of urea on strength gaining of fresh concrete under the cold weather conditions. *Construction and Building Materials*. 2014. 64. Pp. 114–120. DOI: 10.1016/j.conbuildmat.2014.04.008.
29. Çullu, M., Arslan, M. The effects of chemical attacks on physical and mechanical properties of concrete produced under cold weather conditions. *Construction and Building Materials*. 2014. 57. Pp. 53–60. DOI: 10.1016/j.conbuildmat.2014.01.072.
30. Xie, N., Dang, Y., Shi, X. New insights into how  $MgCl_2$  deteriorates Portland cement concrete. *Cement and Concrete Research*. 2019. 120. Pp. 244–255. DOI: 10.1016/j.cemconres.2019.03.026.
31. Hartmann, A., Khakhutov, M., Buhl, J.C. Hydrothermal synthesis of CSH-phases (tobermorite) under influence of Ca-formate. *Materials Research Bulletin*. 2014. 51. Pp. 389–396. DOI: 10.1016/j.materresbull.2013.12.030.

### **Contacts:**

*Evgenii Vdovin, +79196259171; vdovin007@mail.ru*

*Victor Stroganov, +79872901642; svf08@mail.ru*

© Vdovin, E.A., Stroganov, V.F., 2020



DOI: 10.18720/MCE.93.12

## Влияние технологических факторов на свойства цементощебеночных смесей для дорожных одежд

**Е.А. Вдовин, В.Ф. Строганов**

*Казанский государственный архитектурно-строительный университет, г. Казань, Россия,*

\* E-mail: [vdovin007@mail.ru](mailto:vdovin007@mail.ru)

**Ключевые слова:** цементощебеночные смеси, формиат натрия, технологические факторы, удобоукладываемость, плотность, влажность, время технологичности смеси

**Аннотация.** Получены результаты исследований влияния технологических факторов на свойства цементощебеночных смесей, твердеющих при положительных и отрицательных температурах в конструкциях дорожных одежд. Установлены зависимости плотности и прочности цементощебеночных смесей от содержания цемента и воды. Определены значения оптимальной влажности смесей (10,5–11,5 %), обеспечивающие получение максимальных значений плотности материала от 2000 до 2300 кг/м<sup>3</sup> при содержании цемента от 6 до 12 % от массы щебеночной смеси. Изучено влияние комплексных противоморозных добавок на технологические свойства: плотность, удобоукладываемость, время сохранения технологичности смеси. Показано, что добавки формиата натрия способствуют повышению плотности смеси и снижению технологической жесткости (удобоукладываемости) смеси в условиях положительных и отрицательных температур. Рассмотрено влияние температуры и количества функциональных добавок на время технологичности применения цементощебеночных смесей. Установлено, что добавки способствуют сохранению требуемой удобоукладываемости смесей при отрицательных температурах (до (-15)°C) в течение 1–2 часов и обеспечивают необходимые условия для эффективного производства работ без снижения их качества и уменьшения периода технологического цикла

### Литература

- Li K., Stroeven M., Stroeven P., Sluys L.J. Effects of technological parameters on permeability estimation of partially saturated cement paste by a DEM approach // *Cement and Concrete Composites*. 2017. 84. Pp. 222–231. DOI: 10.1016/j.cemconcomp.2017.09.013.
- McElroy P., Emadi H., Surowiec K., Casadonte D.J. Mechanical, rheological, and stability performance of simulated in-situ cured oil well cement slurries reinforced with alumina nanofibers // *Journal of Petroleum Science and Engineering*. 2019. 183. No. 106415. DOI: 10.1016/j.petrol.2019.106415.
- Kostrzanowska-Siedlarz A., Gołaszewski J. Rheological properties and the air content in fresh concrete for self compacting high performance concrete // *Construction and Building Materials*. 2015. 94. Pp. 555–564 DOI: 10.1016/j.conbuildmat.2015.07.051.
- Asghari A.A., Feys D., De Schutter G. Time evolution of rheology of cement pastes affected by mixture design and mixing procedure // *ACI Materials Journal*. 2018. 115(5). Pp. 707–716. DOI:10.14359/51702348.
- Deng X.J., Klein B., Zhang J.X., Hallbom D., de Wit B. Time-dependent rheological behaviour of cemented backfill mixture // *International Journal of Mining, Reclamation and Environment*. 2018. 32(3). Pp. 145–162. DOI: 10.1080/17480930.2016.1239305.
- Saxena S.K., Kumar M., Singh N.B. Effect of Alccofine powder on the properties of Pond fly ash based Geopolymer mortar under different conditions // *Environmental Technology and Innovation*. 2018. 9. Pp. 232–242. DOI: 10.1016/j.eti.2017.12.010.
- Kavyateja B.V., Guru Jawahar J., Sashidhar C. Investigation on ternary blended self compacting concrete using fly ash and alccofine // *International Journal of Recent Technology and Engineering*. 2019. 7(5). Pp. 447–451.
- Visser A.T. Potential of South African road technology for application in China // *Journal of Traffic and Transportation Engineering (English Edition)*. 2017. 4(2). Pp. 113–117. DOI: 10.1016/j.jtte.2017.03.004.
- Öz H.Ö. Properties of pervious concretes partially incorporating acidic pumice as coarse aggregate. *Construction and Building Materials*. 2018. 166. Pp. 601–609 DOI: 10.1016/j.conbuildmat.2018.02.010.
- Mymrin V., Aibuldinov E.K., Alekseev K., Petukhov V., Avanci M.A., Kholodov A., Taskin A., Catai R.E., Iarozinski N.A. Efficient road base material from Kazakhstan's natural loam strengthened by ground cooled ferrous slag activated by lime production waste // *Journal of Cleaner Production*. 2019. 231. Pp. 1428–1436. DOI: 10.1016/j.jclepro.2019.05.250.
- Poulikakos L.D., Papadaskalopoulou C., Hofko B., Gschösser F., Cannone Falchetto A., Bueno M., Arraigada M., Sousa J., Ruiz R., Petit C., Loizidou M., Partl M.N. Harvesting the unexplored potential of European waste materials for road construction // *Resources, Conservation and Recycling*. 2017. 116. Pp. 32–44. DOI: 10.1016/j.resconrec.2016.09.008.
- Vishwakarma V., Ramachandran D. Green Concrete mix using solid waste and nanoparticles as alternatives – A review // *Construction and Building Materials*. 2018. 162, Pp. 96–103. DOI: 10.1016/j.conbuildmat.2017.11.174.
- Mengue E., Mroueh H., Lancelot L., Medjo Eko R. Physicochemical and consolidation properties of compacted lateritic soil treated with cement // *Soils and Foundations*. 2017. 57(1). Pp. 60–79. DOI: 10.1016/j.sandf.2017.01.005.

14. Dołżycki B., Jaskuła P. Review and evaluation of cold recycling with bitumen emulsion and cement for rehabilitation of old pavements // Journal of Traffic and Transportation Engineering (English Edition). 2019. 6(4). Pp. 311–323. DOI: 10.1016/j.jtte.2019.02.002.
15. Anggraini V., Asadi A., Syamsir A., Huat B.B.K. Three point bending flexural strength of cement treated tropical marine soil reinforced by lime treated natural fiber // Measurement: Journal of the International Measurement Confederation. 2017. 111. Pp. 158–166. DOI: 10.1016/j.measurement.2017.07.045.
16. Nguyen L., Fatahi B., Khabbaz H. Predicting the Behaviour of Fibre Reinforced Cement Treated Clay // Procedia Engineering. 2016. 143. Pp. 153–160. DOI: 10.1016/j.proeng.2016.06.020.
17. Rezaeian M., Ferreira P.M.V., Ekinici A. Mechanical behaviour of a compacted well-graded granular material with and without cement // Soils and Foundations. 2019. 59(3). Pp. 687–698. DOI: 10.1016/j.sandf.2019.02.006.
18. Amini O., Ghasemi M. Laboratory study of the effects of using magnesium slag on the geotechnical properties of cement stabilized soil // Construction and Building Materials. 2019. 223. Pp. 409–420. DOI: 10.1016/j.conbuildmat.2019.07.011.
19. MolaAbasi H., Saberian M., Li J. Prediction of compressive and tensile strengths of zeolite-cemented sand using porosity and composition // Construction and Building Materials. 2019. 202. Pp. 784–795. DOI: 10.1016/j.conbuildmat.2019.01.065.
20. Dołżycki B., Jaczewski M., Szydłowski C. The Influence of Binding Agents on Stiffness of Mineral-cement-emulsion Mixtures // Procedia Engineering. 2017. 172. Pp. 239–246. DOI: 10.1016/j.proeng.2017.02.103.
21. Kurta I., Zemlyansky V. Preconditions for Technological Development of the Construction Industry of the North for the Arrangement of the Mineral Complex of the Russian Arctic // Procedia Engineering. 2016. 165. Pp. 1542–1546. DOI: 10.1016/j.proeng.2016.11.891.
22. Shirzadi Javid A.A., Arjmandi Nejad M.A. Packing density and surface finishing condition effects on the mechanical properties of various concrete pavements containing cement replacement admixtures // Construction and Building Materials. 2017. 141. Pp. 307–314. DOI: 10.1016/j.conbuildmat.2017.03.021.
23. Shen A., Lin S., Guo Y., He T., Lyu Z. Relationship between flexural strength and pore structure of pavement concrete under fatigue loads and Freeze-thaw interaction in seasonal frozen regions // Construction and Building Materials. 2018. 174. Pp. 684–692. DOI: 10.1016/j.conbuildmat.2018.04.165.
24. Karagöl F., Demirboga R., Khushefati W.H. Behavior of fresh and hardened concretes with antifreeze admixtures in deep-freeze low temperatures and exterior winter conditions // Construction and Building Materials. 2015. 76. Pp. 388–395. DOI: 10.1016/j.conbuildmat.2014.12.011.
25. Aïtcin P.-C. Historical background of the development of concrete admixtures // Science and Technology of Concrete Admixtures. 2016. Pp. 41–52. DOI: 10.1016/B978-0-08-100693-1.09003-2
26. Polat R. The effect of antifreeze additives on fresh concrete subjected to freezing and thawing cycles // Cold Regions Science and Technology. 2016. 127. Pp. 10–17. DOI: 10.1016/j.coldregions.2016.04.008.
27. Çullu M., Arslan M. The effects of antifreeze use on physical and mechanical properties of concrete produced in cold weather // Composites Part B: Engineering. 2013. 50. Pp. 202–209. DOI: 10.1016/j.compositesb.2013.02.012.
28. Demirboğa R., Karagöl F., Polat R., Kaygusuz M.A. The effects of urea on strength gaining of fresh concrete under the cold weather conditions // Construction and Building Materials. 2014. 64. Pp. 114–120. DOI: 10.1016/j.conbuildmat.2014.04.008.
29. Çullu M., Arslan M. The effects of chemical attacks on physical and mechanical properties of concrete produced under cold weather conditions // Construction and Building Materials. 2014. 57. Pp. 53–60. DOI: 10.1016/j.conbuildmat.2014.01.072.
30. Xie N., Dang Y., Shi X. New insights into how MgCl<sub>2</sub> deteriorates Portland cement concrete // Cement and Concrete Research. 2019. 120. Pp. 244–255. DOI: 10.1016/j.cemconres.2019.03.026.
31. Hartmann A., Khakhutov M., Buhl J.C. Hydrothermal synthesis of CSH-phases (tobermorite) under influence of Ca-formate // Materials Research Bulletin. 2014. 51. Pp. 389–396. DOI: 10.1016/j.materresbull.2013.12.030.

**Контактные данные:**

*Евгений Анатольевич Вдовин, +79196259171; vdovin007@mail.ru*

*Виктор Федорович Строганов, +79872901642; svf08@mail.ru*

© Вдовин Е.А., Строганов В.Ф., 2020



**ПОЛИТЕХ**  
Санкт-Петербургский  
политехнический университет  
Петра Великого

Инженерно-строительный институт  
Центр дополнительных профессиональных программ

195251, г. Санкт-Петербург, Политехническая ул., 29,  
тел/факс: 552-94-60, [www.stroikursi.spbstu.ru](http://www.stroikursi.spbstu.ru),  
[stroikursi@mail.ru](mailto:stroikursi@mail.ru)

Приглашает специалистов проектных и строительных организаций,  
не имеющих базового профильного высшего образования  
на курсы профессиональной переподготовки (от 500 часов)  
по направлению «Строительство» по программам:

**П-01 «Промышленное и гражданское строительство»**

Программа включает учебные разделы:

- Основы строительного дела
- Инженерное оборудование зданий и сооружений
- Технология и контроль качества строительства
- Основы проектирования зданий и сооружений
- Автоматизация проектных работ с использованием AutoCAD
- Автоматизация сметного дела в строительстве
- Управление строительной организацией
- Управление инвестиционно-строительными проектами. Выполнение функций технического заказчика

**П-02 «Экономика и управление в строительстве»**

Программа включает учебные разделы:

- Основы строительного дела
- Инженерное оборудование зданий и сооружений
- Технология и контроль качества строительства
- Управление инвестиционно-строительными проектами. Выполнение функций технического заказчика и генерального подрядчика
- Управление строительной организацией
- Экономика и ценообразование в строительстве
- Управление строительной организацией
- Организация, управление и планирование в строительстве
- Автоматизация сметного дела в строительстве

**П-03 «Инженерные системы зданий и сооружений»**

Программа включает учебные разделы:

- Основы механики жидкости и газа
- Инженерное оборудование зданий и сооружений
- Проектирование, монтаж и эксплуатация систем вентиляции и кондиционирования
- Проектирование, монтаж и эксплуатация систем отопления и теплоснабжения
- Проектирование, монтаж и эксплуатация систем водоснабжения и водоотведения
- Автоматизация проектных работ с использованием AutoCAD
- Электроснабжение и электрооборудование объектов

**П-04 «Проектирование и конструирование зданий и сооружений»**

Программа включает учебные разделы:

- Основы сопротивления материалов и механики стержневых систем
- Проектирование и расчет оснований и фундаментов зданий и сооружений
- Проектирование и расчет железобетонных конструкций
- Проектирование и расчет металлических конструкций
- Проектирование зданий и сооружений с использованием AutoCAD
- Расчет строительных конструкций с использованием SCAD Office

**П-05 «Контроль качества строительства»**

Программа включает учебные разделы:

- Основы строительного дела
- Инженерное оборудование зданий и сооружений
- Технология и контроль качества строительства
- Проектирование и расчет железобетонных конструкций
- Проектирование и расчет металлических конструкций
- Обследование строительных конструкций зданий и сооружений
- Выполнение функций технического заказчика и генерального подрядчика

По окончании курса слушателю выдается диплом о профессиональной переподготовке  
установленного образца, дающий право на ведение профессиональной деятельности

